University of Kent

Applied Optics Group, School of Physical Sciences

Dispersion-Tuned Mode-Locking and Multi-Harmonic Operation for Swept-Source Optical Coherence Tomography

by

Rene Riha

A thesis submitted in partial fulfilment
of the requirements for the degree of
Doctor of Philosophy

Supervised by: Prof. Adrian Podoleanu

July 2025

Declaration of authorship

I declare that this thesis, submitted for the degree of Doctor of Philosophy, is my own work and that all contributions from other researchers have been appropriately acknowledged.

Signed: _____ **Date:** _____

Abstract

Swept sources are central to optical coherence tomography (OCT), which enabled not only high speeds but also longer imaging depths than in the spectrometer-based OCT methods. Among the various types, dispersion-tuned mode-locked (DTML) lasers offer simplified and cost-effective swept source designs. While standard DTML operation has been demonstrated across most wavelength ranges relevant to OCT imaging, its limitations in sweep rate and coherence performance remain a challenge. Moreover, a broader theoretical and experimental understanding of the multi-harmonic DTML operation has been lacking.

This thesis presents a comprehensive theoretical framework and experimental validation of both single- and multi-harmonic DTML regimes. Starting from the analysis of dispersion properties in fibre laser cavities, the principle of wavelength tuning in standard DTML lasers is described. By adopting a spectral filtering approach, notions of the saturation and one round trip operations are introduced, showing trade-offs between the achievable tuning bandwidth and coherence performance. The work then extends to the generalised multi-harmonic DTML operation, introducing the many sweep cycles mathematical framework and establishing the conditions under which wavelength tuning is achieved when sweeping over multiple harmonic bands. Building on the spectral filtering description, the tuning bandwidth limits for the multi-harmonic DTML are derived, showing trade-offs between the achievable tuning bandwidth and coherence performance in this sweeping regime. In the last theoretical chapter, the trends in mathematical modelling of DTML lasers are reviewed, extended with original contributions. Lastly, using the discrete modelling approach, the behaviour of spectral linewidth in a DTML laser as a function of various cavity parameters is investigated.

Experimental work includes the development of three DTML swept sources operating at 850 nm, 1550 nm, 1 µm, respectively, with the latter two demonstrating the multi-harmonic operation at sweep rates approaching 1 MHz. By employing the final 1 µm swept source, the first OCT images employing a multi-harmonic DTML swept laser are captured, and the theoretical predictions regarding bandwidth-coherence trade-offs are

experimentally validated. A set of optimisation steps to improve the multi-harmonic DTML operation to guide the future development is proposed as well.

Given the findings in this thesis, the multi-harmonic DTML laser emerges as a promising fully akinetic, simple in design, low cost solution for megahertz SS-OCT applications.

Acknowledgements

I would like to express my most sincere gratitude to my supervisor Prof. Adrian Podoleanu for his guidance, patience, and insight throughout this project. His scientific skepticism and encouragement during moments of doubt made the theory of the multi-harmonic operation deliverable into a coherent body of work. I am also grateful to Dr. Alejandro Martínez Jiménez for his assistance in OCT images processing. I extend my thanks to my colleague Dr. Ramona Cernat, who served as the NETLAS administrator for my position during my project. This research was supported by the European Commission under Grant Agreement NETLAS-860807, whose support is gratefully acknowledged. Lastly, I would like to thank my family and friends for their emotional support.

Contents

1 Introduction to the thesis **1**

1.1 Why OCT? 1

1.2 Motivation of the thesis 4

1.3 Thesis structure 6

Bibliography 9

2 Optical coherence tomography **15**

2.1 OCT principle 16

2.2 Time-domain OCT (TD-OCT) 21

2.3 Fourier-domain OCT (FD-OCT) 24

Bibliography 29

3 Swept sources for OCT **31**

3.1 Mechanical-based swept sources 33

3.1.1 Mechanically-scanned grating-based swept lasers 33

3.1.2 Micro-electro-mechanical system vertical-cavity surface-emitting lasers (MEMS-VCSELs) 37

3.1.3 Fourier-domain mode-locked (FDML) swept lasers 38

3.2 Akinetic-based swept sources 40

3.2.1 Acousto-optic based swept lasers 40

3.2.2 KTN-scanned grating-based swept lasers 41

3.2.3 All-semiconductor design swept lasers 43

3.2.4 Time-stretching (dispersive Fourier transform) swept lasers 44

3.2.5 Stretched-pulse mode-locked (SPML) swept lasers 45
Bibliography 49

4 Standard single-harmonic dispersion-tuned mode-locked (DTML) swept lasers 59

4.1 Dispersion in optical fibres 59
4.1.1 Chirped fibre Bragg grating (cFBG) 61
4.2 Principle of DTML 63
4.3 Spectral filtering and dynamic tuning bandwidth limits 67
4.4 DTML swept sources 73
4.4.1 1st generation 73
4.4.2 2nd generation 76
4.4.3 3rd generation 78
Bibliography 81

5 From single-harmonic to multi-harmonic DTML 85

5.1 Previous development in the multi-harmonic DTML 85
5.2 Many sweep cycles mathematical framework 87
5.3 Multi-harmonic DTML 93
5.4 Spectral filtering and dynamic tuning bandwidth limits 98
5.5 Comparison of the multi-harmonic DTML with FDML 102
Bibliography 107

6 Mathematical modelling in DTML lasers 109

6.1 Complex envelope and temporal chirp 109
6.2 Average model 111
6.3 Discrete model 113
6.3.1 Loss 114
6.3.2 Dispersion 115
6.3.3 Fibre delay 117
6.3.4 SOA amplification 118

6.3.5 Amplitude modulation . . . 119
6.3.6 Phase noise . . . 122
6.4 Simulation results . . . 123
6.4.1 The amount of dispersion in the cavity . . . 124
6.4.2 The modulation window width . . . 128
Bibliography . . . 132

7 Experimental validations **135**
7.1 An approximative cavity dispersion assessment exploiting DTML . . . 135
7.1.1 Methods . . . 136
7.1.2 Experimental setups and results . . . 136
7.1.3 Conclusion . . . 139
7.2 DTML swept source at 850 nm for OCT using a cFBG and pulse modulation technique . . . 140
7.2.1 Experimental setup . . . 140
7.2.2 Results . . . 144
7.2.3 Conclusion . . . 147
7.3 A 900 kHz multi-harmonic DTML swept source at 1550 nm for OCT using a cFBG and an intensity modulator . . . 148
7.3.1 Experimental setup . . . 148
7.3.2 Results . . . 150
7.3.3 Conclusion . . . 155
7.4 A 1 MHz multi-harmonic DTML swept source at 1 µm for OCT . . . 156
7.4.1 Experimental setup . . . 156
7.4.2 Results . . . 159
7.4.3 Conclusion . . . 167
Bibliography . . . 168

8 Conclusion **171**
Bibliography . . . 177

A Peer-reviewed articles published during the doctoral course **179**

B Mathematical modelling code in MATLAB **181**

List of Figures

1.1 Comparison of ultrasound modality, OCT, and confocal microscopy relative to their penetration depths and imaging axial resolutions [3]. 2

1.2 Two representative OCT images captured with the custom-designed OCT system described in Sec. 7.4. **Top:** A finger tip. **Bottom:** Retina. 3

1.3 A ring DTML laser cavity. SOA: semiconductor optical amplifier, cFBG: chirped fibre Bragg grating, CIRC: circulator, IM: intensity modulator. . . 5

1.4 Multi-harmonic DTML laser cavities. **(a)** First multi-harmonic DTML laser at 1550 nm [39]. **(b)** First multi-harmonic DTML laser at 850 nm [38]. SOA: semiconductor optical amplifier, SG: signal generator, ISO: optical isolator, DC: directional coupler, DCF: dispersion compensation fibre, FRM: Faraday rotator mirror, CIRC: optical circulator. 6

2.1 Schematic of a Michelson interferometer used in OCT. 16

2.2 Spectral OCT interferograms [1, 2, 6]. **Left:** Single sample reflector spectral interferogram with the fringe amplitude of $\sqrt{R_{\mathrm{R}}R_{\mathrm{S},m}}$ and spectral period of $\pi/(z_{\mathrm{R}}-z_{\mathrm{S},m})$ (see Eq. Eq. (2.2)). **Right:** Spectral interferogram of two sample reflectors. 18

2.3 Schematic of generic OCT sample arm optics [1]. θ: scan angle, f: objective lens focal length, Δz_{conf}: confocal axial field of view, Δx_{conf}: confocal lateral field of view, δx: lateral resolution, δz: interferometric axial resolution. . . 20

2.4 Schematic of different OCT scanning orientations relatively to the optical axis z. 20

2.5 Configuration of a TD-OCT system with a reconstructed A-scan profile. . . 21

2.6 Configuration of an Sp-OCT system with a reconstructed A-scan profile. . 25

2.7 Configuration of an SS-OCT system with a reconstructed A-scan profile. . 26

3.1 Two fundamental laser configurations used in mechanically-scanned grating-based tunable lasers [2]. LD: laser diode, L: lens, DG: diffraction grating, M: mirror/deflector. 34

3.2 Mechanically-scanned grating-based tunable lasers implemented in fibre cavities. **(a)** Littman–Metcalf configuration in a fibre linear cavity [5]. **(b)** Littman–Metcalf configuration in a fibre ring cavity [6]. SOA: semiconductor optical amplifier, M: mirror, FC: fibre coupler, L: lens, GM: galvanometer mirror, DG: diffraction grating, CIRC: circulator, ISO: isolator. 35

3.3 A polygon-scanned grating-based tunable laser [7]. SOA: semiconductor optical amplifier, M: mirror, FC: fibre coupler, L: lens, P: polygon mirror, DG: diffraction grating, CIRC: circulator. 36

3.4 Mechanically-scanned grating-based tunable laser using a MEMS mirror as a deflector [9]. LD: laser diode, M: mirror, L: lens, Et: etalon, DG: diffraction grating, PhD: photodiode. 36

3.5 Schematic diagram of the MEMS-VCSEL structure. DBR: distributed Bragg reflector. Redrawn from [14]. 37

3.6 FFP-TF based swept laser [21]. SOA: semiconductor optical amplifier, FFP-TF: fibre Fabry–Pérot tunable filter, SG: signal generator, ISO: isolator, FC: fibre coupler. 39

3.7 FDML swept laser [22]. SOA: semiconductor optical amplifier, FFP-TF: fibre Fabry–Pérot tunable filter, SG: signal generator, ISO: isolator, FC: fibre coupler. 40

3.8 Acousto-optic based swept lasers. **(a)** Littrow laser configuration using AOD as a deflector [33]. **(b)** Ring laser cavity using AOTF [37]. SOA: semiconductor optical amplifier, AOD: acousto-optic deflector, DG: diffraction grating, FC: fibre coupler, ISO: isolator, M: mirror, L: lens, SG: signal generator, AOTF: acousto-optic tunable filter. 42

3.9 Grating-based tunable laser using a KTN as a deflector [44]. SOA: semiconductor optical amplifier, M: mirror, L: lens, DG: diffraction grating, SG: signal generator. 43

3.10 All-semiconductor tunable lasers design. VM: Vernier mirror, G: gain, CLA: cavity length adjustment, SOA: semiconductor optical amplifier. Redrawn from [45]. 44

3.11 Schematics of time-stretching swept lasers using **(a)** a long fibre delay line as a stretcher [51], and **(b)** a chirped fibre Bragg grating [52]. ISO: isolator, HWP: half-wave plate, P: polariser, AL: spheric lens, PM-PCF: polarisation maintaining photonic crystal fibre, SMF: single-mode fibre, WDM: wavelength division multiplexer, YDF: ytterbium doped fibre, PP: pulse picker, cFBG: chirped fibre Bragg grating, CIRC: circulator, SOA: semiconductor optical amplifier. 46

3.12 Schematics of SPML swept lasers using **(a)** two cFBGs [67], and **(b)** a single cFBG [68]. BOA: booster amplifier, FC: fibre coupler, ISO: isolator, SOA: semiconductor optical amplifier, CIRC: circulator, cFBG: chirped fibre Bragg grating, IM: intensity modulator, SG: signal generator, DCF: dispersion compensation fibre. 48

4.1 Dispersion values for selected fibre types commonly used in DTML laser cavities. In each graph, the blue and red lines refer to β_2 and D values, respectively. DCF: dispersion-compensation fibre. 62

4.2 Time delay between different spectral components provided by a cFBG. . . 63

4.3 Comparison of the cavity mode spacing in a non-dispersive and a dispersive cavity. $\nu = \omega/2\pi$ is the optical frequency in units of Hz. 64

4.4 A ring DTML laser cavity with a fibre delay and a cFBG both contributing to the overall cavity dispersion. SOA: semiconductor optical amplifier, cFBG: chirped fibre Bragg grating, CIRC: circulator, IM: intensity modulator. 64

4.5 A graphical representation of the tuning bands $q = q_c + l$ and emission wavelength λ as a function of the modulation frequency f. The connection between Δf and $\Delta\lambda_{\text{single}}$ is given by Eq. Eq. (4.12) or Eq. Eq. (4.13). . . . 65

4.6 Spectral filtering behaviour in the single-harmonic DTML regime. **Top:** Filtered wavelength as a function of time. Each cavity round trip time T_{cav}, the filtered wavelength is tuned by $\Delta\lambda_{\text{round}}$. **Middle:** Snapshots of the sliding spectral window separated in time by T_{cav}. $\delta\lambda_{\text{stat}}$ is the bandwidth of the filter and λ_γ is the wavelength of a photon γ circulating inside the cavity. **Bottom:** Snapshots of the cavity optical field separated in time by T_{cav}, with a specific pulse P circulating inside the cavity. The drawings are inspired by [16, 20, 21]. 69

4.7 1st generation DTML lasers. **(a)** Sigma-configuration at 1.3 µm [15]. **(b)** Ring configuration at 1550 nm [24]. SOA: semiconductor optical amplifier, ISO: isolator, DC: directional coupler, PBS: polarisation beam splitter, DCF: dispersion compensation fibre, FRM: Faraday rotator mirror, PC: polarisation controller. 74

4.8 1st generation DTML lasers. **(a)** Sigma-configuration at 850 nm [25]. **(b)** Ring configuration at 1550 nm [25]. RSOA: reflective semiconductor optical amplifier, DC: directional coupler, DCF: dispersion compensation fibre, FRM: Faraday rotator mirror, IM: intensity modulator, EDFA: erbium-doped fibre amplifier, PMF: polarisation maintaining fibre, PBS: polarisation beam splitter, SMF: single mode fibre. 75

4.9 2nd generation DTML lasers. **(a)** Ring configuration at 1550 nm [27]. **(b)** Linear configuration at 1550 nm [7]. SOA: semiconductor optical amplifier, DC: directional coupler, CIRC: circulator, cFBG: chirped fibre Bragg grating, PC: polarisation controller, RSOA: reflective semiconductor optical amplifier. 77

4.10 2nd generation DTML lasers. **(a)** Ring configuration at 1550 nm [17]. **(b)** Ring configuration at 1310 nm with the shortest DTML cavity of 0.88 m reported [11]. SOA: semiconductor optical amplifier, ISO: optical isolator, IM: intensity modulator, CIRC: optical circulator, cFBG: chirped fibre Bragg grating. 78

4.11 3rd generation DTML lasers. **(a)** Ring configuration using an EDFA as the gain medium [29]. **(b)** Ring configuration operating at 1060 nm [10]. EDFA: erbium-doped fibre amplifier, DC: directional coupler, CIRC: optical circulator, cFBG: chirped fibre Bragg grating, IM: intensity modulator, SOA: semiconductor optical amplifier. 79

5.1 First multi-harmonic DTML lasers. **(a)** First multi-harmonic DTML laser at 1550 nm [2]. **(b)** First multi-harmonic DTML laser at 850 nm [3]. SOA: semiconductor optical amplifier, SG: signal generator, ISO: optical isolator, DC: directional coupler, DCF: dispersion compensation fibre, FRM: Faraday rotator mirror, CIRC: optical circulator. 87

5.2 A graphical representation of the modulation signal $V(t)$ and the modulation frequency $f(t)$ given by Eq. Eq. (5.1) and Eq. Eq. (5.3), respectively. $V_{\mathrm{cycle}}(t)$: single sweep cycle modulation signal given by Eq. Eq. (5.2), T_{s}: sweep period, f_0: central modulation frequency, Δf: modulation frequency range. 89

5.3 **Top:** Simulation of the spectrum of the modulation signal $V(t)$ specified by Eq. Eq. (5.1)-Eq. Eq. (5.4). **Bottom:** Experimentally measured VCO signal for $f_0 \doteq 2330\,\mathrm{MHz}$, $\Delta f \doteq 100\,\mathrm{MHz}$, and $f_{\mathrm{s}} \doteq 1\,\mathrm{MHz}$. 90

5.4 Single-harmonic DTML. **Top:** Emission wavelength λ as a function of the modulation frequency f_l. **Middle:** Optical spectrum consisting of spectral lines at ν_l with an instantaneous linewidth of $\delta\nu = c\delta\lambda/\lambda^2$. **Bottom:** Monochromatic pulse trains with a carrier wavelength λ_l and a pulse rate given by $f_{\mathrm{p},l} = \Delta\nu_{\mathrm{m},l} = q_{\mathrm{c}} f_{\mathrm{cav}}(\lambda_l)$, each corresponding to a single spectral line at ν_l in the spectrum from above. 92

5.5 Multi-harmonic DTML for the case $f_{\mathrm{s}} = f_{\mathrm{cav}}(\lambda_0)$. **Top:** Emission wavelength λ as a function of the modulation frequency f_l. **Middle:** Optical spectrum consisting of a superposition of spectral lines at $\nu_0 = c/\lambda_0$ with an instantaneous linewidth of $\delta\nu = c\delta\lambda/\lambda^2$, with different mode spacing given by $\Delta\nu_{\mathrm{m},l} = (q_{\mathrm{c}} + l)f_{\mathrm{cav}}(\lambda_0)$. **Bottom:** Monochromatic pulse trains with a carrier wavelength λ_0 and a pulse rate given by $f_{\mathrm{p},l} = \Delta\nu_{\mathrm{m},l} = (q_{\mathrm{c}} + l)f_{\mathrm{cav}}(\lambda_0)$, each corresponding to the spectral line at ν_0 from above. . 95

5.6 Multi-harmonic DTML for the case $f_{\mathrm{s}} = f_{\mathrm{cav}}(\lambda_0) + \delta f_{\mathrm{s}}$. **Top:** Emission wavelength λ as a function of modulation frequency f_l. **Middle:** Optical spectrum consisting of several spectral lines at different optical frequencies $\nu_l = c/\lambda_l$ and an instantaneous linewidth of $\delta\nu = c\delta\lambda/\lambda^2$, with different mode spacing given by $\Delta\nu_{\mathrm{m},l} = (q_{\mathrm{c}} + l)f_{\mathrm{cav}}(\lambda_l)$. **Bottom:** Monochromatic pulse trains with a carrier wavelength λ_l and a pulse rate given by $f_{\mathrm{p},l} = \Delta\nu_{\mathrm{m},l} = (q_{\mathrm{c}} + l)f_{\mathrm{cav}}(\lambda_l)$, each corresponding to a spectral line at ν_l from above. 97

5.7 Spectral filtering behaviour in the multi-harmonic DTML regime. **Top:** Filtered wavelength as a function of time. Each cavity round trip time T_{cav}, the filtered wavelength is tuned by $\Delta\lambda_{\mathrm{round}}$. **Middle:** Snapshots of the sliding spectral window separated in time by T_{cav}. The window filters only the modes mode-locked in Fig. 5.6. $\delta\lambda_{\mathrm{stat}}$ is the bandwidth of the filter and λ_γ is the wavelength of a photon γ circulating inside the cavity. **Bottom:** Snapshots of the cavity optical field separated in time by T_{cav} and T_{s}, with a specific pulse P circulating inside the cavity. The drawings are inspired by [4, 11, 12]. 101

5.8 Comparison of the optical fields stored inside a single-harmonic, multi-harmonic DTML, and FDML cavity as snapshots separated in time by T_{s}. 106

6.1 The effect of loss on pulse propagation. Strong loss is applied for illustrative purposes. 115

6.2 The effects of dispersion on pulse propagation. Strong dispersion for illustrative purposes. 116

6.3 The effects of a fibre delay on pulse propagation. Strong dispersion and SPM are applied for illustrative purposes. 118

6.4 The effects of an SOA amplification on pulse propagation. Strong gain is applied for illustrative purposes. $\phi(\Omega)$ represents spectral phase of the envelope spectrum $\widetilde{A}(z,\Omega)$. 120

6.5 The effect of an amplitude modulation on a chirped pulse. 121

6.6 The effect of phase noise on pulse propagation. Strong phase noise is applied for illustrative purposes. 123

6.7 The reference DTML laser cavity for the mathematical modelling, characterised by the round trip transfer function in Eq. Eq. (6.31). 124

6.8 Simulation of the FWHM linewidth $\delta\Omega_{\mathrm{FWHM}}$ linewidth as a function of the cavity dispersion $\mathrm{TDD}_{\mathrm{cav}}$. 126

6.9 Optical power spectra $S(\Omega)$ after 1000 round trips for different cavity dispersions $\mathrm{TDD}_{\mathrm{cav}}$. 127

6.10 Evolution of the lasing spectra over the first 200 round trips N for different modulation window widths τ_{m}. 130

6.11 Evolution of the linewidth $\delta\Omega_{\mathrm{RMS}}$ as a function of round trips N for different modulation window widths τ_{m} and phase noise variances σ_{noise}. 131

6.12 **Left:** Number of round trips N_{stable} needed for the lasing stabilisation for the case $\sigma_{\mathrm{noise}} = 0$ in Fig. 6.11 top left as a function of the modulation window width τ_{m}. **Right:** Linewidth $\delta\Omega_{\mathrm{RMS}}$ (average over the last 100 round trips in Fig. 6.11) as a function of τ_{m} for different phase noise variances σ_{noise}. 131

7.1 **(a)** DTML cavity using direct modulation of the SOA as the mode-locking element and a spool of SMF-28e fibre as the dispersive element. **(b)** DTML cavity using an intensity modulator as the mode-locking element and a cFBG as the dispersive element. SOA: semiconductor optical amplifier, SG: signal generator, ISO: optical isolator, FC: fibre coupler, CIRC: optical circulator, PC: polarisation controller, IM: intensity modulator. 137

7.2 Linear regressions of $\Delta\lambda_{\text{single}}/\Delta f$ against f_0 for different cavity lengths in Fig. 7.1(a). 138

7.3 Cavity dispersion assessments of the DTML cavity in Fig. 7.1(b) for two different cFBGs with unknown dispersions. 139

7.4 DTML swept source 850 nm. SOA: semiconductor optical amplifier, IM: intensity modulator, CIRC: optical circulator, PC: polarisation controller, cFBG: chirped fibre Bragg grating, SG: arbitrary function signal generator, VCO: voltage-controlled oscillator, PG: pulse generator, RFA: RF amplifier, PS: power supply. 141

7.5 SS-OCT setup used for characterisation of the 850 nm DTML swept source in Fig. 7.4. The recirculation of the reference arm right is depicted with an arrow. DTML-SS: dispersion tuned mode-locked swept source, ISO: isolator, BOA: booster optical amplifier, OSA: optical spectrum analyser, FC: fibre coupler, L: launcher lens system, M: mirror, bPhD: balanced photodetector block, OSC: oscilloscope. 142

7.6 Comparison of the stationary tuning spectra using the sinusoidal and pulse modulation. 143

7.7 Comparison of the interferometer output signal using the sinusoidal and pulse modulation for the mirror M distance $z = 25\,\mu\text{m}$ in Fig. 7.5. 144

7.8 Peak-hold spectra without and after the BOA. 144

7.9 Laser output power P_{out} without the BOA as a function of sweep rate f_{s}. . 145

7.10 A-scan sensitivity roll-offs for different sweep rates f_{s}. 146

7.11 Multi-harmonic DTML-SS at 1550 nm. SOA: semiconductor optical amplifier, ISO: optical isolator, CIRC: optical circulator, cFBG: chirped fibre Bragg grating, PC: polarisation controller, IM: fibre intensity modulator, FC: fibre coupler, BOA: booster amplifier, SG: signal generator, VCO: voltage-controlled oscillator, RFA: RF amplifier, PS: power supply. 149

7.12 OCT setup used for characterization of the swept source in Fig. 7.11. The recirculation of the reference light is depicted with an arrow. BOA: booster optical amplifier, FC: fibre coupler, L: launcher lens system, M: mirror, bPhD: balanced photodetector, RFSA: RF spectrum analyser, OSC: oscilloscope. 150

7.13 Experimentally measured spectral content of the signal applied to the IM in Fig. 7.11, with parameters $\Delta f_0 \doteq 1700\,\mathrm{MHz}$, $\Delta f \doteq 185\,\mathrm{MHz}$, and $f_\mathrm{s} \doteq 912\,\mathrm{kHz}$. 151

7.14 Peak-hold spectra as a function of the detuning δf_s from the reference $f_\mathrm{s} \doteq 912\,\mathrm{kHz}$. 152

7.15 Measurements of the laser output power P_out (without the BOA) and tuning bandwidths $|\Delta\lambda_\mathrm{multi}|$ of the spectra in Fig. 7.14 as a functiob of the detuning δf_s from the reference $f_\mathrm{s} \doteq 912\,\mathrm{kHz}$. 152

7.16 A-scan sensitivity roll-off measurements for different tuning bandwidths $|\Delta\lambda_\mathrm{multi}|$. 153

7.17 Axial point spread profiles at 1 mm for different tuning bandwidths $|\Delta\lambda_\mathrm{multi}|$. For better display, the profiles are normalized and aligned exactly at $z = 1\,\mathrm{mm}$. 154

7.18 Multi-harmonic DTML-SS at 1 µm. SOA: semiconductor optical amplifier, CIRC: circulator, PC: polarization controller, SMF: single mode fibre, cFBG: chirped fibre Bragg grating, ISO: isolator, BOA: booster amplifier, IM: intensity modulator, PMF: polarization maintaining fibre, PS: power supply, SG: signal generator, VCO: voltage-controlled oscillator, PG: pulse generator, RFA: RF amplifier, V_DC: DC voltage, $V_\mathrm{AC}(t)$: AC voltage, V_bias: IM bias voltage. 158

7.19 OCT setup. FC: fibre coupler, L: lens, M: mirror, bPhD: balanced photodetector block, HPF: high pass filter. 159
7.20 Large span (top) and small span (bottom) of the VCO modulation signal spectral content applied to the IM in Fig. 7.18, with parameters $f_0 \doteq 2000\,\mathrm{MHz}$, $\Delta f \doteq 740\,\mathrm{MHz}$, and $f_\mathrm{s} \doteq 0.944\,\mathrm{MHz}$. 160
7.21 Theoretical calculation of the tuning bandwidth limits $\Delta\lambda_{\mathrm{multi,sat}}$, $\Delta\lambda_{\mathrm{multi,one}}$, and $\Delta\lambda_{\mathrm{multi,n\text{-}d}}$ using Eq. Eq. (7.9), Eq. Eq. (7.10), and Eq. Eq. (7.11), respectively, as a function of Δf. 161
7.22 Peak-hold optical spectra for various δf_s in Eq. Eq. (7.13). The measured tuning bandwidths as a function of δf_s are plotted in Fig. 7.23. 163
7.23 Measured tuning bandwidths $|\Delta\lambda_{\mathrm{multi}}|$ of the spectra in Fig. 7.22 and the theoretical prediction according to Eq. Eq. (5.14) as a function of δf_s. . . . 163
7.24 Photodetected signal showing the interference signal for a mirror M used as the sample in Fig. 7.19 at the reference arm displacement $z = 0.25\,\mathrm{mm}$, obtained with a tuning bandwidth of $|\Delta\lambda_{\mathrm{multi}}| \doteq 30\,\mathrm{nm}$. 164
7.25 Point spread functions roll-off measurements for three different tuning bandwidths $|\Delta\lambda_{\mathrm{multi}}|$. 165
7.26 B-scans captured with the setup in Fig. 7.19. **Top:** A finger tip. **Bottom:** Retina. 166

List of acronyms and abbreviations

AC: alternating current

AOG: Applied Optics Group

ASE: amplified spontaneous emission

BOA: booster semiconductor optical amplifier

bPhD: balanced photodetector

cFBG: chirped fibre Bragg grating

CIRC: circulator

CLF: Complex Leader-Follower interferometry

DC: direct current

DCF: dispersion-compensating fibre

DG: diffraction grating

DTML: dispersion-tuned mode-locking

DTML-SS: dispersion-tuned mode-locked swept source

EDFA: erbium-doped fibre amplifier

FC: fibre coupler

FD-OCT: Fourier-domain OCT

FDML: Fourier domain mode-locking

FFP-TF: fibre Fabry–Pérot tunable filter

FFSS-OCT: full-field swept source OCT

FWHM: full width at half maximum

IM: intensity modulator

ISO: isolator

LD: laser diode

MEMS: micro-electro-mechanical systems

MEMS-VCSEL: micro-electro-mechanical systems vertical-cavity surface-emitting laser

NETLAS: NExt generation of Tunable LASers for optical coherence tomography

NLSE: nonlinear Schrödinger equation

OCM: optical coherence microscopy

OCT: optical coherence tomography

OPD: optical path difference

OSA: optical spectrum analyser

OSC: oscilloscope

PC: polarisation controller

PG: pulse generator

PM: polarisation-maintaining fibre

PS: power supply

RFA: RF amplifier

RFSA: RF spectrum analyser

RIN: relative intensity noise

RMS: root mean square

RSOA: reflective semiconductor optical amplifier

SG: signal generator

SMF: single-mode fibre

SNR: signal-to-noise ratio

SOA: semiconductor optical amplifier

Sp-OCT: spectrometer-based OCT

SPM: self-phase modulation

SPML: stretched pulse mode-locking

SS-OCT: swept source OCT

TD-OCT: time-domain OCT

VCO: voltage-controlled oscillator

Chapter 1

Introduction to the thesis

1.1 Why OCT?

Optical coherence tomography (OCT) has become a highly relevant non-invasive imaging technique in biomedical optics and medicine [1–5]. OCT generates high-resolution real-time cross-sectional or three-dimensional images by measuring interference of backscattered light. With its axial resolution capabilities of down to 1-10 µm and tissue penetration depth of up to few millimetres, OCT bridges the gap between lower axial resolution but deep penetration depth ultrasound imaging, and higher axial resolution but low penetration depth confocal microscopy (see Fig. 1.1). Additionally, OCT achieves a lateral resolution comparable to that of confocal microscopy.

OCT's most prominent application is in ophthalmology, where the first OCT image was captured from a human retina [6]. Since then, OCT has been extended to other biomedical fields, such as cardiology, dermatology, oncology, and gastroenterology. OCT enables visualization of structural changes in tissue and identification of disease markers. In retina, OCT can identify age-related macular degeneration, glaucoma, diabetic retinopathy, retinal detachments, or corneal diseases [7–12]. Endoscopic OCT technology facilitates minimally invasive imaging of internal tissue and vascular and coronary arteries, aiding in detection of early-stage diseases of gastrointestinal, respiratory, and urinary tracts, and as well as of the cardiovascular system [1, 13–15]. The ability to see beneath the tissue surface enables dermatologists non-invasive imaging of skin layers, assisting in

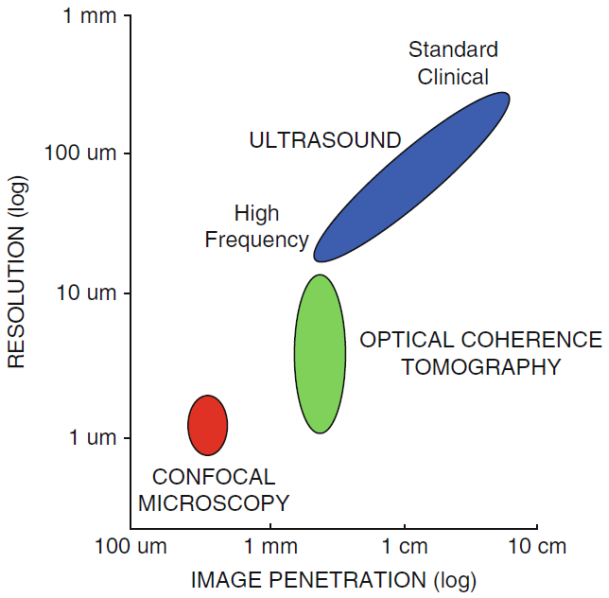

Figure 1.1: Comparison of ultrasound modality, OCT, and confocal microscopy relative to their penetration depths and imaging axial resolutions [3].

skin cancer detection, wound healing assessment, and diagnosis of skin conditions [16–18]. In oncology, OCT is used for cancer diagnosis, namely in distinguishing between benign and malignant tissues and identifying tumour margins [18–20]. OCT is also emerging as a valuable tool in dentistry, neurology, otolaryngology, and surgical guidance [21–24]. Tab. 1.1 lists most common wavelengths and summarises their application in OCT imaging. As an example of true OCT images, Fig. 1.2 displays two images captured with the custom-designed OCT system described in Sec. 7.4, showing depth resolved tissue features like are sweat ducts in a finger tip (top) or retinal layers (bottom).

Table 1.1: Most common wavelengths and their application in OCT imaging [3].

Central wavelength	**OCT main application**
670 nm (visible light)	High resolution retinal imaging, functional imaging
850 nm (near-infrared)	Retinal imaging
1060 nm (near-infrared)	Retinal imaging
1310 nm (O-band)	Highly scattering tissue imaging (skin, teeth, adipose tissue, arteries), material and industrial
1550 nm (C-Band)	Material and industrial

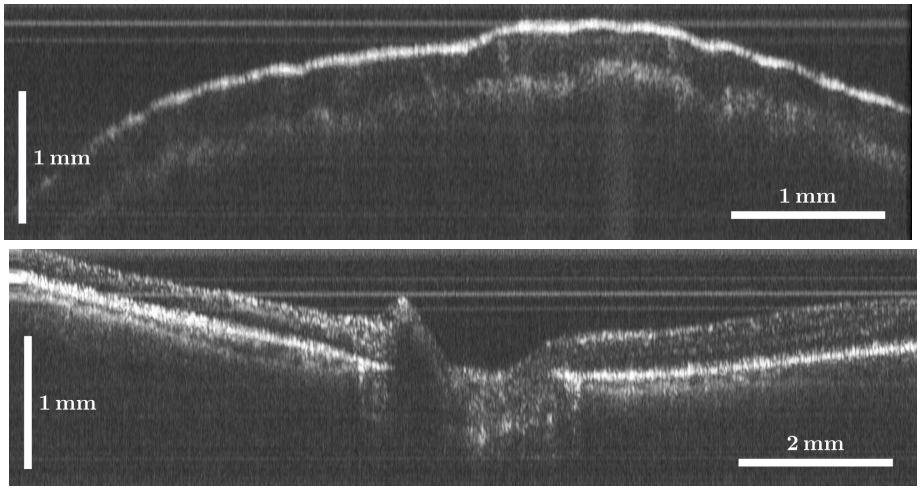

Figure 1.2: Two representative OCT images captured with the custom-designed OCT system described in Sec. 7.4. **Top:** A finger tip. **Bottom:** Retina.

1.2 Motivation of the thesis

One of the OCT methods that in the last decade has proven MHz acquisition rate is the swept source (SS)-OCT [25]. This enables not only higher speed, but larger imaging depths than in the spectrometer-based OCT methods.

Two main approaches to wavelength tuning are used in swept sources for OCT [25]. The first approach relies on mechanical movements, which can be implemented by actuating on the mirrors of a Fabry–Pérot filter [26], or using a polygon mirror scanner [27], or a micro-electromechanical system vertical-cavity surface-emitting laser (MEMS-VCSEL) [28]. The second approach employs akinetic tuning principles, based on an acousto-optic deflection [29], or all-semiconductor designs [30], or time-stretch technology [31], or stretched-pulse mode-locking (SPML) [32], or dispersion-tuned mode-locking (DTML) [33].

A DTML laser in Fig. 1.3 comprises three main elements: a gain medium, typically a semiconductor optical amplifier (SOA), a mode-locking element, based on the direct modulation of the SOA gain or employing a separated intra-cavity intensity modulator, and a dispersive element, realized either by a long optical fibre or a chirped fibre Bragg grating (cFBG). In a standard *single-harmonic* DTML laser, active mode-locking is applied at a single harmonic order. Desirable emission properties from this laser configuration include satisfactory power and a sufficiently long coherence length, which can be achieved by a combination of a relatively short cavity length (units of meters), a narrow temporal modulation window, and a high level of dispersion. Single-harmonic DTML swept sources have been demonstrated across various central wavelengths of interest to OCT, including 850 nm [34, 35], 1 µm [33], 1.3 µm [34, 36], and 1.55 µm [34, 37], with spectral linewidths below 0.1 nm and wavelength tuning bandwidths reaching 100 nm (see Sec. 4.4).

In the previous reports published by the Applied Optics Group (AOG) [38–40], it was demonstrated that an alternative sweeping regime can be established inside DTML cavities in Fig. 1.4. This regime, involving two simultaneous "resonant" conditions, was initially referred as to the *dual resonance sweeping regime* or *dual resonance DTML*. The first resonant condition corresponds to active mode-locking (achieved via the direct modulation

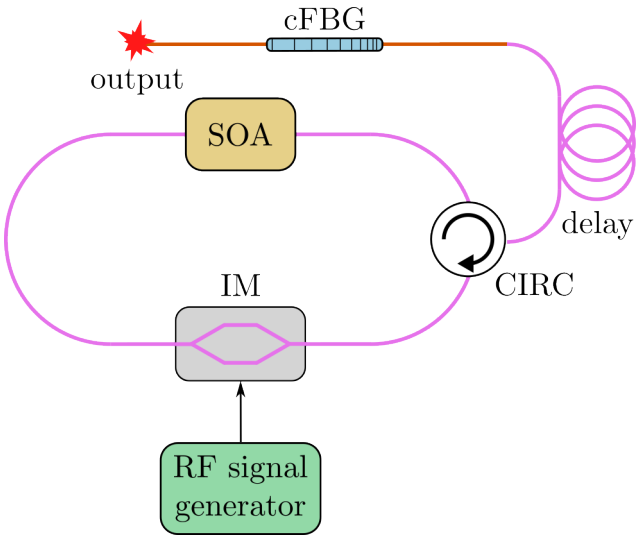

Figure 1.3: A ring DTML laser cavity. SOA: semiconductor optical amplifier, cFBG: chirped fibre Bragg grating, CIRC: circulator, IM: intensity modulator.

of the SOA gain or an external modulator) at a harmonic of the fundamental frequency of the cavity. The second resonant condition is inspired by the Fourier-domain mode-locking (FDML) technology [41], where the mode-locking element (typically a Fabry-Pérot filter) is driven at the cavity fundamental frequency. When both resonant conditions are applied to a DTML cavity, it is observed that, contrary to FDML, wavelength tuning does not occur if the sweep rate precisely matches the fundamental frequency. Instead, only a single wavelength emission appears at the output of the DTML laser. It is experimentally observed that wavelength tuning is achieved if the sweep rate is actually slightly detuned from the fundamental frequency. For the first time, the present work provides a rigorous theoretical explanation for this behaviour. Because multiple orders of harmonics are engaged, a more accurate reference to this regime is proposed in this work, as to the *multi-harmonic DTML*. This regime is fundamentally different from the standard single-harmonic mode-locking presented by all other research groups in the field of DTML swept sources.

The multi-harmonic DTML regime has previously been demonstrated at 850 nm [38] and 1550 nm [39] using direct modulation of the SOA gain. The previous reports reduced to presenting primarily experimental demonstrations. However, a comprehensive theoretical description of the multi-harmonic operation, discussion on its tuning and coherence

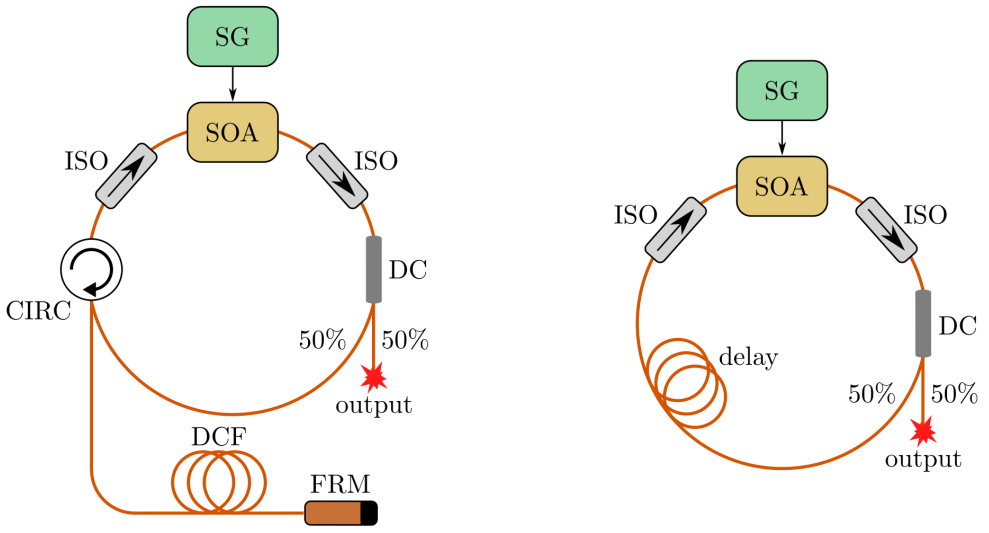

Figure 1.4: Multi-harmonic DTML laser cavities. **(a)** First multi-harmonic DTML laser at 1550 nm [39]. **(b)** First multi-harmonic DTML laser at 850 nm [38]. SOA: semiconductor optical amplifier, SG: signal generator, ISO: optical isolator, DC: directional coupler, DCF: dispersion compensation fibre, FRM: Faraday rotator mirror, CIRC: optical circulator.

performance, its demonstration at 1 µm, and finally actual OCT images produced by employing this regime have not been reported so far. These aspects are addressed in the present work.

1.3 Thesis structure

The thesis is divided into 6 main chapters, of which first 5 are theoretical, focusing on:

- Chap. 2: This opening chapter starts with explanation of basic OCT physical principles. The two main OCT modalities, time-domain (TD-OCT) and Fourier-domain (FD-OCT), are described, and two implementations of FD-OCT, spectrometer-based (Sp-OCT) and swept source (SS-OCT) OCT, are detailed. For the future reference throughout the thesis, specifications of the light source and imaging instruments are linked to key performance parameters of an OCT system, such as axial resolution, imaging depth, and sensitivity.

- Chap. 3: Provides a brief overview of the various types of tunable lasers for SS-OCT reported so far. Each laser type description includes fundamental operating principle, laser designs, and representative performance characteristics relevant to OCT imaging.

- Chap. 4: Starting with a brief description of the dispersion properties of fibre laser cavities, this chapter explains the principle of tuning in dispersion-tuned mode-locked (DTML) swept lasers and rigorously derives an expression for the tuning bandwidth in this type of tunable lasers. By adopting a spectral filtering approach, notions of the saturation and one round trip operations are introduced, showing trade-offs between the achievable tuning bandwidth and coherence performance. The historical development of DTML swept sources with representative performance characteristics relevant to OCT imaging is also reviewed, categorising the lasers chronologically into three generations.

- Chap. 5: This chapter starts with a brief overview of the previous development in multi-harmonic DTML swept lasers within AOG and then introduces a rigorous model for description of the advancement from the standard single-harmonic to multi-harmonic operation. This is accomplished utilising a mathematical framework that connects the laser optical spectrum with the spectral content of the modulation signal over many sweep cycles. Building on the spectral filtering description introduced in Chap. 4, this chapter derives the tuning bandwidth limits for the multi-harmonic DTML operation, showing trade-offs between the achievable tuning bandwidth and coherence performance in this sweeping regime.

- Chap. 6: Two mathematical frameworks are introduced for rigorous modelling of DTML lasers in this chapter: the average model and the discrete model. Both models are appropriately described, and a refined extension of the discrete model, also referred to as the iterative mapping, is utilised for the numerical simulations presented in the last part of the chapter. These simulations are used to investigate the behaviour of the spectral linewidth in a DTML laser as a function of various cavity parameters.

After the theoretical part, Chap. 7 describes a dispersion assessment technique and three custom-designed DTML architectures and their evaluation for OCT imaging:

- Sec. 7.1: Presents a simple yet effective method for an approximative cavity dispersion assessment in a DTML laser cavity without the need for additional components required for DTML itself.

- Sec. 7.2: Presents a standard DTML swept source operating at 850 nm, developed primarily for full-field swept-source optical coherence tomography (FFSS-OCT). The laser combines a cFBG and pulse modulation technique, and, in comparison with previous DTML implementations at 850 nm, this design achieves improved coherence and higher sweep rates.

- Sec. 7.3: Presents a high speed akinetic swept source operating at 1550 nm employing the multi-harmonic DTML regime by utilising a high speed intensity modulator for mode-locking and a cFBG for necessary dispersion in the cavity. This design enables MHz sweep rates with improved coherence and stability in comparison with the previous reports on multi-harmonic DTML lasers.

- Sec. 7.4: Demonstrates the first multi-harmonic DTML laser operating at 1 µm. Owing to its coherence and high signal-to-noise ratio, the first OCT images of a finger tip and the retina are captured for the first time by employing a multi-harmonic DTML swept laser.

Bibliography

[1] J. G. Fujimoto, C. Pitris, S. A. Boppart, and M. E. Brezinski, "Optical coherence tomography: An emerging technology for biomedical imaging and optical biopsy," *Neoplasia*, vol. 2, no. 1, pp. 9–25, 2000.

[2] M. E. Brezinski, *Optical Coherence Tomography: Principles and Applications*. Academic Press, 2006.

[3] W. Drexler and J. G. Fujimoto, *Optical Coherence Tomography: Technology and Applications*, 2nd ed. Springer, 2015.

[4] M. Varghese, S. Varghese, and S. Preethi, "Revolutionizing medical imaging: a comprehensive review of optical coherence tomography (OCT)," *Journal of Optics*, 2024.

[5] J. F. Bille, *High Resolution Imaging in Microscopy and Ophthalmology: New Frontiers in Biomedical Optics*. Springer, 2019.

[6] D. Huang, E. A. Swanson, C. P. Lin, J. S. Schuman, W. G. Stinson, W. Chang, M. R. Hee, T. Flotte, K. Gregory, C. A. Puliafito, and J. G. Fujimoto, "Optical coherence tomography," *Science*, vol. 254, no. 5035, pp. 1178–1181, 1991.

[7] B. Lumbroso, M. Rispoli, and M. C. Savastano, *Practical Handbook of OCT: Fundamentals and Applications*. Jaypee Brothers Medical Publishers, 2012.

[8] M. Adhi and J. S. Duker, "Optical coherence tomography: current and future applications," *Current Opinion in Ophthalmology*, vol. 24, no. 3, pp. 213–221, 2013.

[9] L. M. Sakata, J. Deleon-Ortega, V. Sakata, and C. A. Girkin, "Optical coherence tomography of the retina and optic nerve: a review," *Clinical and Experimental Ophthalmology*, vol. 37, no. 1, pp. 90–99, 2009.

[10] G. J. Jaffe and J. Caprioli, "Optical coherence tomography to detect and manage retinal disease and glaucoma," *American Journal of Ophthalmology*, vol. 137, no. 1, pp. 156–169, 2004.

[11] A. M. Zysk, F. T. Nguyen, A. L. Oldenburg, D. L. Marks, and S. A. Boppart, "Optical coherence tomography: a review of clinical development from bench to bedside," *Journal of Biomedical Optics*, vol. 12, no. 5, p. 051403, 2007.

[12] Y. J. Chong, M. H. Azzopardi, G. Recchioni, and A. Hussain, "Clinical applications of anterior segment optical coherence tomography: an updated review," *Diagnostics*, vol. 14, no. 2, p. 122, 2024.

[13] Z. Yaqoob, J. Wu, E. J. McDowell, X. Heng, and C. Yang, "Methods and application areas of endoscopic optical coherence tomography," *Journal of Biomedical Optics*, vol. 11, no. 6, p. 063001, 2006.

[14] T.-H. Tsai, H.-C. Lee, C.-J. Yu, C.-K. Lee, C.-C. Li, C.-J. Tseng, and Y.-H. Wang, "Endoscopic optical coherence tomography for clinical gastroenterology," *Clinical Endoscopy*, vol. 48, no. 4, pp. 317–328, 2015.

[15] M. J. Gora, M. J. Suter, G. J. Tearney, and X. Li, "Endoscopic optical coherence tomography: technologies and clinical applications," *Biomedical optics express*, vol. 8, no. 5, pp. 2405–2444, 2017.

[16] L. F. di Ruffano, J. Dinnes, J. J. Deeks, N. Chuchu, S. E. Bayliss, Y. Takwoingi, C. Davenport, R. N. Matin, C. O'Sullivan, K. Godfrey, F. M. Walter, H. C. Williams, and C. S. C. D. T. A. Group, "Optical coherence tomography for diagnosing skin cancer in adults," *Cochrane Database of Systematic Reviews*, vol. 12, 2018.

[17] N. S. Greaves, B. Benatar, M. Baguneid, and A. Bayat, "Optical coherence tomography: a reliable alternative to invasive histological assessment of acute wound healing in human skin?" *British Journal of Dermatology*, vol. 170, no. 4, pp. 840–850, 2014.

[18] J. A. Levine, J. V. Wang, and O. Markowitz, "Optical coherence tomography in the diagnosis of skin cancer," *Dermatologic Clinics*, vol. 35, no. 4, pp. 465–469, 2017.

[19] F. T. Nguyen, A. M. Zysk, E. J. Chaney, S. G. Adie, J. G. Kotynek, U. J. Oliphant, F. J. Bellafiore, K. M. Rowland, P. A. Johnson, and S. A. Boppart, "Intraoperative

evaluation of breast tumor margins with optical coherence tomography," *Cancer Research*, vol. 69, no. 22, pp. 8790–8796, 2009.

[20] J. Wang, Y. Xu, and S. A. Boppart, "Review of optical coherence tomography in oncology," *Journal of Biomedical Optics*, vol. 22, no. 12, p. 121711, 2017.

[21] S. Ali, S. Noreen, I. Farooq, A. Bugshan, and F. Vohra, "Optical coherence tomography's current clinical medical and dental applications: A review," *F1000Research*, vol. 10, p. 426, 2021.

[22] M. I. Mokbul, "Optical coherence tomography: Basic concepts and applications in neuroscience research," *Journal of Medical Engineering*, vol. 2017, pp. 1–20, 2017.

[23] T. J. Matthews and R. Adamson, "Optical coherence tomography: current and future clinical applications in otology," *Current Opinion in Otolaryngology and Head and Neck Surgery*, vol. 28, no. 5, pp. 296–301, 2020.

[24] O. M. Carrasco-Zevallos, C. Viehland, B. Keller, M. Draelos, A. N. Kuo, C. A. Toth, and J. A. Izatt, "Review of intraoperative optical coherence tomography: technology and applications," *Biomedical Optics Express*, vol. 8, no. 3, pp. 1607–1637, 2017.

[25] T. Klein and R. Huber, "High-speed OCT light sources and systems," *Biomed. Opt. Express*, vol. 8, no. 2, pp. 828–859, Feb 2017.

[26] M. Klufts, A. M. Jiménez, S. Lotz, M. A. Bashir, T. Pfeiffer, A. Mlynek, W. Wieser, A. Chamorovskiy, A. Bradu, A. Podoleanu, and R. Huber, "828 kHz retinal imaging with an 840 nm Fourier domain mode locked laser," *Biomed. Opt. Express*, vol. 14, no. 12, pp. 6493–6508, Dec 2023.

[27] V.-F. Duma and A. G. Podoleanu, "Polygon mirror scanners in biomedical imaging: a review," in *Optical Components and Materials X*, M. J. F. Digonnet, S. Jiang, and J. C. Dries, Eds., vol. 8621, International Society for Optics and Photonics. SPIE, 2013, p. 86210V.

[28] J. Zhang, T. Nguyen, B. Potsaid, V. Jayaraman, C. Burgner, S. Chen, J. Li, K. Liang, A. Cable, G. Traverso, H. Mashimo, and J. G. Fujimoto, "Multi-MHz MEMS-VCSEL swept-source optical coherence tomography for endoscopic structural and angiographic imaging with miniaturized brushless motor probes," *Biomed. Opt. Express*, vol. 12, no. 4, pp. 2384–2403, Apr 2021.

[29] Superlum Diodes Ltd. (2025) Superlum diodes ltd. official website. [Online]. Available: https://www.superlumdiodes.com/

[30] M. Bonesi, M. P. Minneman, J. Ensher, B. Zabihian, H. Sattmann, P. Boschert, E. Hoover, R. A. Leitgeb, M. Crawford, and W. Drexler, "Akinetic all-semiconductor programmable swept-source at 1550 nm and 1310 nm with centimeters coherence length," *Opt. Express*, vol. 22, no. 3, pp. 2632–2655, Feb 2014.

[31] S. Grelet, A. M. Jimenez, P. B. Montague, and A. Podoleanu, "Shot-noise limited, 10 MHz swept-source optical coherence tomography for retinal imaging," *IEEE Photonics Journal*, pp. 1–5, 2025.

[32] T. S. Kim, J. Joo, I. Shin, P. Shin, W. Kang, B. Vakoc, and W.-Y. Oh, "9.4 MHz A-line rate optical coherence tomography at 1300 nm using a wavelength-swept laser based on stretched-pulse active mode-locking," *Scientific Reports*, vol. 10, p. 9328, 06 2020.

[33] H. D. Lee, G. H. Kim, J. G. Shin, B. Lee, C.-S. Kim, and T. J. Eom, "Akinetic swept-source optical coherence tomography based on a pulse-modulated active mode locking fiber laser for human retinal imaging," *Sci Rep*, vol. 8, p. 17660, 2018.

[34] S. Yamashita, N. Yuichi, K. Ryosei, and K. Osamu, "Wide and fast wavelength-swept fiber laser based on dispersion tuning for dynamic sensing," *Journal of Sensors*, vol. 2009, 01 2009.

[35] R. Riha, A. M. Jimenez, G. Venugopal, M. Klufts, R. Huber, and A. Podoleanu, "Dispersion-tuned mode-locked laser for swept source oct at 850 nm using a cFBG

and the pulse modulation technique," *IEEE Photonics Journal*, vol. 16, no. 4, pp. 1–5, 2024.

[36] H. D. Lee, M. Y. Jeong, C.-S. Kim, J. G. Shin, B. H. Lee, and T. J. Eom, "Linearly wavenumber-swept active mode locking short-cavity fiber laser for in-vivo OCT imaging," *IEEE Journal of Selected Topics in Quantum Electronics*, vol. 20, no. 5, pp. 433–440, 2014.

[37] H. Nagai and S. Yamashita, "Coherence improvement in dispersion-tuned swept laser by pulse modulation," *Electronics Letters*, vol. 50, no. 23, pp. 1729–1731, 2014.

[38] F. Toadere, R.-F. Stancu, W. Poon, D. Schultz, and A. Podoleanu, "1 MHz akinetic dispersive ring cavity swept source at 850 nm," *IEEE Photonics Technology Letters*, vol. 29, no. 11, pp. 933–936, 2017.

[39] R. F. Stancu and A. G. Podoleanu, "Dual-mode-locking mechanism for an akinetic dispersive ring cavity swept source," *Opt. Lett.*, vol. 40, no. 7, pp. 1322–1325, Apr 2015.

[40] R. Riha, A. Bradu, and A. Podoleanu, "Dual resonance akinetic dispersive cavity swept source at 900 kHz using a cFBG and an intensity modulator," *Opt. Lett.*, vol. 47, no. 16, pp. 4032–4035, Aug 2022.

[41] R. Huber, M. Wojtkowski, and J. G. Fujimoto, "Fourier domain mode locking (FDML): a new laser operating regime and applications for optical coherence tomography," *Opt. Express*, vol. 14, no. 8, pp. 3225–3237, Apr 2006.

Chapter 2

Optical coherence tomography

This opening chapter starts with explanation of basic OCT physical principles. The two main OCT modalities, time-domain (TD-OCT) and Fourier-domain (FD-OCT), are described, and two implementations of FD-OCT, spectrometer-based (Sp-OCT) and swept source (SS-OCT) OCT, are detailed. For the future reference throughout the thesis, specifications of the light source and imaging instruments are linked to key performance parameters of an OCT system, such as axial resolution, imaging depth, and sensitivity.

2.1 OCT principle

The principle of optical coherence tomography (OCT) is based on a Michelson interferometer configuration [1–6], depicted in Fig. 2.1. The interferometer is illuminated by a

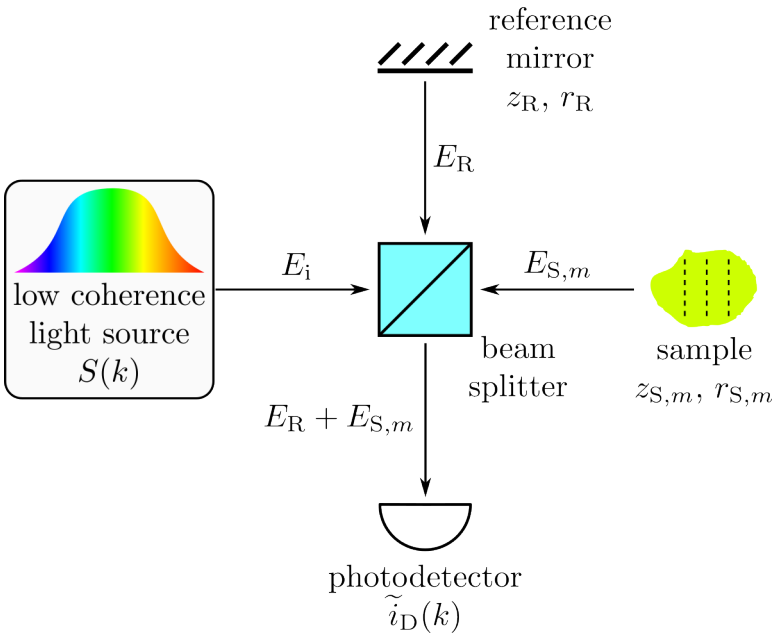

Figure 2.1: Schematic of a Michelson interferometer used in OCT.

complex electrical field E_{i} from a low coherence light source characterised by its amplitude spectrum $S(k)$ as a function of the wavenumber $k = 2\pi/\lambda$, where λ is the optical wavelength. The field E_{i} is incident on a power splitter, which, for simplicity, is assumed to have a power splitting ratio of 0.5. In the reference arm, the light is reflected from the reference mirror, characterised by its amplitude reflectance r_{R} and positioned at a distance of z_{R} from the splitter. The reflected light then returns to the splitter with the incident electric field E_{R}. In the sample (or object) arm, the light is reflected from a series of M sample reflectors, each characterized by its amplitude reflection coefficient $r_{\mathrm{S},m}$ at a distance of $z_{\mathrm{S},m}$ from the splitter. The total field returning from the sample arm is given by $E_{\mathrm{S}} = \sum_{m=1}^{M} E_{\mathrm{S},m}$. After passing through the splitter second time, the fields E_{R} and E_{S} interfere on an optical photodetector. The photodetector generates a photocurrent $\widetilde{i}_{\mathrm{D}}(k)$ proportional to the time-averaged intensity of the incident interferometric field $E_{\mathrm{R}} + E_{\mathrm{S}}$:

$$\widetilde{i}_{\mathrm{D}}(k) = \frac{\varrho}{2} \left\langle |E_{\mathrm{R}} + E_{\mathrm{S}}|^2 \right\rangle , \tag{2.1}$$

where ϱ is the photodetector responsivity (in amperes per watt), and the factor of 1/2 accounts for the second pass of the fields through the splitter. By expanding the squared term in Eq. (2.1) and performing the time-averaging, the spectral interferogram $\widetilde{i}_{\mathrm{D}}(k)$, is obtained as a function of wavenumber k and optical path difference (OPD) $z_{\mathrm{R}} - z_{\mathrm{S},m}$:

$$\widetilde{i}_{\mathrm{D}}(k) = \frac{\varrho}{4} S(k) \left(R_{\mathrm{R}} + \sum_{m=1}^{M} R_{\mathrm{S},m} \right) + \frac{\varrho}{2} S(k) \sum_{m=1}^{M} \sqrt{R_{\mathrm{R}} R_{\mathrm{S},m}} \cos\left[2k(z_{\mathrm{R}} - z_{\mathrm{S},m})\right], \tag{2.2}$$

with $R_{\mathrm{R}} = |r_{\mathrm{R}}|^2$ and $R_{\mathrm{S},m} = |r_{\mathrm{S},m}|^2$ representing the power reflectivities of the reference mirror and the mth sample reflector, respectively. The interferogram in Eq. (2.2) consists of large DC terms proportional to the power reflectivities, as well as cross-correlation terms dependent on the path length difference $(z_{\mathrm{R}} - z_{\mathrm{S},m})$, which are typically smaller than the DC terms. For simplicity, weak and low-frequency autocorrelation terms were neglected in Eq. (2.2).

The power spectral function $S(k)$ in Eq. (2.2) and Fig. 2.1 characterises spectral properties of the light source. In OCT, common spectral shapes of $S(k)$ include Gaussian,

$$S_{\mathrm{Gauss}}(k) \sim \exp\left[-4 \ln 2 \frac{(k - k_0)^2}{\Delta k^2} \right], \tag{2.3}$$

and top-hat distributions,

$$S_{\text{top-hat}}(k) \sim \mathrm{rect}\left(\frac{k - k_0}{\Delta k} \right), \tag{2.4}$$

where $k_0 = 2\pi/\lambda_0$ and λ_0 represent the central wave number and the central wavelength, respectively. The spectral width parameters are $\Delta k = 2\pi\Delta\lambda/\lambda_0^2$ and $\Delta\lambda$, defined as the full width at half maximum (FWHM) bandwidth in units of k and λ, respectively. Illustrative examples of spectral interferograms for a Gaussian-shaped $S_{\mathrm{Gauss}}(k)$ corresponding to a single and two sample reflectors are shown in Fig. 2.2. For a single reflector, the interferogram consists of a DC term with an amplitude of $(R_{\mathrm{R}} + R_{\mathrm{S},m})/2$, spectrally modulated by a cross-correlation component with an amplitude of $\sqrt{R_{\mathrm{R}} R_{\mathrm{S},m}}$ and a spectral period of $\pi/(z_{\mathrm{R}} - z_{\mathrm{S},m})$. A general spectral interferogram results from the superposition of interferograms from multiple M sample reflectors, as expressed in Eq. (2.2).

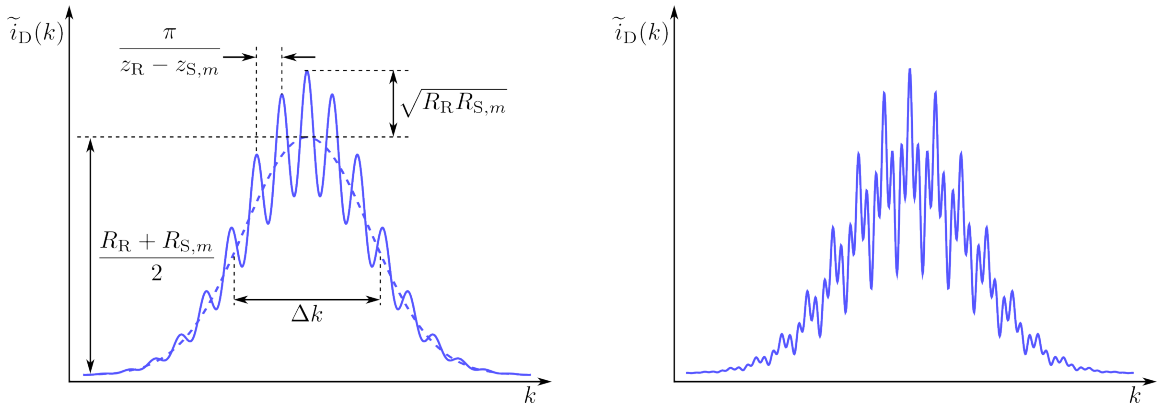

Figure 2.2: Spectral OCT interferograms [1, 2, 6]. **Left:** Single sample reflector spectral interferogram with the fringe amplitude of $\sqrt{R_{\mathrm{R}} R_{\mathrm{S},m}}$ and spectral period of $\pi/(z_{\mathrm{R}} - z_{\mathrm{S},m})$ (see Eq. (2.2)). **Right:** Spectral interferogram of two sample reflectors.

In the space domain, the light source is described by its coherence function $\gamma(z)$, also known as the degree of coherence [3]. This function is obtained through Fourier transform of Eq. (2.3) for Gaussian spectral shape and Eq. (2.4) for top-hat spectral shape, yielding:

$$\gamma_{\mathrm{Gauss}} \sim \exp\left(-\frac{4(z_{\mathrm{R}} - z)^2 \Delta k^2}{16 \ln 2}\right), \quad \gamma_{\text{top-hat}} \sim \operatorname{sinc}\left[2(z_{\mathrm{R}} - z)\Delta k\right]. \tag{2.5}$$

The coherence function is characterised by the free-space coherence length l_{coh}, defined as the FWHM of $\gamma(z)$. For a Gaussian spectral shape, it is given by:

$$l_{\mathrm{coh,Gauss}} = \frac{4 \ln 2}{\Delta k} = \frac{2 \ln 2}{\pi} \frac{\lambda_0^2}{\Delta \lambda} \approx 0.44 \frac{\lambda_0^2}{\Delta \lambda}, \tag{2.6}$$

and for a top-hat spectral shape approximately [7]:

$$l_{\text{coh,top-hat}} \approx \frac{7.58}{\Delta k} = 0.60 \frac{\lambda_0^2}{\Delta \lambda}. \tag{2.7}$$

In OCT, the coherence length is the key parameter that represents the maximum path length difference between the reference and sample arms for which the interference occurs. It directly determines the axial resolution of the system as $\delta z = l_{\mathrm{coh}}$, where a broader $\Delta\lambda$ yields better resolution, as given by Eq. (2.6) and Eq. (2.7).

A combination of confocal and coherence gating is known as optical coherence microscopy (OCM) [1]. The overall axial response of an OCM system is best represented

as a combination (mathematically a convolution) of the confocal gate and the axial response due to the OCT low-coherence interferometry. The key imaging parameters and their corresponding expressions, derived from this confocal-low-coherence description of an OCM system, are labelled in Fig. 2.3 and summarized in Table 2.1.

Table 2.1: The main imaging parameters and their corresponding expressions for an OCM system, considering an objective numerical aperture NA, objective focal length f, and maximum scan angle $\theta_{\max}$ [1] (see also Fig. 2.3).

Parameter	**Expression**
Confocal axial field of view	$\Delta z_{\text{conf}} = \dfrac{0.22\lambda_0}{\sin^2\left[\sin^{-1}(\text{NA})/2\right]}$
Lateral field of view	$\Delta x_{\text{conf}} = 2f\theta_{\max}$
Lateral resolution	$\delta x = 0.37\dfrac{\lambda_0}{\text{NA}}$
Interferometric axial resolution	$\delta z = 0.44\dfrac{\lambda_0^2}{\Delta\lambda}$ (for $S_{\text{Gauss}}(k)$ given by Eq. (2.3)) $\delta z = 0.60\dfrac{\lambda_0^2}{\Delta\lambda}$ (for $S_{\text{top-hat}}(k)$ given by Eq. (2.4))

To produce volumetric OCT images, a scanning device is incorporated in the sample arm, as depicted in Fig. 2.4. By scanning the beam over the sample in the "fast" x-axis, a collection of adjacent A-scans produces an depth resolved cross-sectional image known as a *B-scan*. Extending the scan laterally in the "slow" y-direction, a collection of B-scans produces a volumetric OCT image. Additionally, a lateral scan at a constant depth is referred to as a *T-scan*, and a collection of adjacent T-scans forms a *C-scan*, which represents a transverse cross-sectional image. OCT imaging modality designed to produce T-scans and C-scans is also referred to as *en-face* OCT [8–10].

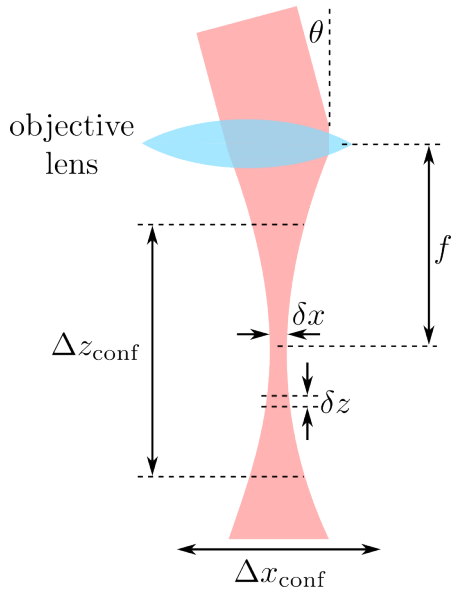

Figure 2.3: Schematic of generic OCT sample arm optics [1]. θ: scan angle, f: objective lens focal length, Δz_{conf}: confocal axial field of view, Δx_{conf}: confocal lateral field of view, δx: lateral resolution, δz: interferometric axial resolution.

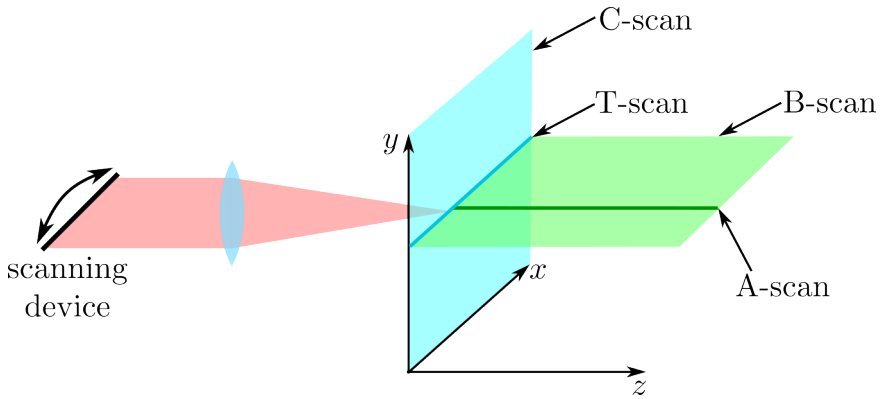

Figure 2.4: Schematic of different OCT scanning orientations relatively to the optical axis z.

2.2 Time-domain OCT (TD-OCT)

The first implementation of OCT was time-domain OCT (TD-OCT) [11–13], where the reference arm path length is varied mechanically to achieve depth-resolved imaging. A schematic diagram of TD-OCT system is shown in Fig. 2.5. It consists of a Michelson interferometer illuminated by a broadband low-coherence light source, a mechanically movable reference mirror with variable path length z_{R}, imaging and scanning optics in the sample arm, and a single photoreceiver with a processing unit to reconstruct the sample depth reflectivity profile.

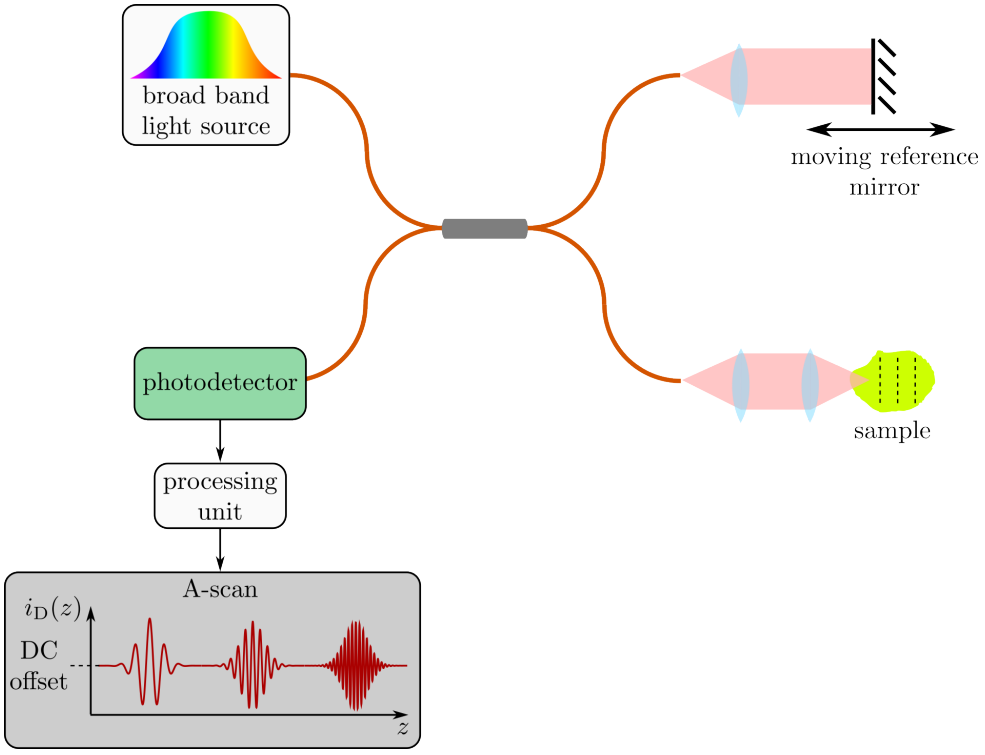

Figure 2.5: Configuration of a TD-OCT system with a reconstructed A-scan profile.

The depth-dependent detector current $i_{\mathrm{D}}(z_{\mathrm{R}})$ is obtained by integrating the interferogram given by Eq. (2.2), displayed also in Fig. 2.2, over all k:

$$i_{\mathrm{D}}(z) = \frac{\varrho}{4} S_0 \cdot \left(R_{\mathrm{R}} + \sum_{m=1}^{M} R_{\mathrm{S},m} \right) + \frac{\varrho}{2} S_0 \cdot \sum_{m=1}^{M} \sqrt{R_{\mathrm{R}} R_{\mathrm{S},m}}\, \gamma(z_{\mathrm{R}} - z_{\mathrm{S,m}}) \cos[2k_0(z_{\mathrm{R}} - z_{\mathrm{S,m}})], \quad (2.8)$$

where $S_0 = \int_0^\infty S(k)\mathrm{d}k$ represents the total spectrally integrated power of the light source. The reconstructed TD-OCT signal, or A-scan, shown in Fig. 2.5 as well, appears as a

series of coherence functions $\gamma(z)$ shifted to the positions of the optical path differences $z_{\mathrm{R}} - z_{\mathrm{S,m}}$, modulated by the fringe term $\cos[2k_0(z_{\mathrm{R}} - z_{\mathrm{S},m})]$ with an amplitude proportional to $\sqrt{R_{\mathrm{R}} R_{\mathrm{S},m}}$. The fringe signal is resident on a DC component arising from the sum of the reference and sample power reflectivities. The theoretically achievable axial resolution δz is determined by the coherence length l_{coh} of the light source, as given by Eq. (2.6) or Eq. (2.7). Because of the adjustment of the reference arm path length z_{R}, each sample arm reflector m in Eq. (2.8) has always the same optical path length $z_{\mathrm{S},m}$ as the reference arm reflector R. Consequently, the fringe amplitude in TD-OCT remains independent of the optical path difference $z_{\mathrm{R}} - z_{\mathrm{S,m}}$, assuming absorption and scattering is not considered in Eq. (2.8).

Another key parameter that determines the quality and sensitivity of images produced by an OCT system is the signal-to-noise ratio (SNR) [1, 7, 14], defined as the ratio of the power of the fringe signal P_{fringe} to the total system noise power P_{noise}:

$$\mathrm{SNR} = \frac{P_{\mathrm{fringe}}}{P_{\mathrm{noise}}}. \tag{2.9}$$

Three primary noise sources contribute to the total noise in an OCT system:

1. **Detector noise:** This is an inherent property of the detector and remains constant, independent of the incident optical power.

2. **Shot noise:** Arising from the random arrival of photons at the detector. Shot noise introduces statistical fluctuations in the detected signal and is determined by the total power incident on the detector.

3. **Excess noise or relative intensity noise (RIN):** This noise originates from fluctuations in the optical intensity of the light source, affecting the stability of the detected signal.

In an ideal TD-OCT system, the highest SNR is achieved when the total noise is dominated by the shot noise of the system (medium reference arm power). In this case, the

$\mathrm{SNR}_{\text{TD-OCT}}$ is given by [1, 7, 15–17]:

$$\mathrm{SNR}_{\text{TD-OCT}} = \frac{\varrho P_{\text{fringe}}}{2e\Delta f_{\text{D}}}, \tag{2.10}$$

where ϱ is the photodetector responsivity, e is the elementary charge, and Δf_{D} is the electronic detection bandwidth.

2.3 Fourier-domain OCT (FD-OCT)

Different to TD-OCT, A-scans in Fourier-domain OCT (FD-OCT) are obtained by applying Fourier transform to the spectral interferograms in Fig. 2.2 during the detection and processing stage of the OCT imaging. Depending on the type of the light source and detection instrumentation, FD-OCT can be implemented in two main configurations.

In a spectrometer-based OCT system (Sp-OCT), depicted in Fig. 2.6, an interferometer is illuminated by a broadband light source, typically a light emitting diode (LED) or a superluminescent diode (SLD). The interference signal is dispersed by a diffraction grating in a spectrometer and detected using a linear photodetector array, such as a charge-coupled device (CCD) or a complementary metal-oxide-semiconductor (CMOS) linear camera.

In a swept-source OCT system (SS-OCT), depicted in Fig. 2.7, an interferometer is illuminated by a rapidly sweeping narrow-linewidth tunable light source. Various operating principles have been proposed for such sources, which will be reviewed in the next chapter. The interference signal is then detected by a single photodetector as the wavelength of the swept source is tuned over time.

The reconstruction of the interferometric signal in both FD-OCT configurations involves inverse Fourier transform of the interferogram given by Eq. (2.2) (see also Fig. 2.2), yielding a depth-resolved A-scan in the form:

$$i_{\mathrm{D}}(z) = \frac{\varrho}{8}\gamma(z)\cdot\left(R_{\mathrm{R}} + \sum_{m=1}^{M} R_{\mathrm{S},m}\right) + \frac{\varrho}{4}\sum_{m=1}^{M}\sqrt{R_{\mathrm{R}}R_{\mathrm{S},m}}[\gamma(z_{\mathrm{R}}-z_{\mathrm{S},m})+\gamma(-z_{\mathrm{R}}+z_{\mathrm{S},m})]. \quad (2.11)$$

The A-scan given by Eq. (2.11), depicted in Fig. 2.6 and 2.7 as well, appears as a series of coherence functions $\gamma(z)$ shifted to the positions of the optical path differences $\pm 2(z_{\mathrm{R}} - z_{\mathrm{S,m}})$, whose amplitude is proportional to $\sqrt{R_{\mathrm{R}}R_{\mathrm{S},m}}$. The large DC term at zero optical path difference arises from the sum of the reference and sample power reflectivities. Similar to the TD-OCT regime, the theoretically achievable axial resolution is determined by the coherence length $\delta z = l_{\mathrm{coh}}$ of the light source, as given by Eq. (2.6) and Eq. (2.7).

In FD-OCT, several additional factors must be taken into account [1, 7], arising from

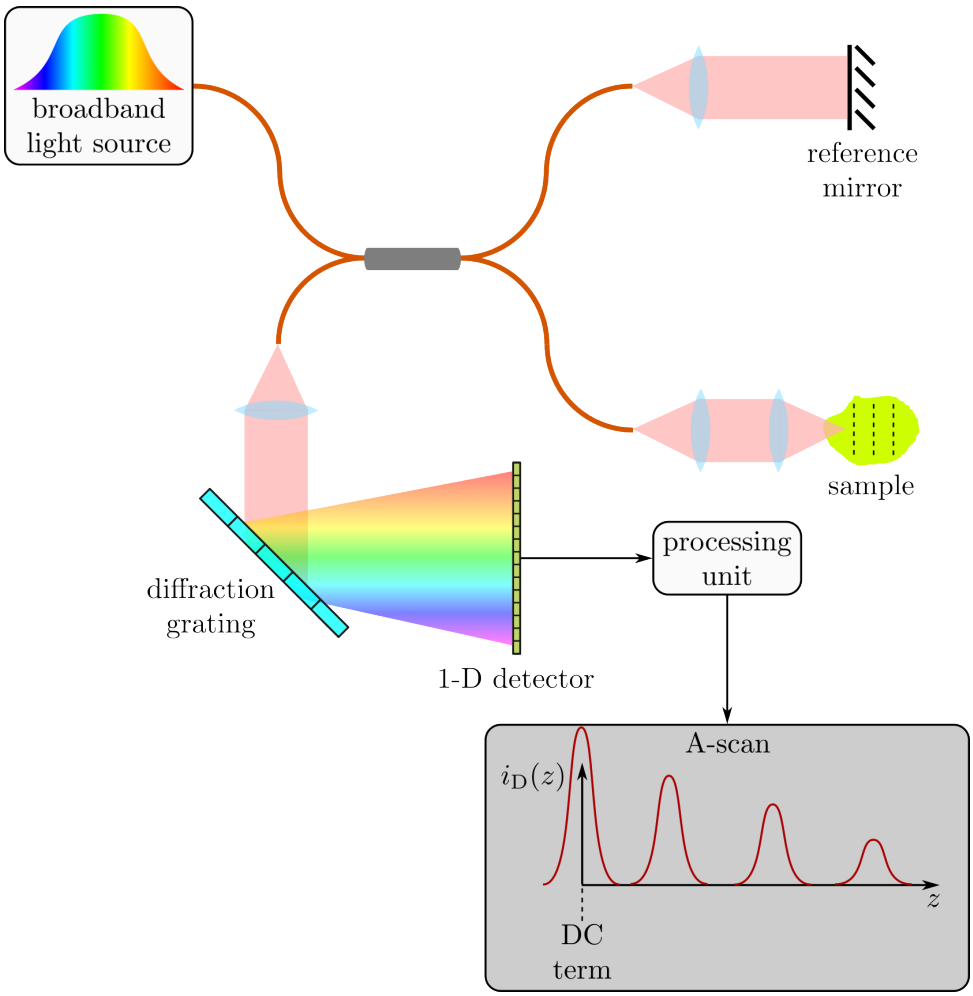

Figure 2.6: Configuration of an Sp-OCT system with a reconstructed A-scan profile.

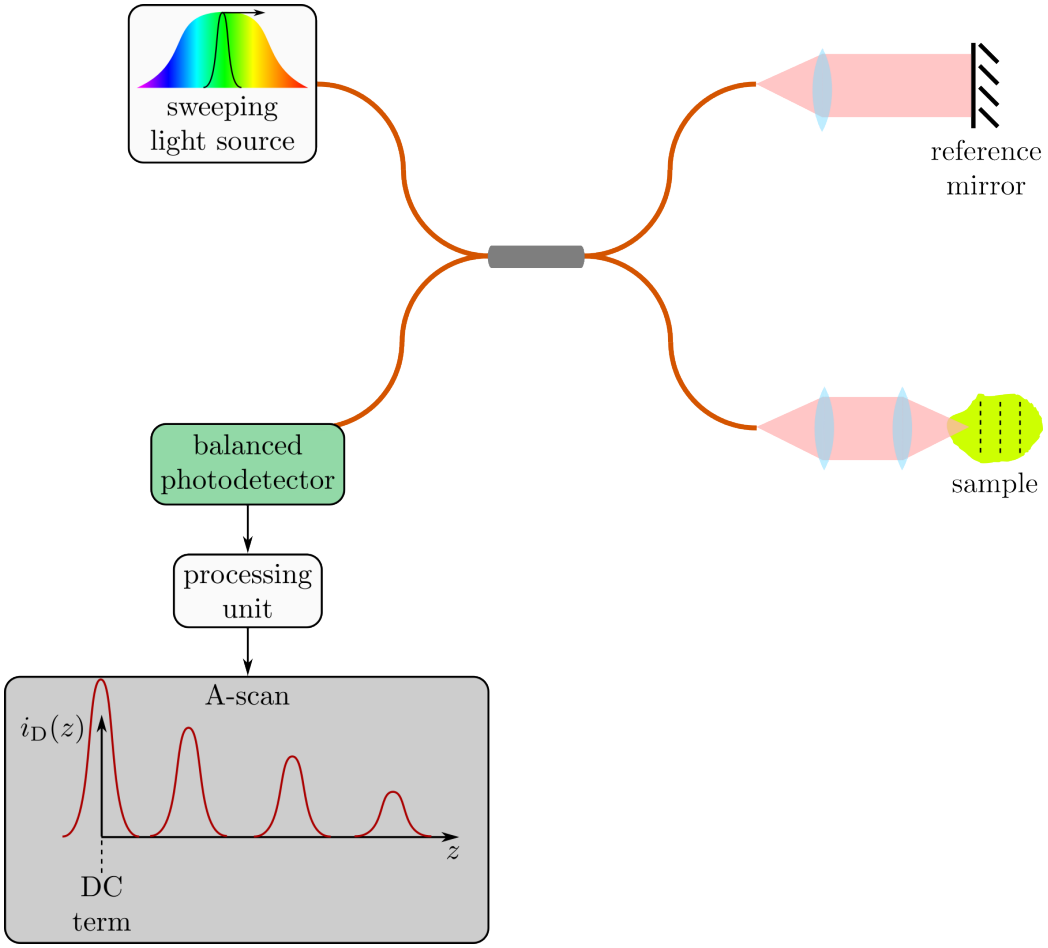

Figure 2.7: Configuration of an SS-OCT system with a reconstructed A-scan profile.

real-life limitations of the instrumentation employed in an FD-OCT system. First, the coherence functions $\gamma(z)$ in Eq. (2.11) are shifted to the positions $\pm 2(z_{\mathrm{R}} - z_{\mathrm{S,m}})$ on both sides of the zero path length due to the symmetry properties of the Fourier transform. This results in the mirroring effect around zero path length unless the sample can be entirely positioned on one side of it only.

Another important factor is the inherently limited spectral resolution of the instrumentation, denoted as δk. In Sp-OCT, δk is determined by the spectral resolution of the spectrometer, while in SS-OCT, it is limited by the instantaneous linewidth of the swept source. This spectral resolution limitation must be incorporated into the interferogram in Eq. (2.2), which can be modelled as a convolution of $\widetilde{i}_{\mathrm{D}}(k)$ with a Gaussian function of FWHM equal to δk:

$$\widetilde{i}_{\mathrm{D}}(k) \circledast \exp\left[-\frac{4\ln(2)k^2}{\delta k^2}\right] \overset{\mathcal{F}}{\Longleftrightarrow} i_{\mathrm{D}}(z)\exp\left[-\frac{(z_{\mathrm{R}}-z)^2\delta k^2}{4\ln 2}\right]. \tag{2.12}$$

The exponential fall-off on the right-hand side of Eq. (2.12) represents the decreasing interferogram visibility as a function of z. This decay, known also as a roll-off, can be quantified by the one-sided depth $\Delta z_{6\mathrm{dB}}$ at which the visibility drops by a factor of 1/2 (corresponding to a 6 dB reduction in signal-to-noise ratio as defined in Eq. (2.9)),

$$\Delta z_{6\mathrm{dB}} = \frac{2\ln 2}{\delta k} = \frac{\ln 2}{\pi}\frac{\lambda_0^2}{\delta\lambda} \approx 0.22\frac{\lambda_0^2}{\delta\lambda}, \tag{2.13}$$

where $\delta\lambda = \delta k\lambda_0^2/(2\pi)$ represents the spectral resolution in wavelength terms.

Another factor to consider when using real-world instrumentation is the rate at which the spectral interferogram can be sampled. If the interferogram is sampled into N spectral channels at sampling interval of δk, the maximum detectable imaging depth $\Delta z_{\max}$ is determined by Nyquist criterion [1, 2, 7]:

$$\Delta z_{\max} = \frac{\pi N}{2\Delta k} = \frac{\lambda_0^2 N}{4\Delta\lambda}. \tag{2.14}$$

In Sp-OCT, N corresponds to the number of pixels in the spectrometer array, while in SS-OCT, it is determined by the number of samples acquired per sweep, which is limited

by the photodetector bandwidth and the data acquisition system.

In terms of SNR analysis, a connection between Sp- and SS-OCT systems has been demonstrated [1, 7, 16–18], showing that both implementations follow the same mathematical framework. Specifically, in the shot-noise-limited case (medium reference arm power), the FD-OCT signal-to-noise ratio $\mathrm{SNR}_{\text{FD-OCT}}$ is given by:

$$\mathrm{SNR}_{\text{FD-OCT}} = \frac{\varrho N P_{\text{fringe}}}{4e\Delta f_{\text{D}}} = \frac{N}{2}\mathrm{SNR}_{\text{TD-OCT}}, \tag{2.15}$$

where the $N/2$ scaling advantage arises from the simultaneous acquisition of information from all depths. In the detector-noise-limited regime (low reference arm power), the signal may become comparable to the detector noise floor independent of the optical power. Consequently, the scaling $N/2$ sensitivity advantage in Eq. (2.15) no longer applies. In the RIN-limited regime (high reference arm power), the noise scales proportionally with the optical power, similarly to the signal. As a result, the scaling sensitivity advantage in Eq. (2.15) is reduced or eliminated as well.

Despite the presence of mirror terms and limited imaging depth, the combination of higher sensitivity and faster imaging capabilities has made FD-OCT greatly preferable to TD-OCT.

Bibliography

[1] W. Drexler and J. G. Fujimoto, Eds., *Optical Coherence Tomography: Technology and Applications*, 2nd ed. Springer, 2015.

[2] J. F. Bille, *High Resolution Imaging in Microscopy and Ophthalmology: New Frontiers in Biomedical Optics*. Springer, 2019.

[3] A. F. Fercher, W. Drexler, C. K. Hitzenberger, and T. Lasser, "Optical coherence tomography—principles and applications," *Reports on Progress in Physics*, vol. 66, no. 2, pp. 239–303, 2003.

[4] P. H. Tomlins and R. K. Wang, "Theory, developments and applications of optical coherence tomography," *Journal of Physics D: Applied Physics*, vol. 38, no. 15, pp. 2519–2535, 2005.

[5] A. G. Podoleanu, "Optical coherence tomography," *The British Journal of Radiology*, vol. 78, no. 935, pp. 976–988, 2005.

[6] ——, "Optical coherence tomography," *Journal of Microscopy*, vol. 247, no. 3, pp. 209–219, 2012.

[7] J. P. Fingler, "Motion contrast using optical coherence tomography," Ph.D. dissertation, California Institute of Technology, 7 2007.

[8] B. Lumbroso, D. Huang, A. Romano, M. Rispoli, and G. Coscas, *Clinical En Face OCT Atlas*. Jaypee Brothers Medical Publishers, 2013.

[9] A. Bradu, K. Kapinchev, F. Barnes, and A. G. Podoleanu, "Master slave en-face OCT/SLO," *Biomedical Optics Express*, vol. 6, no. 9, pp. 3655–3669, 2015.

[10] R. Cernat, A. Martínez Jiménez, and A. G. Podoleanu, "Downconversion master slave optical coherence tomography for simultaneous en-face imaging at two depths," *Optics Express*, vol. 32, no. 17, pp. 30 756–30 769, 2024.

[11] D. Huang, E. A. Swanson, C. P. Lin, J. S. Schuman, W. G. Stinson, W. Chang, M. R. Hee, T. Flotte, K. Gregory, C. A. Puliafito, and J. G. Fujimoto, "Optical coherence tomography," *Science*, vol. 254, no. 5035, pp. 1178–1181, 1991.

[12] J. G. Fujimoto, M. R. Hee, D. Huang, E. A. Swanson, C. A. Puliafito, C. P. Lin, and J. S. Schuman, "Optical coherence tomography: high-resolution imaging of the eye," *Ophthalmology*, vol. 102, no. 2, pp. 217–229, 1995.

[13] J. A. Izatt, M. R. Hee, E. A. Swanson, C. P. Lin, D. Huang, J. S. Schuman, C. A. Puliafito, and J. G. Fujimoto, "Micron-resolution imaging of the macula with optical coherence tomography," *Archives of Ophthalmology*, vol. 114, no. 10, pp. 1183–1185, 1996.

[14] J. F. de Boer, R. Leitgeb, and M. Wojtkowski, "Twenty-five years of optical coherence tomography: the paradigm shift in sensitivity and speed provided by Fourier domain OCT," *Biomedical Optics Express*, vol. 8, no. 7, pp. 3248–3280, 2017.

[15] R. Leitgeb, C. K. Hitzenberger, and A. F. Fercher, "Performance of Fourier domain vs. time domain optical coherence tomography," *Optics Express*, vol. 11, no. 8, pp. 889–894, 2003.

[16] M. A. Choma, M. V. Sarunic, C. Yang, and J. A. Izatt, "Sensitivity advantage of swept source and Fourier domain optical coherence tomography," *Optics Express*, vol. 11, no. 18, pp. 2183–2189, 2003.

[17] J. F. de Boer, B. Cense, B. H. Park, M. C. Pierce, G. J. Tearney, and B. E. Bouma, "Improved signal-to-noise ratio in spectral-domain compared with time-domain optical coherence tomography," *Optics Letters*, vol. 28, no. 21, pp. 2067–2069, 2003.

[18] T. Mitsui, "Dynamic range of optical reflectometry with spectral interferometry," *Japanese Journal of Applied Physics, Part 1: Regular Papers and Short Notes and Review Papers*, vol. 38, no. 10, pp. 6133–6137, 10 1999.

Chapter 3

Swept sources for OCT

This chapter provides a brief overview of the various types of tunable lasers for SS-OCT reported so far. Each laser type description includes fundamental operating principle, laser designs, and representative performance characteristics relevant to OCT imaging. The principle and research history of the akinetic dispersion-tuned mode-locked (DTML) lasers will be examined in detail in the next stand-alone chapter. A summary of the swept laser types described in this chapter and Chaps. 4 and 5, including their basic wavelength tuning principles and highlighting their strengths and limitations, is provided in Tab. 3.1.

Table 3.1: Summary of the swept lasers described in this chapter and Chaps. 4 and 5, including their basic wavelength tuning principles and highlighting their strengths and limitations.

Swept source type	**Principle of tuning**	**Strengths**	**Limitations/drawbacks**
Mechanically-scanned grating-based (Subsec. 3.1.1)	Angular position between a deflector and a diffraction grating	High output power; low complexity; low cost	Tens to hundred kHz sweep rate; millimeters coherence length; low phase stability
MEMS-VCSEL (Subsec. 3.1.2)	Altering cavity length using a MEMS actuator	Chip scaled; MHz sweep rate; high stability; meters coherence length	Mechanical fatigue
FDML (Subsec. 3.1.3)	Fabry–Pérot tunable filter	MHz sweep rate; centimeters coherence length; high output power	Precise synchronization; dispersion compensation, temperature control; high cost
Acousto-optic based (Subsec. 3.2.1)	Dynamic diffraction grating controlled by a sound wave	Centimeters coherence length; programmable sweep profile;	Tens to hundred kHz sweep rate
KTN-scanned grating-based (Subsec. 3.2.2)	Beam bending via electro-optic effect	MHz sweep rate; centimeters coherence length; programmable sweep profile	High driving voltage; temperature control
All-semiconductor design (Subsec. 3.2.3)	Carrier-induced index of refraction tuning/Vernier effect	Chip scaled; precise control; centimeters coherence length;	Invalid points in the wavelength sweep; temperature control;
Time-stretching (Subsec. 3.2.4)	Broadband pulse stretching by large dispersion	Tens to hundreds of MHz sweep rate	High cost
SPML (Subsec. 3.2.5)	Broadband pulse stretching by large dispersion in a cavity	Tens of MHz sweep rate; high output power	Precise synchronization, dispersion compensation, temperature control; millimeters coherence length
Single-harmonic DTML (Chap. 4)	Active mode-locking in a dispersive cavity	Low cost; low complexity; no dispersion compensation; programmable sweep profile	Millimeters coherence length; hundreds of kHz sweep rate
Multi-harmonic DTML (Chap. 5)	Active mode-locking in a dispersive cavity	MHz sweep rate low cost; low complexity; no dispersion compensation; programmable sweep profile	Millimeters coherence length; broad and high spectral purity modulation source

3.1 Mechanical-based swept sources

3.1.1 Mechanically-scanned grating-based swept lasers

Mechanically-scanned grating-based lasers, also sometimes referred to as external-cavity diode lasers, were among the first tunable lasers designed [1, 2]. These lasers operate by placing a diffraction grating in an external cavity of a semiconductor gain chip or a laser diode, where a combination of the diffraction grating and a mirror serve as a tunable wavelength selective filter. The angular position of the grating or mirror determines the lasing λ wavelength through [1]:

$$\lambda = p_{\mathrm{DG}}(\sin\theta_{\mathrm{i}} + \sin\theta_{\mathrm{d}}), \tag{3.1}$$

where p_{DG} denotes the grating period, θ_{i} as the angle between the grating normal and the beam incidence axis, and θ_{d} is the angle between the grating normal to the diffracted beam. The grating-based lasers can be implemented in two fundamental configurations: the Littrow and Littman–Metcalf configurations [2], both schematically depicted in Fig. 3.1. In the Littrow configuration, the first-order diffracted beam is reflected back into the laser diode (LD) for feedback, while the zeroth-order output beam is deflected away by rotating the diffraction grating (DG), usually by using a piezoelectric actuator [3, 4]. In the Littman–Metcalf configuration, in contrast, the grating orientation is fixed and an additional deflector is used to maintain a constant output beam direction while tuning. As the deflector, various devices have been utilised, including galvanometer mirrors [5, 6], polygon scanners [7, 8], or MEMS [9, 10]. In both configurations, rotating the grating or mirror mechanically changes the feedback wavelength, producing a continuously tunable emission suitable for SS-OCT.

Both Littrow and Littman–Metcalf configurations can be implemented within a fibre-based laser cavity. Figure 3.2(a) depicts Littman–Metcalf configuration in a linear fibre cavity, consisting of a fibre-coupled semiconductor optical amplifier (SOA), fibre coupler (FC), and a grating-based wavelength filter. The angle of incidence of the beam illuminating the grating (DG) is deflected using a galvanometer mirror (GM). This tunable laser,

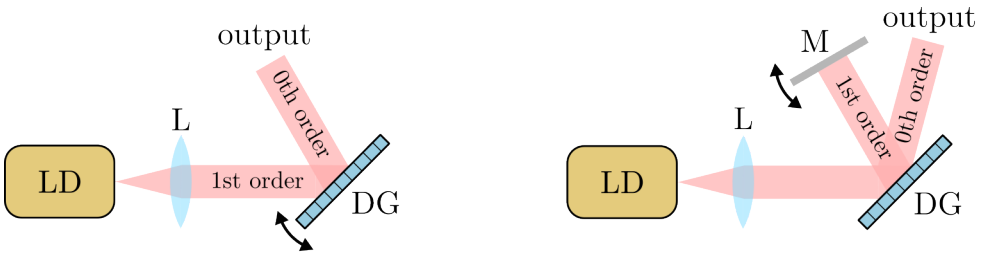

Figure 3.1: Two fundamental laser configurations used in mechanically-scanned grating-based tunable lasers [2]. LD: laser diode, L: lens, DG: diffraction grating, M: mirror/deflector.

operating at 1.2 µm, demonstrated a tuning bandwidth of 94 nm and at a sweep rate of 100 Hz [5]. Another galvanometer-scanned Littman–Metcalf configuration implemented in a fibre ring cavity is shown in Fig. 3.2(b). This laser was employed for full-field OCT (FF-OCT) at a sweep rate of 1 Hz, achieving a tuning bandwidth of 48 nm at a central wavelength of 850 nm [6]. Both lasers shown in Fig. 3.2 demonstrated coherence lengths exceeding 10 mm, corresponding to a spectral linewidth of 0.13 nm at 1.2 µm [5], and a linewidth of 0.05 nm 850 nm [6].

Polygon mirror-based swept lasers are a subclass of Littman–Metcalf configurations, where a rotating multi-facet polygon scanner replaces a galvanometer mirror [7, 8, 11]. This configuration enables high-speed, continuous wavelength tuning by mechanically varying the angle of incidence on the grating as the polygon rotates. A schematic of a polygon-scanned grating-based laser operating at 1.3 µm is depicted in Fig. 3.3 [7]. This well-optimized system achieved an output power of up to 100 mW, a broad tuning bandwidth of 113 nm, and a coherence length of 16 mm, while operating at a sweep rate of 65 kHz. The laser employed Fourier-domain mode-locking (FDML) technique, which is more detailed in Subsec. 3.1.3 and Sec. 5.5. Higher sweep rates can be achieved by increasing the number of reflective facets on the polygon. For example, by displacing the polygon scanner off the optical axis and using a 128-facet polygon, sweep rates of up to 115 kHz have been demonstrated [8].

In the ongoing process toward miniaturization of tunable lasers and OCT systems, the conventionally bulky laser architectures shown in Figs. 3.2 or 3.3 have been sub-

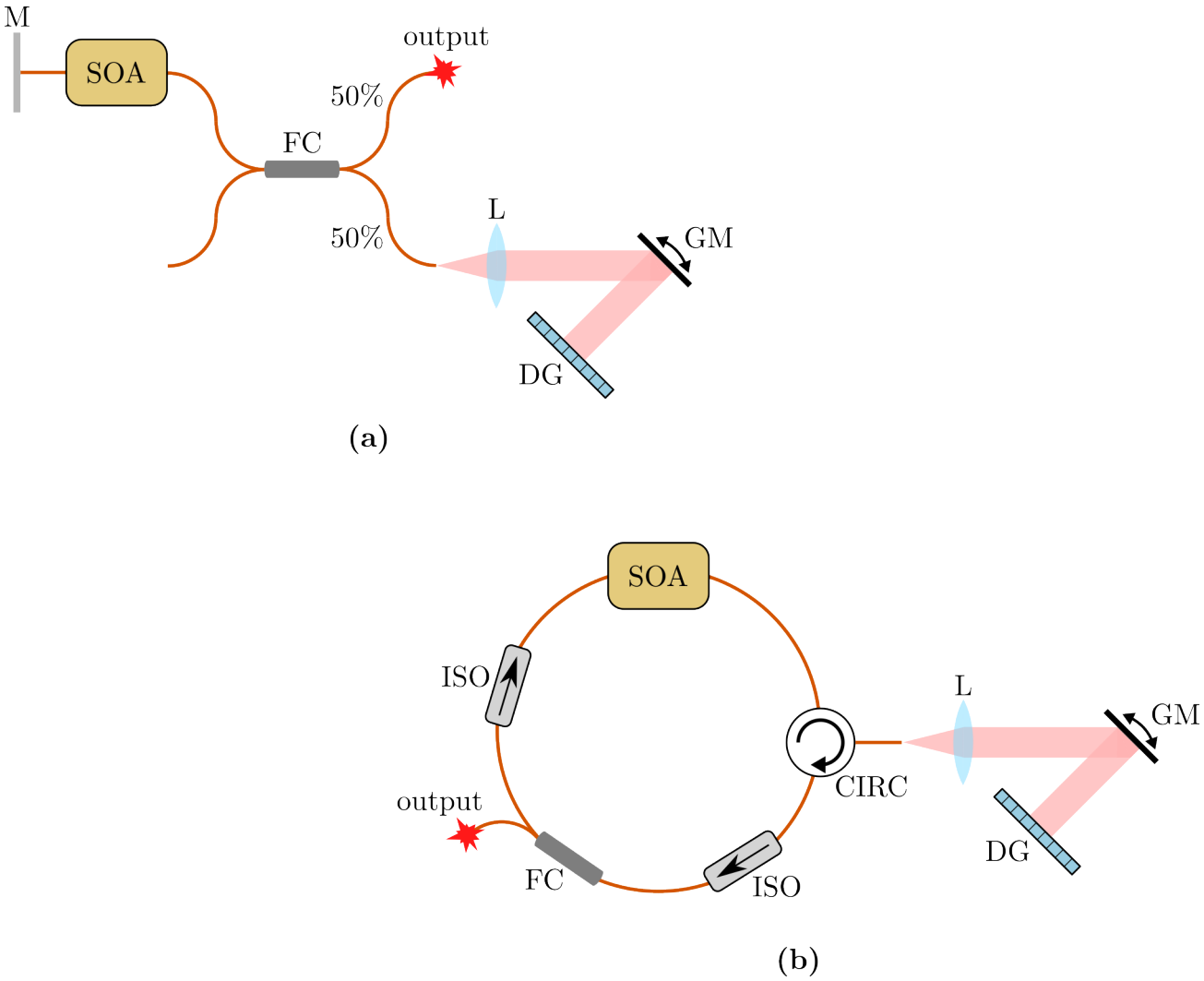

Figure 3.2: Mechanically-scanned grating-based tunable lasers implemented in fibre cavities. **(a)** Littman–Metcalf configuration in a fibre linear cavity [5]. **(b)** Littman–Metcalf configuration in a fibre ring cavity [6]. SOA: semiconductor optical amplifier, M: mirror, FC: fibre coupler, L: lens, GM: galvanometer mirror, DG: diffraction grating, CIRC: circulator, ISO: isolator.

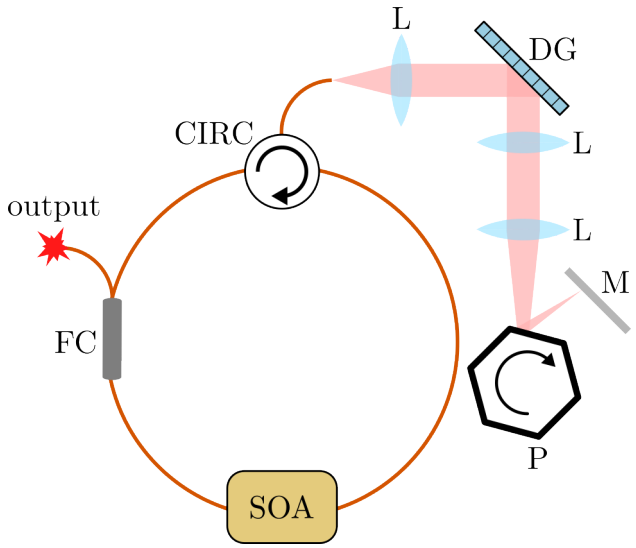

Figure 3.3: A polygon-scanned grating-based tunable laser [7]. SOA: semiconductor optical amplifier, M: mirror, FC: fibre coupler, L: lens, P: polygon mirror, DG: diffraction grating, CIRC: circulator.

stantially downscaled through utilisation of micro-electro-mechanical systems (MEMS) technology [9]. MEMS technology enables an integration of mechanical components, actuators, sensors, and control electronics onto a single chip, allowing compact and highly tunable photonic devices. MEMS are commonly used to actuate wavelength-selective elements, such as diffraction gratings or Fabry–Pérot cavities, with high precision and speed. An example of an integrated laser is schematically depicted in Fig. 3.4, where a miniature MEMS mirror (MEMS M) is used to control the angle of incidence onto a diffraction grating. Using this configuration, an ultra-narrow instantaneous linewidth of 0.28 pm (corresponding to a coherence length of approximately 2.8 m) was achieved [10].

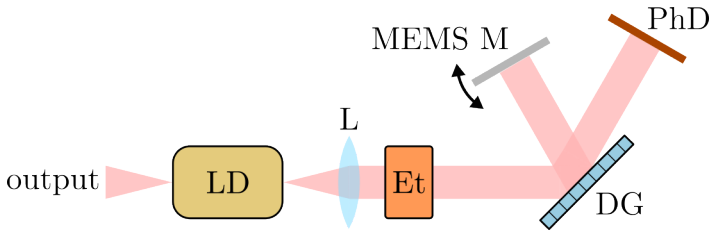

Figure 3.4: Mechanically-scanned grating-based tunable laser using a MEMS mirror as a deflector [9]. LD: laser diode, M: mirror, L: lens, Et: etalon, DG: diffraction grating, PhD: photodiode.

3.1.2 Micro-electro-mechanical system vertical-cavity surface-emitting lasers (MEMS-VCSELs)

A MEMS-VCSEL (micro-electro-mechanical systems vertical-cavity surface-emitting laser), whose structure is illustrated in Fig. 3.5, integrates a micromechanically tunable mirror into a conventional VCSEL architecture [12, 13]. The structure comprises bottom distributed Bragg reflector (DBR), central active region for optical gain, and a movable top MEMS mirror suspended above the cavity on a MEMS actuator. By applying voltage across the MEMS actuator, the mirror is pushed and pulled relative to the substrate, altering the cavity length and shifting the lasing wavelength. The lasing wavelength λ is determined by the cavity resonance condition [13]:

$$q\lambda = 2nL, \tag{3.2}$$

where q is the longitudinal mode number, n is the effective index of refraction of the cavity medium, and L is the cavity length. Unlike traditional mechanically tuned lasers, MEMS-VCSELs are chip-scale, combining high mechanical stability and coherence lengths, making them exceptionally well-suited for integration in compact biomedical imaging systems, particularly OCT.

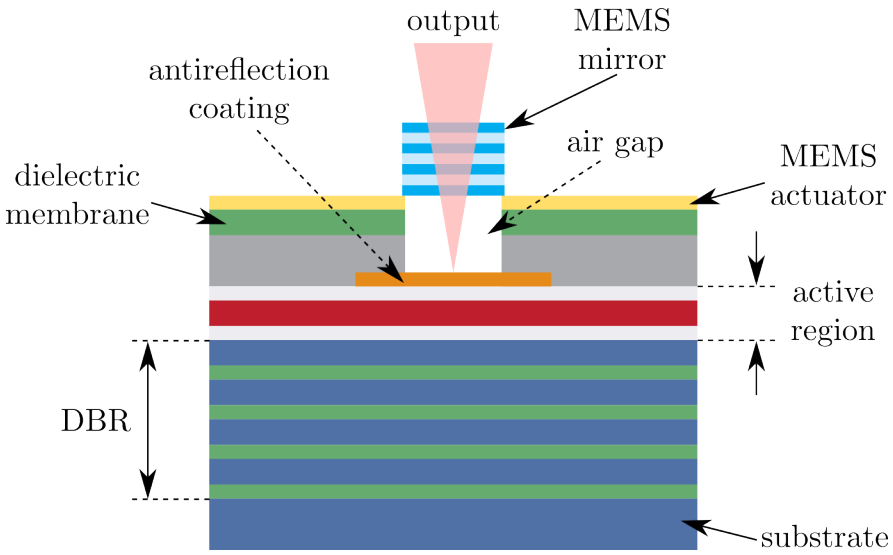

Figure 3.5: Schematic diagram of the MEMS-VCSEL structure. DBR: distributed Bragg reflector. Redrawn from [14].

MEMS-VCSELs have been reported across most wavelengths widely used in OCT. At 1510 nm, a manual wavelength tuning over 100 nm was demonstrated [15]. A MEMS-VCSEL operating at 1310 nm was shown capable of an exceptionally wide tuning bandwidth over 150 nm at a sweep rate of 500 kHz [16]. Commercially available tunable MEMS-VCSELs at 1060 nm and 1310 nm, supplied by companies such as Thorlabs, Santec, Excelitas, or Inphenix, typically provide tuning bandwidths of 100 nm at sweep rates of 100 kHz, 200 kHz, or even 400 kHz [14, 17–19]. Most recently, a MEMS-VCSEL operating at 850 nm was presented, exhibiting tuning of 38 nm at 347 kHz [20]. In general, MEMS-VCSELS are capable of extent coherence lengths exceeding 1 m [14, 17, 18].

3.1.3 Fourier-domain mode-locked (FDML) swept lasers

Fourier domain mode-locked (FDML) lasers are a class of high-speed wavelength-swept lasers specifically designed to overcome the inherent limitations in speed and coherence of conventional tunable lasers architectures shown in Figs. 3.2, 3.3, and 3.4. FDML was originally introduced in a fibre Fabry–Pérot tunable filter (FFP-TF)-based swept laser, schematically depicted in Fig. 3.6 [21–23]. In this laser, the lasing wavelength is determined by the spectral response of the employed FFP-TF, whose time-dependent transmitted wavelength $\lambda(t)$ can be parametrically expressed as [24]:

$$\lambda(t) = \lambda_0 + \frac{1}{2}\Delta\lambda \cos(2\pi f_s t), \tag{3.3}$$

where λ_0 is the central wavelength, $\Delta\lambda$ is the total tuning bandwidth, and f_s is the sweep rate of the laser. Owing to its distinct mode-locking mechanism, FDML is often regarded as a separate category of swept-source lasers, and can be seen as a transitional type between mechanical- and akinetic-based swept lasers.

The laser in Fig. 3.6 adopts a ring cavity geometry [21], comprising of a fibre-coupled semiconductor optical amplifier (SOA) and a piezelectrically actuated fibre Fabry–Pérot tunable filter (FFP-TF), selecting the lasing wavelength based on Eq. (3.3). The FFP-TF is driven by a waveform from a signal generator (SG). In this conventional FFP-TF-based swept laser, the cavity length is minimized to reduce round trip delay, and the filter is

swept at a rate much slower than the inverse of the cavity round trip time (the fundamental frequency of the cavity). Under these conditions, only a small subset of the cavity modes are supported at any given moment, as illustrated by the single colour optical field inside the cavity in Fig. 3.6.

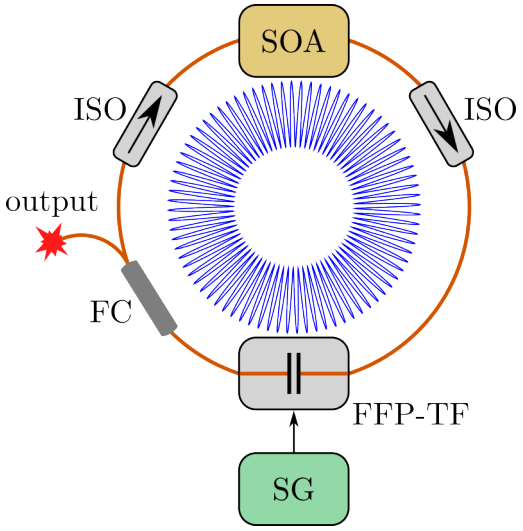

Figure 3.6: FFP-TF based swept laser [21]. SOA: semiconductor optical amplifier, FFP-TF: fibre Fabry–Pérot tunable filter, SG: signal generator, ISO: isolator, FC: fibre coupler.

An FDML laser, depicted in Fig. 3.7, shares a similar architecture with the standard FFP-TF-based laser in Fig.3.6. The key difference is in the incorporation of a dispersion-managed delay line of hundreds of meters or units of kilometers to extend the cavity round trip time. For FDML operation, the FFP-TF is tuned synchronously with the cavity round trip time [22, 23]. As a result, all allowed optical modes are phase-locked, enabling the laser to store the full wavelength bandwidth inside the cavity at any given moment as a long chirped pulse with a period proportional to the round trip time of the cavity. This is conceptually illustrated by the rainbow-like optical field inside the cavity in Fig. 3.7. A more detailed discussion on the similarities and differences between FDML and multi-harmonic DTML will be provided in Sec. 5.5.

Since its introduction, the FDML laser has become the gold standard for SS-OCT systems delivering high-speed imaging and deep tissue penetration. Its advantages include high spectral stability and long coherence lengths of units of centimeters, though these come at the cost of increased system complexity due to the need for precise dispersion,

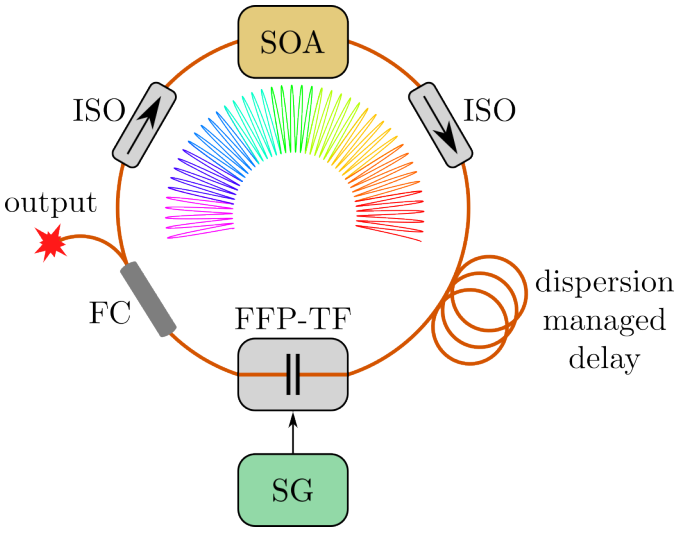

Figure 3.7: FDML swept laser [22]. SOA: semiconductor optical amplifier, FFP-TF: fibre Fabry–Pérot tunable filter, SG: signal generator, ISO: isolator, FC: fibre coupler.

temperature management, and filter synchronization. FDML lasers have been reported at all wavelengths relevant to OCT [25]. Among them, multi-megahertz FDML swept lasers at 1060 nm [26, 27] and 1310 nm [28, 29], using a so-called buffering technique, were demonstrated exceeding 100 nm tuning bandwidths. Nevertheless, the precise dispersion control inside the cavity and the implementation of the buffering technique in FDML swept sources come at the cost of increased manufacturing expense. Commercially available tunable FDML swept lasers at 1060 nm, 1310 nm, and 1550 nm, supplied by Optores company, provide tuning bandwidths of 100 nm and coherence lengths over 1 cm at sweep rates of units of megahertz [30]. Most recently, FDML has been extended to 850 nm central wavelength, providing 40 nm tuning bandwidth and 1.5 cm coherence length at sweep rate of 828 kHz [31].

3.2 Akinetic-based swept sources

3.2.1 Acousto-optic based swept lasers

An acousto-optic tunable filter (AOTF) or acousto-optic deflector (AOD) selects the lasing wavelength by generating a dynamic diffraction grating controlled by a sound wave inside a crystal, such as TeO_2. The acoustic wave in the crystal induces periodic changes in its

refractive index, and only light of a specific wavelength λ is diffracted at a specific angle θ, schematically depicted in the laser in Fig. 3.8(a). The relationship between the diffracted wavelength and the system parameters is given by the phase-matching condition [32]:

$$\lambda = \frac{2nv \sin\theta}{f}, \tag{3.4}$$

where n is the index of refraction of the undisturbed crystal, v is the speed of sound in the crystal, and f is the frequency of the acoustic wave applied to the crystal from a signal generator (SG). By sweeping the Δf, different optical wavelengths are diffracted, as given by Eq. (3.4). This electronically controlled tuning mechanism allows fast akinetic wavelength tuning.

Swept lasers based on the acousto-optic principle have been demonstrated feasible at wavelengths of 1060 nm [33], 1310 nm [34, 35], and 1550 nm [32, 36]. However, their most prominent use is at 850 nm [37, 38] and even in the visible range below 800 nm [39, 40], where other types of swept lasers are less common. The linear and ring cavity acousto-optic tunable lasers shown in Fig. 3.8 demonstrated highly wavenumber-linear tuning characteristics, with 50 nm tuning bandwidth at a 1060 nm central wavelength [33] (Fig. 3.8(a)), and 35 nm tuning at 850 nm [37] (Fig. 3.8(b)). Commercially available acousto-optic based swept lasers around 850 nm, supplied by Superlum company, provide over 50 nm tuning bandwidths at sweep rates up to hundreds of Hz [41], making them suitable for use in full-field swept source (FFSS)-OCT imaging [42, 43].

3.2.2 KTN-scanned grating-based swept lasers

An alternative akinetic tuning mechanism utilizes an electro-optic deflector based on a KTN crystal ($KTa_{1-x}Nb_xO_3$), which can be positioned between the semiconductor optical amplifier (SOA) and the diffraction grating, as schematically depicted in Fig. 3.9 [44]. The applied voltage from a signal generator (SG) induces an index of refraction gradient in the crystal via the electro-optic effect, causing the beam bending effect along the KTN crystal. By modulating the input voltage, the deflection angle of the beam changes continuously, resulting in a dynamic change in the incident angle on the diffraction grating, and thus

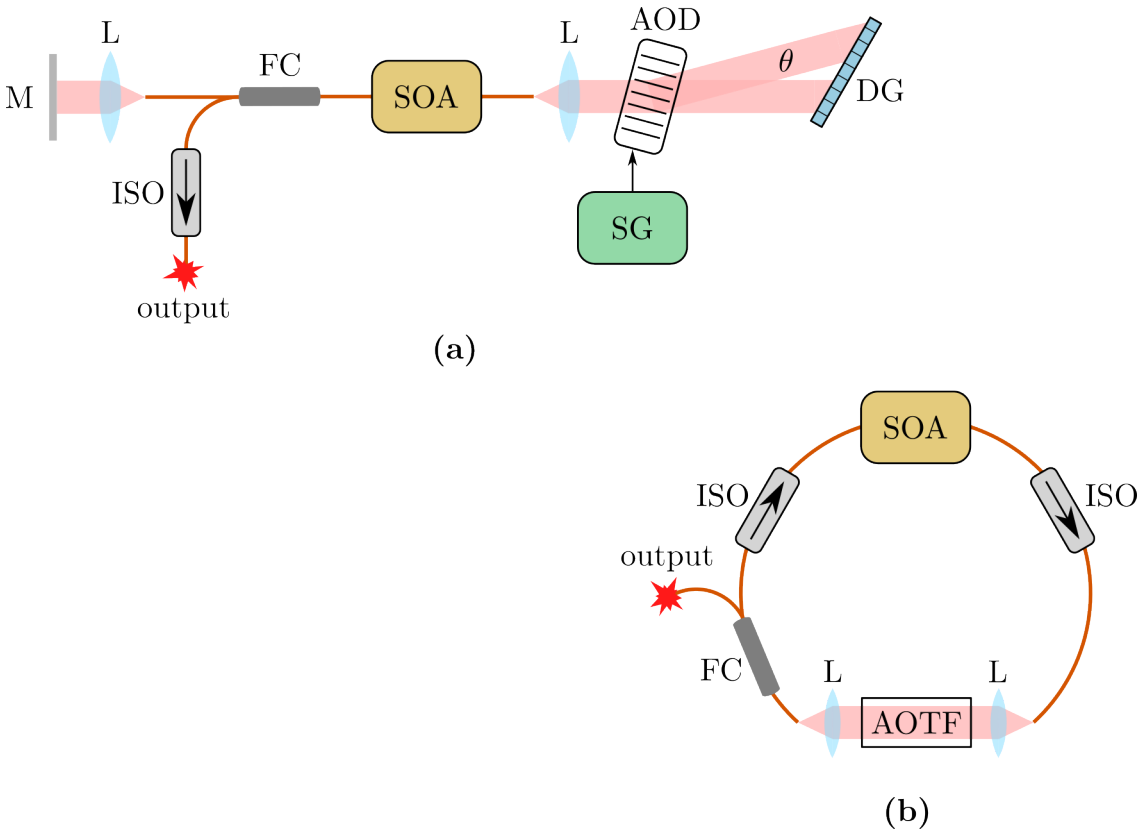

Figure 3.8: Acousto-optic based swept lasers. **(a)** Littrow laser configuration using AOD as a deflector [33]. **(b)** Ring laser cavity using AOTF [37]. SOA: semiconductor optical amplifier, AOD: acousto-optic deflector, DG: diffraction grating, FC: fibre coupler, ISO: isolator, M: mirror, L: lens, SG: signal generator, AOTF: acousto-optic tunable filter.

a tunable lasing wavelength. The laser shown in Fig. 3.9 demonstrated a broad tuning bandwidth exceeding 100 nm around a central wavelength of 1.3 µm, with sweep frequency reaching up to 200 kHz, and exhibiting a coherence length longer than 7 mm.

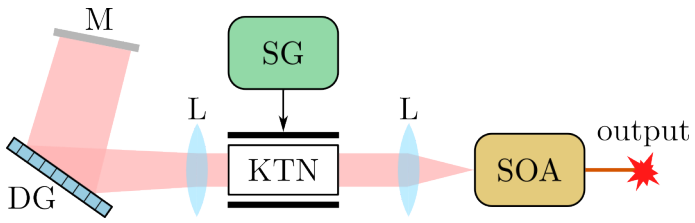

Figure 3.9: Grating-based tunable laser using a KTN as a deflector [44]. SOA: semiconductor optical amplifier, M: mirror, L: lens, DG: diffraction grating, SG: signal generator.

3.2.3 All-semiconductor design swept lasers

Unlike traditional swept lasers that rely on moving parts (e.g., galvanometer scanners, polygon mirrors, MEMS actuators, or mechanically tuned Fabry–Pérot filters), this akinetic swept source uses an all-electronic tuning mechanism, eliminating mechanical components entirely. The laser integrates semiconductor gain and tunable filtering elements on a single chip, as displayed in Fig. 3.10, and exploits carrier-induced index of refraction tuning enhanced by Vernier effect to programmatically sweep the output wavelength [45, 46]. The physical principle of tuning in this type of swept source relies on index of refraction modulation within integrated optical elements, such as tunable Bragg gratings or ring resonators, embedded in the laser cavity. By applying electrical currents to these elements, the effective optical path length changes due to the carrier-induced index of refraction change effect, thereby shifting the resonant wavelength. In some architectures, the Vernier effect is employed by using multiple filters with slightly different free spectral ranges, allowing broad wavelength tuning through small refractive index adjustments. In comparison with most other swept lasers with transition periods only after full wavelength sweeps, the sweep in all-semiconductor designs consists of a sequence of ~ 0.5 nm short micro-sweeps, each separated by a transition period. Within a micro-sweep, these lasers are mode-hop free and do not exhibit coherence revival artifacts. This all-integrated approach enables precise control over tuning bandwidth, speed, direction, and waveform

shape, making the source programmable rather than passively tuned. Its large coherence lengths up to units of meters is sufficient for many OCT applications, particularly where electronic control and system compactness is prioritized.

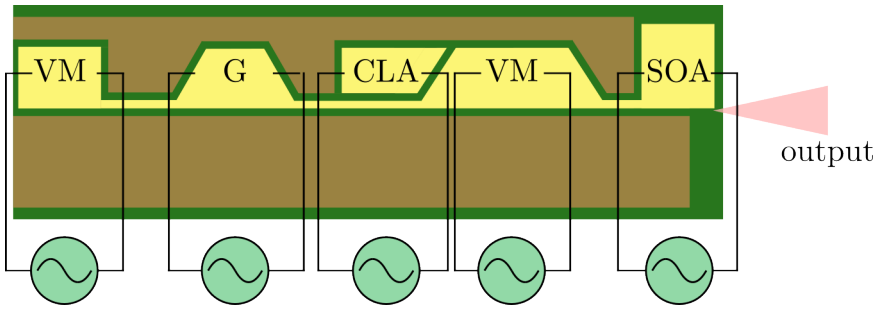

Figure 3.10: All-semiconductor tunable lasers design. VM: Vernier mirror, G: gain, CLA: cavity length adjustment, SOA: semiconductor optical amplifier. Redrawn from [45].

All-semiconductor swept lasers have been so far demonstrated at wavelengths of 1310 nm [45, 47] and 1550 nm [45], with sweep rates ranging from tens to hundreds of kHz. Commercially available swept sources at 1310 nm and 1550 nm, supplied by Insight company, provide tuning bandwidths over 100 nm at sweep rates up to 200 kHz [48].

3.2.4 Time-stretching (dispersive Fourier transform) swept lasers

Time-stretching swept lasers, also known as dispersive Fourier transform (DFT) swept sources, are a class of ultrafast lasers that exploit optical dispersion to convert spectral information into the time domain [49, 50]. Instead of tuning the emission wavelength over time, these sources generate a broadband optical pulse, which is passed through a highly dispersive medium, typically kilometers of optical fibre or chirped fibre Bragg grating with large dispersion. Due to chromatic dispersion, different wavelength components of the pulse travel at different speeds, enabling the separation of spectral components in time. The result is a single-shot time-resolved spectral sweep, with no moving parts and with sweep rates reaching tens of megahertz. These sources are not tunable in the conventional sense, instead, the entire spectrum is encoded into the temporal profile of each stretched pulse, with pulse repetition given by the inverse round trip time of the seed mode-locked laser (see Fig. 3.11). Time-stretching swept lasers are particularly attractive

for ultrafast imaging and spectroscopy, though they are limited by spectral control and coherence compared to cavity-based swept sources.

A full swept source schematic using a long fibre delay line as a stretcher is depicted in Fig. 3.11(a) [51]. As a seed for supercontinuum generation, a femtosecond mode-locked laser is employed. After coupling the light into fibre using an aspheric lens (AL), two nonlinear effects, self-phase modulation and coherent optical wave-breaking, are exploited in a polarisation-maintaining photonic crystal fibre (PM-PCF) to deliver broad and flat spectrum. The broadband pulse is then mapped into the time domain by propagation through a long single-mode fibre (SMF) providing a large time delay dispersion. Finally, an ytterbium-doped fibre (YDF) amplifier is appended to increase the output power. An improved version of the laser in 3.11(a) with reduced power losses using a cFBG was reported by the same author in [52], schematically depicted in Fig. 3.11(b), where a pulse picker (PP) was employed to reduce the repetition rate of the laser.

Time-stretching swept lasers have been demonstrated as feasible across all major wavelengths relevant to OCT, including 2 µm [53], 1550 nm [50, 54–61], 1310 nm [49], 1060 nm [51, 52, 62], 800 nm [63], and even visible at 670 nm [64], with some lasers reaching tens or hundreds of MHz sweep rates and exceeding 100 nm tuning bandwidths.

More recently, a nonlinear polarisation rotation (NPR) passively mode-locked lasers have started being employed to generate broadband ultrashort pulses with flat spectra as seeds for time-stretching [53, 58–61].

3.2.5 Stretched-pulse mode-locked (SPML) swept lasers

Stretched-pulse mode-locking (SPML) is a technique to generate broadband, wavelength-swept output by balancing dispersion and nonlinearity within a fibre laser cavity [65, 66]. In this technique, optical pulses undergo periodic stretching and compressing using elements with large normal and anomalous dispersions, respectively. Due to chromatic dispersion in the stretching stage, spectral components are separated in time, resulting in a time-wavelength mapping at the laser output. The instantaneous linewidth $\delta\lambda$ of the

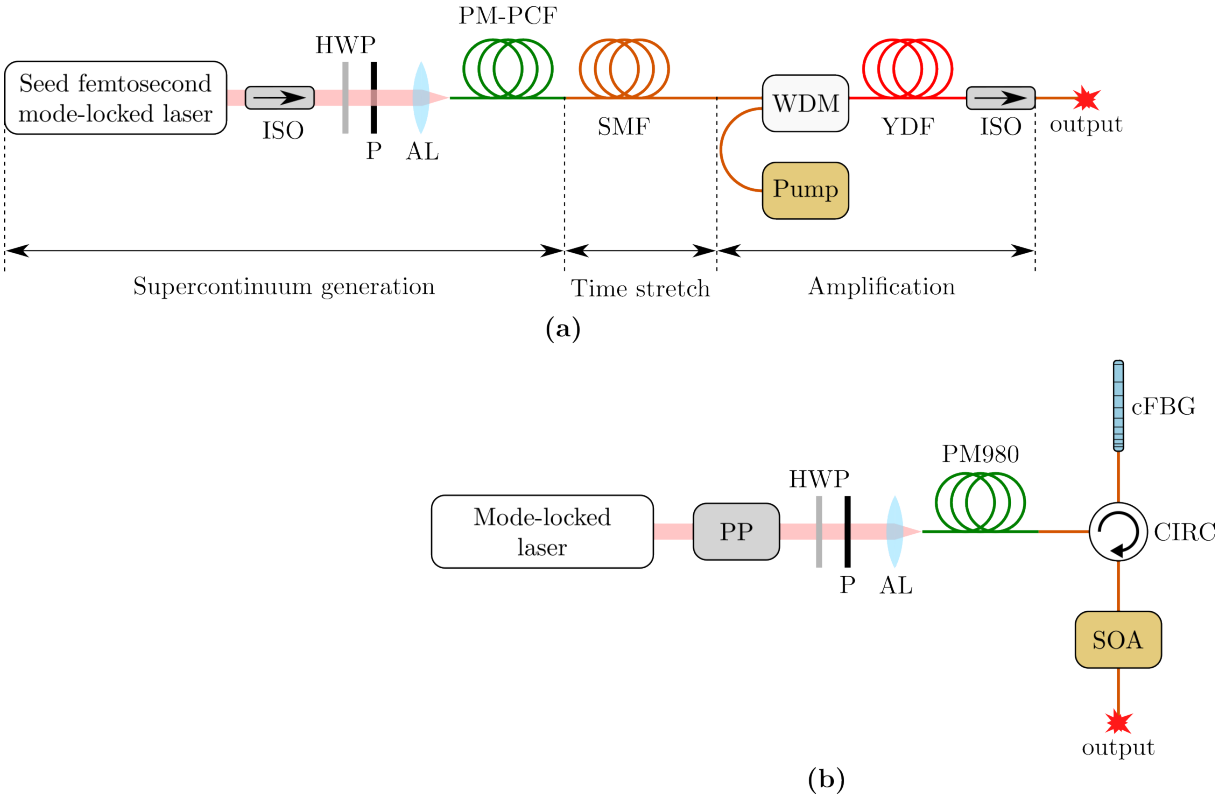

Figure 3.11: Schematics of time-stretching swept lasers using **(a)** a long fibre delay line as a stretcher [51], and **(b)** a chirped fibre Bragg grating [52]. ISO: isolator, HWP: half-wave plate, P: polariser, AL: spheric lens, PM-PCF: polarisation maintaining photonic crystal fibre, SMF: single-mode fibre, WDM: wavelength division multiplexer, YDF: ytterbium doped fibre, PP: pulse picker, cFBG: chirped fibre Bragg grating, CIRC: circulator, SOA: semiconductor optical amplifier.

output can be approximated as [66]:

$$\delta\lambda = \frac{\tau}{\mathrm{TDD}_{\mathrm{stretch}}}, \tag{3.5}$$

where τ is the pulse width before the stretching stage, and $\mathrm{TDD}_{\mathrm{stretch}}$ is the time delay dispersion of the stretching element. The SPML pulse evolution enables stable mode-locking at high repetition rates while supporting a broad spectral bandwidth. Unlike traditional swept sources, the wavelength tuning in SPML is not achieved by shifting a wavelength selective filter, but is inherently governed by the internal pulse dynamics. SPML lasers are of interest in ultra-fast SS-OCT and spectroscopy due to their potential for multi-megahertz and broad tuning capabilities.

An SPML swept laser using two separate cFBGs for the stretching and compressing stages is schematically depicted in Fig. 3.12(a). The laser utilizes an intensity modulator (IM) synchronized to the cavity round trip time to actively shape short optical pulses. To compensate for losses after the time-stretching through a normal dispersion cFBG (+cFBG), the pulse is amplified through a booster (BOA), and coupled out through a fibre coupler (FC). As the SPML requires zero effective dispersion in the cavity for its operation, the pulse is compressed through an anomalous dispersion cFBG (−cFBG), with the same absolute value of dispersion as the +cFBG. At the end of a cycle, the pulse is returned to the IM for shaping. A modified laser configuration using a single cFBG for both stretching and compressing stage, significantly improving the SPML operation, is depicted in Fig. 3.12(b).

SPML swept lasers have been demonstrated as feasible so far at 1550 nm [65, 68], 1310 nm [66, 69–72], and 1060 nm [67, 73], with some lasers reaching tens of MHz sweep rates and 100 nm tuning bandwidths.

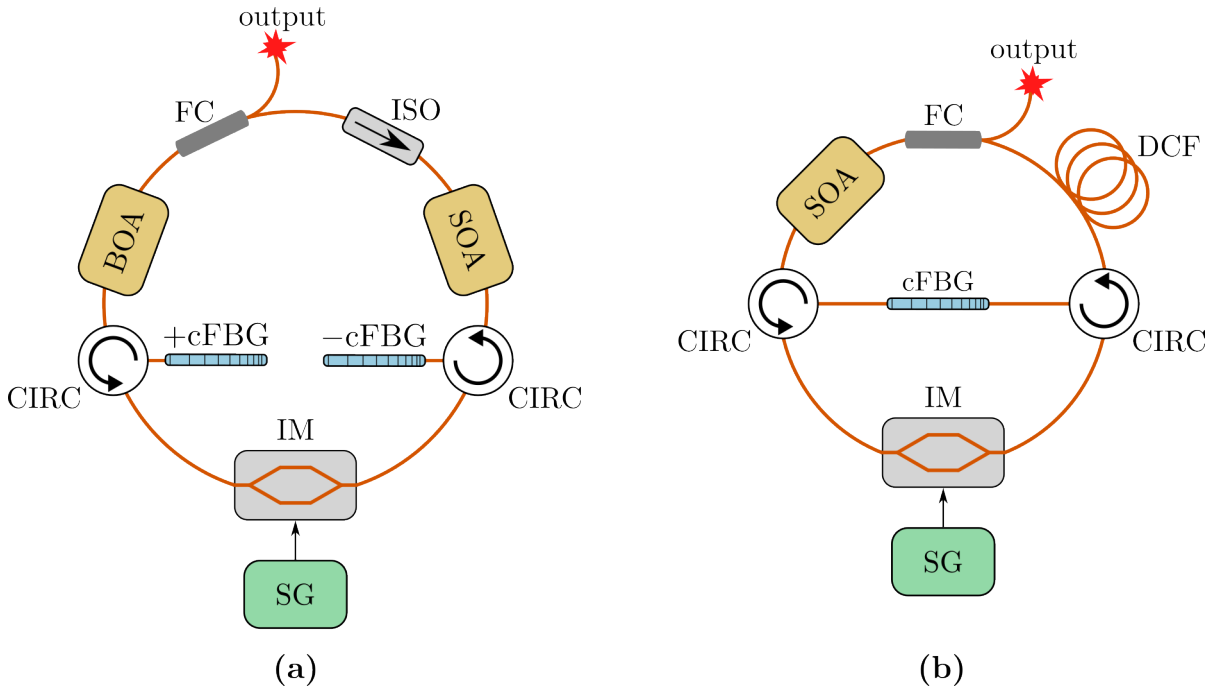

Figure 3.12: Schematics of SPML swept lasers using **(a)** two cFBGs [67], and **(b)** a single cFBG [68]. BOA: booster amplifier, FC: fibre coupler, ISO: isolator, SOA: semiconductor optical amplifier, CIRC: circulator, cFBG: chirped fibre Bragg grating, IM: intensity modulator, SG: signal generator, DCF: dispersion compensation fibre.

Bibliography

[1] K. Liu and M. G. Littman, "Novel geometry for single-mode scanning of tunable lasers," *Optics Letters*, vol. 6, no. 3, pp. 117–118, 1981.

[2] P. Zorabedian, "Tunable external-cavity semiconductor lasers," in *Tunable Lasers Handbook*, F. J. Duarte, Ed. Academic Press, 1995, pp. 349–442.

[3] W. Hong, "Design and characterization of a Littrow configuration external cavity diode laser," 2004, research Science Institute, California Institute of Technology.

[4] S. D. Saliba and R. E. Scholten, "Linewidths below 100 kHz with external cavity diode lasers," *Appl. Opt.*, vol. 48, no. 36, pp. 6961–6966, 12 2009.

[5] N. Krstajić, D. T. D. Childs, S. J. Matcher, D. Livshits, A. Shkolnik, I. Krestnikov, and R. A. Hogg, "Swept-source laser based on quantum-dot semiconductor optical amplifier—applications in optical coherence tomography," *IEEE Photonics Technology Letters*, vol. 23, no. 11, pp. 739–741, 2011.

[6] M. F. Shirazi, P. Kim, M. Jeon, and J. Kim, "Full-field optical coherence tomography using galvo filter-based wavelength swept laser," *Sensors*, vol. 16, no. 11, p. 1933, 2016.

[7] Y. Mao, J. Zhang, J. Wang, and Z. Chen, "High performance wavelength-swept laser with mode-locking technique for optical coherence tomography," *Optics Communications*, vol. 282, no. 1, pp. 88–92, 2009.

[8] W. Y. Oh, S. H. Yun, G. J. Tearney, and B. E. Bouma, "115 kHz tuning repetition rate ultrahigh-speed wavelength-swept semiconductor laser," *Optics Letters*, vol. 30, no. 23, pp. 3159–3161, 2005.

[9] A.-Q. Liu and X. Zhang, "A review of MEMS external-cavity tunable lasers," *Journal of Micromechanics and Microengineering*, vol. 17, no. 1, pp. R1–R13, 2006.

[10] D. Zhang, J. Zhao, Y. Qi, W. Liu, Y. Fu, C. Li, M. Luo, S. Hu, Q. Hu, and L. Wang, "Compact MEMS external cavity tunable laser with ultra-narrow linewidth for coherent detection," *Optics Express*, vol. 20, no. 18, pp. 19 670–19 682, 2012.

[11] S. H. Yun, C. Boudoux, G. J. Tearney, and B. E. Bouma, "High-speed wavelength-swept semiconductor laser with a polygon-scanner-based wavelength filter," *Optics Letters*, vol. 28, no. 20, pp. 1981–1983, 2003.

[12] V. Jayaraman, J. Jiang, B. Potsaid, M. Robertson, P. J. S. Heim, C. Burgner, D. John, G. D. Cole, I. Grulkowski, J. G. Fujimoto, A. M. Davis, and A. E. Cable, "VCSEL swept light sources," in *Optical Coherence Tomography: Technology and Applications*, W. Drexler and J. G. Fujimoto, Eds. Cham: Springer, 2015, pp. 659–686.

[13] H. K. Sahoo, "Wavelength tunable MEMS VCSELs," Ph.D. dissertation, Technical University of Denmark, Department of Photonics Engineering, 2017.

[14] Thorlabs, Inc. (2024) Thorlabs - home. [Online]. Available: https://www.thorlabs.com

[15] C. Gierl, T. Gründl, P. Debernardi, K. Zogal, C. Grasse, H. Davani, G. Böhm, S. Jatta, F. Küppers, P. Meißner, and M.-C. Amann, "Surface micromachined tunable 1.55 µm-VCSEL with 102 nm continuous single-mode tuning," *Optics Express*, vol. 19, no. 18, pp. 17 336–17 343, 2011.

[16] V. Jayaraman, G. D. Cole, M. Robertson, A. Uddin, and A. Cable, "High-sweep-rate 1310 nm MEMS-VCSEL with 150 nm continuous tuning range," *Electronics Letters*, vol. 48, no. 14, pp. 867–869, 2012.

[17] Santec Corporation. (2024) Santec - photonics and optical technology. [Online]. Available: https://www.santec.com

[18] Excelitas Technologies Corp. (2024) Excelitas technologies - home. [Online]. Available: https://www.excelitas.com

[19] InPhenix, Inc. (2025) Inphenix: Superluminescent diodes, swept light source, fp laser. [Online]. Available: https://www.inphenix.com/en/

[20] D. D. John, B. Lee, B. M. Potsaid, A. C. Kennedy, M. E. Roberts, C. B. Burgner, A. E. Cable, J. G. Fujimoto, and V. Jayaraman, "Single-mode and high-speed 850 nm MEMS-VCSEL," in *Advanced Solid State Lasers Conference*, 2016.

[21] R. Huber, M. Wojtkowski, K. Taira, J. G. Fujimoto, and K. Hsu, "Amplified, frequency swept lasers for frequency domain reflectometry and OCT imaging: design and scaling principles," *Optics Express*, vol. 13, no. 9, pp. 3513–3528, 2005.

[22] R. Huber, M. Wojtkowski, and J. G. Fujimoto, "Fourier domain mode locking (FDML): A new laser operating regime and applications for optical coherence tomography," *Optics Express*, vol. 14, no. 8, pp. 3225–3237, 2006.

[23] R. Huber, "FDML (incl. parallelization)," in *Optical Coherence Tomography*, W. Drexler and J. G. Fujimoto, Eds. Berlin, Heidelberg: Springer, 2015, pp. 741–787.

[24] O. E. Asirim, R. Huber, and C. Jirauschek, "Effect of self-phase modulation on the signal quality of Fourier domain mode-locked lasers," in *2022 International Conference on Numerical Simulation of Optoelectronic Devices (NUSOD)*, 2022, pp. 1–2.

[25] T. Klein and R. Huber, "High-speed OCT light sources and systems [invited]," *Biomedical Optics Express*, vol. 8, no. 2, pp. 828–859, 2017.

[26] T. Klein, W. Wieser, C. M. Eigenwillig, B. R. Biedermann, and R. Huber, "Multi-MHz retinal OCT," *Biomedical Optics Express*, vol. 4, no. 10, pp. 1890–1908, 2013.

[27] J. P. Kolb, T. Pfeiffer, M. Eibl, H. Hakert, and R. Huber, "High-resolution retinal swept source optical coherence tomography with an ultra-wideband Fourier-domain mode-locked laser at MHz A-scan rates," *Biomedical Optics Express*, vol. 9, no. 1, pp. 120–130, 2018.

[28] W. Wieser, B. R. Biedermann, T. Klein, C. M. Eigenwillig, and R. Huber, "Multi-megahertz OCT: High quality 3D imaging at 20 million A-scans and 4.5 GVoxels per second," *Optics Express*, vol. 18, no. 14, pp. 14 685–14 704, 2010.

[29] W. Wieser, T. Klein, W. Draxinger, and R. Huber, "Fully automated 1.5 MHz FDML laser with 100 mW output power at 1310 nm," in *Optical Coherence Imaging Techniques and Imaging in Scattering Media*. Optica Publishing Group, 2015, p. 954116.

[30] Optores GmbH. (2024) Optores – ultra-high-speed swept source oct systems. [Online]. Available: https://www.optores.com/

[31] M. Klufts, A. M. Jiménez, S. Lotz, M. A. Bashir, T. Pfeiffer, A. Mlynek, W. Wieser, A. Chamorovskiy, A. Bradu, A. Podoleanu, and R. Huber, "828 kHz retinal imaging with an 840 nm Fourier domain mode locked laser," *Biomed. Opt. Express*, vol. 14, no. 12, pp. 6493–6508, 12 2023.

[32] N. A. Riza and Z. Yaqoob, "Submicrosecond speed optical coherence tomography system design and analysis by use of acousto-optics," *Applied Optics*, vol. 42, no. 16, pp. 3018–3026, 2003.

[33] T. Huo, J. Zhang, J.-g. Zheng, T. Chen, C. Wang, N. Zhang, W. Liao, X. Zhang, and P. Xue, "Linear-in-wavenumber swept laser with an acousto-optic deflector for optical coherence tomography," *Optics Letters*, vol. 39, no. 2, pp. 247–250, 2014.

[34] Z. Hu, B. He, Y. Shi, C. Wang, Z. Chen, Z. Yin, X. Liu, X. Zhang, N. Zhang, L. Jing, G. Wang, and P. Xue, "High-speed k-linear swept laser using acousto-optic deflectors with Doppler shift compensation for optical coherence tomography," *Optics Letters*, vol. 49, no. 1, pp. 101–104, 2023.

[35] X. Ji, T. Suzuki, S. Choi, O. Sasaki, and J. Pu, "Linear-wavenumber swept source based on an acousto-optic device for optical coherence tomography," *Optics Express*, vol. 31, no. 26, pp. 44 611–44 621, 2023.

[36] N. S. Park, S. K. Chun, G.-H. Han, and C.-S. Kim, "Acousto-optic–based wavelength-comb-swept laser for extended displacement measurements," *Sensors*, vol. 17, no. 4, p. 740, 2017.

[37] G.-H. Han, S.-W. Cho, N. S. Park, and C.-S. Kim, "Electro-optic swept source based on AOTF for wavenumber-linear interferometric sensing and imaging," *Fibers*, vol. 4, no. 2, p. 14, 2016.

[38] T. Suzuki, Y. Kaneko, S. Choi, and O. Sasaki, "External-cavity laser diode using acousto-optic deflector as tunable grating," *Optics Letters*, vol. 47, no. 7, pp. 1871–1874, 2022.

[39] A. S. Machikhin, D. I. Khokhlov, V. E. Pozhar, A. S. Kozlov, V. G. Batshev, and A. A. Gorevoy, "Acousto-optical tunable filter for a swept light source with variable transmission function," in *Proceedings of SPIE*, vol. 10815, 2018, p. 108150L.

[40] A. S. Machikhin, V. E. Pozhar, A. V. Viskovatykh, and L. I. Burmak, "Acousto-optical tunable filter for combined wideband, spectral, and optical coherence microscopy," *Applied Optics*, vol. 54, no. 25, pp. 7508–7513, 2015.

[41] Superlum Diodes Ltd. (2025) Superlum diodes ltd. official website. [Online]. Available: https://www.superlumdiodes.com/

[42] J. Fujimoto and W. Drexler, *Optical Coherence Tomography: Technology and Applications*. Springer Berlin Heidelberg, 2008.

[43] E. Auksorius, D. Borycki, P. Stremplewski, K. Liżewski, S. Tomczewski, P. Niedźwiedziuk, B. L. Sikorski, and M. Wojtkowski, "In vivo imaging of the human cornea with high-speed and high-resolution fourier-domain full-field optical coherence tomography," *Biomed. Opt. Express*, vol. 11, no. 5, pp. 2849–2865, 5 2020.

[44] J. Kobayashi, Y. Sasaki, M. Ueno, T. Sakamoto, and S. Toyoda, "200-kHz swept light source using a KTN deflector and a high-speed optical coherence tomography system," *NTT Technical Review*, vol. 12, no. 4, pp. 1–5, 2014.

[45] M. Bonesi, M. P. Minneman, J. Ensher, B. Zabihian, H. Sattmann, P. Boschert, E. Hoover, R. A. Leitgeb, M. Crawford, and W. Drexler, "Akinetic all-semiconductor programmable swept-source at 1550 nm and 1310 nm with centimeters coherence length," *Optics Express*, vol. 22, no. 3, pp. 2632–2655, 2014.

[46] M. Minneman, J. Ensher, M. Crawford, M. Bonesi, B. Zabihian, P. Boschert, E. Hoover, D. Derickson, B. E. Applegate, T. Milner, and W. Drexler, "Akinetik swept sources," in *Optical Coherence Tomography: Technology and Applications*, W. Drexler and J. G. Fujimoto, Eds. Cham: Springer, 2015, pp. 687–739.

[47] S. Song, J. Xu, and R. K. Wang, "Long-range and wide field of view optical coherence tomography for in vivo 3D imaging of large volume object based on akinetic programmable swept source," *Biomedical Optics Express*, vol. 7, no. 11, pp. 4734–4748, 2016.

[48] Insight Photonic Solutions. (2025) Insight photonic solutions official website. [Online]. Available: https://www.sweptlaser.com/

[49] S. Moon and D. Y. Kim, "Ultra-high-speed optical coherence tomography with a stretched pulse supercontinuum source," *Optics Express*, vol. 14, no. 24, pp. 11 575–11 584, 2006.

[50] J. Xu, X. Wei, L. Yu, C. Zhang, J. Xu, K. K. Y. Wong, and K. K. Tsia, "Performance of megahertz amplified optical time-stretch optical coherence tomography (AOT-OCT)," *Optics Express*, vol. 22, no. 19, pp. 22 498–22 512, 2014.

[51] S. Grelet, A. Martínez Jiménez, R. Dybbro Engelsholm, P. Bowen Montague, and A. Podoleanu, "40 MHz swept-source optical coherence tomography at 1060 nm using a time-stretch and supercontinuum spectral broadening dynamics," *IEEE Photonics Journal*, vol. 14, no. 6, pp. 1–6, 2022.

[52] S. Grelet, A. Martinez Jiménez, P. B. Montague, and A. Podoleanu, "Shot-noise limited, 10 MHz swept-source optical coherence tomography for retinal imaging," *arXiv preprint arXiv:2410.15692*, 2024.

[53] Y. Shang, X. Zhang, Y. Li, J. Liu, H. Wang, and Y. Chen, "High-power and high-speed all-optical all-fiber wavelength-swept source at 2 µm based on a femtosecond laser and time stretch technique," *Infrared Physics & Technology*, vol. 135, p. 104845, 2024.

[54] D. Huang, F. Li, Z. Cheng, and P. K. A. Wai, "100 MHz reconfigurable ultrafast swept source by time stretching of 100 nm flat-top spectrum," in *Conference Proceedings*, 2019.

[55] X. Wei, J. Xu, Y. Xu, L. Yu, J. Xu, B. Li, A. K. S. Lau, X. Wang, C. Zhang, K. K. Tsia, and K. K. Y. Wong, "Breathing laser as an inertia-free swept source for high-quality ultrafast optical bioimaging," *Optics Letters*, vol. 39, no. 23, pp. 6593–6596, 2014.

[56] J. Kang, P. Feng, and X. Wei, "102-nm, 44.5-MHz inertial-free swept source by mode-locked fiber laser and time stretch technique for optical coherence tomography," *Optics Express*, vol. 26, no. 4, pp. 4370–4381, 2018.

[57] J. Xu, X. Wei, L. Yu, C. Zhang, J. Xu, K. K. Y. Wong, and K. K. Tsia, "High-performance multi-megahertz optical coherence tomography based on amplified optical time-stretch," *Biomedical Optics Express*, vol. 6, no. 4, pp. 1340–1350, 2015.

[58] H. Chen, Y. Li, D. Huang, F. Li, C. Lu, and P. K. A. Wai, "114 nm broadband all-fiber nonlinear polarization rotation mode-locked laser and time-stretch optical coherence tomography," *Optics Express*, vol. 29, no. 21, pp. 33 322–33 330, 2021.

[59] H. Chen, Y. Li, D. Huang, Y. Shi, F. Li, C. Lu, and P. K. A. Wai, "Highly coherent, flat, and broadband time-stretched swept source based on extra-cavity spectral shaping assisted by a booster semiconductor optical amplifier," *Optics Express*, vol. 30, no. 19, pp. 33 708–33 720, 2022.

[60] L. Dang *et al.*, "Broadband low-repetition-rate mode-locked fiber laser for swept source optical coherence tomography," in *Fifteenth International Conference on Information Optics and Photonics*, vol. 13418, 2024, p. 134183F.

[61] A. Martínez Jiménez, M. Spacek, M. Wacker, R. Huber, A. Bradu, and A. Podoleanu, "MHz time stretch swept source using a commercial Erbium-doped fiber amplifier," in *Optical Coherence Tomography and Coherence Domain Optical Methods in Biomedicine XXVII*, ser. Proceedings of SPIE, vol. 12367, 2023, p. 1236706.

[62] X. Wei, A. K. S. Lau, Y. Xu, K. K. Tsia, and K. K. Y. Wong, "28 MHz swept source at 1.0 µm for ultrafast quantitative phase imaging," *Biomedical Optics Express*, vol. 6, no. 10, pp. 3855–3864, 2015.

[63] K. Goda, K. K. Tsia, and B. Jalali, "High-throughput optical coherence tomography at 800 nm," *Optics Express*, vol. 20, no. 18, pp. 19 612–19 617, 2012.

[64] H. Asghari, "Visible wavelength time-stretch optical coherence tomography," *Optics Express*, vol. 31, no. 15, pp. 24 085–24 095, 2023.

[65] S. Tozburun, M. Siddiqui, and B. J. Vakoc, "A rapid, dispersion-based wavelength-stepped and wavelength-swept laser for optical coherence tomography," *Optics Express*, vol. 22, no. 3, pp. 3414–3424, 2014.

[66] T. S. Kim, J. Joo, I. Shin, P. Shin, W. J. Kang, B. J. Vakoc, and W.-Y. Oh, "9.4 MHz A-line rate optical coherence tomography at 1300 nm using a wavelength-swept laser based on stretched-pulse active mode-locking," *Scientific Reports*, vol. 10, no. 1, p. 9328, 2020.

[67] I. Akkaya and S. Tozburun, "A 1060 nm stretched-pulse mode-locked wavelength-swept laser source providing an A-scan rate of 20 MHz," *Optik*, vol. 266, p. 169648, 2022.

[68] R. Khazaeinezhad, M. Siddiqui, and B. J. Vakoc, "16 MHz wavelength-swept and wavelength-stepped laser architectures based on stretched-pulse active mode locking with a single continuously chirped fiber Bragg grating," *Optics Letters*, vol. 42, no. 10, pp. 2046–2049, 2017.

[69] I. Akkaya and S. Tozburun, "An 18.6 MHz wavelength-swept laser source based on stretched-pulse mode-locking at 1290 nm," in *European Conferences on Biomedical Optics (ECBO)*, 2021.

[70] C. Wang, Z. Yin, B. He, Z. Chen, Z. Hu, Y. Shi, X. Zhang, N. Zhang, L. Jing, G. Wang, and P. Xue, "Polarization-isolated stretched-pulse mode-locked swept laser for 10.3-MHz A-line rate optical coherence tomography," *Optics Letters*, vol. 48, no. 15, pp. 4025–4028, 2023.

[71] J. Joo, T. S. Kim, B. J. Vakoc, and W.-Y. Oh, "Robust and easy-to-operate stretched-pulse mode-locked wavelength-swept laser with an all-polarization-maintaining fiber cavity for 10 MHz A-line rate optical coherence tomography," *Optics Letters*, vol. 46, no. 16, pp. 3857–3860, 2021.

[72] J. Joo, S. Cho, B. J. Vakoc, and W.-Y. Oh, "Stretched-pulse mode-locked laser using post-cavity stretching for ultrahigh-speed OCT," *IEEE Photonics Technology Letters*, vol. 37, no. 1, pp. 49–52, 2025.

[73] I. Akkaya and S. Tozburun, "A stretched-pulse mode-locked (SPML) wavelength-swept laser source at 1.06 µm," in *Laser Resonators, Microresonators, and Beam Control XXIV*, vol. 11987, 2022, pp. 103–106.

Chapter 4

Standard single-harmonic dispersion-tuned mode-locked (DTML) swept lasers

Starting with a brief description of the dispersion properties of fibre laser cavities, this chapter explains the principle of tuning in dispersion-tuned mode-locked (DTML) swept lasers and rigorously derives the expression for the tuning bandwidth in this type of tunable lasers. By adopting a spectral filtering approach, notions of the saturation and one round trip operations are introduced, showing trade-offs between the achievable tuning bandwidth and coherence performance. In the last part of the chapter, the historical development of DTML swept sources with representative performance characteristics relevant to OCT imaging is reviewed, categorising the lasers chronologically into three generations.

4.1 Dispersion in optical fibres

Chromatic dispersion refers to the property of a medium (such as an optical fibre) in which the propagation constant $\beta(\omega)$, defined in terms of the index of refraction $n(\omega)$ as:

$$\beta(\omega) = n(\omega)\frac{\omega}{c}, \tag{4.1}$$

deviates from a linear dependence on the angular optical frequency ω, i.e., when $n(\omega) \neq$ const.. If the spectral width $\delta\omega$ of the light propagating in a dispersive medium is much smaller than the carrier frequency ω_0, it is appropriate to approximate $\beta(\omega)$ using an expansion around ω_0. In this case, $\beta(\omega)$ can be expanded up to the second-order term as [1]:

$$\beta(\omega) \approx \beta(\omega_0) + \left.\frac{\mathrm{d}\beta(\omega)}{\mathrm{d}\omega}\right|_{\omega=\omega_0} \Delta\omega + \frac{1}{2}\left.\frac{\mathrm{d}^2\beta(\omega_0)}{\mathrm{d}\omega^2}\right|_{\omega=\omega_0} \Delta\omega^2, \tag{4.2}$$

where the second and third term on the right-hand side represent the first- and second-order dispersions, respectively, and $\Delta\omega \equiv \omega - \omega_0$. The first two terms in Eq. (4.2) define the phase velocity v_p and the group velocity v_g of the light propagating in the medium, given by the relations:

$$v_\mathrm{p}(\omega) = \frac{\omega}{\beta(\omega)} = \frac{c}{n(\omega)}, \qquad v_\mathrm{g}(\omega) = \frac{1}{\dfrac{\mathrm{d}\beta(\omega)}{\mathrm{d}\omega}} = \frac{c}{n_\mathrm{g}(\omega)}, \tag{4.3}$$

where $n_\mathrm{g}(\omega)$ denotes the group index of refraction. The third term in Eq. (4.2) represents so-called group velocity dispersion β_2, defined as:

$$\beta_2 \equiv \frac{\mathrm{d}^2\beta(\omega)}{\mathrm{d}\omega^2} = \frac{\mathrm{d}}{\mathrm{d}\omega}\left[\frac{1}{v_\mathrm{g}(\omega)}\right], \tag{4.4}$$

with units of s^2/m. In fibre communication, dispersion, also referred to as the dispersion coefficient D, is sometimes defined with respect to wavelength λ rather than optical frequency,

$$D \equiv \frac{\mathrm{d}}{\mathrm{d}\lambda}\left[\frac{1}{v_\mathrm{g}(\lambda)}\right], \tag{4.5}$$

with units of $\mathrm{s/m}^2$. Using Eq. (4.4), Eq. (4.5), and $\mathrm{d}\omega = -2\pi c/\lambda_0^2 \mathrm{d}\lambda$, a straightforward conversion formula between D and β_2 is readily found:

$$D = -\frac{2\pi c}{\lambda_0^2}\beta_2. \tag{4.6}$$

Eq. (4.6) can be expressed in a form which incorporates also the length L of the dispersive medium,

$$\mathrm{TDD} = -\frac{2\pi c}{\lambda_0^2}\mathrm{GDD}, \tag{4.7}$$

where $\mathrm{TDD} = DL$ and $\mathrm{GDD} = \beta_2 L$ denote so-called time delay dispersion and group delay dispersion, respectively.

Chromatic dispersion in optical fibres is generally the sum of two components [2]: material dispersion and waveguide dispersion. Material dispersion arises from the frequency (or wavelength) dependence of the material index of refraction, as indicated in Eq. (4.1). On the other hand, waveguide dispersion originates from the geometry of the fibre waveguide. The situation when $\beta_2 > 0$, or equivalently $D < 0$, is referred to as positive or normal dispersion. Conversely, when $\beta_2 < 0$, or equivalently $D > 0$, the situation is referred to as negative or anomalous dispersion. In the case of normal dispersion, lower-frequency components travel faster than higher-frequency components. The opposite is true in the case of anomalous dispersion. The effect of chromatic dispersion on pulse propagation is discussed in more detail in Chap. 6. Dispersion values for selected fibre types commonly used in DTML laser cavities are plotted in Fig.4.1.

4.1.1 Chirped fibre Bragg grating (cFBG)

Another source of dispersion is a chirped fibre Bragg grating (cFBG). A cFBG consists of reflective structures inscribed in the core of an optical fibre, introducing a periodic or aperiodic variation of the effective index of refraction n_{eff}. A characteristic feature of a cFBG is the variation of the optical period $\Lambda(z)$ of the grating along its length, as illustrated in Fig. 4.2. Since the Bragg condition for reflection $\lambda = 2n_{\mathrm{eff}}\Lambda(z)$ depends on the local grating period, different spectral components are reflected at different positions along the grating. This leads to wavelength-dependent time delays between the reflected components, effectively introducing dispersion. CFBGs can be designed to provide either normal or anomalous dispersion by simply reversing the direction of the input light, however, it is important to consider the directional dependence of the reflection spectrum in fibre Bragg gratings [3].

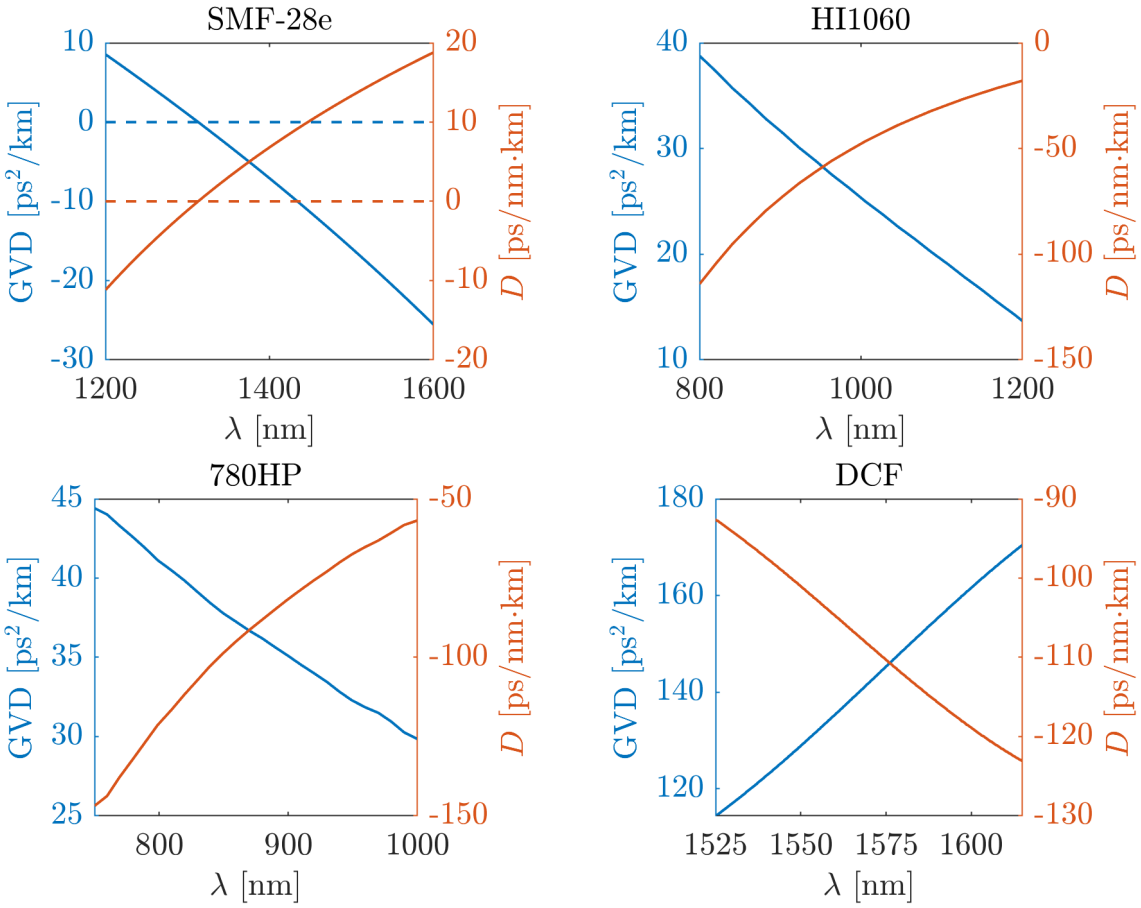

Figure 4.1: Dispersion values for selected fibre types commonly used in DTML laser cavities. In each graph, the blue and red lines refer to β_2 and D values, respectively. DCF: dispersion-compensation fibre.

Considering the time delay between the wavelength components reflected from opposite ends of the grating $\Delta T = 2n_{\text{eff}}L_{\text{cFBG}}/c$ and the relation $\Delta T = D_{\text{cFBG}}L_{\text{cFBG}}\Delta\lambda_{\text{cFBG}}$, the dispersion of a cFBG with spectral bandwidth $\Delta\lambda_{\text{cFBG}}$ can be expressed in a remarkably simple form as [2]:

$$\text{TDD}_{\text{cFBG}} = \frac{2n_{\text{eff}}L_{\text{cFBG}}}{c\Delta\lambda_{\text{cFBG}}}. \tag{4.8}$$

In general, cFBGs can provide very high dispersion values. For example, a grating with a bandwidth of $\Delta\lambda_{\text{cFBG}} = 0.2\,\text{nm}$ can compensate for the dispersion accumulated in a 300 km length of a standard telecommunication fibre.

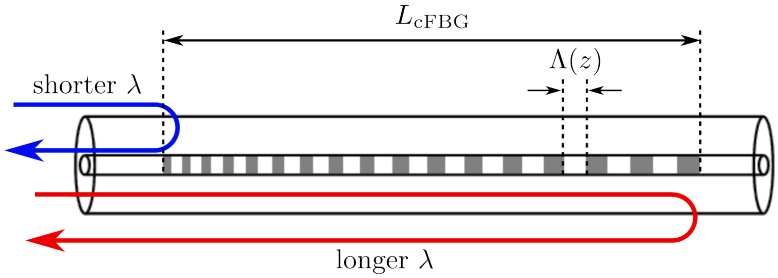

Figure 4.2: Time delay between different spectral components provided by a cFBG.

4.2 Principle of DTML

The principle of DTML is based on active mode-locking in a dispersive cavity (a cavity with a nonzero effective dispersion) [1, 4, 5]. Due to chromatic dispersion, the longitudinal modes at which the laser can lase are spaced unevenly, as depicted in Fig. 4.3, with spacing given by the fundamental frequency of the cavity $f_{\text{cav}}(\lambda)$. For a fibre ring cavity in Fig. 4.4 with a fibre delay of length L_{fibre} and a cFBG of length $L_{\text{cFBG}}(\lambda)$, $f_{\text{cav}}(\lambda)$ can be generally expressed as [6]:

$$f_{\text{cav}}(\lambda) = \frac{c}{n_{\text{g}}(\lambda)L_{\text{fiber}} + n_{\text{g}}(\lambda_0)L_{\text{cFBG}}(\lambda)}, \tag{4.9}$$

where c is the speed of light $n_{\text{g}}(\lambda)$ is the group index of refraction of the fibre, and λ_0 denotes the central wavelength of the gain spectrum. Wavelength dependent contributions to the overall cavity dispersion due to the fibre delay and the cFBG are contained in $n_{\text{g}}(\lambda)$ and $L_{\text{cFBG}}(\lambda)$, respectively. As for practical DTML implementations, it can be

assumed that $D_{\mathrm{cFBG}}/D_{\mathrm{fibre}} \sim 10^4$-$10^5$. This means that dispersion originating in the fibre index of refraction over the cFBG length can be neglected and only dispersion arising from its grating is considered. Therefore, in comparison with the form of Eq. (4.9) in [6], the expression is here slightly modified by considering the index of refraction of the cFBG as $n_{\mathrm{g}}(\lambda) = n_{\mathrm{g}}(\lambda_0)$. This approximation will simplify the following mathematical treatment, while still be applicable to a general case of a long fibre delay and a cFBG both contributing to the overall cavity dispersion.

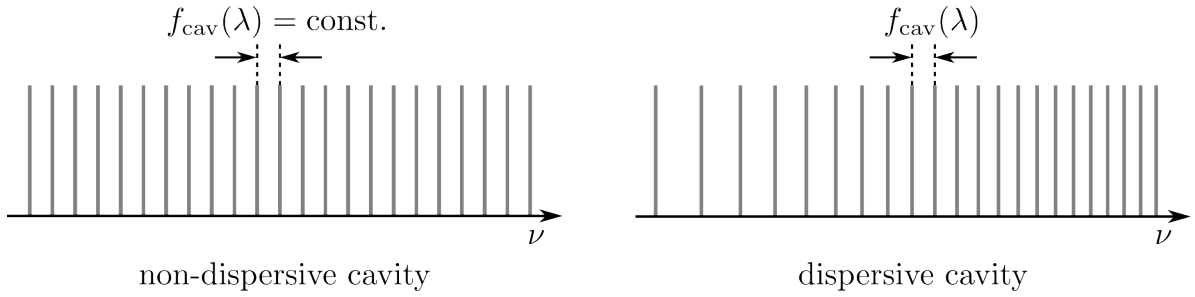

Figure 4.3: Comparison of the cavity mode spacing in a non-dispersive and a dispersive cavity. $\nu = \omega/2\pi$ is the optical frequency in units of Hz.

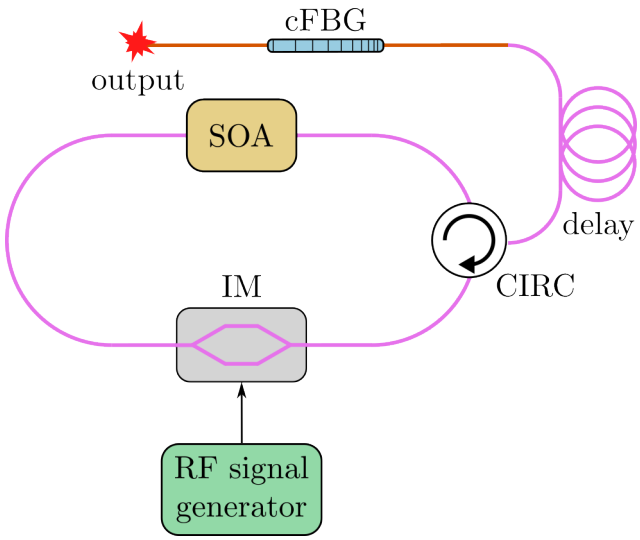

Figure 4.4: A ring DTML laser cavity with a fibre delay and a cFBG both contributing to the overall cavity dispersion. SOA: semiconductor optical amplifier, cFBG: chirped fibre Bragg grating, CIRC: circulator, IM: intensity modulator.

To mode-lock the cavity, the losses or gain must be periodically modulated at a modulation frequency f which matches an integer multiple q of the fundamental frequency of

the cavity $f_{\mathrm{cav}}(\lambda)$,

$$f = q f_{\mathrm{cav}}(\lambda), \tag{4.10}$$

where q is also called the harmonic order of mode-locking. By mode-locking the laser, the modes are forced to maintain a specific phase relationship with each other - thus the term *mode-locking* - resulting in a coherent lasing and pulsed operation with a repetition rate of $f_{\mathrm{p}} = f$. A graphical representation of the emission wavelength λ as a function of f in Fig. 4.5 consists of tuning bands, where each band corresponds to a different harmonic order $q = q_{\mathrm{c}} + l$, with q_{c} as the reference harmonic order and l as an integer.

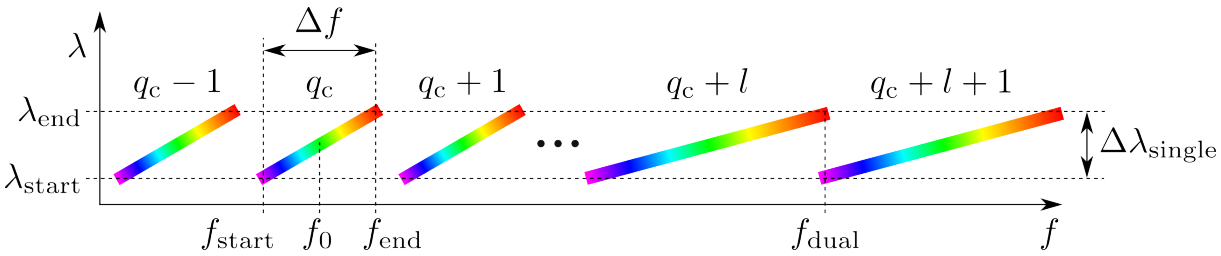

Figure 4.5: A graphical representation of the tuning bands $q = q_{\mathrm{c}} + l$ and emission wavelength λ as a function of the modulation frequency f. The connection between Δf and $\Delta\lambda_{\mathrm{single}}$ is given by Eq. (4.12) or Eq. (4.13).

To find the relationship between a shift in the emission wavelength $\Delta\lambda_{\mathrm{single}}$ within a single harmonic tuning band q in Fig. 4.5 and a change in the modulation frequency Δf, the slope $\mathrm{d}f/\mathrm{d}\lambda$ is first obtained by differentiating Eq. (4.10) with respect to λ as:

$$\begin{aligned}
\frac{\mathrm{d}\lambda}{\mathrm{d}f} &= -\frac{q}{f^2}\left[\frac{L_{\mathrm{fiber}}}{c}\frac{\mathrm{d}n_{\mathrm{g}}(\lambda)}{\mathrm{d}\lambda} + \frac{n_{\mathrm{g}}(\lambda_0)}{c}\frac{\mathrm{d}L_{\mathrm{cFBG}}(\lambda)}{\mathrm{d}\lambda}\right]^{-1} \\
&= -\frac{q}{f^2(\mathrm{TDD}_{\mathrm{fiber}} + \mathrm{TDD}_{\mathrm{cFBG}})} \\
&= -\frac{q}{f^2 \mathrm{TDD}_{\mathrm{cav}}},
\end{aligned} \tag{4.11}$$

where TDD is the time delay dispersion in units of s/m, and $\mathrm{TDD}_{\mathrm{cav}}$ denotes the overall cavity dispersion. $\mathrm{TDD}_{\mathrm{cav}}$ generally includes dispersion contributions from both the fibre, $\mathrm{TDD}_{\mathrm{fibre}} = D_{\mathrm{fibre}} L_{\mathrm{fibre}}$, and the cFBG, $\mathrm{TDD}_{\mathrm{cFBG}} = D_{\mathrm{cFBG}} L_{\mathrm{cFBG}}$ (L_{cFBG} is the geometrical cFBG length independent of λ). The dispersion relations used in Eq. (4.11) can be found in [1]. In the 1st generation of DTML-SSs (long cavities with fibre alone contributing

to the cavity dispersion, see more in Subsec. 4.4.1), dispersion in the cavity is given by $\mathrm{TDD}_{\mathrm{fibre}}$, while in the 2nd and 3rd generation DTML lasers (short cavity with a cFBG, see more in Subsec. 4.4.2 and 4.4.3), dispersion in the cavity is dominated by $\mathrm{TDD}_{\mathrm{cFBG}}$ (i.e., $\mathrm{TDD}_{\mathrm{fibre}}$ can be neglected). Apparently, the larger the frequency f in Eq. (4.11), the smaller the slope $\mathrm{d}\lambda/\mathrm{d}f$, as graphically depicted in Fig. 4.5. Provided a change in the modulation frequency $\Delta f = f_{\mathrm{end}} - f_{\mathrm{start}}$ is applied to the IM, a general expression for $\Delta\lambda_{\mathrm{single}} = \lambda_{\mathrm{end}} - \lambda_{\mathrm{start}}$ can be obtained by integration of Eq. (4.11) over Δf, as shown below:

$$\begin{aligned}\Delta\lambda_{\mathrm{single}} &= \int_{f_0-\Delta f/2}^{f_0+\Delta f/2} \frac{\mathrm{d}\lambda}{\mathrm{d}f}\mathrm{d}f = -\frac{q}{\mathrm{TDD}_{\mathrm{cav}}} \int_{f_0-\Delta f/2}^{f_0+\Delta f/2} \frac{\mathrm{d}f}{f^2} \\ &= -\frac{q}{\mathrm{TDD}_{\mathrm{cav}}}\left(-\frac{1}{f_0+\Delta f/2} + \frac{1}{f_0-\Delta f/2}\right),\end{aligned} \tag{4.12}$$

with $f_0 \equiv q f_{\mathrm{cav}}(\lambda_0)$. Because all modulation frequencies within Δf in Eq. (4.12) lock the laser at a single qth harmonic order, this mode-locking regime is referred to as the *single-harmonic regime*. The expression in Eq. (4.12) is also applicable for very low harmonic orders cases when the slope $\mathrm{d}\lambda/\mathrm{d}f$ given by Eq. (4.11) changes significantly within a single tuning band $q = q_{\mathrm{c}} + l$ from Fig. 4.5 [6]. If $f = q f_{\mathrm{cav}}(\lambda) \gg \Delta f/2$, Eq. (4.12) can be approximated by a first order expansion of the terms in the parentheses, leading to a linear relationship commonly found in DTML swept sources literature [7–13]:

$$\Delta\lambda_{\mathrm{single}} \approx -\frac{1}{\mathrm{TDD}_{\mathrm{cav}} f_{\mathrm{cav}} f_0}\Delta f = S(f_0)\Delta f, \tag{4.13}$$

where $f_{\mathrm{cav}} \equiv f_{\mathrm{cav}}(\lambda_0)$ represents the effective fundamental frequency of the cavity, and $S(f_0)$ denotes the tuning sensitivity, which generally depends on the cavity dispersion, its length, and central modulation frequency f_0. Considering an anomalous dispersive cavity, i.e., when $\mathrm{TDD}_{\mathrm{cav}} > 0$, if $\Delta f > 0$, the laser's emission is tuned from short to long wavelengths (the forward direction), while if $\Delta f < 0$, the emission is tuned from long to short wavelengths (the backward direction). The directions of the wavelength tuning are reversed for the case of a normal dispersive cavity, i.e., when $\mathrm{TDD}_{\mathrm{cav}} < 0$.

In the time domain, the wavelength tuning during the sweeping of f arises from a slight temporal delay between a mode-locked chirped pulse (caused by chromatic dispersion) and the modulation window as the pulse passes through the modulator, as explained in more detail in [14].

The fact that it is the effective cavity dispersions D_{cav} and $\mathrm{TDD}_{\mathrm{cav}}$ which appear in the linear expression Eq. (4.13) allows for a simple yet effective method for an approximate effective cavity dispersion assessment in a DTML cavity without the need for additional components required for DTML itself. The method involves measuring the tuning sensitivity $S(D_{\mathrm{cav}}, f_0)$ across large range of modulation frequencies f_0 and extracting D_{cav} or $\mathrm{TDD}_{\mathrm{cav}}$ from a linear regression of the measured data. This method is described in more detail and experimentally validated in Sec. 7.1. With the knowledge of the dispersion value inside the cavity, important parameters such as tuning and coherence properties of an DTML laser can be evaluated.

4.3 Spectral filtering and dynamic tuning bandwidth limits

Several factors in a DTML laser limit the achievable tuning bandwidth $|\Delta\lambda_{\mathrm{single}}|$. An important factor is the gain bandwidth of the employed SOA, and to some extent the optical bandwidths of the other cavity components. Another factor is related to the condition preventing emission from neighbouring tuning bands $q_{\mathrm{c}} + l$ and $q_{\mathrm{c}} + l + 1$ in Fig. 4.5. To prevent the laser from an undesired dual wavelength emission at $f_{\mathrm{dual}} = (q_{\mathrm{c}} + l) f_{\mathrm{cav}}(\lambda_{\mathrm{end}}) = (q_{\mathrm{c}} + l + 1) f_{\mathrm{cav}}(\lambda_{\mathrm{start}})$, where two wavelengths λ_{end} and λ_{start} are emitted at the same time, the range Δf in Eq. (4.13) should not exceed the fundamental frequency f_{cav}. This condition provides an estimation for the maximum single-harmonic non-dual wavelength operation tuning bandwidth $\Delta\lambda_{\mathrm{single,n\text{-}d}}$ as:

$$\Delta\lambda_{\mathrm{single,n\text{-}d}} \approx |S(f_0)| f_{\mathrm{cav}} = \frac{1}{|\mathrm{TDD}_{\mathrm{cav}}| f_0}. \tag{4.14}$$

Apparently, $\Delta\lambda_{\text{single,n-d}}$ reduces with f_0. However, it is advisable to find a trade-off between $\Delta\lambda_{\text{single,n-d}}$ and $S(f) \sim 1/f$, since with a small $S(f)$ the wavelength tuning is less sensitive to instabilities in the modulation frequency f, which may lead to linewidth broadening [15].

The achievable tuning bandwidth is also affected by the sweep rate f_{s}, provided that the output power of the laser and its coherence should stay comparable to those achieved in the stationary regime (i.e., when $f_{\text{s}} = 0$). To examine the effects of fast tuning, the scaling guidelines developed in [16] for swept lasers can be adopted to DTML lasers as well [10, 11], for the purposes of this study elaborated here in a more detail. A Fabry-Pérot (FP) wavelength filter in [16] is replaced in a DTML laser by a "virtual" spectral filter created by a combination of a cFBG with an intensity modulator. The spectral selection achieved by this filter can be assimilated with the operation of an FP filter, with a spectral bandwidth of the virtual filter equal to the stationary regime linewidth $\delta\lambda_{\text{stat}}$, as depicted in the middle panel of Fig. 4.6, measured on an optical spectrum analyser. In general, according to the predictions in [14, 17–19], the larger anomalous dispersion in the cavity ($\gtrsim 10\,\text{ps/nm}$), combined with the narrower temporal modulation window ($\lesssim 100\,\text{ps}$), the smaller values of $\delta\lambda_{\text{stat}}$ are obtainable. A high anomalous dispersion enhances wavelength selectivity, while a narrow temporal modulation window better suppresses the amplified spontaneous emission (ASE) inside the cavity (see also simulation results in Subsecs. 6.4.1 and 6.4.2). When the modulation frequency f is swept, the laser emission wavelength λ in Eq. (4.10) is tuned correspondingly, outlined in the top panel of Fig. 4.6, with an average wavelength shift $\Delta\lambda_{\text{round}}$ per round trip time $T_{\text{cav}} = 1/f_{\text{cav}}$. Fig. 4.6 displays the wavelength filtering over a span of a few T_{cav} periods only.

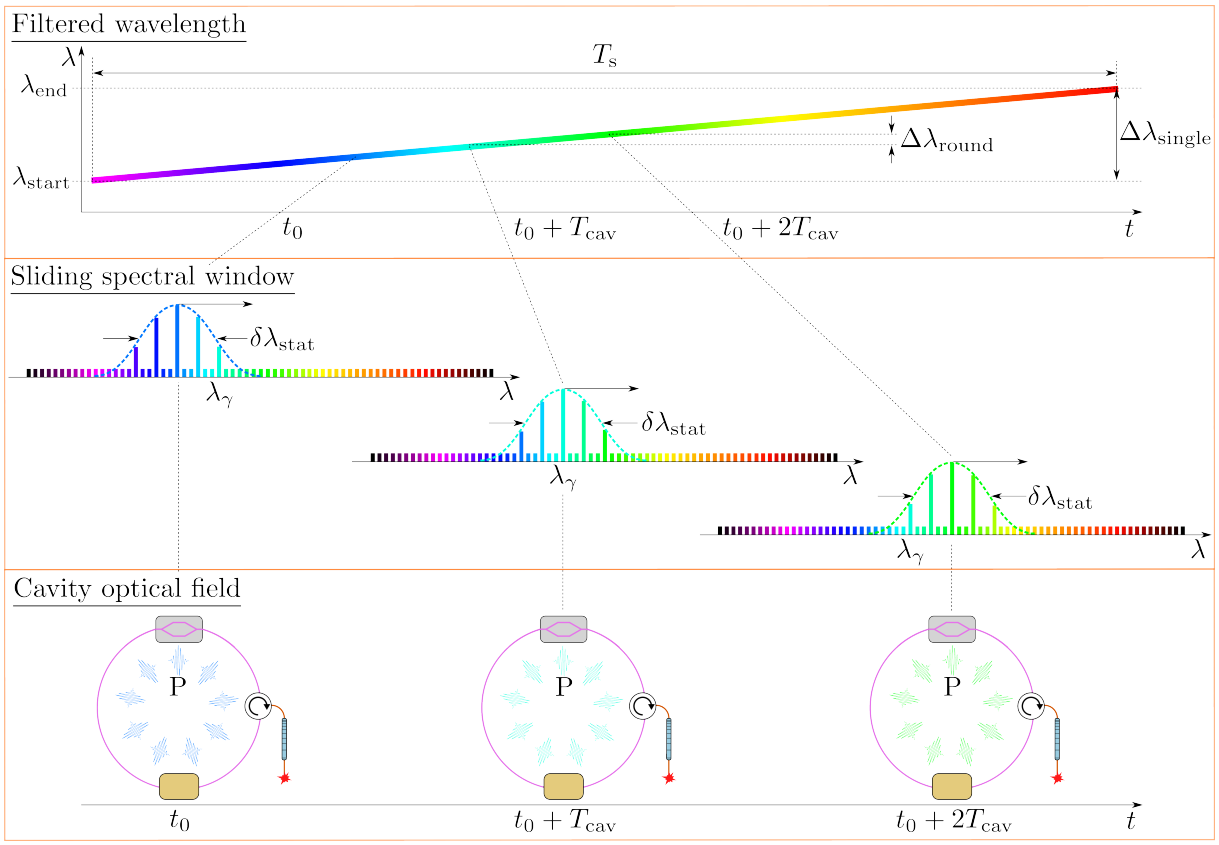

Figure 4.6: Spectral filtering behaviour in the single-harmonic DTML regime. **Top:** Filtered wavelength as a function of time. Each cavity round trip time T_{cav}, the filtered wavelength is tuned by $\Delta\lambda_{\text{round}}$. **Middle:** Snapshots of the sliding spectral window separated in time by T_{cav}. $\delta\lambda_{\text{stat}}$ is the bandwidth of the filter and λ_γ is the wavelength of a photon γ circulating inside the cavity. **Bottom:** Snapshots of the cavity optical field separated in time by T_{cav}, with a specific pulse P circulating inside the cavity. The drawings are inspired by [16, 20, 21].

The prerequisite for saturated laser operation is that a photon γ of wavelength λ_γ circulating inside the cavity should complete on average at least R_{sat} round trips needed for gain saturation before its wavelength is outside of the spectral filtering window. This phenomenon is graphically depicted in the middle panel of Fig. 4.6, with the photon wavelength λ_γ approaching the left side of the sliding spectral window of width $\delta\lambda_{\text{stat}}$ after each round trip inside the cavity. This imposes a limit on $\Delta\lambda_{\text{round}}$ in the form of:

$$\Delta\lambda_{\text{round}} \lesssim \frac{\delta\lambda_{\text{stat}}}{R_{\text{sat}}}. \tag{4.15}$$

The carrier wavelength of a specific pulse P in the bottom panel of Fig. 4.6 matches the

instantaneous filtered wavelength of the spectral window at the moment when the pulse passes through the modulator. Because the spectral window moves at a rate $f_{\mathrm{s}} \ll f_{\mathrm{cav}}$, only a fraction of the tuning bandwidth is stored inside the cavity at a time. R_{sat} in Eq. (4.15) can be estimated as [16]:

$$R_{\mathrm{sat}} \approx \frac{\log\left(\dfrac{P_{\mathrm{sat}}\Delta\lambda_{\mathrm{SOA}}}{\delta\lambda_{\mathrm{stat}}P_{\mathrm{ASE}}}\right)}{\log[G_{\mathrm{SOA}}(1-\rho_{\mathrm{cav}})]}, \tag{4.16}$$

where P_{sat} is the saturation power, $\Delta\lambda_{\mathrm{SOA}}$ is the gain bandwidth of the SOA, P_{ASE} is the total ASE power, G_{SOA} is the small signal gain, and ρ_{cav} represents all losses inside the cavity, including the output coupling. Due to the logarithmic form of Eq. (4.16), R_{sat} varies only weakly with uncertainties in determining the values of the parameters unless they exceed an order of magnitude.

A maximum (single-harmonic) saturation operation tuning bandwidth limit $\Delta\lambda_{\mathrm{single,sat}}$ can be estimated by substituting $\Delta\lambda_{\mathrm{round}} \approx \Delta\lambda_{\mathrm{single,sat}} f_{\mathrm{s}}/f_{\mathrm{cav}}$ in Eq. (4.15), where $f_{\mathrm{cav}}/f_{\mathrm{s}}$ represents the total number of round trips needed for the carrier wavelength of the pulse P to be tuned from λ_{start} to λ_{end} in the single-harmonic DTML regime (assuming a linear wavelength tuning in the top panel of Fig. 4.6). By rearranging the terms in Eq. (4.15), the saturation operation tuning bandwidth limit $\Delta\lambda_{\mathrm{single,sat}}$ for $|\Delta\lambda_{\mathrm{single}}|$ is obtained as:

$$|\Delta\lambda_{\mathrm{single}}| \lesssim \Delta\lambda_{\mathrm{single,sat}} \approx \frac{\delta\lambda_{\mathrm{stat}} f_{\mathrm{cav}}}{R_{\mathrm{sat}} f_{\mathrm{s}}}. \tag{4.17}$$

The inequality in Eq. (4.17) provides a rough estimation for the maximum $|\Delta\lambda_{\mathrm{single}}|$ below which the output power and coherence are expected to remain comparable to those achieved in the stationary regime. One way to increase the value on the right side is via shortening the cavity length that leads to increase in f_{cav}. However, this approach faces a technical limitation due to the nominal fibre length required for the cFBG [10, 11]. This cavity length constraint, that ultimately limits the sweep rate and the achievable tuning bandwidth, is addressed by the long cavity multi-harmonic DTML discussed in the next chapter.

Another fast tuning limitation is obtained when a photon γ of wavelength λ_γ circu-

lating inside the cavity completes on average only one round trip before its wavelength is outside of the sliding spectral window in the middle panel of Fig. 4.6. This imposes a limit on $\Delta\lambda_{\mathrm{round}}$ in the form of:

$$\Delta\lambda_{\mathrm{round}} \lesssim \delta\lambda_{\mathrm{stat}}. \tag{4.18}$$

The maximum (single-harmonic) one round trip operation tuning bandwidth limit $\Delta\lambda_{\mathrm{single,sat}}$ can be estimated by substituting $\Delta\lambda_{\mathrm{round}} \approx \Delta\lambda_{\mathrm{single,one}} f_{\mathrm{s}}/f_{\mathrm{cav}}$ in Eq. (4.18). By rearranging the terms in Eq. (4.18), the one round trip operation tuning bandwidth limit $\Delta\lambda_{\mathrm{single,one}}$ for $|\Delta\lambda_{\mathrm{single}}|$ is obtained as:

$$|\Delta\lambda_{\mathrm{single}}| \lesssim \Delta\lambda_{\mathrm{single,one}} \approx \frac{\delta\lambda_{\mathrm{stat}} f_{\mathrm{cav}}}{f_{\mathrm{s}}}. \tag{4.19}$$

Once the tuning bandwidth $|\Delta\lambda_{\mathrm{single}}|$ is above the saturation limit $\Delta\lambda_{\mathrm{single,one}}$, given by Eq. (4.17), the output power and coherence begin to degrade more rapidly until the one round trip limit $\Delta\lambda_{\mathrm{single,one}}$, given by Eq. (4.19), is reached. Beyond this limit, the laser enters a free-running operation, where coherence is typically lost entirely. In Chap. 5, the single-harmonic parameters $\Delta\lambda_{\mathrm{single}}$, $\Delta\lambda_{\mathrm{single,sat}}$, and $\Delta\lambda_{\mathrm{single,one}}$ will be replaced by their multi-harmonic counterparts $\Delta\lambda_{\mathrm{multi}}$, $\Delta\lambda_{\mathrm{multi,sat}}$, and $\Delta\lambda_{\mathrm{multi,one}}$, respectively. The stationary regime linewidth $\delta\lambda_{\mathrm{stat}}$, which appears in Eq. (4.16), Eq. (4.17), and Eq. (4.19), and its dependence on various cavity parameters, such are dispersion or modulation window width, is discussed in more detail in Chap. 6.

For better guidance throughout Sec. 4.4, Tab. 4.1 contains some of the basic parameters describing DTML lasers and corresponding expressions.

Table 4.1: Basic parameters describing DTML lasers and corresponding expressions.

Parameter	**Definition**	**Expression**
Fundamental frequency of the cavity f_{cav}	Inverse round trip time of the cavity T_{cav}	$f_{\mathrm{cav}}(\lambda) = \frac{c}{n_{\mathrm{g}}(\lambda)L_{\mathrm{fiber}} + n_{\mathrm{g}}(\lambda_0)L_{\mathrm{cFBG}}(\lambda)}$ (Eq. (4.9))
Modulation frequency f	Frequency of a periodic losses modulation to mode-lock the cavity	$f = qf_{\mathrm{cav}}(\lambda)$ (Eq. (4.10))
Central emission wavelength λ_0	Central emission wavelength of the gain spectrum	$\lambda_0 \approx (\lambda_{\mathrm{end}} - \lambda_{\mathrm{start}})/2$
Tuning range $\Delta\lambda$ (or $\Delta\nu$ in optical frequency terms)	Emission wavelength change $\Delta\lambda = \lambda_{\mathrm{end}} - \lambda_{\mathrm{start}}$ as a function of change in the modulation frequency $\Delta f = f_{\mathrm{end}} - f_{\mathrm{start}}$	$\Delta\lambda \approx S(f_0)\Delta f$ (Eq. (4.13))
Sweep rate f_{s}	Inverse sweep time T_{s} for the emission wavelength to be periodically tuned from λ_{start} to λ_{end}	$f_{\mathrm{s}} = 1/T_{\mathrm{s}}$
Axial resolution δz	Minimum distance to differentiate two structures in depth	$\delta z = 0.44\frac{\lambda_0^2}{\Delta\lambda}$ or $\delta z = 0.60\frac{\lambda_0^2}{\Delta\lambda}$ (Eq. (2.6))
Instantaneous linewidth $\delta\lambda$	Experimentally measured spectral linewidth when the laser is swept at f_{s}	———
Imaging depth $\Delta z_{6\mathrm{dB}}$	Depth with 6 dB reduction in signal-to-noise ratio	$\Delta z_{6\mathrm{dB}} \approx 0.22\frac{\lambda_0^2}{\delta\lambda}$ or $\Delta z_{6\mathrm{dB}} \approx \frac{\lambda_0^2}{\delta\lambda}$ (Eq. (2.13))
Mode spectral density $N_{1\mathrm{nm}}$	Number of longitudinal modes per unit length in the spectral domain	$N_{1\mathrm{nm}}$ = number of modes in 1 nm interval (with spacing given by Eq. (4.9))
OCT system signal sensitivity	Measured A-scan peak relative to the noise floor	Related to SNR $= \frac{P_{\mathrm{fringe}}}{P_{\mathrm{noise}}}$ (Eq. (2.9))

4.4 DTML swept sources

4.4.1 1st generation

A DTML laser in Fig. 4.4 consists of three main elements: a gain medium, a dispersive element, and a modulation (or mode-locking) element. The first demonstrations of wavelength tuning using a fibre cavity with large dispersion were reported in two articles published in 1998 [22, 23]. In the former, a spool of dispersion-compensating fibre was used as the dispersive element, while the latter employed a cFBG. In both studies, only the stationary (no fast sweeping) regime was investigated, and the potential of this tuning technique for OCT had not yet been recognised, as the concept of SS-OCT was still in its early stages of development in the early 2000s.

The first implementation of a rapid wavelength sweeping using DTML was reported in 2006 [15], described as a "wide and fast wavelength-tunable mode-locked fibre laser". In a sigma-configuration depicted in Fig. 4.7(a), a semiconductor optical amplifier (SOA) operating at 1.3 µm was employed as the gain medium, while dispersion-compensating fibre (DCF) served to provide intracavity dispersion. Active mode-locking was achieved by directly modulating the SOA injection current using a radio-frequency (RF) generator. Although a sweep rate of 200 kHz across a 100 nm tuning bandwidth was demonstrated, the coherence properties of the laser were not evaluated. The authors, however, correctly acknowledged the trade-off between the tuning bandwidth and coherence, attributed to the limited number of a photon round trips inside the cavity, a phenomenon discussed in more detail in Subsec. 4.3. DTML lasers employing long fibres as the dispersive elements in the cavities will be further referred to as the 1st generation DTML lasers. The cavity lengths in the 1st generation range between 100-1000 m [7, 12, 15, 24, 25], with a corresponding mode spectral density of 10^4-10^6 per 1 nm (see Tab. 4.1).

Shortly thereafter, the same research group reported a DTML laser operating at 1550 nm using a ring configuration depicted in Fig. 4.7(b) [24]. In the laser, a DCF served as the dispersive element, and mode-locking was achieved through a direct modulation of the SOA injection current. At a sweep rate of 20 kHz across a 91 nm tuning bandwidth, the laser exhibited a relatively broad spectral linewidth of 0.6 nm, correspond-

ing to a coherence length of approximately 1.8 mm at 1550 nm. The study concluded that by optimising some of the cavity parameters, such as the cavity length, modulation frequency, or dispersion value, wider tuning bandwidths and higher sweep rates could be realised while preserving the coherence properties of the laser.

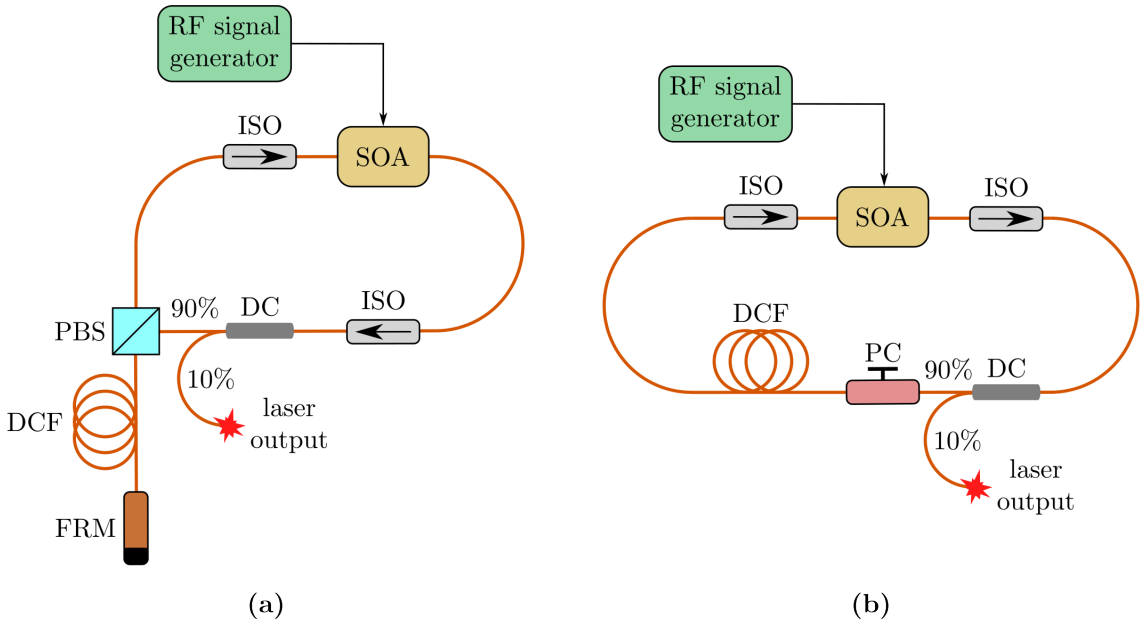

Figure 4.7: 1st generation DTML lasers. **(a)** Sigma-configuration at 1.3 µm [15]. **(b)** Ring configuration at 1550 nm [24]. SOA: semiconductor optical amplifier, ISO: isolator, DC: directional coupler, PBS: polarisation beam splitter, DCF: dispersion compensation fibre, FRM: Faraday rotator mirror, PC: polarisation controller.

DTML lasers operating at three wavelength ranges, 850 nm, 1300 nm, and 1550 nm, were examined in a review study using various configurations with a focus on dynamic sensing applications [25]. An 850 nm linear configuration, depicted in Fig. 4.8(a), employed a reflective semiconductor optical amplifier (RSOA) and a Faraday rotator mirror (FRM) as the cavity mirrors. Additionally, the review presented a DTML laser at 1550 nm using an erbium-doped fibre amplifier (EDFA) as the gain medium in a sigma-configuration shown in Fig. 4.8(b). In the same laser, mode-locking via an intensity modulator (IM) was introduced in place of direct modulation of the gain medium. While EDFAs typically offer higher output power and lower noise figure compared to SOAs [26], their gain bandwidth is generally limited to 40 nm, in comparison with SOAs providing 100 nm and wider bandwidths. The advantages of using an IM instead of direct gain

modulation will be discussed further in Subsec. 4.4.3. A similar linear configuration to Fig. 4.8(a), but operating at 1550 nm, was studied in [12]. The primary finding of the study was that a larger dispersion in the cavity together with a higher modulation frequency lead generally to a narrower linewidth.

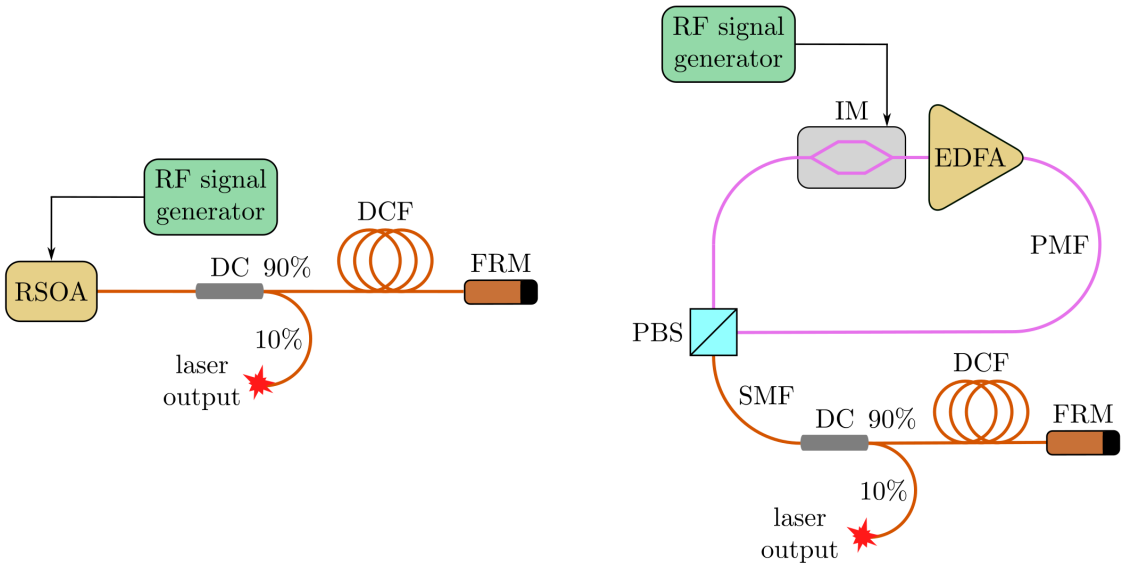

Figure 4.8: 1st generation DTML lasers. **(a)** Sigma-configuration at 850 nm [25]. **(b)** Ring configuration at 1550 nm [25]. RSOA: reflective semiconductor optical amplifier, DC: directional coupler, DCF: dispersion compensation fibre, FRM: Faraday rotator mirror, IM: intensity modulator, EDFA: erbium-doped fibre amplifier, PMF: polarisation maintaining fibre, PBS: polarisation beam splitter, SMF: single mode fibre.

The application of DTML lasers for SS-OCT was summarised in a review study from 2013 [7]. The study examined three configurations operating at 1.3 µm: a ring cavity using a DCF, a ring cavity using a cFBG, and a linear cavity using a cFBG as the dispersive elements. Notably, the study also presented the first OCT images obtained with a DTML laser, capturing an adhesive tape.

To summarise the 1st generation DTML lasers, these features characterise their designs and limit their performance, improved in the 2nd (see Subsec. 4.4.2) and 3rd (see Subsec. 4.4.3) generations:

1. **Extended cavity length due to the use of fibre as the dispersive element:** Achieving sufficient chromatic dispersion requires long lengths of fibre, which signif-

icantly increases the cavity length in the 1st generation DTML lasers. However, a longer cavity length limits the achievable dynamic tuning bandwidths, as explained in detail in Subsec. 4.3.

2. **Normal dispersion wavelength regions of fibre:** As shown in plots in Fig. 4.1, optical fibres commonly used for DTML lasers exhibit only normal dispersion values within specific wavelength ranges. Due to the interplay between dispersion and nonlinear effects inside the cavity, normal dispersion values generate broader linewidths compared to anomalous dispersion values [17, 18]. This interplay will be theoretically examined in Chap. 6.

3. **Direct modulation of the gain medium:** The majority of the 1st generation DTML lasers employed direct modulation of the gain medium to achieve mode-locking inside the cavity. As will be shown in Chap. 6, sub-nanosecond modulation windows are preferable for enhanced lasing stability and coherence. However, generating such short modulation windows is challenging with SOA chips and their associated electronics, which are typically designed for electrical frequencies below 1 GHz.

4.4.2 2nd generation

Incorporating a cFBG in place of fibre as the dispersive element substantially reduces the cavity length and ensures anomalous dispersion inside the cavity across any wavelength range. This adaptation will be furthered referred to as the 2nd generation DTML lasers. The cavity lengths in the 2nd generation range between 1-10 m [6, 7, 11, 17, 27], with a corresponding mode spectral density of 10^2-10^4 per 1 nm (see Tab. 4.1).

The first DTML laser using a cFBG in a configuration shown in Fig. 4.9(a) as the dispersive element was demonstrated operating at 1550 nm, with a sweep rate of 500 kHz, a tuning bandwidth of 40 nm, and a relatively broad linewidth of 0.77 nm [27]. An improvement in coherence was achieved by reducing the sweep rate to 50 kHz in a linear configuration displayed in Fig. 4.9(b) operating at 1310 nm [7].

In the first exact theoretical study on DTML lasers [17], it was shown that, due to the

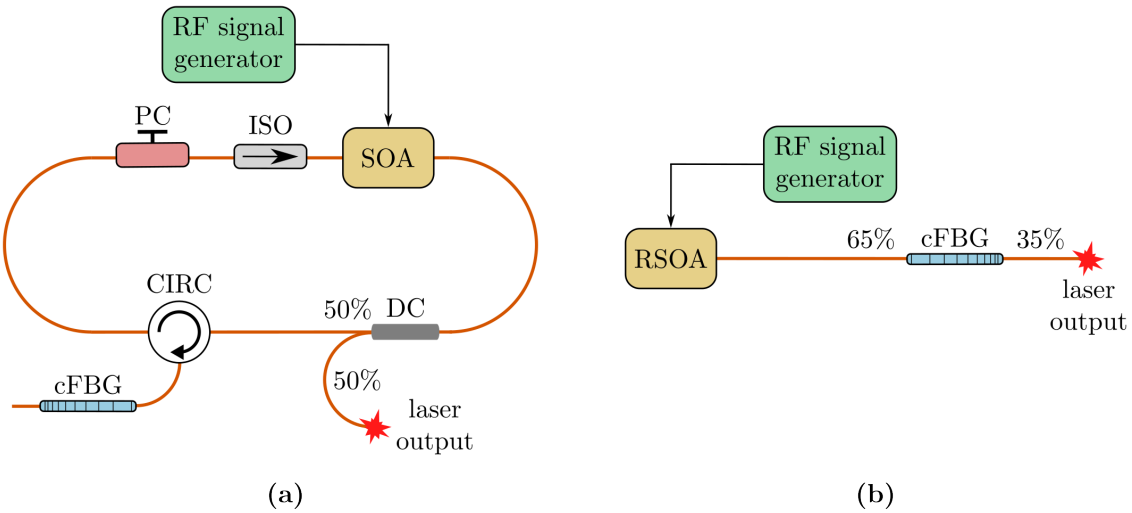

Figure 4.9: 2nd generation DTML lasers. **(a)** Ring configuration at 1550 nm [27]. **(b)** Linear configuration at 1550 nm [7]. SOA: semiconductor optical amplifier, DC: directional coupler, CIRC: circulator, cFBG: chirped fibre Bragg grating, PC: polarisation controller, RSOA: reflective semiconductor optical amplifier.

interplay between dispersion and nonlinear effects inside the cavity, anomalous dispersion values produce narrower linewidths than normal dispersion values. Additionally, the study researched the laser depicted in Fig. 4.10(a) operating at 1550 nm. The laser achieved an imaging depth of 2 mm and an axial resolution of 60 µm at a sweep rate of 150 kHz.

The last studies on the 2nd generation DTML lasers were published in 2014 by two different research groups [6, 11]. Employing a similar linear configuration to that depicted in Fig. 4.9(b), the group in [6] demonstrated the narrowest linewidth of 0.033 nm (corresponding to a 3 cm coherence length at 1550 nm) reported from a DTML cavity, although without dynamic coherence properties examined. The same group contributed to better understanding of dynamics in DTML lasers and mathematical modelling in this class of lasers in their another study [28]. The other group in [11] reported the shortest DTML cavity of 0.88 m, depicted in Fig. 4.10(b). This compact laser enabled a linear-in-wavenumber tuning with an 1.8 mm imaging depth, 22 µm axial resolution, and a remarkable sensitivity of 109 dB at a 100 kHz sweep rate, making it well-suited for in-vivo OCT imaging applications.

One ongoing limitation of DTML lasers at that time was persistent deterioration of coherence at higher sweep rates. This limitation was to some extent addressed by

employing pulse modulation technique, discussed in more detail in Subsec. 4.4.3.

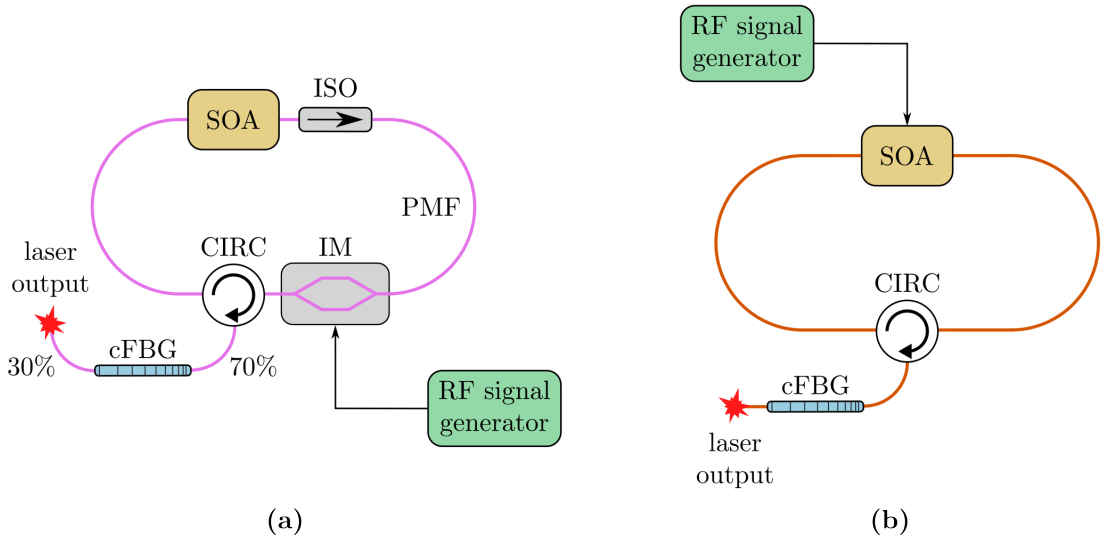

Figure 4.10: 2nd generation DTML lasers. **(a)** Ring configuration at 1550 nm [17]. **(b)** Ring configuration at 1310 nm with the shortest DTML cavity of 0.88 m reported [11]. SOA: semiconductor optical amplifier, ISO: optical isolator, IM: intensity modulator, CIRC: optical circulator, cFBG: chirped fibre Bragg grating.

4.4.3 3rd generation

The integration of a fast intensity modulator inside a DTML laser cavity decouples the mode-locking element from the gain medium. This separation leads to a more stable amplification inside the cavity as the gain medium is no longer directly modulated. Furthermore, this modification enables the use of sub-nanosecond modulation windows by employing pulse modulation technique instead of conventional sinusoidal modulation. Using this approach, it has been demonstrated that the laser can maintain coherence even at higher sweep rates [10, 19]. DTML lasers incorporating a fast intensity modulator as the mode-locking element will be referred to as the 3rd generation DTML lasers. Similarly as in the case of 2nd generation lasers, the cavity lengths in the 2nd generation range between 1-10 m [10, 19, 29–31], with a corresponding mode spectral density of 10^2-10^4 per 1 nm (see Tab. 4.1).

The first utilisation of an intensity modulator in a fibre cavity for DTML dates back to 2010 [29] in a configuration depicted in Fig. 4.11(a), incorporating an EDFA as the gain

medium. The authors presented a versatile "rapidly tunable, electronically controlled, pulse duration adjustable, arbitrarily programmable wavelength, picosecond mode-locked fibre laser" modulated by electrical pulses ranging from 20 ps to 4 ns. In the subsequent study [30], the same research group reported a pulse-modulated DTML laser using an SOA at 1550 nm as the gain medium, in a configuration similar to that shown in Fig. 4.11(b). This swept laser achieved an imaging depth of 1 mm at a sweep rate of 25 kHz, with a wide tuning bandwidth of 100 nm. The first actual discussion on coherence improvement by employing the pulse modulation technique instead of conventional sinusoidal modulation was then presented in a letter from 2014 [19].

The only DTML laser operating at 1060 nm was not demonstrated until 2018 [10]. Using this laser, depicted in Fig. 4.11(b), distinct *in-vivo* human retinal images at a sweep rate of 100 kHz and sensitivity of 120 dB were captured. This laser can be regarded as the culmination of the knowledge and optimisation practises accumulated for DTML lasers so far.

The most recent DTML laser operating at 850 nm was demonstrated by employing a cFBG and the pulse modulation technique in 2024 [31], described in detail in Sec. 7.2.

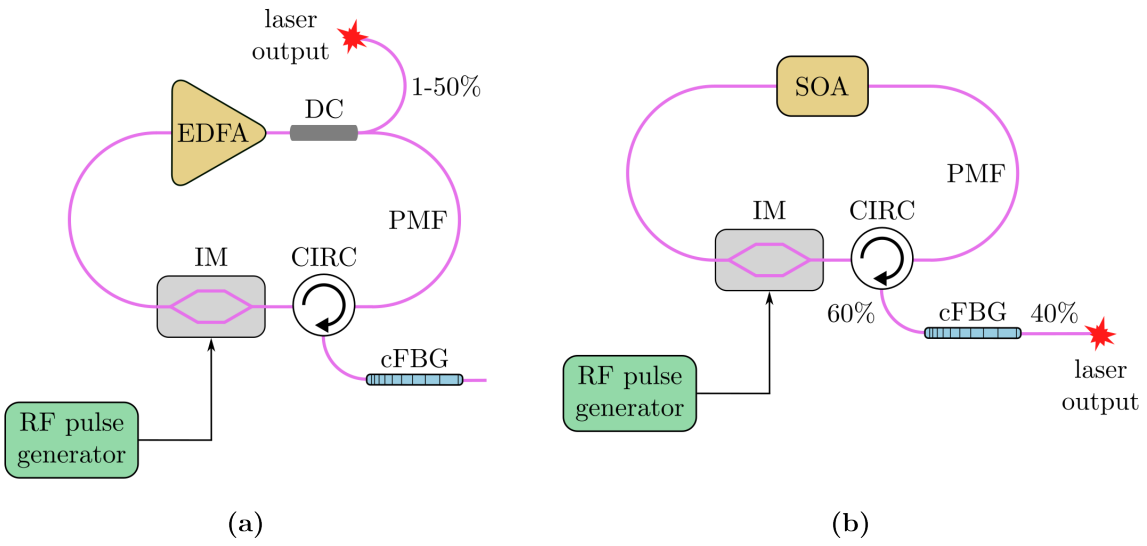

Figure 4.11: 3rd generation DTML lasers. **(a)** Ring configuration using an EDFA as the gain medium [29]. **(b)** Ring configuration operating at 1060 nm [10]. EDFA: erbium-doped fibre amplifier, DC: directional coupler, CIRC: optical circulator, cFBG: chirped fibre Bragg grating, IM: intensity modulator, SOA: semiconductor optical amplifier.

To summarise the history of research on DTML lasers, these features in their design to optimise their performance for SS-OCT applications have been established:

1. **Short cavity length:** The cavity length should be as short as possible to preserve coherence even at higher sweep rates, as explained in detail in Sec. 4.3.

2. **Anomalous dispersion:** Due to the interplay between dispersion and nonlinear effects inside the cavity, anomalous dispersion values produce narrower linewidths in comparison with normal dispersion values. This interplay will be theoretically examined in Chap. 6.

3. **Short modulation window:** An enhanced mode-locking and better coherence properties are achievable by applying sub-nanosecond modulation windows by utilising the pulse modulation technique. This lasing improvement will be theoretically examined in Chap. 6 and experimentally validated in Sec. 7.2.

4. **Forward sweeping:** Due to the red shift in an SOA, output pulse energies and coherence are enhanced if the laser is swept from shorter to longer wavelengths [10, 32].

Bibliography

[1] U. Keller, *Ultrafast Lasers: A Comprehensive Introduction to Fundamental Principles with Practical Applications*. Springer International Publishing, 2022.

[2] G. P. Agrawal, *Fiber-Optic Communications Systems*, 3rd ed. John Wiley & Sons, Inc, 2002.

[3] D. J. Kitcher, A. Nand, S. A. Wade, R. Jones, G. W. Baxter, and S. F. Collins, "Directional dependence of spectra of fiber Bragg gratings due to excess loss," *J. Opt. Soc. Am. A*, vol. 23, no. 11, pp. 2906–2911, Nov 2006.

[4] I. Duling, *Compact Sources of Ultrashort Pulses*. Cambridge University Press, 1995.

[5] A. E. Siegman, *Lasers*. University Science Books, 1986.

[6] C. Zhang, P. Liao, B. Burgoyne, Y. Kim, F. Trépanier, A. Villeneuve, and O. Liboiron-Ladouceur, "Low-cost dispersion-tuned active harmonic mode-locked laser with a 3-cm coherence length," *IEEE Journal of Selected Topics in Quantum Electronics*, vol. 20, no. 5, pp. 399–405, 2014.

[7] S. Yamashita and Y. Takuba, "Wide and fast wavelength-swept fiber lasers based on dispersion tuning and their application to optical coherence tomography," *Photonic Sensors*, vol. 3, no. 4, pp. 320–321, 2013.

[8] S. Yamashita, N. Yuichi, K. Ryosei, and K. Osamu, "Wide and fast wavelength-swept fiber laser based on dispersion tuning for dynamic sensing," *Journal of Sensors*, vol. 2009, 01 2009.

[9] Y. Takubo and S. Yamashita, "High-speed dispersion-tuned wavelength-swept fiber laser using a reflective SOA and a chirped FBG," *Opt. Express*, vol. 21, no. 4, pp. 5130–5139, Feb 2013.

[10] H. D. Lee, G. H. Kim, J. G. Shin, B. Lee, C.-S. Kim, and T. J. Eom, "Akinetic swept-source optical coherence tomography based on a pulse-modulated active mode locking fiber laser for human retinal imaging," *Scientific Reports*, vol. 8, 2018.

[11] H. D. Lee, M. Y. Jeong, C.-S. Kim, J. G. Shin, B. H. Lee, and T. J. Eom, "Linearly wavenumber-swept active mode locking short-cavity fiber laser for in-vivo OCT imaging," *IEEE Journal of Selected Topics in Quantum Electronics*, vol. 20, no. 5, pp. 433–440, 2014.

[12] H. D. Lee, J. H. Lee, M. Y. Jeong, and C.-S. Kim, "Characterization of wavelength-swept active mode locking fiber laser based on reflective semiconductor optical amplifier," *Opt. Express*, vol. 19, no. 15, pp. 14 586–14 593, Jul 2011.

[13] H. Lee, G. H. Kim, M. Villiger, H. Jang, B. E. Bouma, and C.-S. Kim, "Linear-in-wavenumber actively-mode-locked wavelength-swept laser," *Opt. Lett.*, vol. 45, no. 19, pp. 5327–5330, Oct 2020.

[14] Y. Hasegawa, T. Shirahata, and S. Yamashita, "Analysis of dynamic properties of dispersion-tuned swept lasers," *Journal of Lightwave Technology*, vol. 33, no. 1, pp. 219–226, 2015.

[15] S. Yamashita and M. Asano, "Wide and fast wavelength-tunable mode-locked fiber laser based on dispersion tuning," *Opt. Express*, vol. 14, no. 20, pp. 9299–9306, Oct 2006.

[16] R. Huber, M. Wojtkowski, K. Taira, J. G. Fujimoto, and K. Hsu, "Amplified, frequency swept lasers for frequency domain reflectometry and OCT imaging: design and scaling principles," *Opt. Express*, vol. 13, no. 9, pp. 3513–3528, May 2005.

[17] A. Takada, M. Fujino, and S. Nagano, "Dispersion dependence of linewidth in actively mode-locked ring lasers," *Opt. Express*, vol. 20, no. 4, pp. 4753–4762, Feb 2012.

[18] A. Takada, M. Saika, and S. Nagano, "Effect of linewidth enhancement factor in actively mode-locked ring laser," vol. 8961, p. 896135, 2014.

[19] H. Nagai and S. Yamashita, "Coherence improvement in dispersion-tuned swept laser by pulse modulation," *Electronics Letters*, vol. 50, no. 23, pp. 1729–1731, 2014.

[20] R. Huber, M. Wojtkowski, and J. G. Fujimoto, "Fourier domain mode locking (FDML): A new laser operating regime and applications for optical coherence tomography," *Opt. Express*, vol. 14, no. 8, pp. 3225–3237, Apr 2006.

[21] R. Huber, "FDML (incl. parallelization)," in *Optical Coherence Tomography*, W. Drexler and J. G. Fujimoto, Eds. Berlin, Heidelberg: Springer, 2015, pp. 741–787.

[22] S. Li and K. T. Chan, "Electrical wavelength tunable and multiwavelength actively mode-locked fiber ring laser," *Applied Physics Letters*, vol. 72, no. 16, pp. 1954–1956, Apr 1998.

[23] ——, "Electrical wavelength-tunable actively mode-locked fiber ring laser with a linearly chirped fiber Bragg grating," *IEEE Photonics Technology Letters*, vol. 10, no. 6, pp. 799–801, 1998.

[24] M. Asano, S. Yamashita, and K. Hsu, "Widely and fast wavelength-tunable mode-locked fiber laser at 1.55 µm region using intracavity dispersion," in *2006 Conference on Lasers and Electro-Optics and 2006 Quantum Electronics and Laser Science Conference*, 2006.

[25] Y. Nakazaki and S. Yamashita, "Fast and wide tuning range wavelength-swept fiber laser based on dispersion tuning and its application to dynamic FBG sensing," *Opt. Express*, vol. 17, no. 10, pp. 8310–8318, May 2009.

[26] A. W. Setiawan Putra, M. Yamada, S. Ambran, and T. Maruyama, "Theoretical comparison of noise characteristics in semiconductor and fiber optical amplifiers," *IEEE Photonics Technology Letters*, vol. 30, no. 8, pp. 756–759, 2018.

[27] S. Yamashita and Y. Takubo, "Fast wavelength-swept dispersion-tuned fiber laser over 500 kHz using a wideband chirped fiber Bragg grating," in *21st International Conference on Optical Fiber Sensors*, vol. 7753. SPIE, 2011.

[28] B. Burgoyne, A. Dupuis, and A. Villeneuve, "An experimentally validated discrete model for dispersion-tuned actively mode-locked lasers," *IEEE Journal of Selected Topics in Quantum Electronics*, vol. 20, no. 5, pp. 390–398, 2014.

[29] B. Burgoyne and A. Villeneuve, "Programmable lasers: design and applications," in *Fiber Lasers VII: Technology, Systems, and Applications*, vol. 7580, International Society for Optics and Photonics. SPIE, 2010.

[30] Y. Kim, B. Burgoyne, N. Godbout, A. Villeneuve, G. Lamouche, and S. Vergnole, "Picosecond programmable laser sweeping over 50 mega-wavelengths per second," in *Fiber Lasers VIII: Technology, Systems, and Applications*, vol. 7914, International Society for Optics and Photonics. SPIE, 2011.

[31] R. Riha, A. M. Jimenez, G. Venugopal, M. Klufts, R. Huber, and A. Podoleanu, "Dispersion-tuned mode-locked laser for swept source OCT at 850 nm using a cFBG and the pulse modulation technique," *IEEE Photonics Journal*, vol. 16, no. 4, pp. 1–5, 2024.

[32] B. Johnson, W. Atia, M. Kuznetsov, B. D. Goldberg, P. Whitney, and D. C. Flanders, "Coherence properties of short cavity swept lasers," *Biomed. Opt. Express*, vol. 8, no. 2, pp. 1045–1055, Feb 2017.

Chapter 5

From single-harmonic to multi-harmonic DTML

This chapter is based on the study [1]. It starts with a brief overview of the previous development in multi-harmonic DTML swept lasers within Applied Optics Group at University of Kent and then introduces a rigorous model for description of the advancement from the standard single-harmonic to multi-harmonic operation. This is accomplished utilising a mathematical framework that connects the laser optical spectrum with the spectral content of the modulation signal over many sweep cycles. Building on the spectral filtering description introduced in the previous chapter for the single-harmonic case, this chapter derives the tuning bandwidth limits for the multi-harmonic DTML operation, showing trade-offs between the achievable tuning bandwidth and coherence performance in this sweeping regime.

5.1 Previous development in the multi-harmonic DTML

In the prior reports published by the AOG [2, 3], it was demonstrated that an alternative sweeping regime to the single-harmonic DTML described in Chap. 4 can be established inside a DTML cavity. This regime, involving two simultaneous "resonant" conditions, was initially referred as to the *dual resonance sweeping regime* or *dual resonance DTML*. The first resonant condition corresponds to active mode-locking (achieved

via direct modulation of the gain medium or an external modulator) at a harmonic of the fundamental frequency of the cavity. The second resonant condition is inspired by the Fourier-domain mode-locking (FDML) technology [4], where the mode-locking element (typically a Fabry–Pérot filter) is driven at the fundamental frequency. When both resonant conditions are applied to a DTML cavity, it is observed that, contrary to FDML, wavelength tuning does not occur if the sweep rate precisely matches the fundamental frequency. Instead, only a single wavelength emission appears at the output of the DTML laser. It is experimentally observed that wavelength tuning is achieved if the sweep rate is actually slightly detuned from the fundamental frequency. For the first time, this work provides a rigorous theoretical explanation for this behaviour. Because multiple orders of harmonics are engaged, a more accurate reference to this regime is proposed here, as to the *multi-harmonic DTML*. This regime is fundamentally different from the standard single-harmonic mode-locking presented in Chap.4.

The multi-harmonic DTML regime was previously demonstrated first at 1550 nm in 2015 [2] and subsequently at 850 nm in 2017 [3], using the laser configurations depicted in Fig. 5.1. These early lasers achieved wavelength tunings over a 20 nm bandwidth at a 800 kHz sweep rate and 15 nm at 1 MHz, respectively. However, the coherence performance under these parameters was extremely limited. In both cases, these two key design features limited their performance:

1. **Direct modulation of the SOA gain:** As SOA chips and their associated electronics are typically designed for electrical frequencies below 1 GHz, no short sub-nanosecond modulation windows could be applied for enhanced coherence (see Subsec. 4.4.3 and Subsec. 6.4.2). To overcome this limitation, high speed intensity modulators are used instead in the multi-harmonic laser configurations researched in Sec. 7.3 and Sec. 7.4.

2. **Employing fibre as the dispersive element:** Although extended cavity lengths of 100 -1000 m are needed for the multi-harmonic operation, optical fibres commonly used for DTML lasers with dispersions plotted in Fig. 4.1 exhibit only normal dispersion values within specific wavelength ranges. Due to the interplay between

dispersion and nonlinear effects inside the cavity, normal dispersion values generate broader linewidths compared to anomalous dispersion values (see Chap. 6). To overcome this limitation, cFBGs are incorporated in the multi-harmonic laser configurations researched in Sec. 7.3 and Sec. 7.4.

The previous reports presented primarily experimental demonstrations. However, a comprehensive theoretical description of the multi-harmonic operation, discussion on its tuning and coherence performance, its demonstration at 1 µm, and finally actual OCT images produced by employing this regime have not been reported so far. These aspects are addressed in the present work.

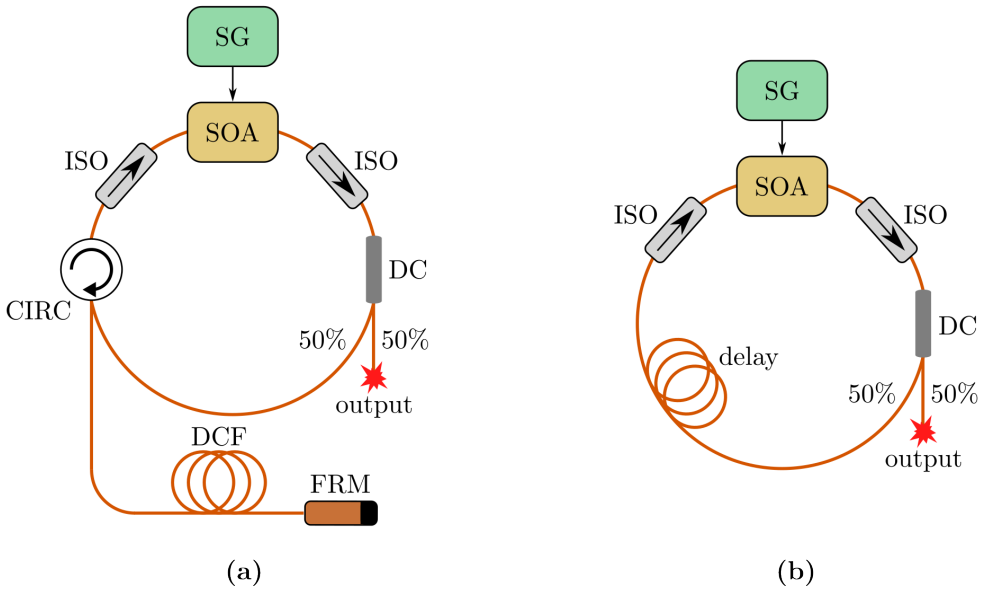

Figure 5.1: First multi-harmonic DTML lasers. **(a)** First multi-harmonic DTML laser at 1550 nm [2]. **(b)** First multi-harmonic DTML laser at 850 nm [3]. SOA: semiconductor optical amplifier, SG: signal generator, ISO: optical isolator, DC: directional coupler, DCF: dispersion compensation fibre, FRM: Faraday rotator mirror, CIRC: optical circulator.

5.2 Many sweep cycles mathematical framework

For better comprehension of the advance from the standard single-harmonic to the novel multi-harmonic DTML, it will be helpful to describe the laser optical spectrum in relation

to the spectral content of the modulation signal over large number of sweep cycles (periods $T_\mathrm{s} = 1/f_\mathrm{s}$). Using the properties of the convolution operation $x(t) \circledast y(t)$ and of the Dirac comb $\sum_l \delta(t-l)$ [5], the modulation signal $V(t)$ in Fig. 5.2 produced by the VCO can be written in the form:

$$V(t) = V_\mathrm{cycle}(t) \circledast \sum_{l=-\infty}^{+\infty} \delta(t - lT_\mathrm{s}). \tag{5.1}$$

$V_\mathrm{cycle}(t)$ here represents the single sweep cycle modulation signal inside the red dashed rectangle in Fig. 5.2:

$$V_\mathrm{cycle}(t) = \mathrm{rect}\left(\frac{t - T_\mathrm{s}/2}{T_\mathrm{s}}\right) \sin\left[2\pi \int_0^t f(t')\mathrm{d}t'\right], \tag{5.2}$$

where a modulation depth of 1 is considered. The rectangular function $\mathrm{rect}(t)$ [5] in Eq. (5.2) constraints the $V_\mathrm{cycle}(t)$ to one period T_s interval, and the integral calculates the time-domain instantaneous phase of the signal. Assuming a linear sweeping of the modulation frequency, $f(t)$ can be represented by a sawtooth shape, as depicted in Fig. 5.2, according to:

$$f(t) = \Delta f \left(f_\mathrm{s} t - \lfloor f_\mathrm{s} t + 1 \rfloor\right) + f_0 + \frac{\Delta f}{2} \mathrm{sgn}\, \Delta f, \tag{5.3}$$

while still following the relationship between $\Delta\lambda$ and Δf, as given by Eq. (4.12) or Eq. (4.13). $\lfloor x \rfloor$ in Eq. (5.3) denotes the floor function, which rounds a real number x down to the nearest integer. When $\Delta f > 0$, Eq. (5.3) represents a positive sawtooth signal, while when $\Delta f < 0$, Eq. (5.3) describes a negative sawtooth signal. Combining Eq. (5.1)-Eq. (5.3), the signal in Eq. (5.1) is constructed by repeating $V_\mathrm{cycle}(t)$ at a rate f_s, with the modulation frequency varying according to $f(t)$ specified by Eq. (5.3).

Using the Fourier transform properties [5] and omitting multiplicative constants, the spectrum $\widetilde{V}(f)$ of the modulation signal $V(t)$ specified by Eq. (5.1) can be expressed as:

$$\begin{aligned} \widetilde{V}(f) &\sim \widetilde{V}_\mathrm{cycle}\left(\frac{f - f_0}{\Delta f}\right) \sum_{l=-\infty}^{+\infty} \delta\left(f - lf_\mathrm{s} - f_0 + \left\lfloor \frac{f_0}{f_\mathrm{s}} \right\rfloor f_\mathrm{s}\right) \\ &= \widetilde{V}_\mathrm{cycle}\left(\frac{f - f_0}{\Delta f}\right) \sum_{l=-\infty}^{+\infty} \delta(f - f_0 - lf_\mathrm{s}), \end{aligned} \tag{5.4}$$

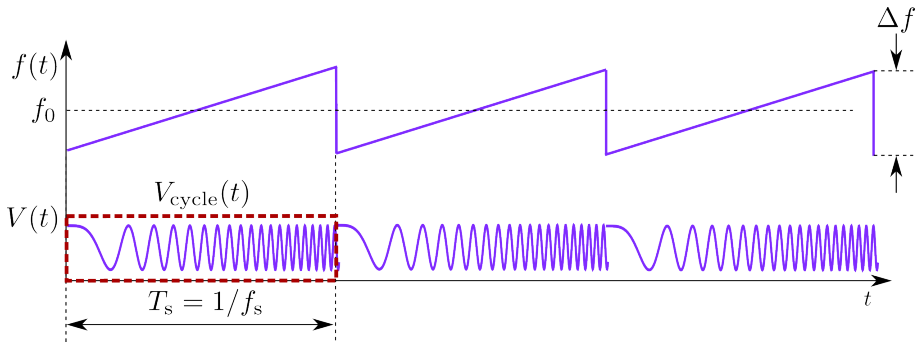

Figure 5.2: A graphical representation of the modulation signal $V(t)$ and the modulation frequency $f(t)$ given by Eq. (5.1) and Eq. (5.3), respectively. $V_{\text{cycle}}(t)$: single sweep cycle modulation signal given by Eq. (5.2), T_s: sweep period, f_0: central modulation frequency, Δf: modulation frequency range.

where $\widetilde{V}_{\text{cycle}}[(f - f_0)/\Delta f]$ represents the spectral amplitude envelope, $f_0 - \lfloor f_0/f_s \rfloor f_s$ is the frequency comb offset, and f_s is the spacing between the comb frequency components $f_l = f_0 + l f_s$. Note that the envelope is centered around f_0 and that, due to the offset $f_0 - \lfloor f_0/f_s \rfloor f_s$, there is always a comb component at f_0 for $l = 0$, regardless of the value of f_s. A simulation of the spectrum $\widetilde{V}(f)$ for a signal $V(t)$ as defined through Eq. (5.1)-Eq. (5.3) is displayed in the top panel of Fig. 5.3, with parameters $f_0 = 2330\,\text{MHz}$, $\Delta f = 100\,\text{MHz}$, and $f_s = 1\,\text{MHz}$. It can be observed that the frequency extension of $\widetilde{V}(f)$ is approximately equal to Δf, and that the spectrum contains approximately $\Delta f/f_s \approx 100$ frequency components. The experimentally measured spectral content of the VCO signal using an RF spectrum analyser, for the same parameters, is displayed in the bottom panel of Fig. 5.3, demonstrating a good agreement with the theoretical model above. The measured spectra of the modulation signals specifically used in the laser designs in Secs. 7.3 and 7.4 are also presented in those sections.

When the laser is mode-locked, the frequency components $f_l = f_0 + l f_s$, given by Eq. (5.4), match the resonant frequencies $q_c f_{\text{cav}}(\lambda_l)$ of the cavity,

$$\begin{aligned} f_l &= f_0 + l f_s = q_c f_{\text{cav}}(\lambda_0) + l f_s \\ &= q_c f_{\text{cav}}(\lambda_l), \end{aligned} \tag{5.5}$$

where an arbitrary single q_cth tuning band was chosen to simplify the notation. As depicted in the top panel of Fig. 5.4, each component f_l (vertical blue bars) corresponds to

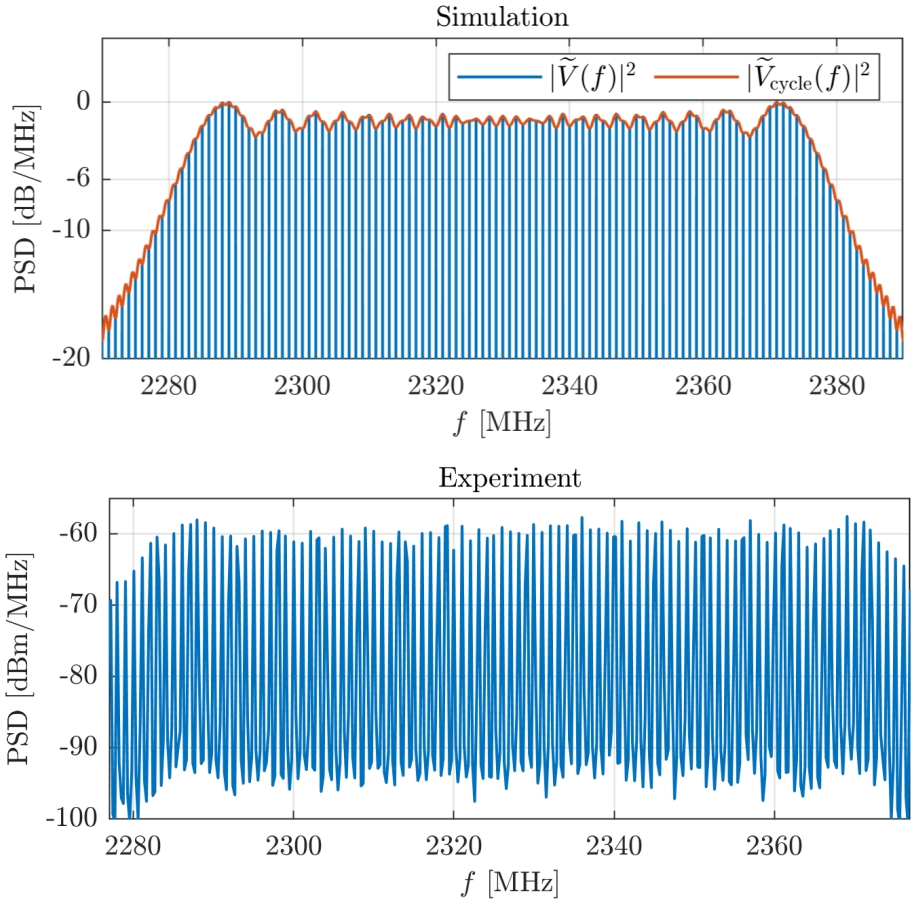

Figure 5.3: Top: Simulation of the spectrum of the modulation signal $V(t)$ specified by Eq. (5.1)-Eq. (5.4). **Bottom:** Experimentally measured VCO signal for $f_0 \doteq 2330\,\mathrm{MHz}$, $\Delta f \doteq 100\,\mathrm{MHz}$, and $f_\mathrm{s} \doteq 1\,\mathrm{MHz}$.

a different emission wavelength λ_l from the single q_cth tuning band. In the single-harmonic DTML, Δf is not bigger than f_{cav}, and f_s is much smaller than f_{cav}. Considering the total number of frequency components as $\approx \Delta f/f_s + 1$ and assuming a constant tuning sensitivity $S(f_0)$ across the q_cth tuning band, the tuning bandwidth $\Delta\lambda_{single}$ given by Eq. (4.13) can be expressed alternatively as a sum of fractional bandwidths $\Delta\lambda_{l+1,l} = \lambda_{l+1} - \lambda_l$:

$$\begin{aligned}\Delta\lambda_{single} &\approx \sum_{l=-\Delta f/2f_s}^{\Delta f/2f_s} \Delta\lambda_{l+1,l} = \sum_{l=-\Delta f/2f_s}^{\Delta f/2f_s} S(f_0) f_s \\ &\approx S(f_0)\frac{\Delta f}{f_s} f_s = S(f_0)\Delta f,\end{aligned} \tag{5.6}$$

leading to the same result as derived in Eq. (4.13). The laser optical spectrum for the single-harmonic regime is graphically depicted in the middle panel of Fig. 5.4. Such a spectrum can be observed on an optical spectrum analyser for an integration time much larger than T_s. The spectrum consists of $\approx \Delta f/f_s + 1$ spectral lines (5 lines in the diagram) with an instantaneous linewidth of $\delta\lambda$ (optical linewidth $\delta\nu = c\delta\lambda/\lambda^2$ in Fig. 5.4) at wavelengths λ_l (optical frequencies $\nu_l = c/\lambda_l$ in Fig. 5.4). The exact spectral shape and linewidth of the lines can be evaluated using a perturbed Gaussian or hyperbolic secant function, as follows from mathematical modelling of the cavity components and their effects on pulse propagation inside a DTML laser cavity [5–9]. For the graphical purposes, the spectral lines in Fig. 5.4 are approximated by a Gaussian spectral line with an instantaneous linewidth $\delta\nu$. In the single-harmonic DTML, the modes within each spectral line (the vertical bars) are locked at the same q_cth harmonic order with spacing given by $\Delta\nu_{m,l} = q_c f_{cav}(\lambda_l)$. An inverse Fourier transform of the each individual spectral line represents a monochromatic pulse train (5 trains in the diagram) with a carrier wavelength λ_l and a pulse rate given by $f_{p,l} = \Delta\nu_{m,l} = q_c f_{cav}(\lambda_l)$, perpetually circulating inside the cavity (indicated by the curved arrow at its centre), as depicted in the bottom panel of Fig. 5.4. A superposition of these monochromatic trains in time leads to a pulse train with a carrier wavelength varying over time, shown as snapshots of the optical field inside the cavity at two periods of T_{cav} in the bottom panel of Fig. 5.4.

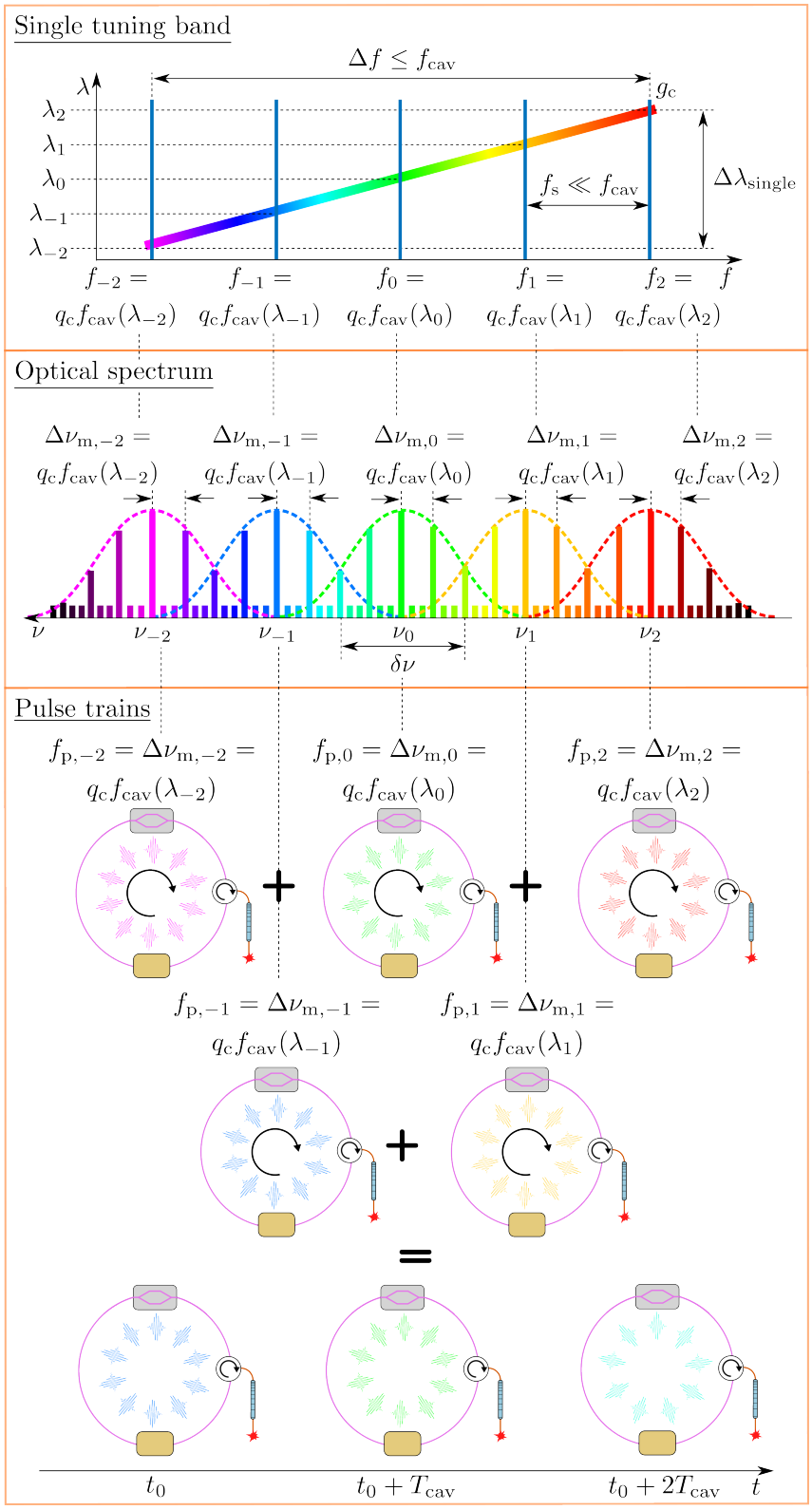

Figure 5.4: Single-harmonic DTML. **Top:** Emission wavelength λ as a function of the modulation frequency f_l. **Middle:** Optical spectrum consisting of spectral lines at ν_l with an instantaneous linewidth of $\delta\nu = c\delta\lambda/\lambda^2$. **Bottom:** Monochromatic pulse trains with a carrier wavelength λ_l and a pulse rate given by $f_{\mathrm{p},l} = \Delta\nu_{\mathrm{m},l} = q_{\mathrm{c}} f_{\mathrm{cav}}(\lambda_l)$, each corresponding to a single spectral line at ν_l in the spectrum from above.

5.3 Multi-harmonic DTML

As discussed in Sec. 4.3, fast sweeping in the single-harmonic DTML regime requires reduction of the cavity length. This represents a technical limitation, as fibre components may not allow shortening the cavity below a few meters. This cavity length constraint is addressed here by employing a long cavity ($\sim$ 100-1000 m) and introducing a different DTML regime: the multi-harmonic mode-locking. To examine the laser optical spectrum in this regime, the large number sweep cycles framework will be exploited, developed in the previous chapter. The basic concept of the multi-harmonic DTML is that the modulation frequency f in Fig. 4.5, satisfying the resonant condition given by Eq. (4.10), is not restricted to just a single tuning band q_{c}. To involve harmonic orders beyond q_{c}, two additional conditions are imposed on $f(t)$ (i.e., on the modulation signal $V(t)$). First, while Eq. (5.1)-Eq. (5.3) remain valid, the sweep rate is set close to the fundamental frequency of the cavity, $f_{\mathrm{s}} \approx f_{\mathrm{cav}}$. Therefore, the spacing f_{s} between the frequency components f_l in Eq. (5.4) is now much larger than in the single-harmonic case in Fig 5.4, to the extent that each individual f_l corresponds to a separate tuning band $q_{\mathrm{c}}+l$ (see the top panel of Fig. 5.5 and 5.6). To engage multiple tuning bands $q_{\mathrm{c}}+l$, the modulation frequency range Δf is extended significantly, as shown in the top panels of Figs. 5.5 and 5.6, greatly exceeding the fundamental frequency of the cavity, $\Delta f \gg f_{\mathrm{cav}} \approx f_{\mathrm{s}}$. In this way, many tuning bands $q_{\mathrm{c}}+l$ are involved in wavelength tuning. The total number of tuning bands Q involved is then estimated as:

$$Q \approx \frac{\Delta f}{f_{\mathrm{s}}} + 1. \tag{5.7}$$

When the two multi-harmonic conditions, i.e., $f_{\mathrm{s}} \approx f_{\mathrm{cav}}$ and $\Delta f \gg f_{\mathrm{cav}}$, are accomplished, wavelength tuning can be experimentally observed only if f_{s} is slightly detuned from the reference $f_{\mathrm{cav}}(\lambda_0)$. Also, it is observed that the tuning bandwidth increases linearly with this detuning. An approximate formula for this dependency was proposed in [10], and its more general form applicable to any large Δf will be derived here.

For convenience, f_s can be expressed in the form:

$$f_s = f_{cav}(\lambda_0) + \delta f_s, \tag{5.8}$$

where $f_{cav}(\lambda_0)$ is the fundamental frequency for the emission wavelength λ_0, and δf_s represents the sweep frequency detuning from $f_{cav}(\lambda_0)$. For the cavity to be mode-locked, the frequency components $f_l = f_0 + l f_s$, with the spacing f_s given by Eq. (5.8), has to satisfy the resonant condition according to Eq. (4.10),

$$f_l = f_0 + l f_s = q_c f_{cav}(\lambda_0) + l[f_{cav}(\lambda_0) + \delta f_s]. \tag{5.9}$$

If $\delta f_s = 0$, that is $f_s = f_{cav}(\lambda_0)$, each component f_l (vertical blue bars in the top panel of Fig. 5.5) corresponds to a single emission wavelength λ_0 from several tuning bands $q_c + l$,

$$f_l = (q_c + l) f_{cav}(\lambda_0). \tag{5.10}$$

In this case, the optical spectrum in the middle panel of Fig. 5.5 consists of a single spectral line at an optical frequency $\nu_0 = c/\lambda_0$ with an instantaneous linewidth $\delta\nu = c\delta\lambda/\lambda^2$. This single line results from a superposition of lines at the same optical frequency ν_0, but with modes locked at different $(q_c + l)$th harmonic order with mode spacing given by $\Delta\nu_{m,l} = (q_c + l) f_{cav}(\lambda_0)$. Again, for the graphical purposes, the spectral lines in Figs. 5.5 and 5.6 are approximated by a Gaussian spectral line shape with a linewidth $\delta\nu$. An inverse Fourier transform each invidual group of modes with spacing $\Delta\nu_{m,l}$ represents a monochromatic pulse train (5 trains in the diagram) with a carrier wavelength λ_0 and a pulse rate given by $f_{p,l} = \Delta\nu_{m,l} = (q_c + l) f_{cav}(\lambda_0)$, perpetually circulating inside the cavity (indicated by the curved arrow at its centre), as depicted in the bottom panel of Fig. 5.5. Despite the modulation frequency being swept fast, only one emission wavelength λ_0 is stored inside the cavity at a given time, similarly to the single-harmonic case for $f_s = 0$, as displayed at the bottom of Fig. 5.5.

If $\delta f_s \neq 0$, each component f_l in Eq. (5.9) (vertical blue bars in the top panel of Fig. 5.6) corresponds to a different emission wavelength λ_l from several tuning bands

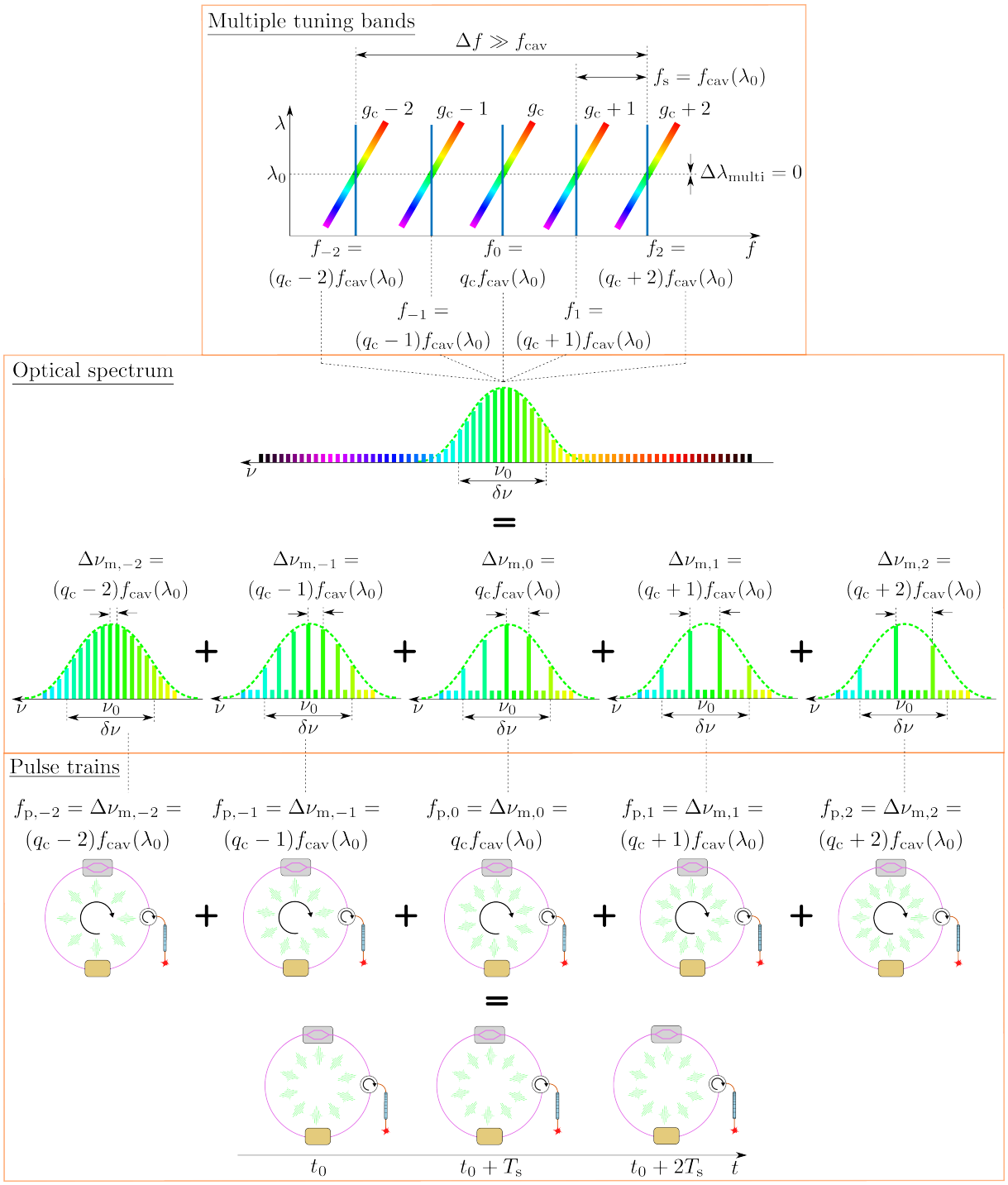

Figure 5.5: Multi-harmonic DTML for the case $f_{\mathrm{s}} = f_{\mathrm{cav}}(\lambda_0)$. **Top:** Emission wavelength λ as a function of the modulation frequency f_l. **Middle:** Optical spectrum consisting of a superposition of spectral lines at $\nu_0 = c/\lambda_0$ with an instantaneous linewidth of $\delta\nu = c\delta\lambda/\lambda^2$, with different mode spacing given by $\Delta\nu_{\mathrm{m},l} = (q_{\mathrm{c}} + l)f_{\mathrm{cav}}(\lambda_0)$. **Bottom:** Monochromatic pulse trains with a carrier wavelength λ_0 and a pulse rate given by $f_{\mathrm{p},l} = \Delta\nu_{\mathrm{m},l} = (q_{\mathrm{c}} + l)f_{\mathrm{cav}}(\lambda_0)$, each corresponding to the spectral line at ν_0 from above.

$q_c + l$,

$$f_l = (q_c + l) f_{cav}(\lambda_l), \tag{5.11}$$

and a wavelength tuning takes place. In this case, the optical spectrum in the middle panel of Fig. 5.6 consists of several spectral lines (5 lines in the diagram) at different optical frequencies ν_l. The modes within each line are locked at different (q_c+l)th harmonic order with spacing given by $\Delta\nu_{m,l} = (q_c + l) f_{cav}(\lambda_l)$. An inverse Fourier transform of the each individual spectral line represents a monochromatic pulse train (5 trains in the diagram) with a carrier wavelength λ_l and a pulse rate given by $f_{p,l} = \Delta\nu_{m,l} = (q_c + l) f_{cav}(\lambda_l)$, perpetually circulating inside the cavity (indicated by the curved arrow at its centre), as depicted in the bottom panel of Fig. 5.6. A superposition of these monochromatic trains in time leads to a pulse train with a carrier wavelength varying over time, shown as snapshots of the optical field inside the cavity at two periods of T_s in the bottom panel of Fig. 5.6.

In order to derive a quantitative formula for the tuning bandwidth $\Delta\lambda_{multi}$ in the multi-harmonic regime in Fig. 5.6, the same summing approach of fractional bandwidths $\Delta\lambda_{l+1,l} = \lambda_{l+1} - \lambda_l$ in Eq. (5.6) will be used. As the modulation frequency is now swept over a range of $\Delta f \gg f_{cav}$, $\Delta\lambda_{l+1,l}$ must be expressed as:

$$\begin{aligned} \Delta\lambda_{l+1,l} &\approx S\left(\frac{f_{l+1} - f_l}{2}\right)[f_{l+1} - f_l - f_{cav}(\lambda_0)] \\ &\approx S\left(\frac{f_{l+1} - f_l}{2}\right)\delta f_s, \end{aligned} \tag{5.12}$$

where $S((f_{l+1} - f_l)/2)$ is the average tuning sensitivity between components f_{l+1} and f_l. $\Delta\lambda_{multi}$ is then given by a summation of all bandwidths $\Delta\lambda_{l+1,l}$:

$$\begin{aligned} \Delta\lambda_{multi} &\approx \sum_{l=-(Q-1)/2}^{(Q-1)/2} \Delta\lambda_{l+1,l} \\ &= \sum_{l=-(Q-1)/2}^{(Q-1)/2} S\left(\frac{f_{l+1} - f_l}{2}\right)\delta f_s, \end{aligned} \tag{5.13}$$

with the total number of tuning bands Q given by Eq. (5.7). Since the modulation signal

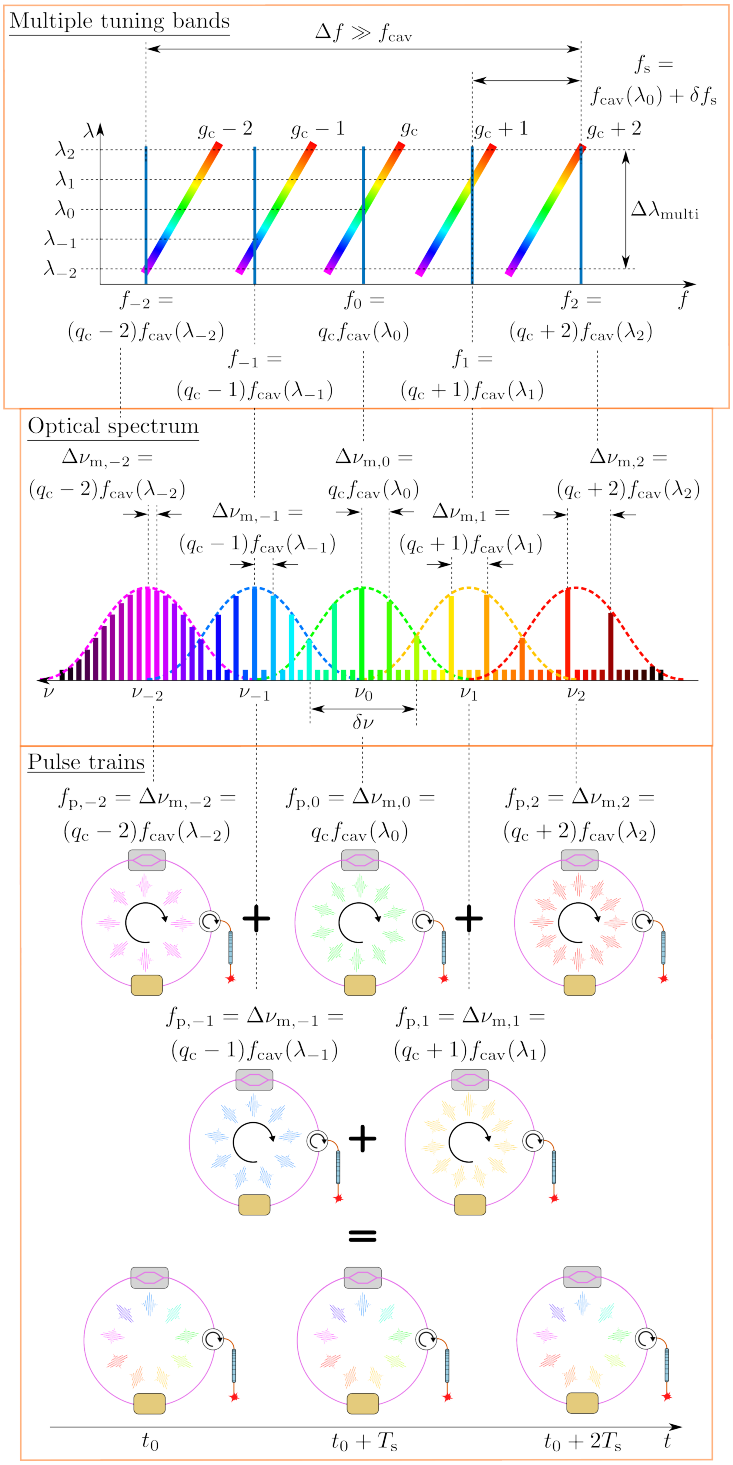

Figure 5.6: Multi-harmonic DTML for the case $f_{\mathrm{s}} = f_{\mathrm{cav}}(\lambda_0) + \delta f_{\mathrm{s}}$. **Top:** Emission wavelength λ as a function of modulation frequency f_l. **Middle:** Optical spectrum consisting of several spectral lines at different optical frequencies $\nu_l = c/\lambda_l$ and an instantaneous linewidth of $\delta\nu = c\delta\lambda/\lambda^2$, with different mode spacing given by $\Delta\nu_{\mathrm{m},l} = (q_{\mathrm{c}} + l) f_{\mathrm{cav}}(\lambda_l)$. **Bottom:** Monochromatic pulse trains with a carrier wavelength λ_l and a pulse rate given by $f_{\mathrm{p},l} = \Delta\nu_{\mathrm{m},l} = (q_{\mathrm{c}} + l) f_{\mathrm{cav}}(\lambda_l)$, each corresponding to a spectral line at ν_l from above.

comb-like spectrum in Fig. 5.3 consists usually of many components f_l, Eq. (5.13) can be further simplified by replacing the sum with an integral with $\mathrm{d}q$ as an infinitesimal variable. By evaluating the integral, a general formula for $\Delta\lambda_{\mathrm{multi}}$ is obtained:

$$\begin{aligned}\Delta\lambda_{\mathrm{multi}} &\approx \int_{-(Q-1)/2}^{(Q-1)/2} S(f)\delta f_{\mathrm{s}}\mathrm{d}q \\ &= -\frac{\delta f_{\mathrm{s}}}{\mathrm{TDD}_{\mathrm{cav}} f_{\mathrm{cav}}^2}\int_{f_0-\Delta f/2}^{f_0+\Delta f/2}\frac{\mathrm{d}f}{f} \\ &= -\frac{\delta f_{\mathrm{s}}}{\mathrm{TDD}_{\mathrm{cav}} f_{\mathrm{cav}}^2}\ln\left(\frac{f_0+\Delta f/2}{f_0-\Delta f/2}\right),\end{aligned} \tag{5.14}$$

where $\mathrm{d}q = \mathrm{d}f/f_{\mathrm{s}} \approx \mathrm{d}f/f_{\mathrm{cav}}$ was used. Remarkably, $\Delta\lambda_{\mathrm{multi}}$ is linearly proportional to δf_{s}. Considering for instance an anomalous dispersive cavity, i.e., when $\mathrm{TDD}_{\mathrm{cav}} > 0$, for $\Delta f > 0$, the laser emission wavelength is tuned in the backward direction for $\delta f_{\mathrm{s}} > 0$, and in the forward direction for $\delta f_{\mathrm{s}} < 0$. The tuning directions are reversed for $\Delta f < 0$. Eq. (5.14) can be further summarized into a simpler linear relation:

$$\Delta\lambda_{\mathrm{multi}} = S'_{\mathrm{multi}}\delta f_{\mathrm{s}}, \tag{5.15}$$

with S'_{multi} denoting the multi-harmonic tuning sensitivity, which generally depends on the cavity dispersion, its length, central modulation frequency f_0, and tuning range Δf. For $\Delta f/(2f_0) \ll 1$, Eq. (5.14) can be linearized in terms of Δf by first order expansion of the logarithm, leading to an approximative relationship, as already reported in [10]:

$$\Delta\lambda_{\mathrm{multi}} \approx -\frac{\Delta f}{\mathrm{TDD}_{\mathrm{cav}} f_{\mathrm{cav}}^2 f_0}\delta f_{\mathrm{s}}. \tag{5.16}$$

5.4 Spectral filtering and dynamic tuning bandwidth limits

Similarly as in the single-harmonic case, the achievable tuning bandwidth $|\Delta\lambda_{\mathrm{multi}}|$ in the multi-harmonic DTML is limited by several factors. The main factor is the gain bandwidth

of the employed SOA and the bandwidths of the other cavity components. Another factor is due to the condition to prevent the laser from the undesired dual wavelength operation. Such a condition provides an estimation for the maximum non-dual wavelength operation multi-harmonic tuning bandwidth $\Delta\lambda_{\text{multi,n-d}}$. In analogy to Eq. (4.14), this can be estimated at the largest modulation frequency of the signal applied to the IM:

$$\Delta\lambda_{\text{multi,n-d}} = \frac{1}{|\text{TDD}_{\text{cav}}|(f_0 + \Delta f/2)}. \tag{5.17}$$

The achievable tuning bandwidth is further limited by the phenomena associated with the high speed of tuning, such as reduction of the output power and coherence length. To examine the multi-harmonic laser dynamic limitations, the scaling guidelines in [11] are adopted for the multi-harmonic DTML as well, with the combination of the cFBG and the IM operating as a tunable spectral filter. Fig. 5.7 graphically depicts such wavelength filtering over a span of a few periods T_{cav}. The carrier wavelength of a specific pulse P in the bottom panel of Fig. 5.7 matches the instantaneous filtered wavelength of the spectral window at the moment the pulse passes through the modulator. Because the spectral window moves at a rate of $f_{\text{s}} = f_{\text{cav}}(\lambda_0) + \delta f_{\text{s}} \approx f_{\text{cav}}$, the whole tuning bandwidth is stored within the cavity at any time. With the same reasoning leading to Eq. (4.15), the saturation laser operation imposes same limit on $\Delta\lambda_{\text{round}}$ in the top panel of Fig. 5.7. The maximum (multi-harmonic) saturation operation tuning bandwidth limit $\Delta\lambda_{\text{multi,sat}}$ can be estimated by substituting $\Delta\lambda_{\text{round}} \approx \Delta\lambda_{\text{multi,sat}} f_{\text{cav}}/|\delta f_{\text{s}}|$ in Eq. (4.15), where $f_{\text{cav}}/|\delta f_{\text{s}}|$ represents the total number of round trips needed for the carrier wavelength of the pulse P to be tuned from λ_{start} to λ_{end} in the multi-harmonic DTML regime (assuming a linear wavelength tuning in the top panel of Fig. 5.7). Rearranging the terms in Eq. (4.15), the saturation operation tuning bandwidth limit $\Delta\lambda_{\text{multi,sat}}$ for $|\Delta\lambda_{\text{multi}}|$ is obtained as:

$$|\Delta\lambda_{\text{multi}}| \lesssim \Delta\lambda_{\text{multi,sat}} \approx \frac{\delta\lambda_{\text{stat}} f_{\text{cav}}}{R_{\text{sat}}|\delta f_{\text{s}}|}. \tag{5.18}$$

However, as derived in Eq. (5.14), $\Delta\lambda_{\text{multi,sat}}$ and δf_{s} are not independent. By substituting for δf_{s} from Eq. (5.14) into Eq. (5.18) and rearranging it, the saturation operation

bandwidth limit is obtained in the form:

$$\begin{aligned} |\Delta\lambda_{\text{multi}}| \lesssim & \Delta\lambda_{\text{multi,sat}} \\ & \approx \left[\frac{\delta\lambda_{\text{stat}}}{R_{\text{sat}}|\text{TDD}_{\text{cav}}|f_{\text{cav}}}\left|\ln\left(\frac{f_0+\Delta f/2}{f_0-\Delta f/2}\right)\right|\right]^{1/2}. \end{aligned} \tag{5.19}$$

The inequality in Eq. (5.19) provides a rough estimation for the maximum $|\Delta\lambda_{\text{multi}}|$ below which the output power and coherence performance are expected to remain comparable to those achieved in the stationary regime. One way to increase the limit is by decreasing f_{cav} through extending the cavity length, while maintaining same $\text{TDD}_{\text{cav}} = D_{\text{fibre}}L_{\text{fibre}} + \text{TDD}_{\text{cFBG}}$ by employing a larger dispersion cFBG. However, this leads to a lower sweep rate, as given by $f_{\text{s}} \approx f_{\text{cav}}$ in the multi-harmonic regime. To raise the limit in Eq. (5.19) while preserving the sweep rate, an easy way would be to increase the logarithm, i.e., to increase Δf. Additionally, the limit can be also slightly raised by optimizing R_{sat}, given by Eq. (4.16), via reducing losses in the cavity by splicing the fibre components in the cavity, for instance.

Another bandwidth limit is obtained when a photon γ of wavelength λ_γ circulating inside the cavity completes on average only one round trip before its wavelength is outside of the sliding spectral window in the middle panel of Fig. 5.7. This imposes a limit on $\Delta\lambda_{\text{round}}$ in the form of Eq. (4.18). The maximum (multi-harmonic) one round trip operation tuning bandwidth limit $\Delta\lambda_{\text{multi,sat}}$ can be estimated by substituting $\Delta\lambda_{\text{round}} \approx \Delta\lambda_{\text{multi,one}}f_{\text{cav}}/|\delta f_{\text{s}}|$ in Eq. (4.18). Rearranging the terms in Eq. (4.18), the one round trip operation tuning bandwidth limit $\Delta\lambda_{\text{multi,one}}$ for $|\Delta\lambda_{\text{multi}}|$ is obtained as:

$$\begin{aligned} |\Delta\lambda_{\text{multi}}| \lesssim & \Delta\lambda_{\text{multi,one}} \\ & \approx \left[\frac{\delta\lambda_{\text{stat}}}{|\text{TDD}_{\text{cav}}|f_{\text{cav}}}\ln\left(\frac{f_0+\Delta f/2}{f_0-\Delta f/2}\right)\right]^{1/2}. \end{aligned} \tag{5.20}$$

To conclude the comparison between the single- and multi-harmonic DTML regimes, Tab. 5.1 lists side by side the main parameters and expressions characterising their operations and tuning performances discussed in this work. The stationary regime linewidth $\delta\lambda_{\text{stat}}$, which appears in Eq. (5.19) and Eq. (5.20), and its dependence on dispersion and modu-

lation window width, is discussed in more detail in Chap. 6.

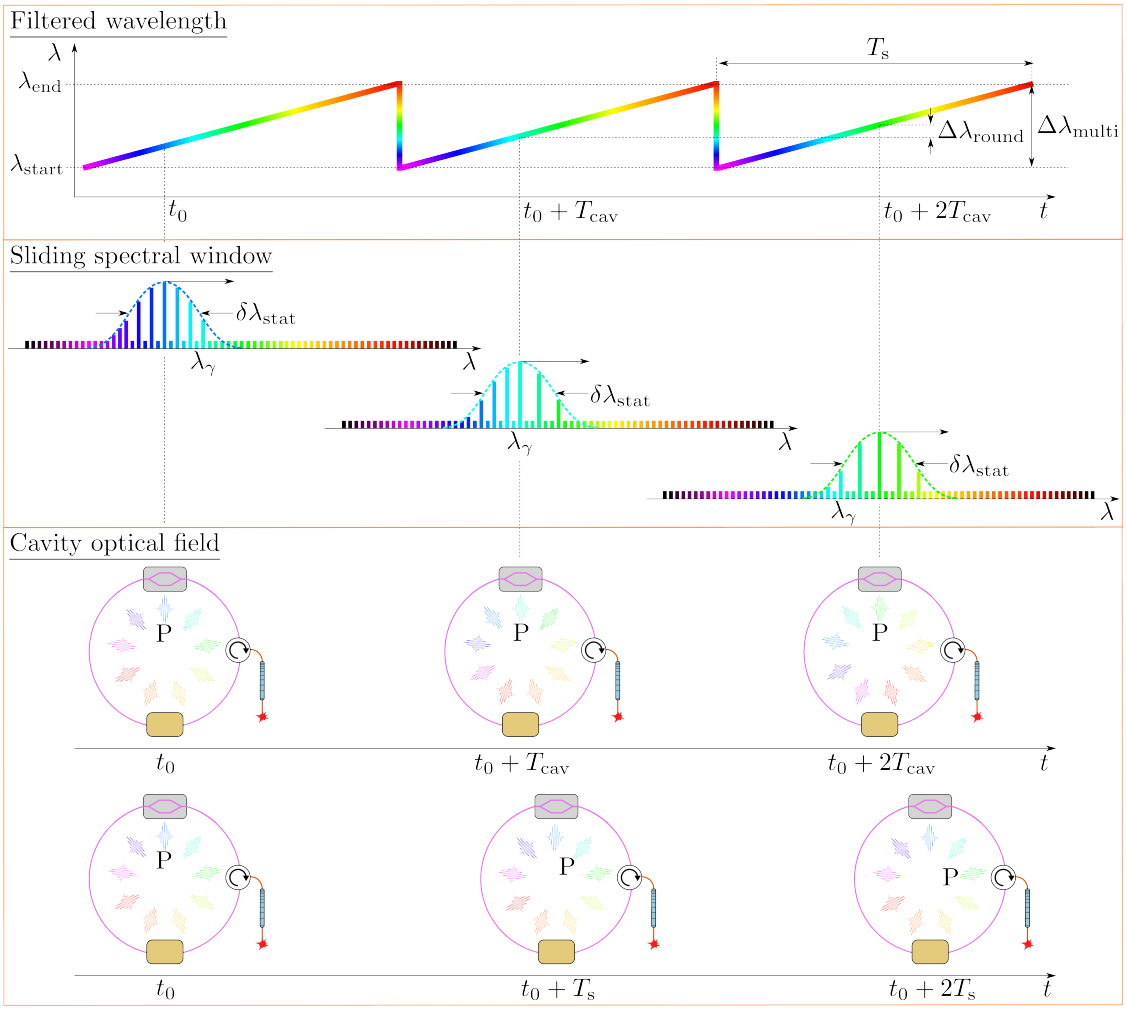

Figure 5.7: Spectral filtering behaviour in the multi-harmonic DTML regime. **Top:** Filtered wavelength as a function of time. Each cavity round trip time T_{cav}, the filtered wavelength is tuned by $\Delta\lambda_{\text{round}}$. **Middle:** Snapshots of the sliding spectral window separated in time by T_{cav}. The window filters only the modes mode-locked in Fig. 5.6. $\delta\lambda_{\text{stat}}$ is the bandwidth of the filter and λ_γ is the wavelength of a photon γ circulating inside the cavity. **Bottom:** Snapshots of the cavity optical field separated in time by T_{cav} and T_{s}, with a specific pulse P circulating inside the cavity. The drawings are inspired by [4, 11, 12].

5.5 Comparison of the multi-harmonic DTML with FDML

One prominent feature of the multi-harmonic tuning in Fig. 5.7 is that, because $f_s \approx f_{cav}$, the spectral window is tuned so fast that light (a photon of wavelength λ_γ in Fig. 5.7), when arrives back at the modulator after a round trip inside the cavity, is filtered in the next tuning cycle (see the top panel in Fig. 5.7). This means that approximately $f_{cav}/|\delta f_s|$ tuning cycles are needed for the pulse P carrier wavelength to be tuned from λ_{start} to λ_{end}, unlike in the single-harmonic DTML in Fig. 5.4, where the light is filtered within a single tuning cycle. As the laser is tuned at a sweep rate close to the fundamental frequency of the cavity, the whole wavelength bandwidth is stored inside the cavity at any time. This feature makes the multi-harmonic DTML regime similar to a quasi-FDML operation [4, 12]. A comparison of the optical fields stored inside a single-harmonic, a multi-harmonic DTML, and a FDML cavity is graphically depicted in Fig. 5.8. Nevertheless, some differences between the two regimes can be identified. First, the cFBG-modulator pair in the multi-harmonic DTML creates an akinetic "virtual" spectral filter, while a mechanical tunable FP filter in FDML is employed. However, the akinetic filtering mechanism in DTML is generally less selective than the narrowband filters used in FDML systems or the single-mode operation of MEMS-VCSELs, limiting coherence lengths to a few millimeters [1, 10, 13, 14]. Second, as the mode-locking is achieved via the modulator, the optical field in a DTML cavity consists of short pulses with the repetition rate of the modulation frequency f, whereas optical field in an FDML cavity is in the form of long chirped pulses with a period comparable to T_s. Finally, a DTML cavity is inherently dispersive, inflicting a time delay between a pulse and the modulation window, needed for the wavelength tuning. This means that the number of round trips of a photon inside the cavity before it is blocked by the spectral filter decreases with increasing sweep rate. This is different from FDML, where, if dispersion is well compensated, a large number of round trips for a photon is achieved. This drawback is to some extent compensated by a low complexity and much lower cost of a multi-harmonic DTML cavity in comparison to an FDML cavity, where dispersion must be accurately brought to zero. In DTML, on

the other hand, dispersion in the cavity is necessary for the wavelength tuning, but its value does not have to be accurately managed (as long as it is $\gtrsim 10\,\mathrm{ps/nm}$). Due to the mechanical nature of tunable FP filters and their tuning speed limitations typically up to a few hundred kHz, buffering technique [12] is employed to extend the sweep rate into the MHz range. This further increases both the complexity and cost of an FDML system. As DTML is inherently akinetic without mechanical moving parts, no buffering is needed to achieve MHz sweep rates (provided that conditions for the saturation and one trip operations given by Eq. (5.19) and Eq. (5.20), respectively, are satisfied). In addition, DTML can exhibit linear-in-wavenumber tuning by tailoring the voltage signal applied to the VCO, and so eliminating the need for k-clock triggering or post-processing linearisation procedures [15, 16]. The comparison of the main parameters and terms between multi-harmonic DTML and FDML lasers is summarized in Tab. 5.2.

Table 5.1: Comparison of the main parameters and expressions characterising the single- and multi-harmonic DTML regimes.

Parameter	**Single-harmonic DTML**	**Multi-harmonic DTML**
Cavity length	$L_{\mathrm{cav}} \lesssim 10\,\mathrm{m}$	$L_{\mathrm{cav}} \sim 100\text{-}1000\,\mathrm{m}$
Cavity dispersion	$\mathrm{TDD}_{\mathrm{cav}} \gtrsim 10\,\mathrm{ps/nm}$	$\mathrm{TDD}_{\mathrm{cav}} \gtrsim 10\,\mathrm{ps/nm}$
Modulation frequency range	$\Delta f \leq f_{\mathrm{cav}}$	$\Delta f \gg f_{\mathrm{cav}}$
Sweep rate	$f_{\mathrm{s}} \ll f_{\mathrm{cav}}$	$f_{\mathrm{s}} \approx f_{\mathrm{cav}}$
Tuning bandwidth	$\lvert\Delta\lambda_{\mathrm{single}}\rvert = \dfrac{1}{\lvert\mathrm{TDD}_{\mathrm{cav}}\rvert f_{\mathrm{cav}} f_0}\lvert\Delta f\rvert$	$\lvert\Delta\lambda_{\mathrm{multi}}\rvert = \dfrac{\lvert\delta f_{\mathrm{s}}\rvert}{\lvert\mathrm{TDD}_{\mathrm{cav}}\rvert f_{\mathrm{cav}}^2}\left\lvert\ln\left(\dfrac{f_0+\Delta f/2}{f_0-\Delta f/2}\right)\right\rvert$
Saturation operation tuning bandwidth limit	$\Delta\lambda_{\mathrm{single,sat}} \approx \dfrac{\delta\lambda_{\mathrm{stat}} f_{\mathrm{cav}}}{R_{\mathrm{sat}} f_{\mathrm{s}}}$	$\Delta\lambda_{\mathrm{multi,sat}} \approx \left[\dfrac{\delta\lambda_{\mathrm{stat}}}{R_{\mathrm{sat}}\lvert\mathrm{TDD}_{\mathrm{cav}}\rvert f_{\mathrm{cav}}}\left\lvert\ln\left(\dfrac{f_0+\Delta f/2}{f_0-\Delta f/2}\right)\right\rvert\right]^{1/2}$
One round trip operation tuning bandwidth limit	$\Delta\lambda_{\mathrm{single,one}} \approx \dfrac{\delta\lambda_{\mathrm{stat}} f_{\mathrm{cav}}}{f_{\mathrm{s}}}$	$\Delta\lambda_{\mathrm{multi,one}} \approx \left[\dfrac{\delta\lambda_{\mathrm{stat}}}{\lvert\mathrm{TDD}_{\mathrm{cav}}\rvert f_{\mathrm{cav}}}\left\lvert\ln\left(\dfrac{f_0+\Delta f/2}{f_0-\Delta f/2}\right)\right\rvert\right]^{1/2}$

Table 5.2: Summary of the comparison of the key parameters and architectures between the multi-harmonic DTML and FDML. The information related to FDML lasers is primarily based on [12].

Parameter/architecture	**Multi-harmonic DTML**	**FDML**
Cavity length	$L_{\text{cav}} \sim 100\,\text{m}$	$L_{\text{cav}} \sim 100\text{-}1000\,\text{m}$
Tunable element	Combination of mode-locking and dispersive element	FP tunable filter
Cavity dispersion	$\text{TDD}_{\text{cav}} \gtrsim 10\,\text{ps/nm}$	$\text{TDD}_{\text{cav}} \doteq 0\,\text{ps/nm}$
Synchronisation with the cavity round trip time	Slightly off	Exactly synchronised
Mode-locking orders	Multiple	Single
Optical field	Short pulses with a rate given by the modulation frequency $f_{\text{p}} \approx f$	Long pulses with a rate comparable to the sweep frequency $f_{\text{p}} \sim f_{\text{s}}$
Coherence length	Units of mm	Units of cm
Sweep linearity	Programmable sweep profile	Linear interval of a sinusoidal sweep profile
Dominant jitter source	Modulation source frequency/phase noise	FP filter synchronisation
Jitter tolerance	Moderate (reasonable spectral purity of the modulation source)	Very low (picosecond-level synchronisation)
Cavity complexity	Large modulation range Δf, polarisation control	Precise synchronisation, dispersion compensation, polarisation and temperature control, buffering

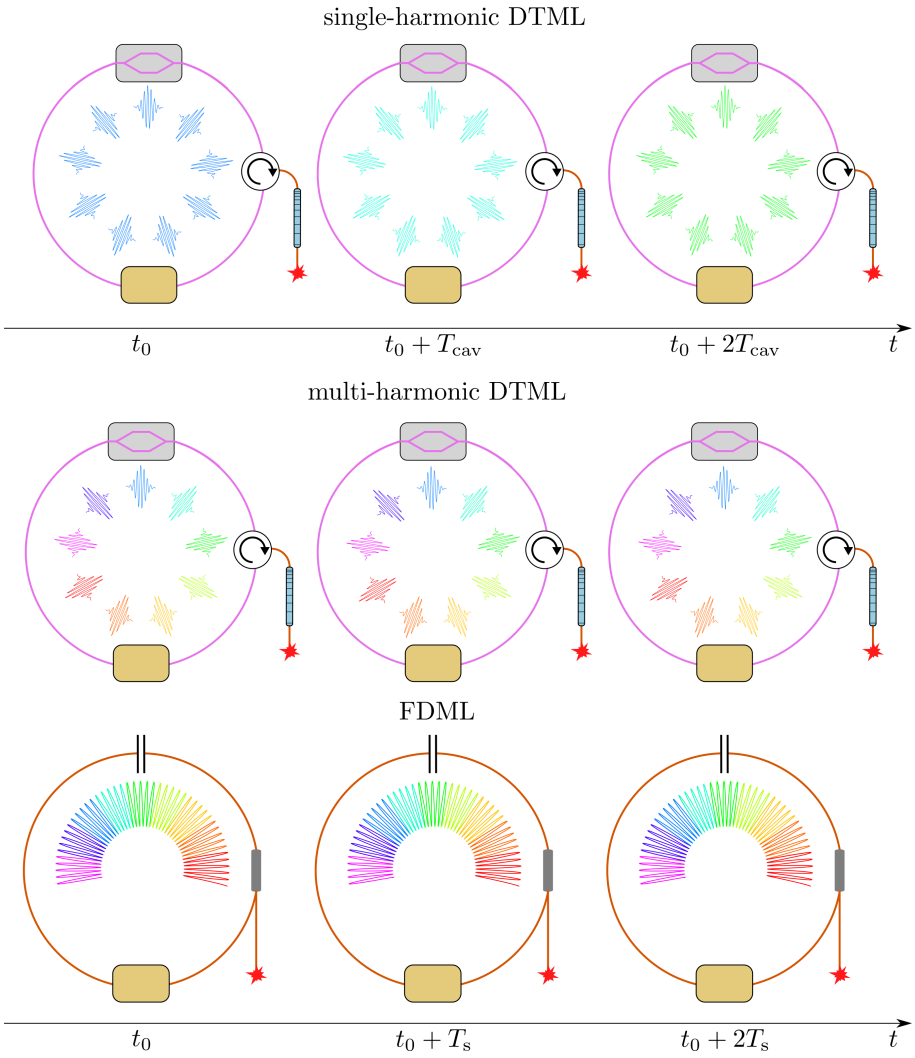

Figure 5.8: Comparison of the optical fields stored inside a single-harmonic, multi-harmonic DTML, and FDML cavity as snapshots separated in time by T_{s}.

Bibliography

[1] R. Riha, A. M. Jimenez, and A. Podoleanu, "Comprehensive theoretical model for multi-harmonic dispersion-tuned mode-locking (DTML) for use in swept-source OCT," *Opt. Express*, vol. 33, no. 19, pp. 40 969–40 996, Sep 2025.

[2] R. F. Stancu and A. G. Podoleanu, "Dual-mode-locking mechanism for an akinetic dispersive ring cavity swept source," *Opt. Lett.*, vol. 40, no. 7, pp. 1322–1325, Apr 2015.

[3] F. Toadere, R.-F. Stancu, W. Poon, D. Schultz, and A. Podoleanu, "1 MHz akinetic dispersive ring cavity swept source at 850 nm," *IEEE Photonics Technology Letters*, vol. 29, no. 11, pp. 933–936, 2017.

[4] R. Huber, M. Wojtkowski, and J. G. Fujimoto, "Fourier domain mode locking (FDML): A new laser operating regime and applications for optical coherence tomography," *Opt. Express*, vol. 14, no. 8, pp. 3225–3237, Apr 2006.

[5] U. Keller, *Ultrafast Lasers: A Comprehensive Introduction to Fundamental Principles with Practical Applications*, ser. IOP Series in Coherent Sources, Quantum Fundamentals, and Applications. IOP Publishing, 2021.

[6] A. Takada, M. Fujino, and S. Nagano, "Dispersion dependence of linewidth in actively mode-locked ring lasers," *Opt. Express*, vol. 20, no. 4, pp. 4753–4762, Feb 2012.

[7] A. Takada, M. Saika, and S. Nagano, "Effect of linewidth enhancement factor in actively mode-locked ring laser," in *Fiber Lasers XI: Technology, Systems, and Applications*, vol. 8961, International Society for Optics and Photonics. SPIE, 2014, p. 896135.

[8] H. Nagai and S. Yamashita, "Coherence improvement in dispersion-tuned swept laser by pulse modulation," *Electronics Letters*, vol. 50, no. 23, pp. 1729–1731, 2014.

[9] Y. Hasegawa, T. Shirahata, and S. Yamashita, "Analysis of dynamic properties of dispersion-tuned swept lasers," *Journal of Lightwave Technology*, vol. 33, no. 1, pp. 219–226, 2015.

[10] R. Riha, A. Bradu, and A. Podoleanu, "Dual resonance akinetic dispersive cavity swept source at 900 kHz using a cFBG and an intensity modulator," *Opt. Lett.*, vol. 47, no. 16, pp. 4032–4035, Aug 2022.

[11] R. Huber, M. Wojtkowski, K. Taira, J. G. Fujimoto, and K. Hsu, "Amplified, frequency swept lasers for frequency domain reflectometry and OCT imaging: design and scaling principles," *Opt. Express*, vol. 13, no. 9, pp. 3513–3528, May 2005.

[12] R. Huber, "FDML (incl. parallelization)," in *Optical Coherence Tomography*, W. Drexler and J. G. Fujimoto, Eds. Berlin, Heidelberg: Springer, 2015, pp. 741–787.

[13] H. D. Lee, G. H. Kim, J. G. Shin, B. Lee, C.-S. Kim, and T. J. Eom, "Akinetic swept-source optical coherence tomography based on a pulse-modulated active mode locking fiber laser for human retinal imaging," *Sci Rep*, vol. 8, p. 17660, 2018.

[14] R. Riha, A. M. Jimenez, G. Venugopal, M. Klufts, R. Huber, and A. Podoleanu, "Dispersion-tuned mode-locked laser for swept source oct at 850 nm using a cfbg and the pulse modulation technique," *IEEE Photonics Journal*, vol. 16, no. 4, pp. 1–5, 2024.

[15] H. D. Lee, M. Y. Jeong, C.-S. Kim, J. G. Shin, B. H. Lee, and T. J. Eom, "Linearly wavenumber-swept active mode locking short-cavity fiber laser for in-vivo OCT imaging," *IEEE Journal of Selected Topics in Quantum Electronics*, vol. 20, no. 5, pp. 433–440, 2014.

[16] H. Lee, G. H. Kim, M. Villiger, H. Jang, B. E. Bouma, and C.-S. Kim, "Linear-in-wavenumber actively-mode-locked wavelength-swept laser," *Opt. Lett.*, vol. 45, no. 19, pp. 5327–5330, Oct 2020.

Chapter 6

Mathematical modelling in DTML lasers

Mathematical modelling assists in analysing the various physical phenomena inside a laser cavity and their effects on the lasing properties. Two mathematical frameworks have been developed for rigorous modelling of DTML lasers: the average model and the discrete model. Both models are here appropriately described, and a refined extension of the discrete model, also referred to as the iterative mapping, is utilised for the numerical simulations presented in the last part of this chapter. These simulations are used to investigate the behaviour of the stationary stationary regime linewidth $\delta\lambda_{\mathrm{stat}}$, which appears in the expressions for dynamic tuning bandwidth limits in Eq. (4.16), Eq. (4.17), Eq. (4.19), Eq. (5.19), and Eq. (5.20), as a function of various cavity parameters.

6.1 Complex envelope and temporal chirp

For the mathematical modelling presented in this chapter, a scalar approach will be adopted, assuming that the optical field maintains its polarisation state inside the fibre cavity. While this assumption does not strictly hold unless a polarisation-maintaining fibre is used, it is nevertheless a reasonable approximation in practice assuming that the shape of the pulse does not change too rapidly compared to the carrier frequency [1, 2]. Within

this approach, the scalar optical field $E(z,t)$ propagating along fibre can be expressed as:

$$E(z,t) = A(z,t)\exp[\mathrm{i}(\beta_0 z - \omega_\mathrm{c} t)], \tag{6.1}$$

where $A(z,t)$ is the slowly varying envelope of the field. This representation does not include the spatial modal distribution, which, in the case of single-mode fibre, can typically be approximated by a simple Gaussian profile [3].

The envelope $A(z,t)$ in Eq. (6.1) is inherently complex, containing information about both amplitude $|A(z,t)|$ as well as the temporal phase distribution of the field $\phi(z,t) = \arg[A(z,t)]$. For example, a complex Gaussian shape envelope at $z = z_0$ with a linear phase chirp C has a mathematical form [1, 4]:

$$A(z_0,t) = A_0 \exp\left(-\frac{1+\mathrm{i}C}{2\tau_0^2}t^2\right) = A_0 \exp\left[-\frac{2\ln 2}{\tau_\mathrm{p}^2}(1+\mathrm{i}C)t^2\right], \tag{6.2}$$

where τ_0 and $\tau_\mathrm{p} = 2\sqrt{\ln 2}\tau_0$ are the pulse 1/e half width and FWHM pulse width, respectively. A general temporal chirp $\delta\Omega(t)$ may be nonlinear and is defined as [5]:

$$\delta\Omega(t) = -\frac{\mathrm{d}\phi(t)}{\mathrm{d}t}, \tag{6.3}$$

where the minus sign arises from the $\exp(-\mathrm{i}\omega_\mathrm{c}t)$ convention used in Eq. (6.1). For the case of a linearly chirped Gaussian pulse given by Eq. (6.2), the chirp parameter C is related to the temporal chirp $\delta\Omega(t)$ in Eq. (6.3) via $C = -\delta\Omega(t)\tau_\mathrm{p}^2/(4\ln 2\, t)$.

Lastly, for the calculations of the envelope spectrum $\widetilde{A}(z,\Omega)$, the forward $\mathcal{F}\{A(z,t)\}$ and the inverse $\mathcal{F}^{-1}\{A(z,t)\}$ Fourier transform operators will be defined as follows:

$$\begin{aligned} \widetilde{A}(z,\Omega) = \mathcal{F}\{A(z,t)\} &\equiv \int_{-\infty}^{+\infty} A(z,t)\exp(\mathrm{i}\Omega t)\mathrm{d}t, \\ A(z,t) = \mathcal{F}^{-1}\{\widetilde{A}(z,\Omega)\} &\equiv \frac{1}{2\pi}\int_{-\infty}^{+\infty} \widetilde{A}(z,\Omega)\exp(-\mathrm{i}\Omega t)\mathrm{d}\Omega, \end{aligned} \tag{6.4}$$

where $\Omega = \omega - \omega_\mathrm{c}$ represents the optical frequency offset from the carrier frequency ω_c.

6.2 Average model

In the average model, it is assumed that a pulse experiences only small perturbations while propagating inside a laser cavity. The primary equation used to describe the evolution of the slowly varying pulse envelope A along fibre is the nonlinear Schrödinger equation (NLSE) [1, 2, 6]. For the pulse envelope analysis purposes, the NLSE is typically transformed into a reference frame moving with the pulse at the group velocity v_g by introducing the retarded time variable $T = t - z/v_\mathrm{g}$. In this frame, the NLSE takes a form:

$$\frac{\partial A}{\partial z} = \left(-\frac{\rho}{2} - \mathrm{i}\frac{\beta_2}{2}\frac{\partial^2}{\partial T^2} + \mathrm{i}\gamma|A|^2 \right) A. \tag{6.5}$$

NLSE in Eq. (6.5) comprises three main phenomena affecting the pulse propagating in fibre: attenuation, dispersion, and Kerr effect, represented by the symbols ρ, β_2, γ, respectively. Higher-order dispersions and higher-order nonlinear effects can be neglected in the NLSE for pulses much longer than 5 ps [1]. Examples of higher-order nonlinear effects are self-steepening, resulting from the intensity dependence of the group velocity, and Raman scattering, causing spectral red shift [1, 2]. These higher-order effects leads to significant asymmetric distortions of the pulse and its spectrum.

In DTML lasers, pulses durations typically extend from tens of picoseconds to units of nanoseconds.

It is useful to introduce two length scales, the dispersion length, L_d, and the nonlinear length, L_nl, defined as [1]:

$$L_\mathrm{d} = \frac{\tau_0^2}{|\beta_2|}, \quad L_\mathrm{nl} = \frac{1}{\gamma P_\mathrm{peak}}, \tag{6.6}$$

where P_peak denotes the pulse peak power. L_d and L_nl provide length scales over which dispersive or nonlinear effects become important for the pulse evolution. Depending on relative magnitudes of the fibre length L and lengths L_d and L_nl, the propagation behaviour can be classified into distinct categories, more detailed in Sec. 6.3.

For its fundamental importance in the theory of pulse propagation and applications, it is worth to note a soliton form solution of Eq. (6.5) given by [1, 2]:

$$A(\xi, T) = \eta \,\mathrm{sech}(\eta T/\tau_0) \exp(\mathrm{i}\eta^2\xi/2), \tag{6.7}$$

where η is the soliton parameter. Soliton pulses are formed as a result of certain interplay between dispersive and nonlinear effects, and can propagate undistorted over long distances.

To describe the actual pulse propagation inside a DTML fibre cavity, Eq. (6.5) must be generalised to include gain and amplitude modulation as well. This generalised NLSE, also known as Ginzburg–Landau master equation of mode-locking, averages all effects in the cavity over its length (hence the "average" model). Assuming that an SOA is employed as the gain medium, the commonly used form of the master equation for an actively mode-locked cavity is [7, 8]:

$$\frac{\partial A}{\partial z} = \left[\frac{g}{2}(1 - \mathrm{i}\alpha) - \frac{\rho}{2} - \frac{\mathrm{i}}{2}\beta_2\frac{\partial^2}{\partial T^2} - 2\pi^2 M f^2 T^2 + \mathrm{i}\gamma|A|^2\right] A. \tag{6.8}$$

The individual colours in Eq. (6.8) mark these cavity effects:

- Gain, where α is the linewidth enhancement factor, representing the nonlinear effects in the gain medium, and g is the gain, following its own differential equation:

$$\frac{\partial g}{\partial T} = \frac{g_{\mathrm{small}}}{\tau_{\mathrm{c}}} - \frac{g}{\tau_{\mathrm{eff}}} - \frac{|A|^2}{E_{\mathrm{sat}}}[\exp(g) - 1], \tag{6.9}$$

  where g_{small} is the small signal gain, τ_{c} and τ_{eff} are the carrier lifetime and the effective gain recovery time, respectively, and E_{sat} is the saturation energy of the SOA.

- Losses, where ρ sums all losses in the cavity, including coupling.

- Dispersion, where β_2 is the effective group velocity dispersion of the cavity (see Sec. 4.1).

- Modulation, which approximates sinusoidal modulation with the modulation depth of M and the modulation frequency of f.

- Nonlinear fibre effects, where γ is the fibre nonlinear coefficient.

The individual cavity processes in Eq. (6.8) and their effect on pulse propagation will be more detailed in the next section. No general analytical solution is known for Eq. (6.8),

however a big group of solutions resemble chirped Gaussian or chirped hyperbolic secant profiles like in Eq. (6.2) and Eq. (6.7). These profiles are perturbed to the extent of the relative magnitudes of the terms in Eq. (6.8) [6].

6.3 Discrete model

While the origin of Eq. (6.8) arises from the historical development of mathematical modelling for mode-locking, it does not precisely represent the real pulse propagation inside a laser cavity. As previously noted, the average model assumes that each physical process in Eq. (6.8) is distributed and averaged over the entire cavity length. However, as seen in the cavity configurations discussed in Sec. 4.4, many processes, such as amplification and modulation, are spatially localised, which occur exclusively inside the gain medium and the modulation element, respectively. A more realistic representation of a laser cavity is achieved by modelling each physical process independently. In this discrete model, it is assumed that inside each laser element, only one dominant physical process (or the most dominant processes) affects the pulse, while all others are negligible. For each cavity element, the general master equation in Eq. (6.8) is reduced to describe only one effect on the pulse propagation (Subsecs. 6.3.1, 6.3.4, 6.3.5, and 6.3.6). If more physical processes must be included to appropriately describe the effects of the cavity element on the pulse propagation, the more terms are retained in the equation (Subsecs. 6.3.2 and 6.3.3). The relationship between the input and output pulse in each element is described by a transfer function. These transfer functions are then concatenated in a sequence, following the order of the cavity elements through which the pulse propagates. This discrete description provides more intuitive and physically accurate modelling compared to the averaging approach in Eq. (6.8). The discrete model has been employed in several reports on DTML lasers [8–10], demonstrating as well good agreement with experimental results. However, in those studies, while the transfer functions were suitably chosen to reflect the effects observed in the laboratory, they were selected rather phenomenologically, not necessarily derived directly from the underlying physics. More recently, a refined formulation known as iterative functional mapping has been proposed [11], in which a generalised NLSE

(such as Eq. (6.8)) is applied to each cavity element individually. In the following, the mathematical forms of the individual transfer functions are derived, and their effects on pulse propagation are described in detail.

6.3.1 Loss

One inevitable characteristic of a fibre cavity is the presence of losses. These can originate from intrinsic fibre attenuation, insertion losses in fibre components, or coupling losses. From the perspective of pulse propagation, if the fibre length L satisfies $L \ll L_{\mathrm{d}}$ and $L \ll L_{\mathrm{nl}}$, as defined in Eq. (6.6), the fibre acts as a mere transporter, except for reducing the pulse energy due to the fibre attenuation. Under these conditions, both dispersion and nonlinear effects play a minor role, and the NLSE in Eq. (6.5) is reduced so it only includes the attenuation factor ρ, easily solved analytically:

$$\frac{\partial A}{\partial z} = -\frac{\rho}{2}A \quad \Longrightarrow \quad A = A_0 \exp(-\rho L/2), \tag{6.10}$$

where A_0 denotes the input pulse envelope and L is the propagation length. For optical components, the loss transfer function $\mathcal{L}_{\mathrm{comp}}\{A\}$ is implemented as a scalar multiplication of the pulse envelope by the component insertion loss:

$$\mathcal{L}_{\mathrm{comp}}\{A\} \equiv \sqrt{1 - l_{\mathrm{comp}}}A \quad \text{or} \quad \mathcal{L}_{\mathrm{comp}}\{A\} \equiv 10^{-l_{\mathrm{comp,dB}}/10}A, \tag{6.11}$$

where l_{comp} is the fractional power loss and $l_{\mathrm{comp,dB}}$ is the insertion loss in decibels. For a cFBG with power reflectivity R_{cFBG}, the loss transfer function is defined as:

$$\mathcal{L}_{\mathrm{cFBG}}\{A\} \equiv \sqrt{R_{\mathrm{cFBG}}}A. \tag{6.12}$$

The effect of loss on pulse propagation is straightforward, resulting only in a reduction in the pulse peak power (or energy) without altering its shape, as illustrated in Fig. 6.1, where P_{in} is the input pulse peak power.

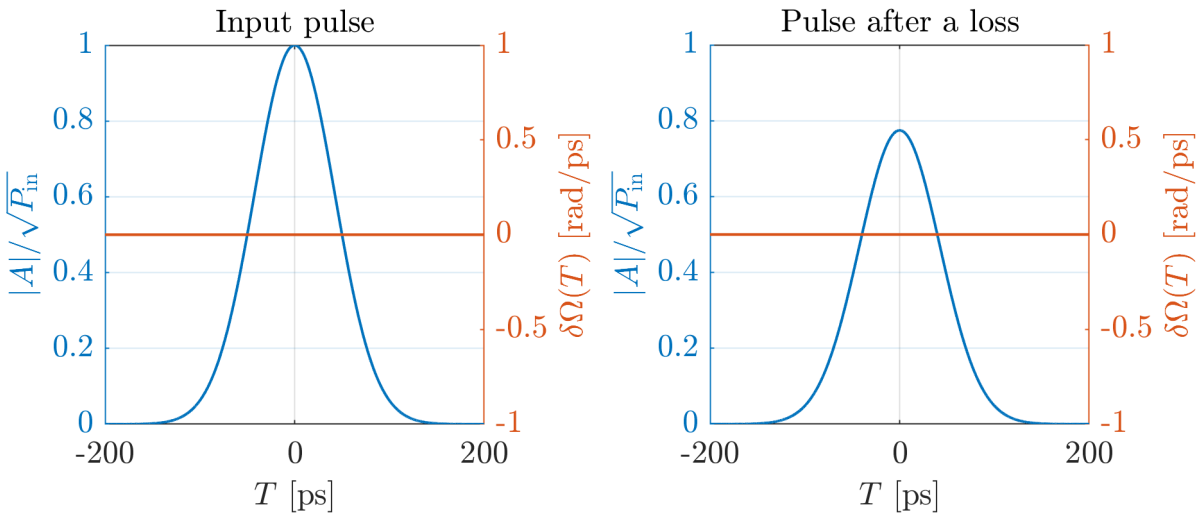

Figure 6.1: The effect of loss on pulse propagation. Strong loss is applied for illustrative purposes.

6.3.2 Dispersion

An essential parameter for DTML operation is high cavity dispersion, which originate from fibre or a cFBG. If the fibre length L satisfies $L \sim L_{\mathrm{d}}$ but $L \ll L_{\mathrm{nl}}$, as defined in Eq. (6.6), the nonlinear term in Eq. (6.5) is negligible compared to the other two. Under these conditions, pulse propagation along the fibre is governed by a simplified equation:

$$\frac{\partial A}{\partial z} = \left(-\frac{\rho}{2} - \mathrm{i}\frac{\beta_2}{2}\frac{\partial^2}{\partial T^2} \right) A. \tag{6.13}$$

Using standard techniques for solving linear partial differential equations in the frequency domain, Eq. (6.13) is solved analytically [2]:

$$A = \exp(-\rho L/2)\mathcal{F}^{-1}\{\exp(\mathrm{i}\Omega^2\beta_2 L/2)\mathcal{F}\{A_0\}\}. \tag{6.14}$$

In short cavities characteristic to 2nd and 3rd generations DTML lasers, dispersion is dominated by a cFBG, while the dispersion due to the fibre is negligible in comparison. The dispersion transfer function $\mathcal{D}_{\mathrm{cFBG}}\{A\}$ for a cFBG characterised by its group delay dispersion $\mathrm{GDD}_{\mathrm{cFBG}}$ is defined as:

$$\mathcal{D}_{\mathrm{cFBG}}\{A\} \equiv \mathcal{F}^{-1}\{\exp(\mathrm{i}\Omega^2\mathrm{GDD}_{\mathrm{cFBG}}/2)\mathcal{F}\{A\}\}. \tag{6.15}$$

Two principal effects on pulse propagation inside a dispersive medium are observed in Fig. 6.2. First, due to the varying phase delays experienced by different spectral components in Eq. (6.15), the pulse obtains a temporal chirp, essential for DTML operation [8]. Second, as the spectral components are delayed to each other, the pulse broadens correspondingly. For an initially unchirped Gaussian pulse with temporal width τ_0 as an input, propagating inside fibre of length L, the width τ_1 and temporal chirp $\delta\Omega_1(T)$ of the output pulse can be found analytically as [1]:

$$\tau_1 \approx \tau_0 \sqrt{\left(1 + \frac{L|\beta_2|}{\tau_0^2}\right)}, \quad \delta\Omega_1(T) \approx \frac{\mathrm{sgn}(\beta_2)(2L|\beta_2|/\tau_0^2)}{1 + (2L|\beta_2|/\tau_0^2)^2} \frac{T}{\tau_0^2}. \tag{6.16}$$

When a cFBG is used instead of fibre, $L|\beta_2|$ in Eq. (6.16) is replaced with $\mathrm{GDD}_{\mathrm{cFBG}}$. The analytical expression for $\delta\Omega_1(T)$ implies that the pulse undergoes a temporal chirp linear in T. Both the temporal chirp and pulse broadening are inherently accounted for in the dispersion transfer function in Eq. (6.15), with a freedom of an arbitrary input pulse shape A.

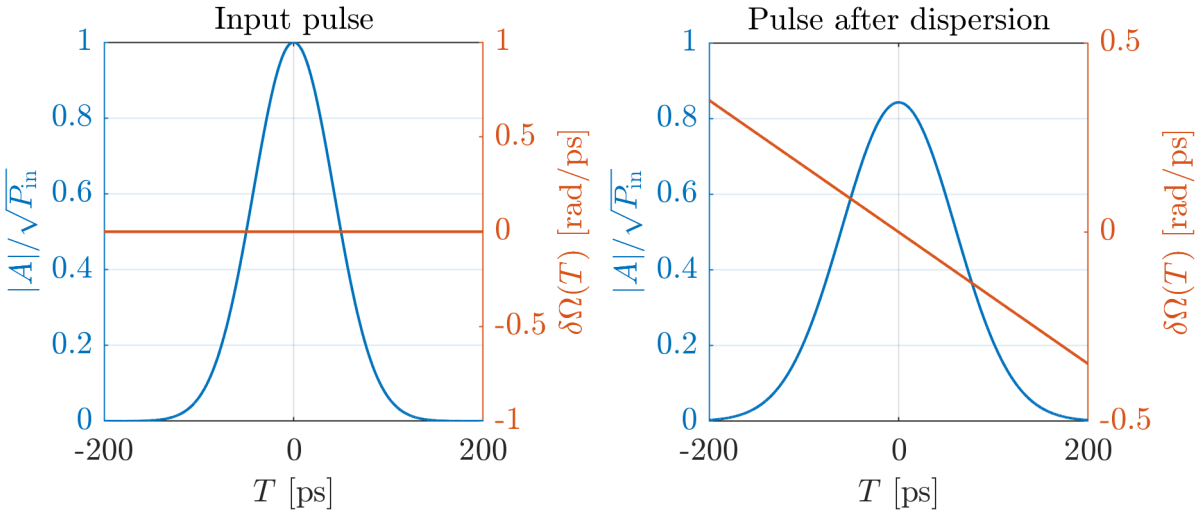

Figure 6.2: The effects of dispersion on pulse propagation. Strong dispersion for illustrative purposes.

6.3.3 Fibre delay

When the fibre length L is comparable to both L_{d} and L_{nl}, as defined in Eq. (6.6), both dispersion and nonlinearity must be taken into account, and pulse propagation is described by the fibre NLSE given by Eq. (6.5). Assuming the pulse peak power is $P_{\mathrm{peak}} \lesssim 1\,\mathrm{W}$, which is typical in DTML lasers designed for SS-OCT [7, 8, 10] and in which case self-steepening can be neglected [12], Eq. (6.5) can be solved semi-analytically. The resulting fibre propagation transfer function $\mathcal{P}\{A\}$ is then given by [12]:

$$\mathcal{P}\{A\} \equiv \exp(-\rho L/2)\mathcal{F}^{-1}\{\exp(\mathrm{i}\phi_{\mathrm{lin}})\mathcal{F}\{A\exp(\mathrm{i}\phi_{\mathrm{nl}})\}\}. \tag{6.17}$$

where the linear ϕ_{lin} and nonlinear ϕ_{nl} phase delays are defined as:

$$\phi_{\mathrm{lin}} = \frac{\Omega^2\beta_2 L}{2}, \quad \phi_{\mathrm{nl}} = \gamma\left[\frac{1-\exp(-\rho L/2)}{\rho}\right]|A|^2, \tag{6.18}$$

where ϕ_{nl} accounts for self-phase modulation (SPM), an intensity-induced phase shift originating in optical Kerr effect [1, 2, 6]. The Kerr effect refers to the intensity-dependent index of refraction $n(I)$:

$$n(I) = n + n_{\mathrm{nl}}I, \tag{6.19}$$

where n_{nl} is the nonlinear index of refraction and I is the optical intensity. The fibre nonlinear coefficient γ appearing in Eq. (6.5), Eq. (6.8), and Eq. (6.18)is then defined as [1]:

$$\gamma = \frac{n_{\mathrm{nl}}\omega_0}{cA_{\mathrm{eff}}}, \tag{6.20}$$

where A_{eff} is known as the effective core area of the fibre.

In the previous reports on mathematical modelling of DTML lasers [7, 8, 10, 13, 14], fibre delay and its effects on pulse propagation were typically neglected. These studies focused only on short cavity 2nd and 3rd generations lasers (see Subsec. 4.4.2 and 4.4.3), where dispersion is dominated by a cFBG and its effect is modelled by the transfer function given by Eq. (6.15). In contrast, the generalised model developed here, with the fibre delay transfer function defined by Eq. (6.17), is also applicable to the long cavity 1st generation

lasers (see Subsec. 4.4.1) and, in particular, multi-harmonic DTML lasers described in Chap. 5.

The effects of a fibre delay on pulse propagation are illustrated in Fig. 6.3. An initial unchirped pulse obtains mostly a linear chirp due to the dispersion, with a small nonlinear contribution from the SPM and a reduction in the pulse peak power due to the fibre attenuation.

For the sake of completeness, if the fibre length is such that $L \ll L_\mathrm{d}$ but $L \sim L_\mathrm{nl}$, the dispersion term in Eq. (6.5) is negligible relative to the nonlinear term. In this regime, the reduced fibre NLSE containing only the SPM term can be solved analytically as:

$$\frac{\partial A}{\partial z} = \mathrm{i}\gamma|A|^2 A \Longrightarrow A = \exp(\mathrm{i}\gamma|A|^2 L). \tag{6.21}$$

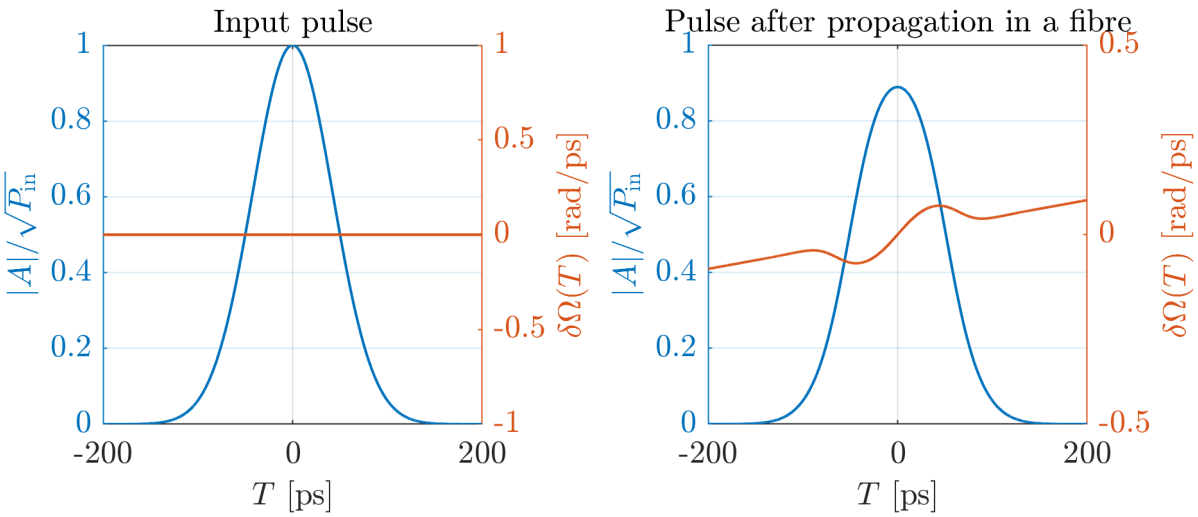

Figure 6.3: The effects of a fibre delay on pulse propagation. Strong dispersion and SPM are applied for illustrative purposes.

6.3.4 SOA amplification

In DTML lasers, an SOA is typically employed as the gain medium. The pulse propagation inside an SOA is governed by the travelling-wave equation [8, 13, 14]:

$$\frac{\partial A}{\partial z} = \frac{g}{2}(1 - \mathrm{i}\alpha)A, \tag{6.22}$$

where g is the optical gain, and α is the linewidth enhancement factor. The gain g evolves dynamically and follows its own rate equation [5, 13, 14]:

$$\frac{\partial g}{\partial T} = \frac{g_{\text{small}}}{\tau_{\text{c}}} - \frac{g}{\tau_{\text{eff}}} - \frac{|A|^2}{E_{\text{sat}}}[\exp(g) - 1], \tag{6.23}$$

where g_{small}, τ_{c}, τ_{eff}, and E_{sat} are the small signal gain, carrier lifetime, effective gain recovery time, and saturation energy, respectively. Without going into excessive detail, the SOA gain arises from carrier injection into the active medium, creating a population of electrons and holes. The carrier-induced index of refraction change leads to SPM inside the SOA, accounted in Eq. (6.22) via the linewidth enhancement factor α. Typical values of the linewidth enhancement factor are $\alpha \approx 1$ for quantum-dot SOAs in the 1 µm wavelength range, and $\alpha \approx 5$ for quantum-well SOAs in the 1.5 µm range [14]. Once Eq. (6.23) is solved numerically, the SOA gain transfer function can be obtained by solving Eq. (6.22) as:

$$\mathcal{G}_{\text{SOA}}\{A\} \equiv \exp\left[\frac{g}{2}(1 - \mathrm{i}\alpha)\right] A \quad \text{(numerically solving Eq. (6.23) for } g\text{)}. \tag{6.24}$$

The effect of an SOA amplification on pulse propagation is illustrated in Fig. 6.4. As expected, the pulse undergoes an amplification, apparent from the increase in its peak power. In the spectral domain, the amplification introduces modulations to the pulse spectrum, resulting in the spectral broadening and a red shift, both more pronounced with larger α.

6.3.5 Amplitude modulation

In Eq. (6.8), the amplitude modulation is represented by the term $-2\pi^2 M f_{\text{m}}^2 t^2$, which describes sinusoidal window of frequency f approximated by a quadratic function. In the context of the discrete model, this modulation is assumed to be applied from an external source, affecting the pulse shape.

For sinusoidal modulation, the effect of amplitude modulation on the pulse shape can

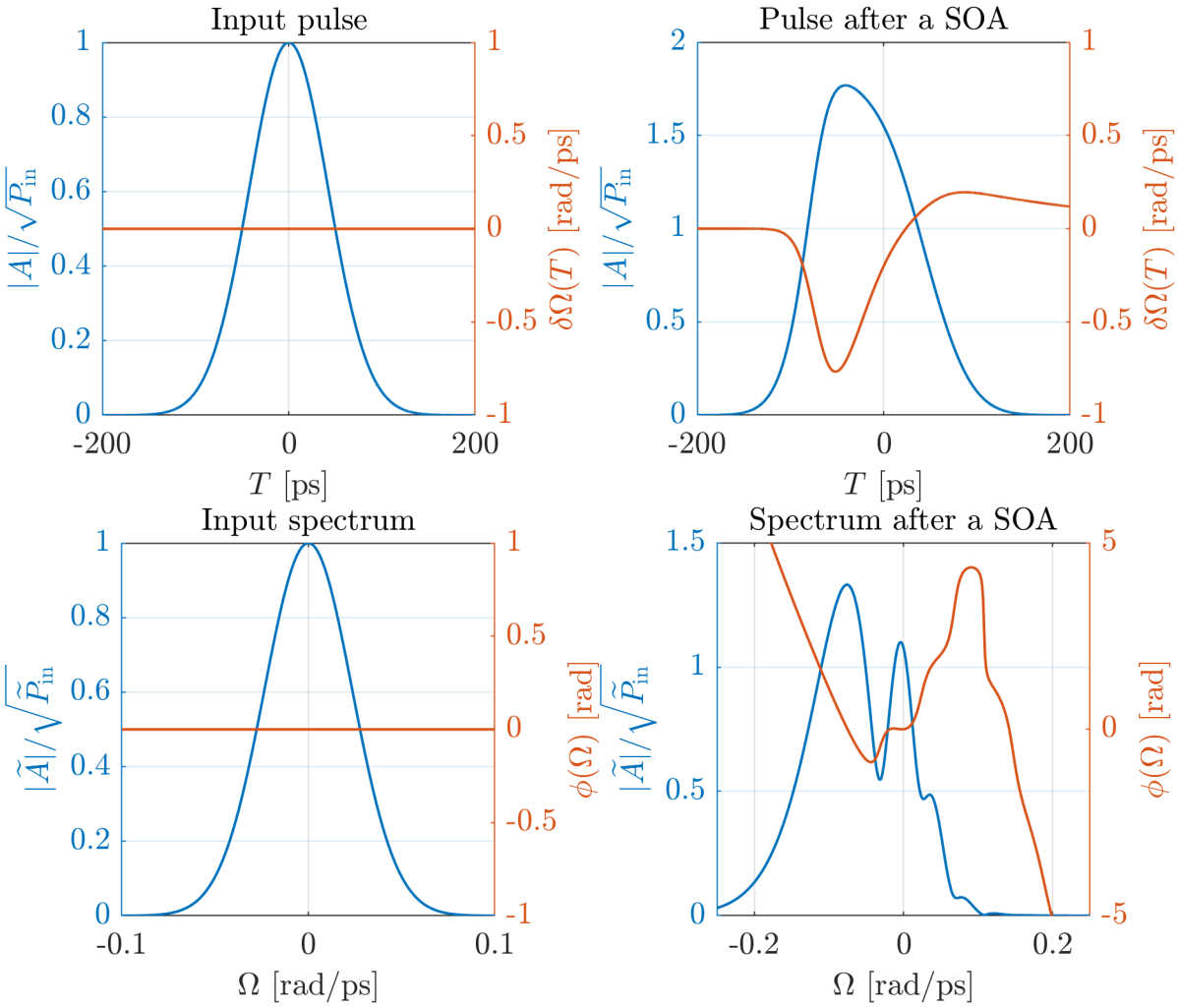

Figure 6.4: The effects of an SOA amplification on pulse propagation. Strong gain is applied for illustrative purposes. $\phi(\Omega)$ represents spectral phase of the envelope spectrum $\widetilde{A}(z, \Omega)$.

be modelled via a quadratic function:

$$A_{\text{out}} = -2\pi^2 M f^2 T^2 A_{\text{in}} = -\frac{\pi^2 M}{2\tau_{\text{m}}^2} T^2 A_{\text{in}}, \tag{6.25}$$

where $\tau_{\text{m}} \approx 1/(2f)$ is the sinusoidal modulation FWHM window width. In the case of pulse modulation technique [15–17], characterised by the window width τ_{m} independent of f, the effect of amplitude modulation can be modelled by a Gaussian window [11]:

$$A_{\text{out}} = M \exp\left(-\frac{2\ln 2}{\tau_{\text{m}}^2} T^2\right) A_{\text{in}}. \tag{6.26}$$

Eq. (6.25) and Eq. (6.26) lead to amplitude modulation transfer functions $\mathcal{M}\{A\}$ in forms:

$$\mathcal{M}_{\text{sine}}\{A\} \equiv -2\pi^2 M f^2 T^2 A, \quad \mathcal{M}_{\text{pulse}}\{A\} \equiv \exp\left(-\frac{2\ln 2}{\tau_{\text{m}}^2} T^2\right) A. \tag{6.27}$$

The effect of an amplitude modulation on a chirped pulse is illustrated in Fig. 6.5. The pulse shape is altered correspondingly to the width of the modulation window, while its temporal chirp is maintained.

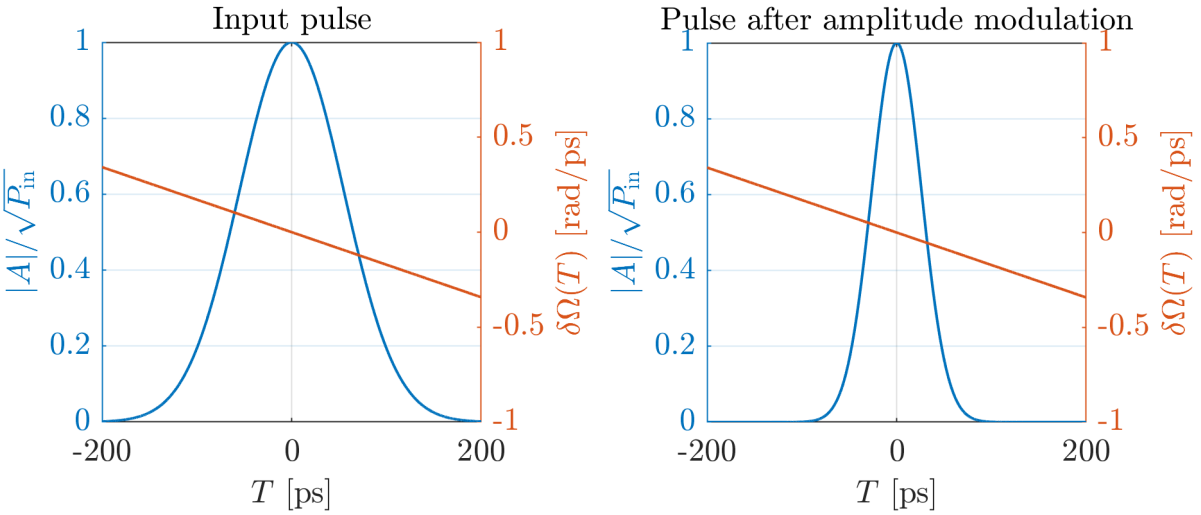

Figure 6.5: The effect of an amplitude modulation on a chirped pulse.

6.3.6 Phase noise

The last physical process that should be considered in the modelling of DTML lasers (in fact, any mode-locked laser) is noise inside a cavity. As the spectral linewidth broadening and coherence deterioration of a DTML laser are dominated by phase fluctuations, only phase noise is here considered, while amplitude fluctuations can be usually neglected in ultrafast lasers [2]. Phase noise can originate from various sources, such as gain fluctuations, length and refractive index fluctuations (including time jitter in the amplitude modulation), spontaneous emission fluctuations, or temperature fluctuations [18–20]. While many of these noise sources exhibit finite correlation times (SOA carrier lifetime, RF jitter, or temperature drift), the net phase fluctuations arise from their cumulative effect. Under these conditions, the phase noise can be modelled as a stochastic diffusive (random walk) process with with Gaussian-distributed increments, and the probability density function of the phase increments $p(\Delta\phi_{\text{noise}})$ is given by [2]:

$$p(\Delta\phi_{\text{noise}}) = \frac{1}{\sqrt{2\pi\sigma^2_{\text{noise}}}} \exp\left(-\frac{\Delta\phi^2_{\text{noise}}}{2\sigma^2_{\text{noise}}}\right), \tag{6.28}$$

with the phase noise variance $\sigma^2_{\text{noise}} = \langle\Delta\phi^2_{\text{noise}}\rangle$. It can be shown that σ^2_{noise} increases linearly with the time delay δT, as defined by a random walk [2]:

$$\sigma^2_{\text{noise}} = 2\pi\delta\nu_{\text{noise}}\delta T, \tag{6.29}$$

where $\delta\nu_{\text{noise}}$ is the FWHM optical linewidth of the phase noise. Here, δT is the temporal resolution of the discrete simulation grid (approximately $\delta T \approx 0.1\,\text{ps}$ in the simulations presented in Sec. 6.4). Although it is generally not straightforward to evaluate $\delta\nu_{\text{noise}}$ in view of its dependence on many laser parameters [18–20], a rough interval 1-100 MHz can be determined from measuring phase noise linewidths in mode-locked lasers prior to stabilisation techniques [2, 21–23]. To conservatively account for actual DTML cavities with SOA gain dynamics and modulation signal jitter, the upper bound of the interval is extended to 500 MHz. Using Eq. (6.29) with $\delta T = 0.1\,\text{ps}$, the interval 1-500 MHz transfers to 0.001-0.018 in σ_{noise}. Finally, the corresponding phase noise transfer function acting on

a pulse A is then implemented according to:

$$\mathcal{N}\{A\} \equiv A \exp[\mathrm{i}2\pi\Delta\phi_{\mathrm{noise}}(T_m)], \tag{6.30}$$

where the notation $\Delta\phi_{\mathrm{noise}}(T_m)$ indicates that the phase noise increment is evaluated independently for each discrete temporal point m of the simulation grid.

The effect of phase noise on a pulse is illustrated in Fig. 6.6, where a random phase shift is applied independently at each temporal point of the simulation grid.

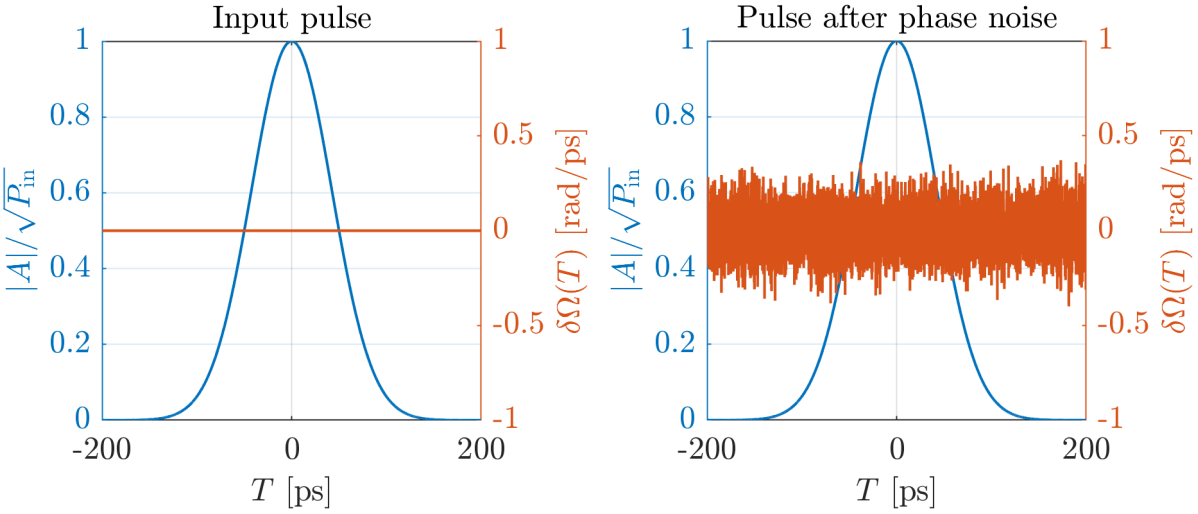

Figure 6.6: The effect of phase noise on pulse propagation. Strong phase noise is applied for illustrative purposes.

6.4 Simulation results

The reference DTML laser cavity used for mathematical modelling is displayed in Fig. 6.7. The laser comprises an SOA as the gain medium (transfer function $\mathcal{G}_{\mathrm{SOA}}\{A\}$), a cFBG as the dispersive element (transfer function $\mathcal{D}_{\mathrm{cFBG}}\{A\}$), an IM as the modulation element (transfer function $\mathcal{M}_{\mathrm{pulse}}\{A\}$), a fibre delay (transfer function $\mathcal{P}\{A\}$), and a CIRC. The optical components are also characterised by their insertion losses (transfer functions $\mathcal{L}_{\mathrm{CIRC}}\{A\}$, $\mathcal{L}_{\mathrm{cFBG}}\{A\}$, $\mathcal{L}_{\mathrm{IM}}\{A\}$). Finally, phase noise (transfer function $\mathcal{N}\{A\}$) is added to appropriately model the real world laser. The characteristic round trip transfer function $\mathcal{R}\{A\}$ is formulated by mapping the cavity elements and their transfer functions

in the direction of the circulation of light inside the cavity (the direction of the CIRC arrow):

$$\mathcal{R}\{A\} = \mathcal{N}\{\mathcal{G}_{\mathrm{SOA}}\{\mathcal{P}\{\mathcal{M}_{\mathrm{pulse}}\{\mathcal{L}_{\mathrm{IM}}\{\mathcal{L}_{\mathrm{CIRC}}\{\mathcal{D}_{\mathrm{cFBG}}\{\mathcal{L}_{\mathrm{cFBG}}\{\mathcal{L}_{\mathrm{CIRC}}\{A\}\}\}\}\}\}\}\}. \quad (6.31)$$

The laser parameters which remain constant for the numerical simulations are listed in Tab. 6.1. The numerical modelling is performed here using MATLAB language, with the code for the individual transfer functions appeared throughout Sec. 6.3 and in Eq. (6.31) provided in Appx. B.

For their critical impact on coherence performance of a DTML laser, two parameters with adjustable values will be examined in the simulations: the amount of dispersion in the cavity and the modulation window width.

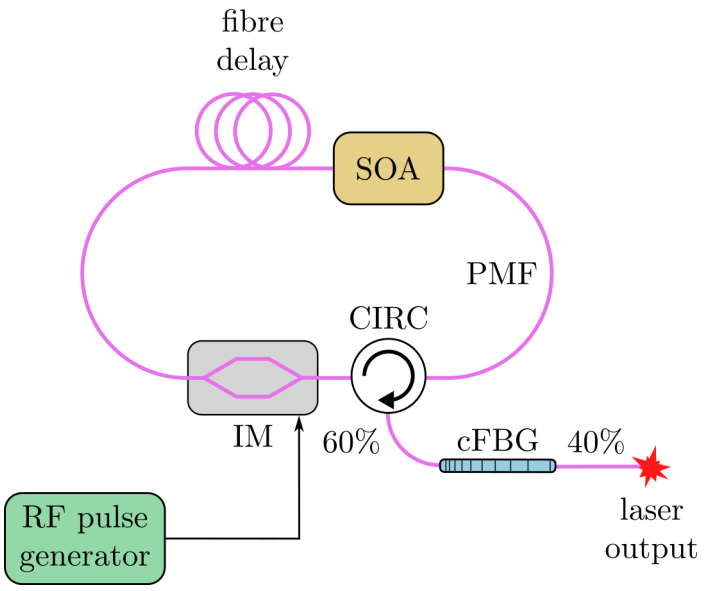

Figure 6.7: The reference DTML laser cavity for the mathematical modelling, characterised by the round trip transfer function in Eq. (6.31).

6.4.1 The amount of dispersion in the cavity

As discussed in Subsec. 6.3.2, a pulse propagating inside a dispersive medium (fibre or a cFBG) obtains a temporal chirp due to the phase delays experienced by different spectral components. When such a chirped pulse undergoes an amplitude modulation, only the

Table 6.1: Cavity parameters for the DTML laser in Fig. 6.7.

Parameter	**Value**
Central wavelength λ_c	1060 nm
Fibre length L	1.542 m [16]
Small signal gain g_{small}	32 dB [24]
Carrier lifetime τ_c	200 ps [8]
Effective gain recovery time τ_{eff}	200 ps [8]
Saturation energy E_{sat}	0.824 pJ [7, 8, 10, 13, 14]
Linewidth enhancement factor α	1 [14]
cFBG reflectivity R_{cFBG}	0.4 [16]
Circulator insertion loss L_{circ}	2 dB [25]
Modulator insertion loss L_{mod}	3.5 dB [26]
Modulation depth M	1
Fibre attenuation ρ_{fibre}	0.5 dB/km [27]
Fibre dispersion coefficient D_{fibre}	-35 ps/(nm $\cdot$ km) (used the technique in [28])
Fibre nonlinear coefficient γ_{fibre}	10^{-3} 1/(W $\cdot$ m) [11]

spectral components near the pulse peak are transmitted through the modulation window, enhancing the spectral filtering effect. To examine this filtering mechanism only as a function of dispersion in the cavity, the following simulation considers an idealised noiseless laser.

Assuming a cavity length of 1.542 m as listed in Tab. 6.1, the dispersion introduced by such short fibre is negligible and the total cavity dispersion is dominated by the cFBG, i.e., $\text{TDD}_{\text{cav}} \approx \text{TDD}_{\text{cFBG}}$. Using the cavity parameters in Tab. 6.1, a modulation window width of $\tau_m = 100$ ps, and considering an idealised noiseless cavity ($\sigma_{\text{noise}} = 0$ in Eq. (6.28)), Fig. 6.8 displays FWHM linewidth $\delta\Omega_{\text{FWHM}}$ of the lasing spectrum as a function of dispersion TDD_{cav} after 1000 round trips inside the cavity. This was obtained by applying the round trip transfer function $\mathcal{R}\{A\}$ given by Eq. (6.31) 1000 times, starting with a white noise as the initial spectrum for the first round trip. From the graph, it is evident that positive dispersion values (i.e., anomalous dispersion) yield narrower linewidths than negative values (i.e., normal dispersion), in agreement with the findings in [13]. This behaviour arises from the interplay between dispersion and SPM in the cavity, with SPM primarily occuring inside the gain medium. In the anomalous dispersion regime, the linear chirp due to dispersion partially compensates for the nonlinear temporal chirp due to SPM, reducing the broadening. On the contrary, in the normal dispersion

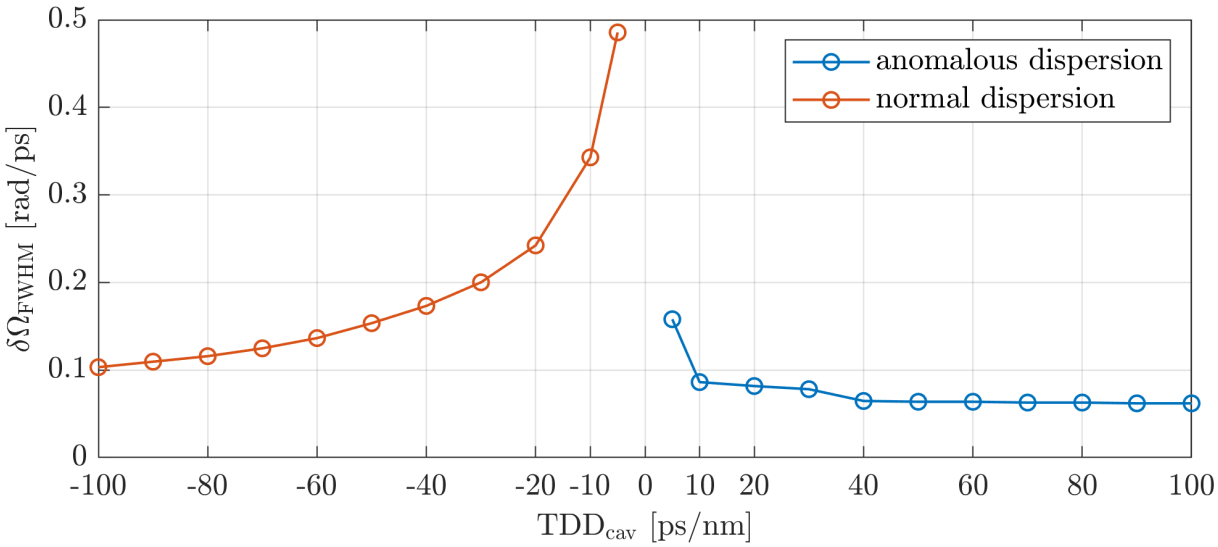

Figure 6.8: Simulation of the FWHM linewidth $\delta\Omega_{\mathrm{FWHM}}$ linewidth as a function of the cavity dispersion $\mathrm{TDD}_{\mathrm{cav}}$.

regime, the compensation is less effective, and dispersion values below $-100\,\mathrm{ps/nm}$ would be required to produce linewidths comparable to those achieved in the anomalous regime in the simulation.

Fig. 6.9 shows the resulting power spectra $S(\Omega)$ after 1000 round trips inside the cavity for selected dispersion values $\mathrm{TDD}_{\mathrm{cav}}$. The redshift induced by SPM inside the SOA is observed to decrease with increasing $|\mathrm{TDD}_{\mathrm{cav}}|$, in agreement with the findings in [14].

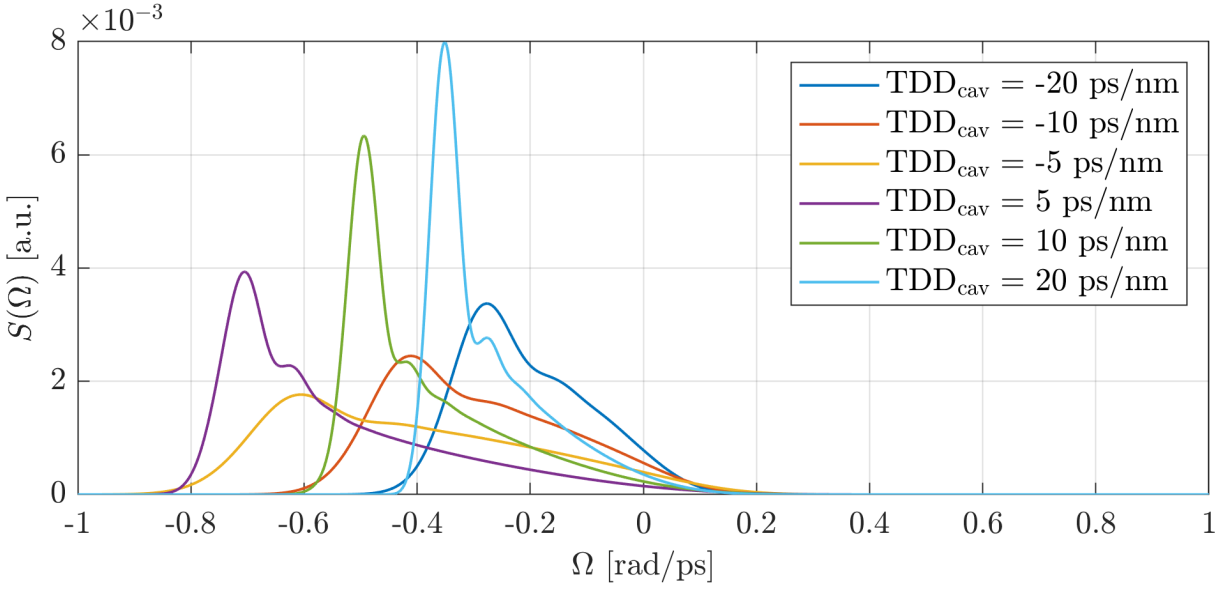

Figure 6.9: Optical power spectra $S(\Omega)$ after 1000 round trips for different cavity dispersions $\mathrm{TDD}_{\mathrm{cav}}$.

6.4.2 The modulation window width

As mentioned in Sec. 4.4, it has been experimentally observed that narrower modulation windows lead to an enhanced mode-locking stability and improved coherence of the lasing, even at higher sweep rates. In this simulation, the stability and coherence are examined by observing the evolution of the lasing spectra over multiple round trips inside the cavity for various modulation window widths and phase noise levels. Notably, the phase noise and its effects on the lasing are here included in modelling of DTML lasers for the first time, extending the previous studies [7–10, 13, 14].

First, using the cavity parameters listed in Tab. 6.1, a cavity dispersion of $\mathrm{TDD_{cav}} = 10\,\mathrm{ps/nm}$, and considering an idealised noiseless cavity ($\sigma_{\mathrm{noise}} = 0$) for now, the charts in Fig. 6.10 display the evolution of the lasing spectra over the first 200 round trips for various modulation windows widths τ_{m}, starting again with a white noise as the initial spectrum for the first round trip. During the initial build-up from the white noise, the lasing exhibits strong spectral modulation, more pronounced and enduring longer for larger values of τ_{m}. As it is questionable to simply evaluate the FWHM linewidth for these build-up round trips, a more general root mean square linewidth $\delta\Omega_{\mathrm{RMS}}$ is used here instead [2]:

$$\delta\Omega_{\mathrm{RMS}} = \langle(\Omega - \langle\Omega\rangle)^2\rangle^{1/2} = \left[\frac{\int_{-\infty}^{+\infty}(\Omega - \langle\Omega\rangle)^2 S(\Omega)\mathrm{d}\Omega}{\int_{-\infty}^{+\infty} S(\Omega)\mathrm{d}\Omega}\right]^{1/2}, \tag{6.32}$$

where $\langle\Omega\rangle$ is the centre of gravity of the power spectrum $S(\Omega) = |\widetilde{A}(\Omega)|^2$,

$$\langle\Omega\rangle = \frac{\int_{-\infty}^{+\infty}\Omega S(\Omega)\mathrm{d}\Omega}{\int_{-\infty}^{+\infty} S(\Omega)\mathrm{d}\Omega}. \tag{6.33}$$

The evaluated $\delta\Omega_{\mathrm{RMS}}$ for $\sigma_{\mathrm{noise}} = 0$ are plotted over 1000 round trips for different values of τ_{m} in Fig. 6.11 top left. Apparently, the lasing reaches its stabilised state (no more alterations in $\delta\Omega_{\mathrm{RMS}}$) after fewer number of round trips N_{stable} for smaller values of τ_{m}. This dependence is plotted as a function of τ_{m} in Fig. 6.12 left. This behaviour can be explained by the shorter modulation windows transmitting a more limited interval of

the temporal noise during the lasing build-up from white noise, smoothing the spectral modulation in Fig. 6.10 more rapidly and reducing N_{stable}. In this idealised noiseless case, after reaching N_{stable} for a given τ_{m}, longer modulation windows yield narrower linewidths, in agreement with the findings in [7–9].

Finally, a non-negligible phase noise is added to the simulations to model a realistic DTML laser cavity. The effect of this noise on the lasing build-up and the evolution of the linewidth $\delta\Omega_{\text{RMS}}$ is observed in plots in Fig. 6.11 for the variance σ_{noise} values of 0.006, 0.012, and 0.018, as for "mildly", "moderately", and "heavily" noisy cavities, respectively. The corresponding stabilised $\delta\Omega_{\text{RMS}}$ as a function of τ_{m} for different values of σ_{noise} are plotted in Fig. 6.12 right. From the plots, it is concluded that the phase noise introduces linewidth broadening in all cases, but the amount of broadening is moderated by employing shorter modulation windows, consistent with the experimental observations reported in [10, 15–17].

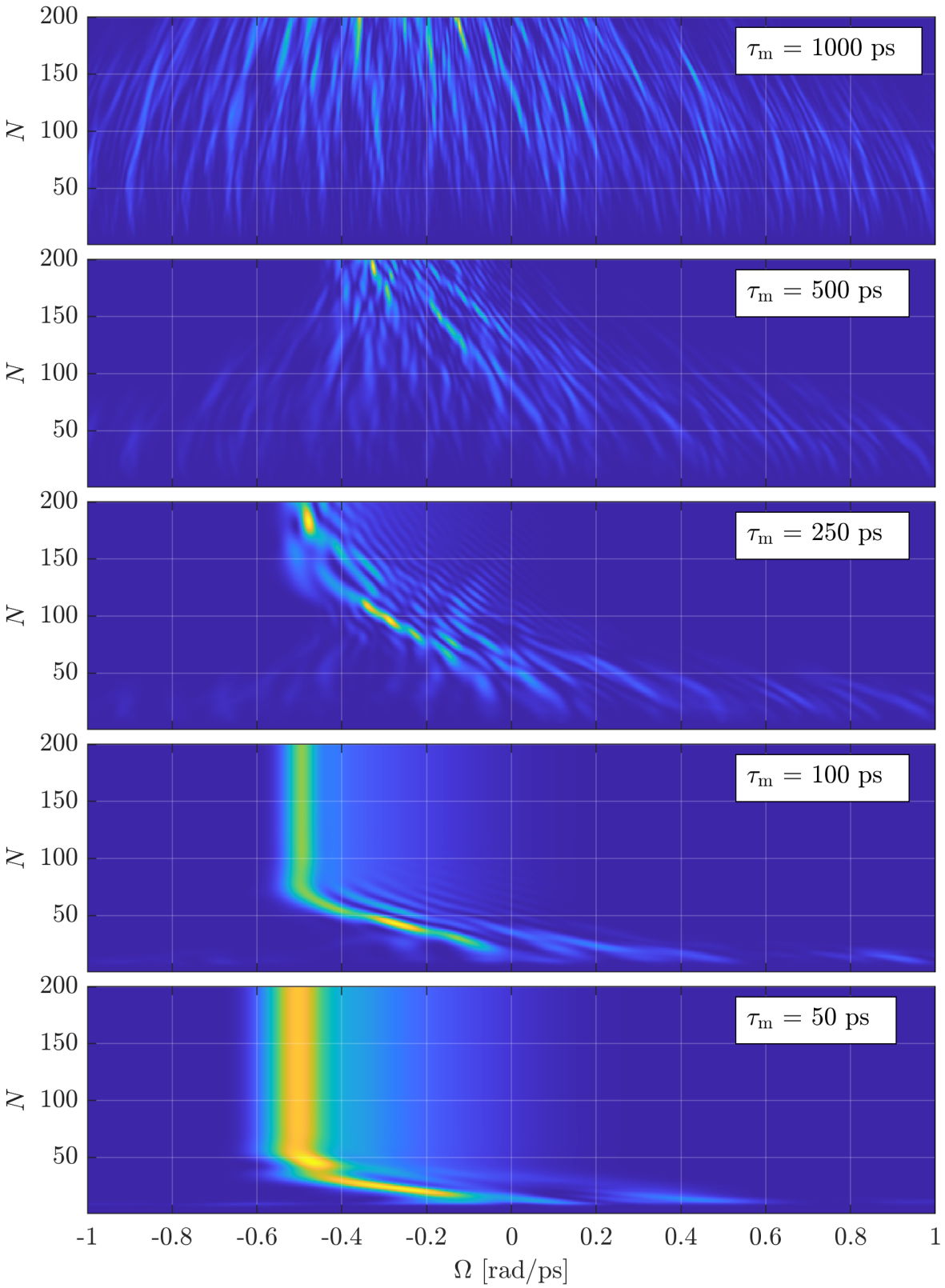

Figure 6.10: Evolution of the lasing spectra over the first 200 round trips N for different modulation window widths τ_m.

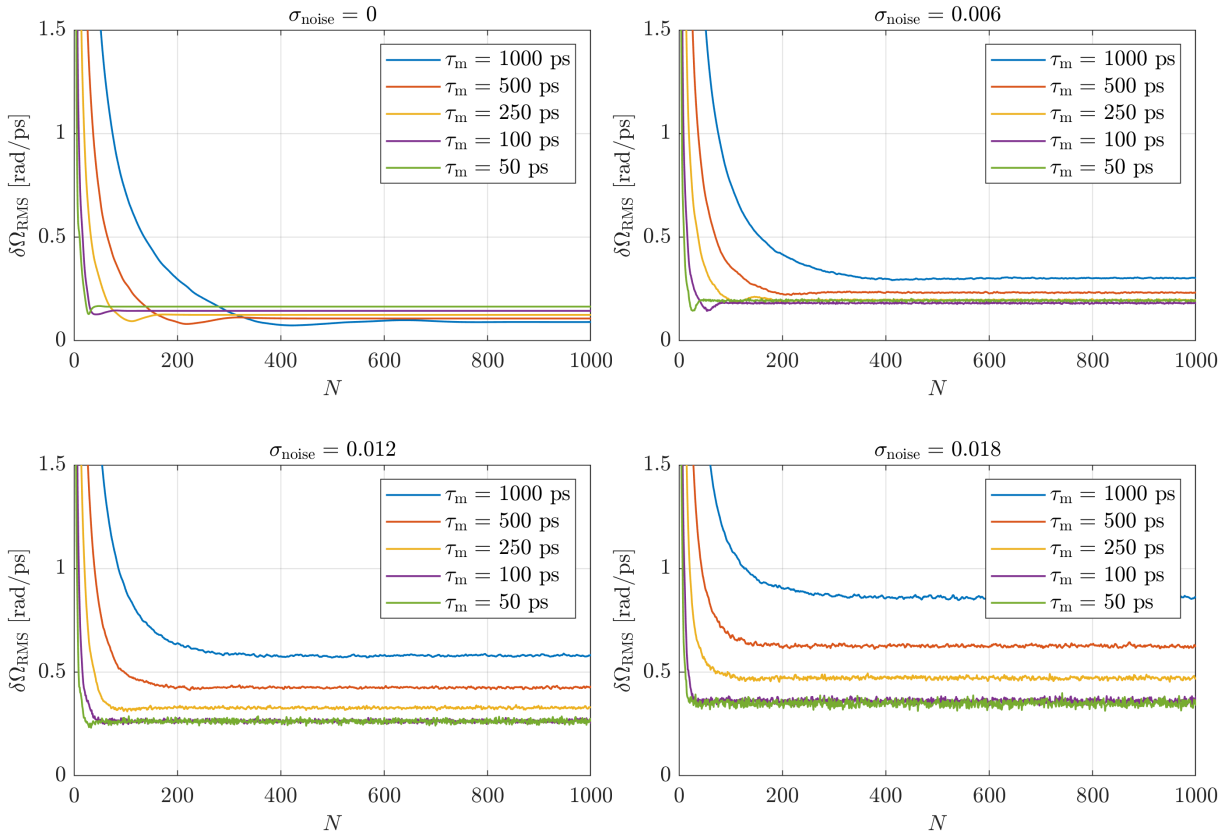

Figure 6.11: Evolution of the linewidth $\delta\Omega_{\text{RMS}}$ as a function of round trips N for different modulation window widths τ_{m} and phase noise variances σ_{noise}.

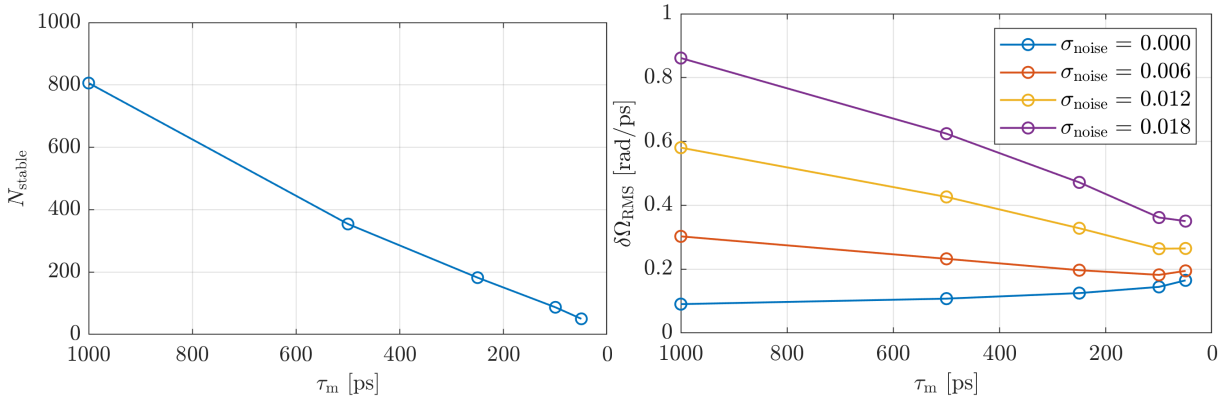

Figure 6.12: Left: Number of round trips N_{stable} needed for the lasing stabilisation for the case $\sigma_{\text{noise}} = 0$ in Fig. 6.11 top left as a function of the modulation window width τ_{m}. **Right:** Linewidth $\delta\Omega_{\text{RMS}}$ (average over the last 100 round trips in Fig. 6.11) as a function of τ_{m} for different phase noise variances σ_{noise}.

Bibliography

[1] G. P. Agrawal, *Nonlinear Fiber Optics*, 6th ed. Academic Press, 2019.

[2] U. Keller, *Ultrafast Lasers: A Comprehensive Introduction to Fundamental Principles with Practical Applications*. Springer International Publishing, 2022.

[3] G. P. Agrawal, *Fiber-Optic Communications Systems*, 3rd ed. John Wiley & Sons, Inc, 2002.

[4] A. E. Siegman, *Lasers*. University Science Books, 1986.

[5] P. P. Baveja, A. M. Kaplan, D. N. Maywar, and G. P. Agrawal, "Pulse amplification in semiconductor optical amplifiers with ultrafast gain-recovery times," *Optical Components and Materials VII*, vol. 7598, p. 759817, 2010.

[6] I. Duling, *Compact Sources of Ultrashort Pulses*. Cambridge University Press, 1995.

[7] Y. Hasegawa and S. Yamashita, "Analysis of dynamic properties of dispersion-tuned lasers," in *2014 Conference on Lasers and Electro-Optics (CLEO) - Laser Science to Photonic Applications*, 2014.

[8] Y. Hasegawa, T. Shirahata, and S. Yamashita, "Analysis of dynamic properties of dispersion-tuned swept lasers," *Journal of Lightwave Technology*, vol. 33, no. 1, pp. 219–226, 2015.

[9] B. Burgoyne, A. Dupuis, and A. Villeneuve, "An experimentally validated discrete model for dispersion-tuned actively mode-locked lasers," *IEEE Journal of Selected Topics in Quantum Electronics*, vol. 20, no. 5, pp. 390–398, 2014.

[10] Y. Takubo, T. Shirahata, and S. Yamashita, "Optimization of a dispersion-tuned wavelength-swept fiber laser for optical coherence tomography," *Appl. Opt.*, vol. 55, no. 27, pp. 7749–7755, Sep 2016.

[11] B. Metherall and C. S. Bohun, "Predicting instabilities of a tunable ring laser with an iterative map model," *J. Opt. Soc. Am. B*, vol. 38, no. 9, pp. 2479–2487, Sep 2021.

[12] M. J. Potasek, G. P. Agrawal, and S. C. Pinault, "Analytic and numerical study of pulse broadening in nonlinear dispersive optical fibers," *J. Opt. Soc. Am. B*, vol. 3, no. 2, pp. 205–211, Feb 1986.

[13] A. Takada, M. Fujino, and S. Nagano, "Dispersion dependence of linewidth in actively mode-locked ring lasers," *Opt. Express*, vol. 20, no. 4, pp. 4753–4762, Feb 2012.

[14] A. Takada, M. Saika, and S. Nagano, "Effect of linewidth enhancement factor in actively mode-locked ring laser," vol. 8961, p. 896135, 2014.

[15] H. Nagai and S. Yamashita, "Coherence improvement in dispersion-tuned swept laser by pulse modulation," *Electronics Letters*, vol. 50, no. 23, pp. 1729–1731, 2014.

[16] H. D. Lee, G. H. Kim, J. G. Shin, B. Lee, C.-S. Kim, and T. J. Eom, "Akinetic swept-source optical coherence tomography based on a pulse-modulated active mode locking fiber laser for human retinal imaging," *Scientific Reports*, vol. 8, 2018.

[17] R. Riha, A. M. Jimenez, G. Venugopal, M. Klufts, R. Huber, and A. Podoleanu, "Dispersion-tuned mode-locked laser for swept source OCT at 850 nm using a cFBG and the pulse modulation technique," *IEEE Photonics Journal*, vol. 16, no. 4, pp. 1–5, 2024.

[18] H. A. Haus and A. Mecozzi, "Noise of mode-locked lasers," *IEEE Journal of Quantum Electronics*, vol. 29, no. 3, pp. 983–996, 1993.

[19] R. Paschotta, "Noise of mode-locked lasers (part i): Numerical model," *Applied Physics B*, vol. 79, no. 2, pp. 153–162, 2004.

[20] ——, "Noise of mode-locked lasers (part ii): Timing jitter and other fluctuations," *Applied Physics B*, vol. 79, no. 2, pp. 163–173, 2004.

[21] T. Habruseva, S. O'Donoghue, N. Rebrova, F. Kéfélian, S. P. Hegarty, and G. Huyet, "Optical linewidth of a passively mode-locked semiconductor laser," *Optics Letters*, vol. 34, no. 21, pp. 3307–3309, 2009.

[22] R. Maldonado-Basilio, J. Parra-Cetina, S. Latkowski, and P. Landais, "Timing-jitter, optical, and mode-beating linewidths analysis on subpicosecond optical pulses generated by a quantum-dash passively mode-locked semiconductor laser," *Optics Letters*, vol. 35, no. 8, pp. 1184–1186, 2010.

[23] Y. Mao, G. Liu, K. Zeb, Z. Lu, J. Liu, P. J. Poole, C.-Y. Song, and P. Barrios, "Ultralow noise and timing jitter semiconductor quantum-dot passively mode-locked laser for terabit/s optical networks," *Photonics*, vol. 9, no. 10, p. 695, 2022.

[24] Innolume GmbH. (2025) Innolume – quantum dot and quantum well laser diodes. [Online]. Available: https://www.innolume.com/

[25] OZ Optics Ltd. (2025) Oz optics – fiber optic components and test equipment. [Online]. Available: https://www.ozoptics.com/

[26] Optilab LLC. (2025) Optilab – fiber optic and photonics solutions. [Online]. Available: https://www.optilab.com/

[27] AFW Technologies Pty Ltd. (2025) AFW technologies – fiber optic and micro optic components. [Online]. Available: https://www.afwtechnologies.com.au/

[28] R. Riha and A. Podoleanu, "An approximative fiber laser cavity dispersion assessment technique using mode-locked wavelength tuning," in *Optical Coherence Tomography and Coherence Domain Optical Methods in Biomedicine XXVII*. Optica, 2022, p. 512.

Chapter 7

Experimental validations

In this last experimentally focused chapter, an approximative cavity dispersion assessment method is first proposed and validated. Subsequently, three DTML swept lasers architectures operating at 850 nm, 1 µm, and 1550 nm, respectively, are presented and experimentally evaluated.

7.1 An approximative cavity dispersion assessment exploiting DTML

This section presents presents a simple yet effective method for an approximative cavity dispersion assessment in a DTML laser cavity without the need for additional components required for DTML itself [1]. The method exploits the linear dependence between the shift in the emission wavelength and change in the modulation frequency. The validation of the method is first performed using spools of SMF-28e fibre, yielding results consistent with dispersion values found in the literature. After the validation, cavity dispersions are evaluated for two different cFBGs with unknown dispersions inserted in a DTML cavity. This method is then employed in Sec. 7.2 [2], Sec. 7.3 [3], and Sec. 7.4 [4]. With the knowledge of the dispersion value inside the cavity, important parameters such as tuning and coherence properties of an DTML laser can be evaluated.

7.1.1 Methods

As derived in Eq. (4.13), the shift in the emission wavelength $\Delta\lambda_{\text{single}}$ from a standard single-harmonic DTML laser is for high harmonic orders linearly proportional to the change in the modulation frequency Δf of the RF signal applied to the mode-locking element. This linear relationship is given by Eq. (4.13):

$$\Delta\lambda_{\text{single}} \approx S(D_{\text{cav}}, f_0)\Delta f = -\frac{n_{\text{g}}}{cD_{\text{cav}}f_0}\Delta f = -\frac{1}{\text{TDD}_{\text{cav}}f_{\text{cav}}f_0}\Delta f \tag{7.1}$$

where n_{g}, D_{cav}, and $\text{TDD}_{\text{cav}} = L_{\text{cav}}D_{\text{cav}}$ are effective group index of refraction, dispersion coefficient, and time delay dispersion of the cavity, respectively, and the tuning sensitivity $S(D_{\text{cav}}, f_0)$ generally depends on chromatic dispersion in the cavity D_{cav} and modulation frequency f_0. Inspired by [5], the method of the cavity dispersion assessment in a DTML laser is based on a linear regression of measurements of $\Delta\lambda_{\text{single}}/\Delta f$ against f_0:

$$\frac{\Delta\lambda_{\text{single}}}{\Delta f} = \frac{K}{f_0}, \tag{7.2}$$

where

$$K = -\frac{n_{\text{g}}}{cD_{\text{cav}}} \tag{7.3}$$

is the slope of the linear regression from which D_{cav} or TDD_{cav} can be extracted.

7.1.2 Experimental setups and results

To evaluate the accuracy and potential limitations of the dispersion assessment method, the measurements were first carried out for a cavity composed solely of SMF-28e fibre. The experimental setup for measuring the fibre dispersion is shown in Fig. 7.1(a). Contributions to the cavity dispersion from non-fibre components, such as the semiconductor optical amplifier gain medium or the electro-optic crystal inside the intensity modulator, can be considered negligible as their physical lengths (on the order of millimetres) are at least three orders of magnitude smaller than the overall cavity length (on the order of metres and more).

Dispersion assessments were conducted for three spools of a SMF-28e fibre of differ-

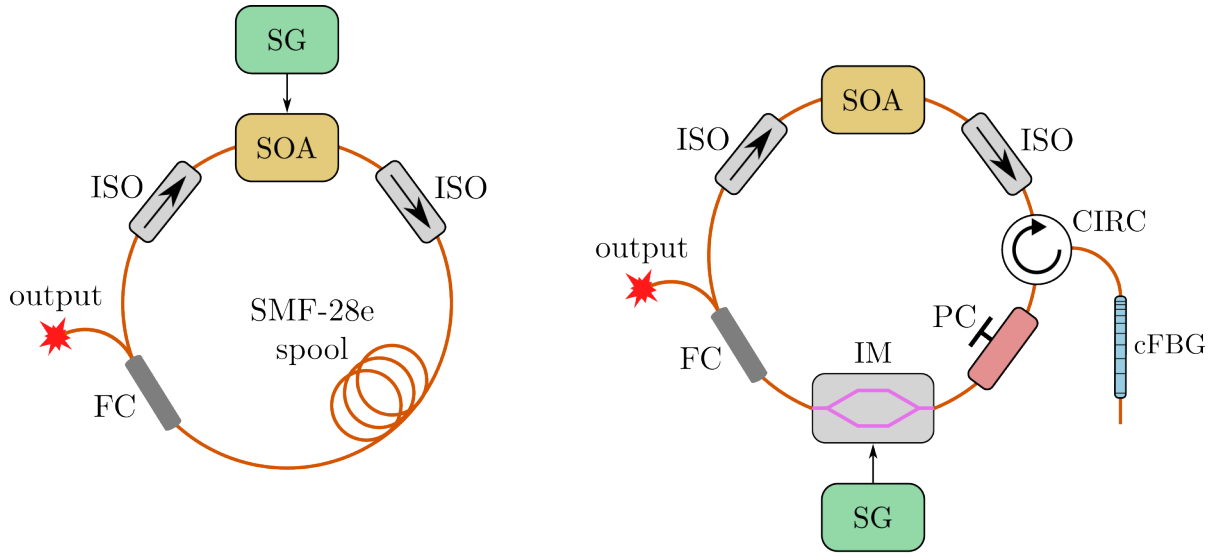

Figure 7.1: **(a)** DTML cavity using direct modulation of the SOA as the mode-locking element and a spool of SMF-28e fibre as the dispersive element. **(b)** DTML cavity using an intensity modulator as the mode-locking element and a cFBG as the dispersive element. SOA: semiconductor optical amplifier, SG: signal generator, ISO: optical isolator, FC: fibre coupler, CIRC: optical circulator, PC: polarisation controller, IM: intensity modulator.

ent lengths inserted into the cavity in Fig. 7.1(a). To evaluate D_{cav}, 10 measurements of $\Delta\lambda_{\text{single}}/\Delta f$ for different f_0 were performed. Although only one measured value of $\Delta\lambda_{\text{single}}/\Delta f$ at single f_0 is sufficient to evaluate D_{cav} in principle, performing a linear regression over multiple measurements (e.g., 10) reduces the uncertainty in determining $\Delta\lambda_{\text{single}}$ from the optical spectral analyser. The linear regressions of $\Delta\lambda_{\text{single}}/\Delta f$ against f_0 are displayed in Fig. 7.2, and the dispersion assessment results D_{cav} are presented in Tab. 7.1, along with the wavelengths λ_0 at which the assessments were performed. For all fibre spool lengths, the measured uncertainties in the evaluations of D_{cav} are below 1% of the evaluated value, and it is not expected to be significantly improved with more measurements of $\Delta\lambda_{\text{single}}/\Delta f$. The values $D_{\text{SMF-28e}}(\lambda_0)$ found in the literature [6] are listed in the last column of Tab. 7.1. For all fibre spool lengths, the comparison with the literature values show a difference below $1\,\text{ps}/(\text{nm}\cdot\text{km})$, sufficient for an approximative cavity dispersion assessment in a DTML laser.

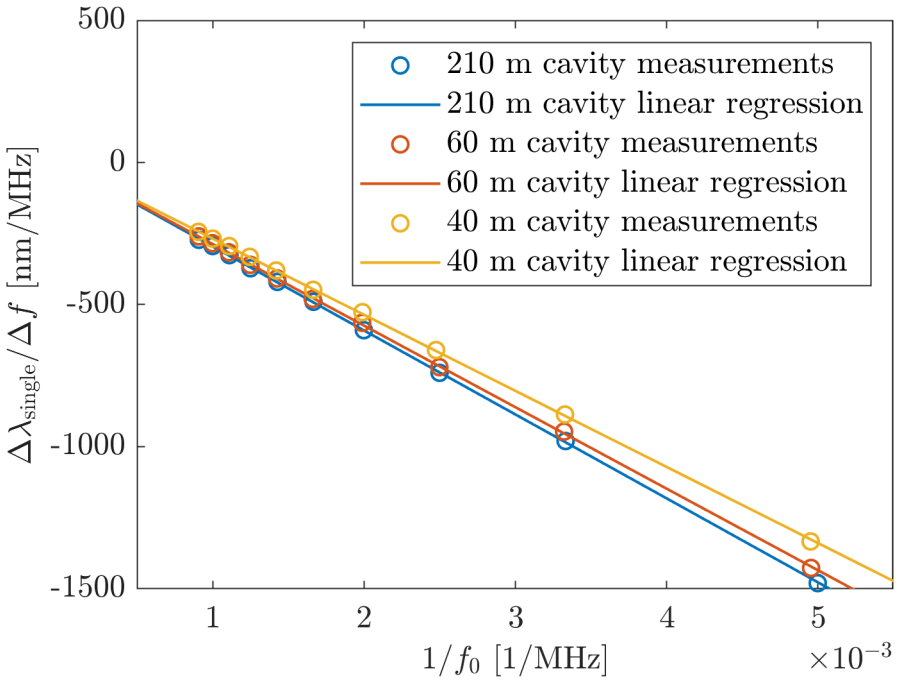

Figure 7.2: Linear regressions of $\Delta\lambda_{\text{single}}/\Delta f$ against f_0 for different cavity lengths in Fig. 7.1(a).

Table 7.1: DTML cavity dispersion assessments D_{cav} for different cavity (SMF-28e spools) lengths L_{cav}.

L_{cav} [m]	λ_0 [nm]	D_{cav} [ps/(nm·km)]	$D_{\text{SMF-28e}}(\lambda_0)$ [ps/(nm·km)]
210	1553	16.58 ± 0.05	16.10
60	1564	17.07 ± 0.07	17.47
40	1568	18.29 ± 0.08	17.90

Using the same method, it was now possible to assess the dispersion of the cavity in Fig. 7.1(b), including all fibre components and a cFBG as the dispersive element. The linear regressions are displayed in Fig. 7.3, along with the measured values of $\mathrm{TDD}_{\mathrm{cav}}(\lambda_0)$ for two different cFBGs from suppliers VFibre [7] and O/E Land [8], with unknown dispersions. In both cases, the cavity length was evaluated as 26 m.

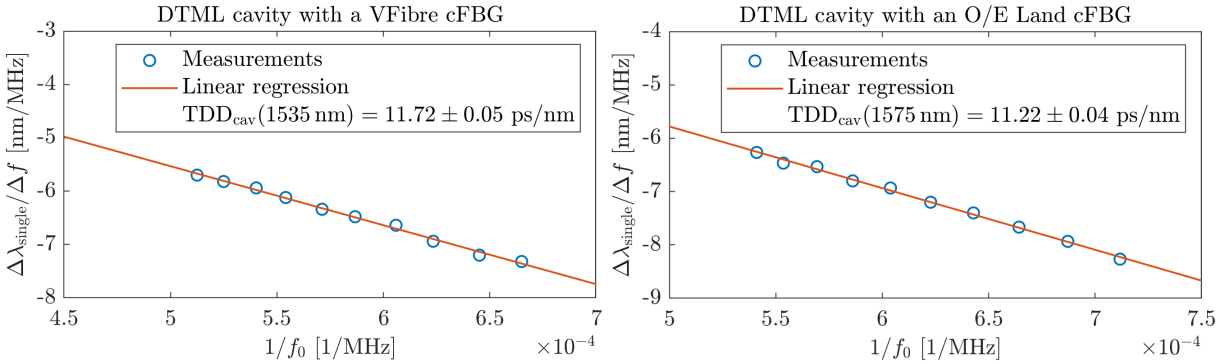

Figure 7.3: Cavity dispersion assessments of the DTML cavity in Fig. 7.1(b) for two different cFBGs with unknown dispersions.

7.1.3 Conclusion

A simple and effective dispersion assessment method was demonstrated, showing good accuracy in practical measurements. Its advantage lies in utilising the same components intended for DTML itself. While this method is limited to evaluating only effective dispersion of the cavity, neglecting higher order dispersions or polarisation-dependent dispersion, it can be used to determine $\Delta\lambda_{\mathrm{single,n\text{-}d}}$ and $\Delta\lambda_{\mathrm{multi,n\text{-}d}}$ in Eq. (4.14) and Eq. (5.17) or for mathematical modelling in Chap. 6.

7.2 DTML swept source at 850 nm for OCT using a cFBG and pulse modulation technique

The study in [2] presents a (single-harmonic) DTML swept source operating at 850 nm, developed primarily for full-field swept-source optical coherence tomography (FFSS-OCT). The laser combines a cFBG and pulse modulation technique to enable stable emission over tuning bandwidth of 35 nm at sweep rates up to 20 kHz. Unlike previous DTML implementations at 850 nm relying on an SOA direct modulation or long dispersive fibre as the dispersive element, this design achieves improved coherence and higher sweep rates. The results demonstrate the viability of DTML operation at shorter wavelengths and show a promise for replacing slower acousto-optic based swept sources (see Subsec. 3.2.1) in next generation FFSS-OCT systems.

7.2.1 Experimental setup

The studied DTML swept source is depicted in Fig. 7.4. The swept source consists of three main components: a semiconductor optical amplifier (SOA, Superlum SOA-372, optical gain bandwidth 40 nm), an intensity modulator (IM, Exail NIR-MX800-LN-20, RF bandwidth 20 GHz), and a chirped fibre Bragg grating (cFBG, Teraxion PSR-840-72(+D16.77-0.035)-0S1-0R, reflection bandwidth 72 nm, reflectivity 90%, dispersion 17 ps/nm). The SOA acts as the gain medium, the IM as the mode-locking element, and the cFBG as the dispersive element. The operational wavelength and bandwidth of the swept source are mainly determined by the employed SOA. The light is directed to the cFBG through an optical circulator (CIRC, OZ Optics FOC-12P-111-6/125-PPP-1060-50-3A3A3A-1-1-WB, optical bandwidth 100 nm), which serves also as an optical isolator in the cavity. The light is then coupled out in transmission through the cFBG. The cFBG employs single mode fibre via a polarisation controller (PC). The rest of the cavity consists of polarisation maintaining fibre. The total cavity round trip length is evaluated as 13.6 m (fundamental frequency of 15.1 MHz) and cavity dispersion is estimated as 14.6 ps/nm using the dispersion assessment method described in Sec. 7.1.

A schematic diagram of the intensity modulator driver is detailed in Fig. 7.4 as well

(inside the green dashed rectangle). A voltage-controlled oscillator (VCO, Mini-Circuits ZX95-1240-S+, 1-2 GHz), is driven with DC, V_{DC}, and AC, V_{AC}, voltage signals from a signal generator (SG, Agilent Technologies 81160A). Due to the maximum output voltage limitation of $V_{DC} + V_{AC}$ delivered by the SG, an in-house bias-tee is employed to separate the control of V_{DC} and V_{AC}. The VCO output signal is directed to a pulse generator (PG, AlnairLabs EPG-210M-0050-S-P-N-N), which generates a short pulse of width 50 ps per each period of the input sinusoidal signal. This means that the pulse repetition frequency f is that of the instantaneous input sinusoidal signal provided by the VCO. The pulses are then amplified through a pair of cascaded RF amplifiers (RFA, Mini-Circuits ZVA-01243+ and Xmicrowave XM-A3E6-0804C-01), and applied to the IM. Finally, the bias of the IM is controlled separately by DC voltage from a regulated power supply (PS).

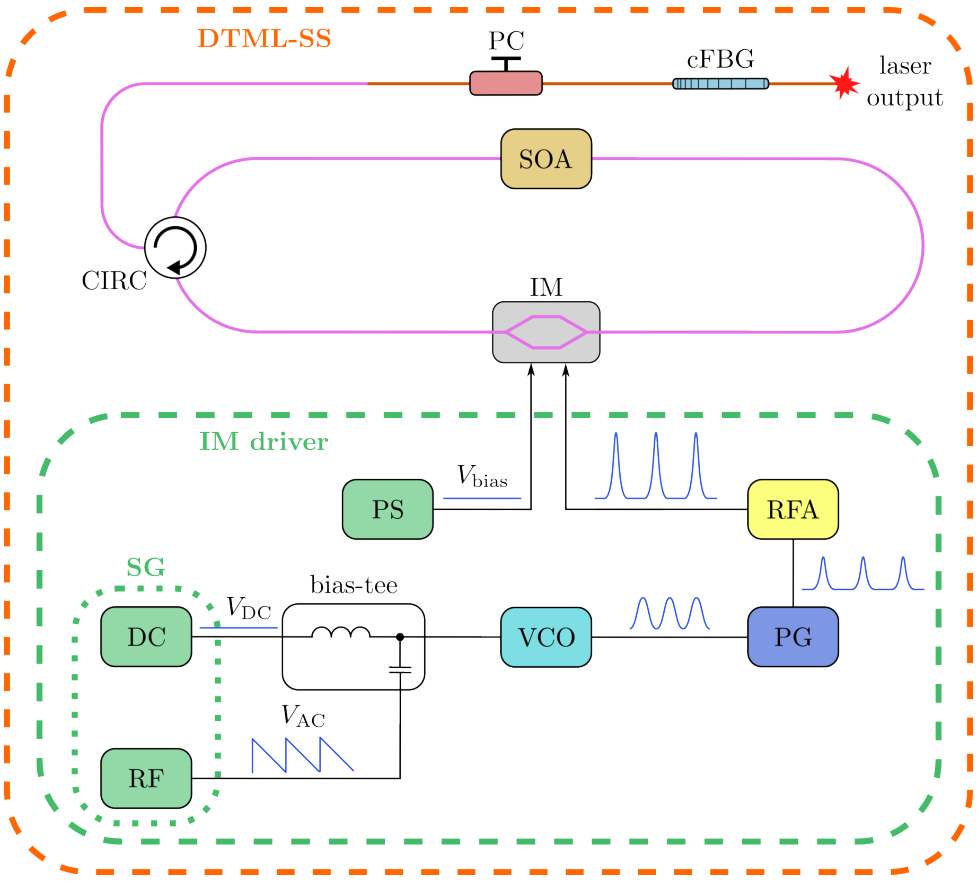

Figure 7.4: DTML swept source 850 nm. SOA: semiconductor optical amplifier, IM: intensity modulator, CIRC: optical circulator, PC: polarisation controller, cFBG: chirped fibre Bragg grating, SG: arbitrary function signal generator, VCO: voltage-controlled oscillator, PG: pulse generator, RFA: RF amplifier, PS: power supply.

The light exiting the cFBG is amplified by another semiconductor optical amplifier (BOA, the same model as the gain medium inside the cavity, now operating as a booster) and directed to an interferometer, the configuration of which is shown in Fig. 7.5. The optical spectrum of the BOA output is monitored using an optical spectrum analyser (OSA, Agilent Technologies 86145B). The interferometer consists of two couplers arranged to recirculate the reference arm light, preventing light from being reflected back into the swept source. The interferometer is terminated with a balanced photodetector (bPhD, New Focus 1607). The output signals from the interferometer are observed on an oscilloscope (OSC, Teledyne Lecroy WaveRunner 104MXi-A). The optical path difference (OPD) in the interferometer is adjusted by translating the mirror M along the z-axis from the position where OPD = 0.

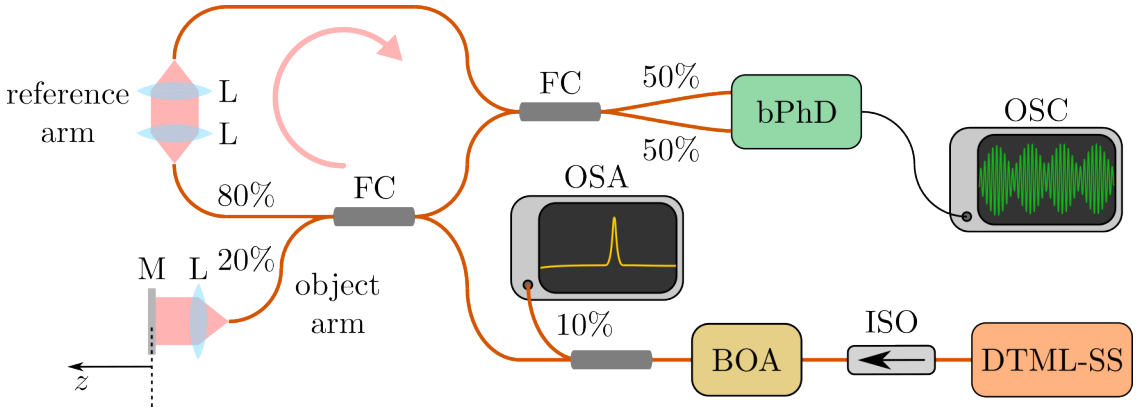

Figure 7.5: SS-OCT setup used for characterisation of the 850 nm DTML swept source in Fig. 7.4. The recirculation of the reference arm right is depicted with an arrow. DTML-SS: dispersion tuned mode-locked swept source, ISO: isolator, BOA: booster optical amplifier, OSA: optical spectrum analyser, FC: fibre coupler, L: launcher lens system, M: mirror, bPhD: balanced photodetector block, OSC: oscilloscope.

The relationship between the shift in the lasing wavelength $\Delta\lambda_{\text{single}}$ and the change in the modulation frequency Δf is given by the high harmonic expression in Eq. (4.13),

$$\Delta\lambda_{\text{single}} \approx -\frac{1}{\text{TDD}_{\text{cav}} f_{\text{cav}} f_0}\Delta f = S(f_0)\Delta f. \tag{7.4}$$

The VCO central modulation frequency is determined by V_{DC} and its frequency is tuned from 1113.80 MHZ to 1122.60 MHz by repeatedly applying V_{AC}. Experimentally, the polarisation state in the cavity is adjusted actuating on the PC in Fig. 7.4, affecting

both the central lasing wavelength and the tuning bandwidth. The polarisation state was optimised to achieve the best compromise between the tuning bandwidth and the low amplitude ripple within the spectrum.

Fig. 7.6 shows stationary tuning (no fast tuning) spectra obtained by sinusoidal modulation (modulation window width of $\approx 1/2f_0 \doteq 500\,\text{ps}$) and by pulse modulation technique (modulation window width of $\doteq 50\,\text{ps}$), both at $f_0 \doteq 1.1\,\text{GHz}$. Fig. 7.6 illustrates three improvements due to the pulse modulation: (i) the detrimental ASE is reduced, (ii) spectral peaks are better defined, and (iii), tuning bandwidth is enlarged from 25 nm to 35 nm, in agreement with experimental findings in [9]. These observations are consequences of applying shorter modulation windows, of which effect on the lasing spectra is exactly modelled in Subsec. 6.4.2. To document further the advantage of the pulse modulation in comparison with the sinusoidal modulation, Fig. 7.7 shows the interferometer output signals at the mirror M position of $z = 25\,\mu\text{m}$ (see Fig. 7.5). This measurement was performed using the bPhD monitor output in order to provide a proportional value to both the ASE power as well as to the fringes imprinted by the interference. The source was tuned for this measurement within a 25 nm tuning bandwidth at a 10 kHz sweep rate. The fringe depth, defined as $(V_{\max} - V_{\min})/(V_{\max} + V_{\min})$, where V represents the voltage of the photodetected signal, was measured to be 0.62 and 0.72 for the sinusoidal modulation and the pulse modulation, respectively.

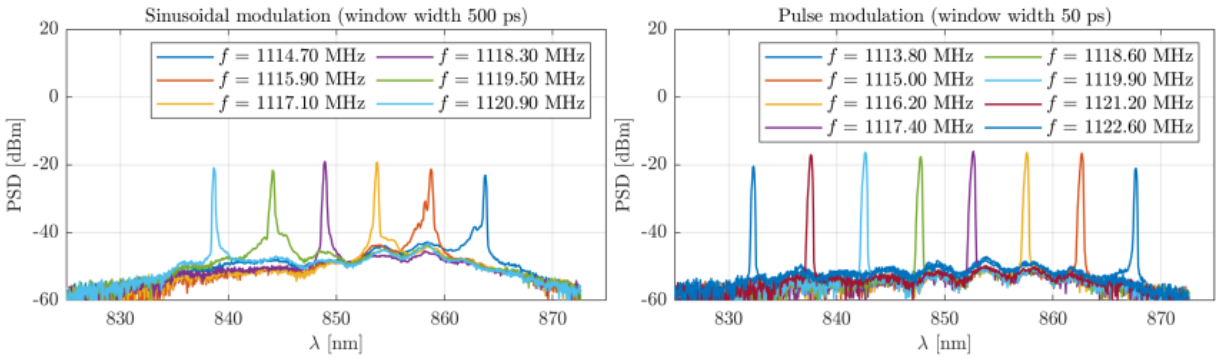

Figure 7.6: Comparison of the stationary tuning spectra using the sinusoidal and pulse modulation.

By applying the pulse modulation in the stationary regime, the linewidth was measured as $\delta\lambda_{\text{stat}} \doteq 0.09\text{-}0.11\,\text{nm}$, which is also the narrowest linewidth achievable from the laser.

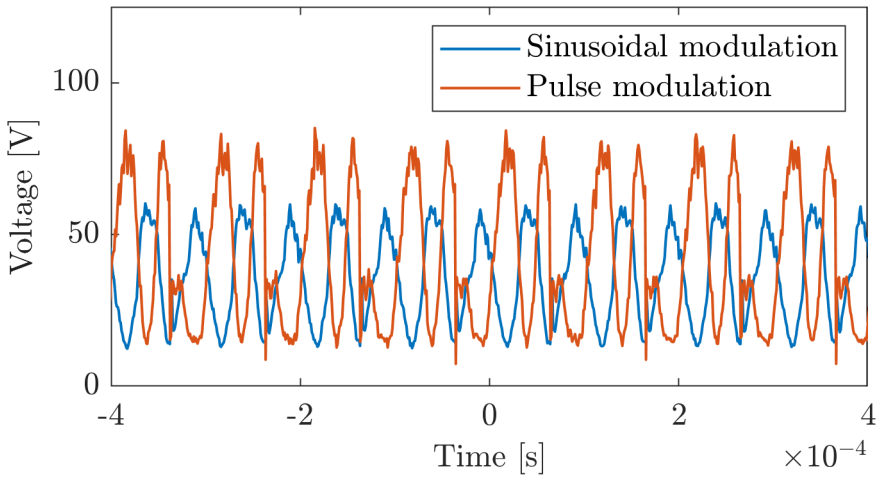

Figure 7.7: Comparison of the interferometer output signal using the sinusoidal and pulse modulation for the mirror M distance $z = 25\,\mu\text{m}$ in Fig. 7.5.

7.2.2 Results

The peak-hold spectra obtained from the swept source (without the BOA) using the pulse modulation technique at three different sweep rates f_s are shown in Fig. 7.8 left. As the sweep rate increases, spectral degradation becomes more pronounced, as predicted by the sweep rate limitations given by Eq. (4.17) and Eq. (4.19). This degradation is primarily observed as a reduction in power spectral density (PSD) within the first half of the tuning bandwidth. This effect can be attributed to the lower gain of the SOA on the shorter-wavelength side of 850 nm, which may require more cavity round trips for the emission to reach saturation, compared to those in the longer-wavelength portion of the gain spectrum, as described by R_{sat} in Eq. (4.16). Fig. 7.9 shows the total output power of the swept source (without the BOA) as a function of sweep rate f_s.

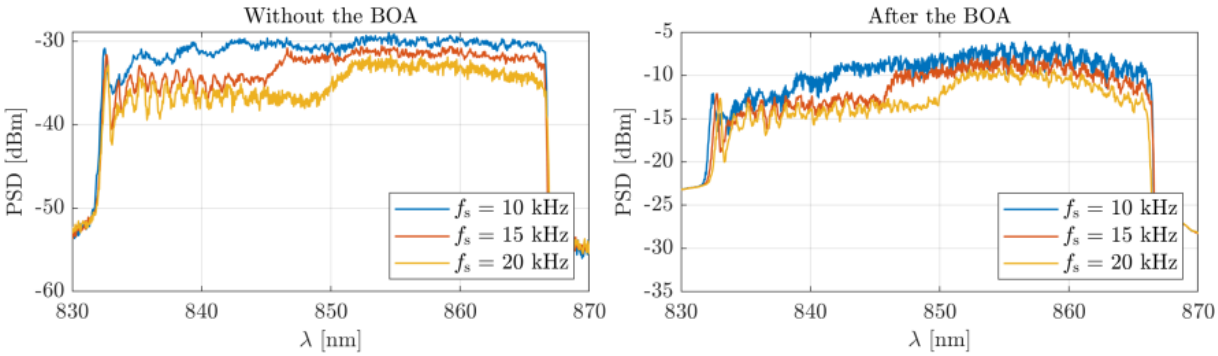

Figure 7.8: Peak-hold spectra without and after the BOA.

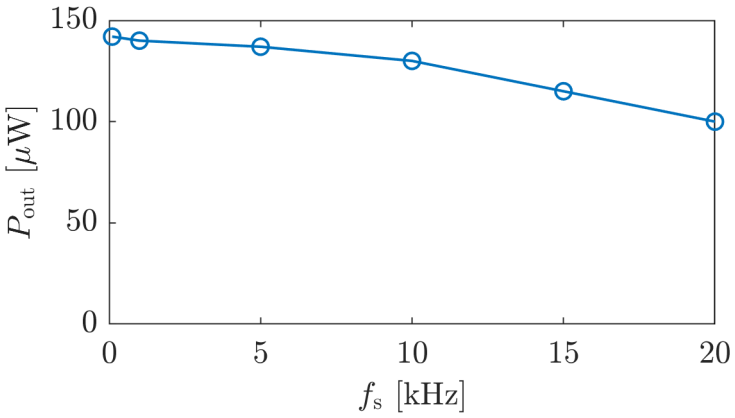

Figure 7.9: Laser output power P_{out} without the BOA as a function of sweep rate f_{s}.

By adding the BOA to the DTML swept source output in Fig. 7.5, the output power increases to 8.2 mW at 10 kHz sweep rate. However, there is an ASE contribution from the BOA, visible in the spectra in Fig. 7.8 right. The reflective profiles (A-scans) roll-off measurements utilising the interferometer and the method of Leader-Follower interferometry [10] are displayed in Fig. 7.10. First, a roll-off measurement for 25 nm tuning range using the sinusoidal modulation was performed. It can be seen that a short imaging depth of only $\Delta z_{\text{6dB}} = 0.3$ mm was achievable. Then, the operating regime was switched to the pulse modulation, whose roll-off measurements for 35 nm tuning bandwidth are plotted in Fig. 7.10 as well. As can be predicted using Eq. (4.17) and Eq. (4.19), the faster the sweeping, the lower the output power. The degradation in the axial resolution is expected due to the narrowing of the tuning bandwidth with f_{s} shown in Fig. 7.8. The FWHM axial resolutions (measured on an A-scan peak close to zero axial coordinate z) for 10 kHz, 15 kHz, and 20 kHz sweep rates were measured as 15 µm, 22 µm, and 44 µm, respectively. The measured value of 15 µm at 10 kHz sweep rate is close to the theoretical value given by $\delta z_{\text{top-hat}} = 0.60\lambda^2/\Delta\lambda \doteq 12$ µm for a top-hat tuning spectral shape (see Eq. (2.7)). However, no significant degradation in the imaging depth is observed, as for all three sweep frequencies similar values of $\Delta z_{\text{6dB}} \doteq 1$ mm are obtained for a 50% drop in A-scan sensitivity.

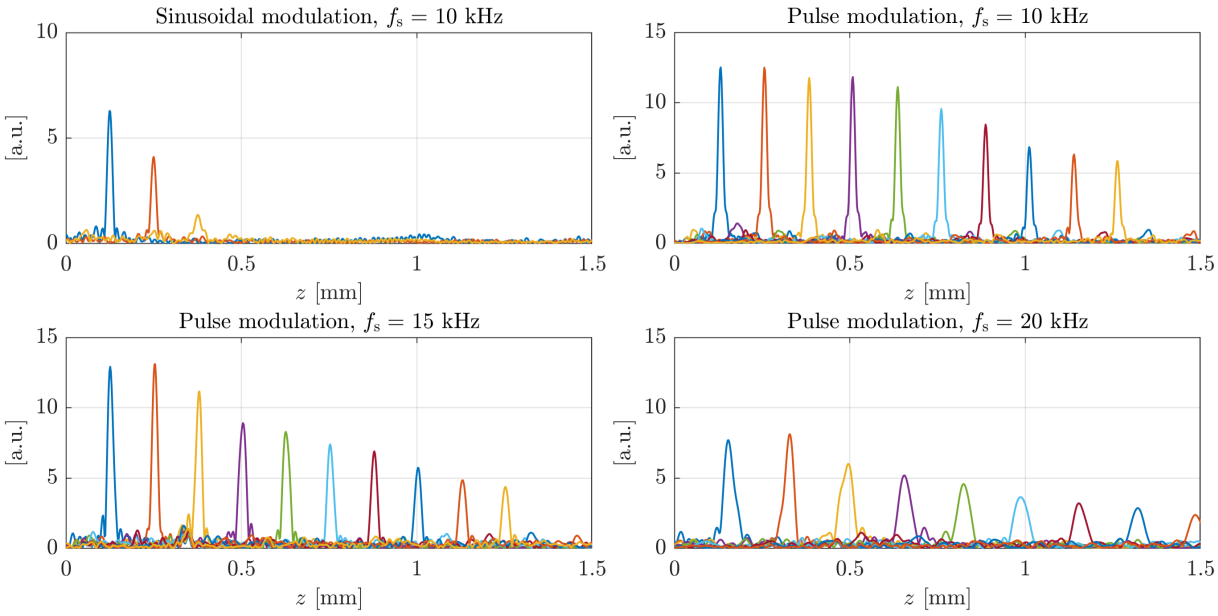

Figure 7.10: A-scan sensitivity roll-offs for different sweep rates f_s.

7.2.3 Conclusion

In the study, the combined use of a cFBG and a high-speed intensity modulator driven by short electrical pulses is demonstrated to enable DTML operation at shorter wavelengths of 850 nm. The laser achieved a tuning bandwidth exceeding 30 nm and showed improved performance compared to previously reported DTML swept sources utilising an SOA direct modulation [11]. A sweep rate of 10 kHz was obtained, with potential for further increase through cavity length reduction, as suggested by the saturation operation condition in Eq. (4.17). Coherence was significantly enhanced by applying narrow modulation windows with a temporal window width of 50 ps, yielding a linewidth comparable to that achieved in galvo- and acousto-optic based swept sources [12, 13]. Further improvements in coherence length are anticipated using even shorter modulation windows, allowed by advances in ultrashort electrical pulse generation. The presented swept source is well suited for integration into FFSS-OCT systems, offering a compact, high-speed alternative to current commercial sources that are limited to 2 kHz sweep rates. With ongoing refinements, such as cavity length reduction, this laser architecture may support volume acquisition rates compatible with tens-of-kHz high-speed 2D CMOS cameras.

7.3 A 900 kHz multi-harmonic DTML swept source at 1550 nm for OCT using a cFBG and an intensity modulator

The study [3] presents a high-speed akinetic swept source operating at 1550 nm employing the multi-harmonic DTML described in Chap. 5. The architecture achieves mode-locking through a high-speed intensity modulator and incorporates a cFBG to provide the necessary dispersion in the cavity. This design enables MHz sweep rates with improved coherence and stability in comparison with the previous reports on multi-harmonic DTML [14, 15] lasers and offers an electronically controllable alternative for next-generation akinetic OCT systems.

7.3.1 Experimental setup

The schematic of the researched DTML laser is depicted in Fig. 7.11. As the gain medium, a semiconductor optical amplifier (SOA, CIP Technologies SOA-S-C-14-FCA, optical bandwidth 60 nm at a current of 100 mA) is employed. The SOA is followed by a polarisation-insensitive optical isolator (ISO, FOCI Inc.), and by SMF-28e fibre delay of approximately 200 m in length. An optical circulator (CIRC, AFW Technologies) conveys the light to a chirped fibre Bragg grating (cFBG, VFibre, optical bandwidth 40 nm). The mode-locking is achieved by modulating a high-speed intensity modulator (IM, Sumitomo Osaka Cement Co. 14 GHz). The modulator fibre pigtails consist of a polarisation maintaining fibre, while all other fibre connections are implemented using non-polarisation maintaining single-mode fibre. To maximize transmission in the cavity, inline polarisation controllers (PC) are employed. Output light is extracted via a fibre coupler (FC) with 80% of power reinjected back into the cavity. The ISO together with the CIRC ensure unidirectional lasing in the laser cavity. After isolation, the cavity output is amplified with a booster amplifier (BOA, CIP Technologies SOA-L-C-14-FCA). Fundamental frequency of the cavity is evaluated to be 912 kHz, corresponding to a total cavity length of 226 m, and effective dispersion was estimated as 14.1 ps/nm using the

assessment technique described in Sec. 7.1.

A schematic diagram of the electronic circuitry driving the IM is detailed in Fig. 7.11 as well (inside the green dashed rectangle). A voltage-controlled oscillator (VCO, Mini-Circuits ZX95-1790-S+), is driven by a DC off-set, V_{DC}, and a sawtooth AC signal, V_{AC}, from a signal generator (SG, Agilent Technologies 81160A) through an in-house bias-tee. The VCO output sinusoidal signal $V(t)$ is amplified by a radio frequency amplifier (RFA, Mini-Circuits ZHL-42W) and then applied to the IM through a high-speed bias-tee. Finally, the bias of the IM is controlled separately by a DC bias voltage, V_{bias}, from a regulated power supply (PS, PowerLine Electronics).

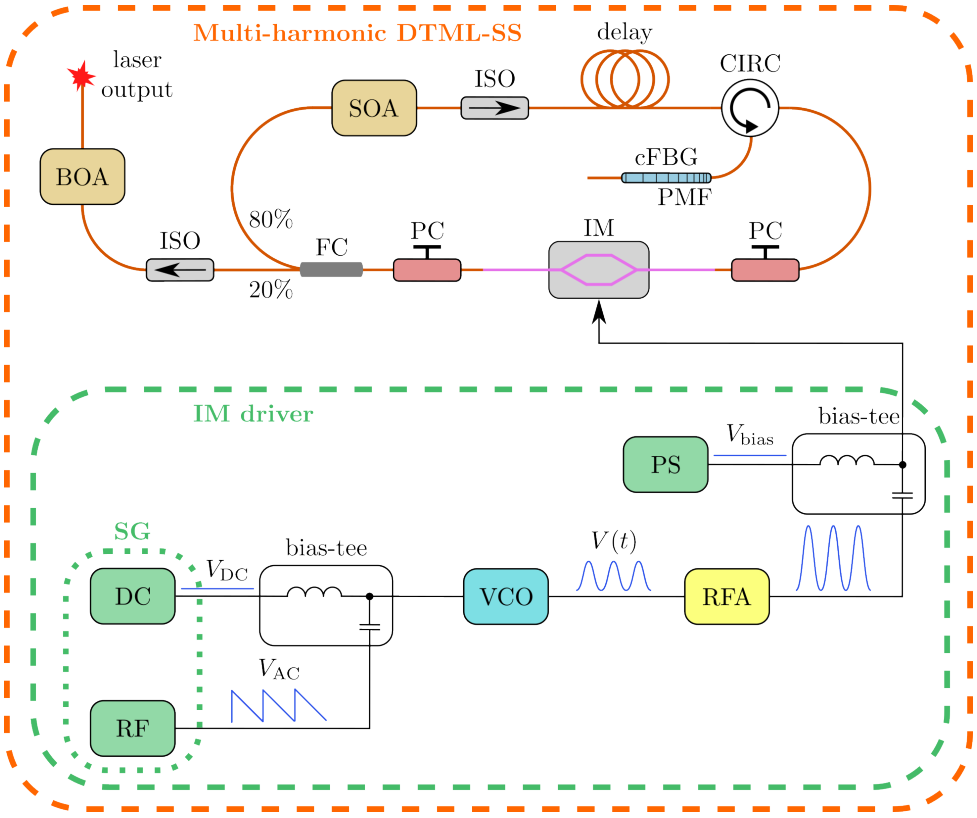

Figure 7.11: Multi-harmonic DTML-SS at 1550 nm. SOA: semiconductor optical amplifier, ISO: optical isolator, CIRC: optical circulator, cFBG: chirped fibre Bragg grating, PC: polarisation controller, IM: fibre intensity modulator, FC: fibre coupler, BOA: booster amplifier, SG: signal generator, VCO: voltage-controlled oscillator, RFA: RF amplifier, PS: power supply.

For the lasing characterisation of the swept source, the output light is directed to an interferometer, whose schematic is depicted in Fig. 7.12. The interferometer consists of

two couplers with recirculation of the reference arm light to avoid light being directed back into the optical source, terminated with a balanced photodetector (bPhD, Thorlabs PDB460C). The signal from the bPhD was observed on an RF spectrum analyser (RFSA, Agilent E4411B), and an oscilloscope (OSC, Agilent 54622A).

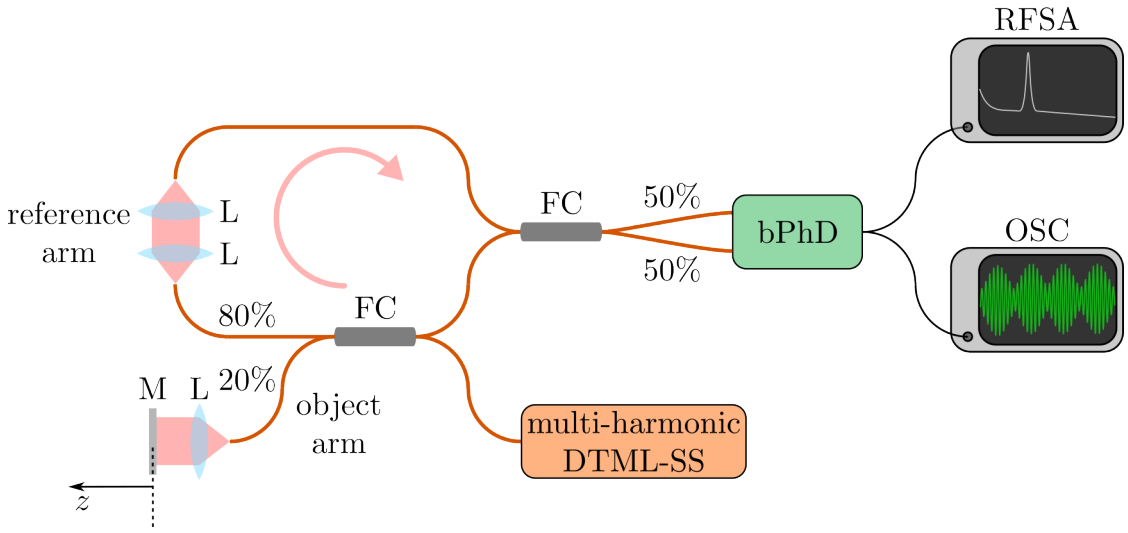

Figure 7.12: OCT setup used for characterization of the swept source in Fig. 7.11. The recirculation of the reference light is depicted with an arrow. BOA: booster optical amplifier, FC: fibre coupler, L: launcher lens system, M: mirror, bPhD: balanced photodetector, RFSA: RF spectrum analyser, OSC: oscilloscope.

7.3.2 Results

A positive sawtooth signal with a DC offset of 5 V and peak-to-peak amplitude of 10 V at sweep rate of $f_s \doteq 912\,\text{kHz}$ was applied to the VCO. The negative direction of the ramp function was used, as it was observed that better coherence properties were achieved in comparison with using a negative positive sawtooth signal. For an anomalous cavity dispersion of 14.1 ps/nm and detunings $\delta f_s < 0$, that determines wavelength tuning from shorter to longer wavelengths (forward sweeping), as given by Eq. (5.14),

$$\Delta\lambda_{\text{multi}} = -\frac{\delta f_s}{\text{TDD}_{\text{cav}} f_{\text{cav}}^2} \ln\left(\frac{f_0 + \Delta f/2}{f_0 - \Delta f/2}\right). \tag{7.5}$$

An experimentally recorded RF spectrum of the VCO output signal is displayed in Fig. 7.13. The spectrum consists of a frequency comb with the spacing given by $f_s \doteq$

912 kHz and a spectral spread of $\Delta f \doteq 185$ MHz, measured as FWHM of the power spectral density (PSD).

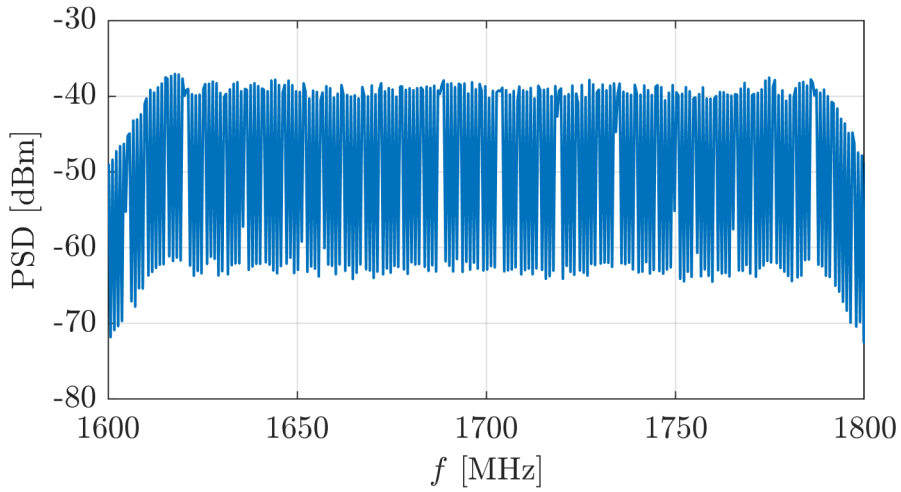

Figure 7.13: Experimentally measured spectral content of the signal applied to the IM in Fig. 7.11, with parameters $\Delta f_0 \doteq 1700$ MHz, $\Delta f \doteq 185$ MHz, and $f_\mathrm{s} \doteq 912$ kHz.

Optical peak-hold spectra obtained without the BOA for different values of δf_s from the reference $f_\mathrm{s} \doteq 912$ kHz are displayed in Fig. 7.14. To obtain flat optical spectral shapes, the polarisation state was altered by fine adjustments applied to the PCs in Fig. 7.11. The right vertical axis in Fig. 7.15 plots tuning bandwidths $|\Delta\lambda_\mathrm{multi}|$ as a function of δf_s. According to the experimental measurements in Fig. 7.15, $|\Delta\lambda_\mathrm{multi}|$ exhibits a linear tuning sensitivity of $S'_\mathrm{multi} \doteq 9$ nm/kHz, in good agreement with the approximative formula in Eq. (5.16),

$$\Delta\lambda_\mathrm{multi} \approx -\frac{\Delta f}{\mathrm{TDD}_\mathrm{cav} f_\mathrm{cav}^2 f_0}\delta f_\mathrm{s} = S'_\mathrm{multi}\delta f_\mathrm{s}. \tag{7.6}$$

The laser output power as a function of δf_s without the BOA is plotted on the left vertical axis of the plot in Fig. 7.15.

By employing the BOA in the swept source in Fig. 7.11, the laser output power increased to 6.9 mW. The A-scan sensitivity roll-off measurements displayed in Fig. 7.16 were obtained using the interferometer in Fig. 7.12. For the tuning bandwidths $|\Delta\lambda_\mathrm{multi}| \doteq$ 15 nm, 20 nm and 25 nm, the roll-offs exhibit decay with one sided 50% sensitivity drop imaging depth above 1 mm. For $|\Delta\lambda_\mathrm{multi}| \doteq 28$ nm, however, a degradation in coherence was observed. The degradation can be associated with the decrease of number of round

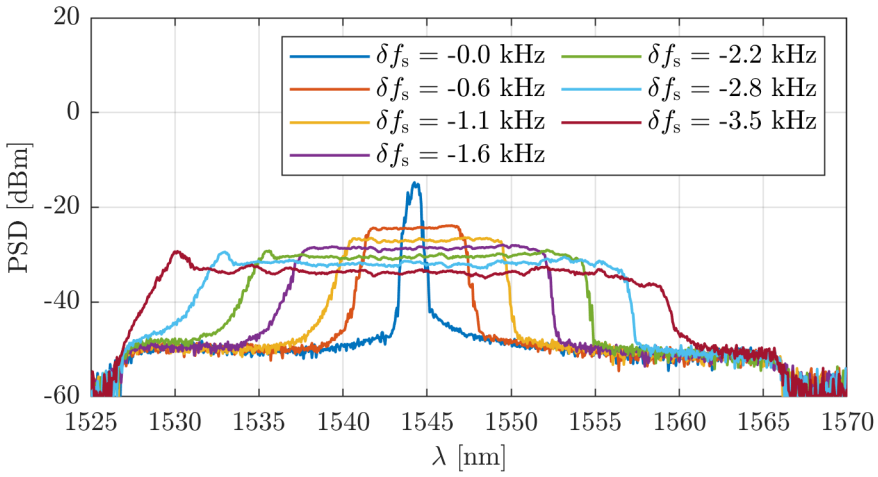

Figure 7.14: Peak-hold spectra as a function of the detuning δf_s from the reference $f_\mathrm{s} \doteq 912\,\mathrm{kHz}$.

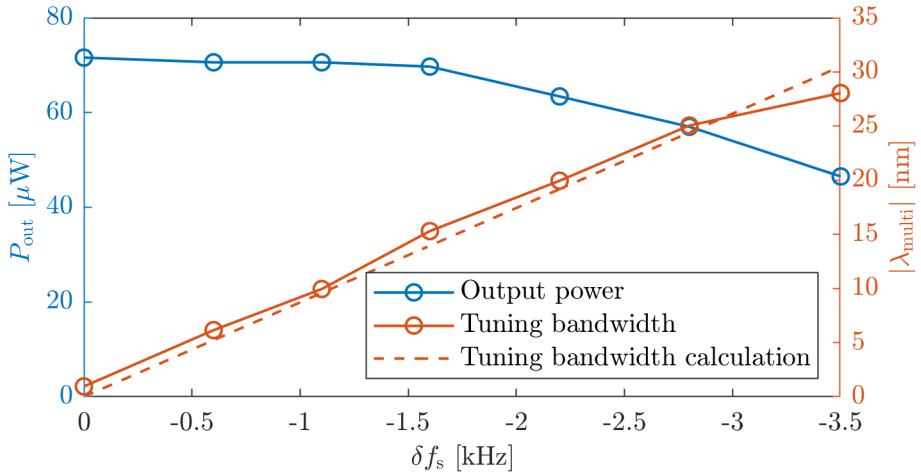

Figure 7.15: Measurements of the laser output power P_out (without the BOA) and tuning bandwidths $|\Delta\lambda_\mathrm{multi}|$ of the spectra in Fig. 7.14 as a functiob of the detuning δf_s from the reference $f_\mathrm{s} \doteq 912\,\mathrm{kHz}$.

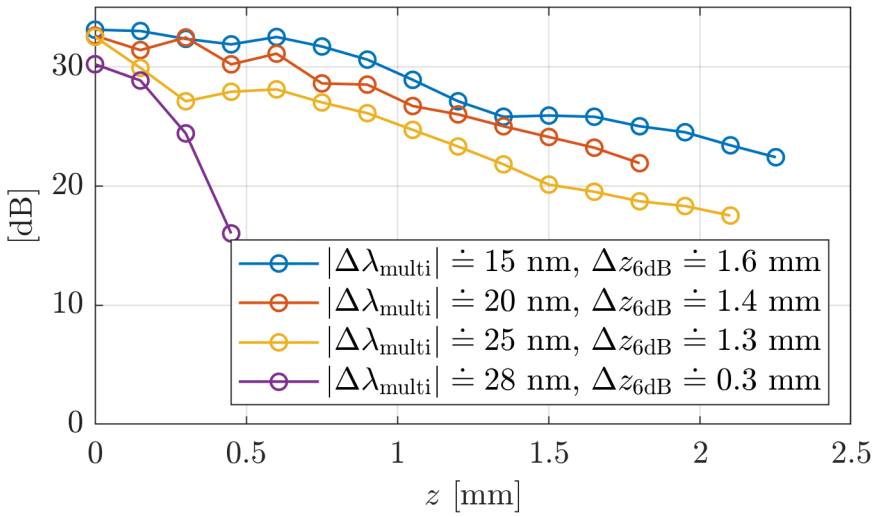

Figure 7.16: A-scan sensitivity roll-off measurements for different tuning bandwidths $|\Delta\lambda_{\text{multi}}|$.

trips of photons circulating inside the cavity, the phenomenon described in Sec. 5.4.

The system sensitivity obtained from the interferometer is measured for z coordinate close to zero, calculated as $20\log(A_{\text{signal}}/A_{\text{floor}})$, where A_{signal} and A_{floor} represent the A-scan amplitude and the floor level noise, respectively. The noise level was measured with the object arm in Fig. 7.12 blocked. A sensitivity of 66 dB without the BOA was obtained. By adding the BOA, the sensitivity at the same depth increased to 82 dB.

In order to measure the axial resolution, post-processing corrections are necessary for the chirp in the interference signal, due to the nonlinear sweeping from the source and unbalanced dispersions in the interferometer arms. For this purpose, the method of Leader-Follower interferometry was utilised [10]. The axial point spread profiles displayed in Fig. 7.17 for different tuning bandwidths were produced at $z = 1\,\text{mm}$. In Tab. 7.2, the measured axial resolution values δz are compared with the theoretical $\delta z_{\text{top-hat}} \approx 0.60\lambda^2/|\Delta\lambda_{\text{multi}}|$ values calculated for a top-hat optical spectral shape (see Eq. (2.7)). The measured resolution values are in good agreement with the theoretical calculations.

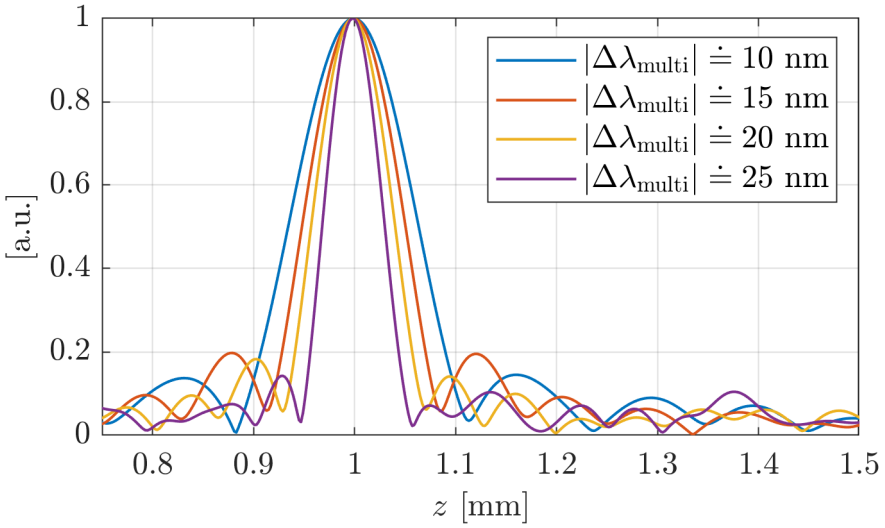

Figure 7.17: Axial point spread profiles at 1 mm for different tuning bandwidths $|\Delta\lambda_{\text{multi}}|$. For better display, the profiles are normalized and aligned exactly at $z = 1\,\text{mm}$.

Table 7.2: Comparison of the measured axial resolution δz values of the profiles in Fig. 7.17 with the theoretical $\delta z_{\text{top-hat}} \approx 0.60\lambda^2/|\Delta\lambda_{\text{multi}}|$ values obtained for a top-hat optical spectral shape (see Eq. (2.7)).

$\lvert\Delta\lambda_{\text{multi}}\rvert$ [nm]	10	15	20	25
δz [mm]	0.13	0.10	0.08	0.06
$\delta z_{\text{top-hat}}$ [mm]	0.14	0.10	0.07	0.06

7.3.3 Conclusion

The multi-harmonic operation was demonstrated for a DTML swept source at 1550 nm using a high-speed intensity modulator and a cFBG. A sweep rate of approximately 900 kHz and a tuning bandwidth of 25 nm were achieved, with the OCT system sensitivity of 82 dB and improved coherence compared to previous SOA-modulated multi-harmonic implementations [14, 15]. The coherence degradation observed at large tuning bandwidths confirms the trade-off between the tuning bandwidth and coherence derived in Subsec. 5.4. Based on the theoretical findings developed in Chap. 5, improved laser performance is demonstrated in a multi-harmonic DTML system operating at 1 µm described in Sec. 7.4.

7.4 A 1 MHz multi-harmonic DTML swept source at 1 µm for OCT

This multi-harmonic DTML swept source is a part of the study [4]. It represents the first demonstration of this type of laser operating at 1 µm, with a tuning bandwidth of 30 nm achieved at nearly 1 MHz sweep rate. Owing to its coherence and high signal-to-noise ration reaching 90 dB, OCT images of a finger tip and the retina are captured for the first time by using the multi-harmonic DTML regime.

7.4.1 Experimental setup

The DTML swept source (DTML-SS) researched is schematically depicted in Fig. 7.18. Gain in the cavity is provided by a semiconductor optical amplifier (SOA, Innolume SOA-1060-90-PM-30dB, full bandwidth 90 nm), whilst dispersion is produced by a chirped fibre Bragg grating (cFBG, Teraxion PSR-1040-200(+21.9-0.046)-0S2-0L, dispersion 22 ps/nm, bandwidth 200 nm). Mode-locking in the cavity is achieved by employing an intensity modulator (IM, Optilab IMP-1064-20-PM, electronic bandwidth 20 GHz, optical bandwidth 60 nm). Through an optical circulator (CIRC, OZ Optics FOC-12P-111-6/125-PPP-1060-50-3A3A3A-1-1-WB, bandwidth 100 nm), the light is directed to the cFBG, and 20% of the power is coupled out through its transmission end. A 100 m fibre delay is inserted between the CIRC and the cFBG, providing an additional 200 m to the cavity length. After transmission through an isolator (ISO, AFW ISOS-64-B-1-2), the output light is amplified through a booster amplifier (BOA, Innolume BOA-1060-80-HI-120mW, bandwidth 80 nm). The fundamental frequency of the cavity is evaluated to be 944 kHz, corresponding to a total cavity round trip length of 217 m, and the cavity dispersion is estimated to be 14.3 ps/nm using the evaluation technique described in Sec. 7.1.

A schematic diagram of the signal generator driving the IM is depicted in Fig. 7.18 in the green dashed box. A voltage-controlled oscillator (VCO, Mini-Circuits ROS-3000-819+) is driven by DC voltage (V_{DC}) from a regulated power supply (PS) and AC voltage ($V_{\mathrm{AC}}(t)$) from a signal generator (SG, Agilent Technologies 81160A). The VCO produces

a sinusoidal wave signal $V(t)$ with a frequency $f(t)$ proportional to V_{DC} and $V_{\mathrm{AC}}(t)$,

$$f(t) = \eta_{\mathrm{VCO}}[V_{\mathrm{DC}} + V_{\mathrm{AC}}(t)], \tag{7.7}$$

where η_{VCO} is the Hz/V tuning sensitivity. A VCO instead of a professional signal generator is employed here for its large RF bandwidth that it can provide (units of GHz). Such a large RF bandwidth is necessary for the multi-harmonic DTML, where many mode-locking harmonic orders are engaged. In addition, VCOs are generally of significantly lower cost and more compact size than professional signal generators. As a trade-off, due to the large ratio between its bandwidth and central frequency, the VCO tuning sensitivity $\eta_{\mathrm{VCO}} = \eta_{\mathrm{VCO}}(V_{\mathrm{DC}}, V_{\mathrm{AC}}(t))$ may not be precisely constant over a large range of input voltages. The VCO signal is then directed to a pulse generator (PG, AlnairLabs EPG-210M-0050-S-P-N-N), which generates a short pulse of 50 ps width per each period of the input sinusoidal signal. This means that the pulse repetition frequency f is that of the instantaneous input sinusoidal signal provided by the VCO. The pulses are then amplified up to 5 V peak-to-peak amplitude with a negligible distortion through a pair of cascaded RF amplifiers (RFA, Mini-Circuits ZVA-01243+, 1-22 GHz, 22 dBm, and Xmicrowave XM-A3E6-0804C-01, DC-20 GHz, 25 dBm) and applied to the IM. Finally, the bias of the IM is controlled separately by a DC voltage (V_{bias}) from a second output of the PS.

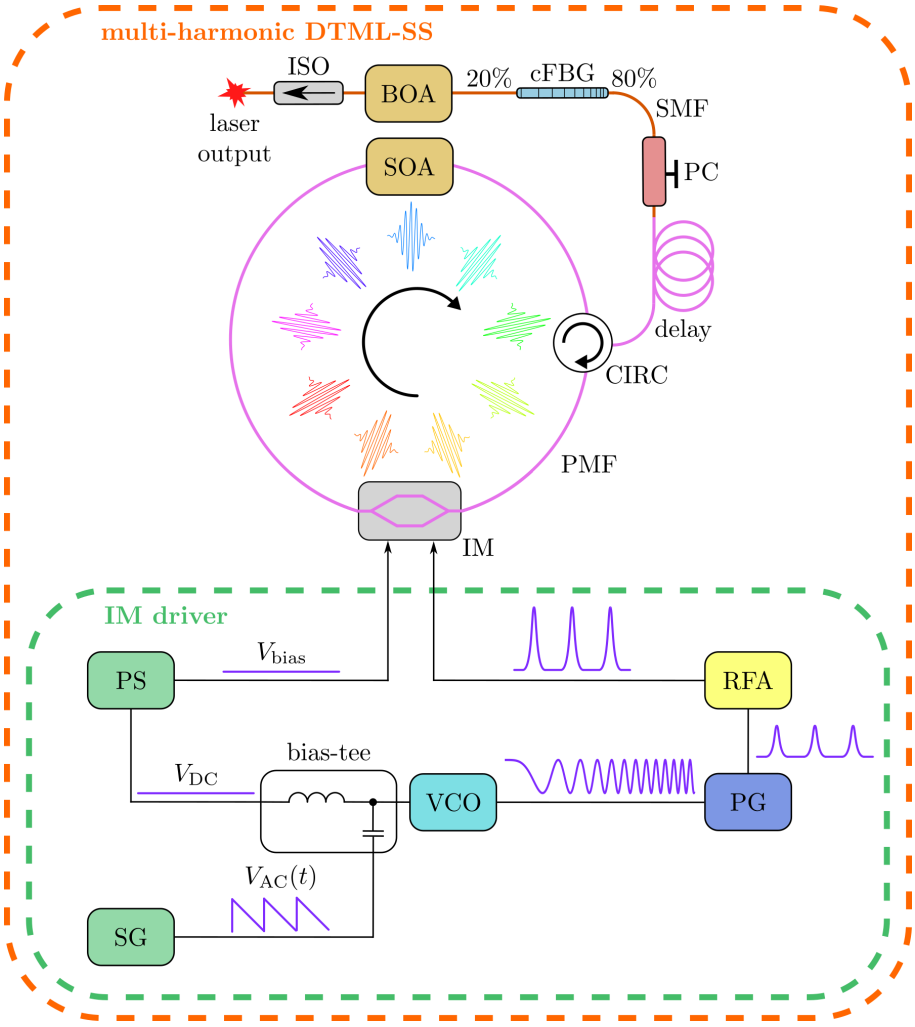

Figure 7.18: Multi-harmonic DTML-SS at 1 µm. SOA: semiconductor optical amplifier, CIRC: circulator, PC: polarization controller, SMF: single mode fibre, cFBG: chirped fibre Bragg grating, ISO: isolator, BOA: booster amplifier, IM: intensity modulator, PMF: polarization maintaining fibre, PS: power supply, SG: signal generator, VCO: voltage-controlled oscillator, PG: pulse generator, RFA: RF amplifier, V_{DC}: DC voltage, $V_{\text{AC}}(t)$: AC voltage, V_{bias}: IM bias voltage.

The experimental OCT setup driven by the multi-harmonic DTML-SS is displayed in Fig. 7.19. The interferometer comprises two couplers, with a recirculation path in the reference arm to prevent the light being directed back into the swept source. In the object arm, 20% of the coupled light is deflected by a system of two galvanometer scanning mirrors. The interferometer is terminated on a balanced photodetector block (bPhD, Thorlabs PDB481C-AC). A 12-bit waveform digitizer board samples the photodetected signal at a rate of 4 GS/s (AlazarTech ATS9373). Using the Leader-Follower (CLF) interferometry method [10, 16, 17], A-scan and B-scan OCT images are obtained.

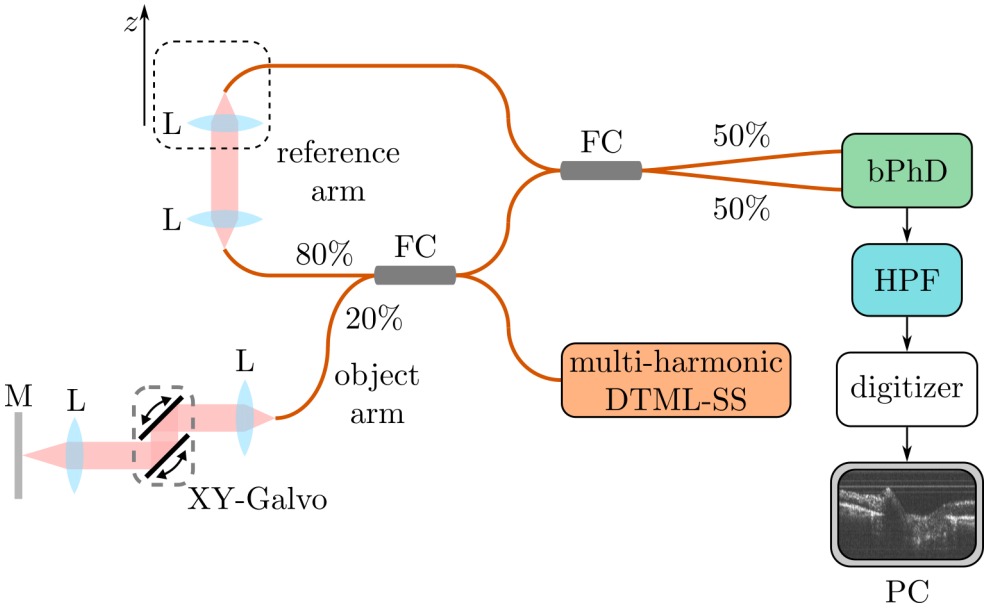

Figure 7.19: OCT setup. FC: fibre coupler, L: lens, M: mirror, bPhD: balanced photodetector block, HPF: high pass filter.

7.4.2 Results

The multi-harmonic DTML-SS in Fig. 7.18 was employed in the OCT setup in Fig. 7.19. The VCO modulation signal spectral content used for mode-locking of the laser is displayed in Fig. 7.20. The modulation frequency f was swept approximately linearly using a negative saw-tooth wave shape of $V_{\mathrm{AC}}(t)$ at a sweep rate of $f_{\mathrm{s}} \approx f_{\mathrm{cav}} \doteq 0.944\,\mathrm{MHz}$ over a $\Delta f \doteq 740\,\mathrm{MHz}$ frequency range, and centered around the offset frequency of $f_0 \doteq 2000\,\mathrm{MHz}$. The spectrum contains approximately $\Delta f / f_{\mathrm{s}} \doteq 780$ frequency components. Any noise on the input of the VCO is translated into jittering in the modulation

frequency, therefore a low pass filter was employed, which however also reduced the maximum voltage that could be applied from the SG to the VCO in Fig. 7.18.

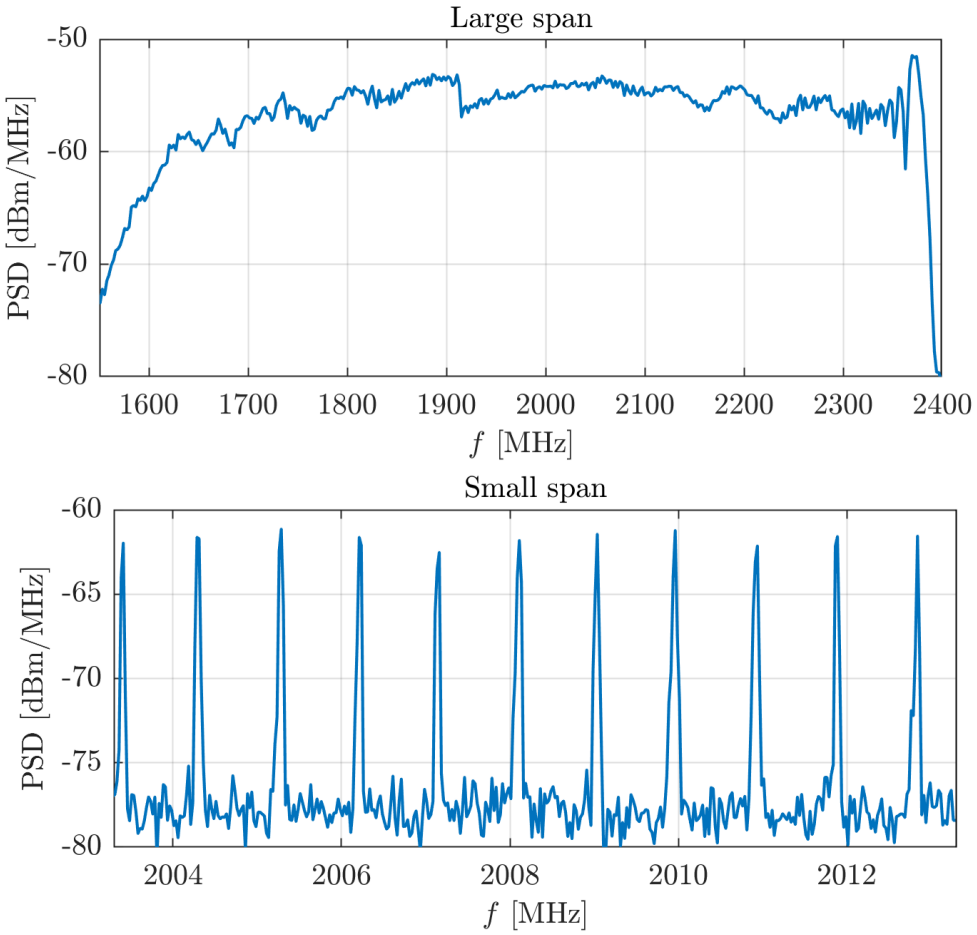

Figure 7.20: Large span (top) and small span (bottom) of the VCO modulation signal spectral content applied to the IM in Fig. 7.18, with parameters $f_0 \doteq 2000\,\text{MHz}$, $\Delta f \doteq 740\,\text{MHz}$, and $f_\text{s} \doteq 0.944\,\text{MHz}$.

An average stationary regime linewidth $\delta\lambda_\text{stat} \doteq 0.11\,\text{nm}$ was measured on the optical spectrum analyser. By substituting the measured parameters $P_\text{sat} \doteq 31\,\text{mW}$, $\Delta\lambda_\text{SOA} \doteq 60\,\text{nm}$, $P_\text{ASE} \doteq 2.75\,\text{mW}$, $G_\text{SOA} \doteq 1000$ (for the SOA injection current of 220 mA), and $\rho_\text{cav} \doteq 0.995$ into Eq. (4.16),

$$R_\text{sat} \approx \frac{\log\left(\dfrac{P_\text{sat}\Delta\lambda_\text{SOA}}{\delta\lambda_\text{stat}P_\text{ASE}}\right)}{\log[G_\text{SOA}(1-\rho_\text{cav})]}, \tag{7.8}$$

$R_\text{sat} \doteq 5.7$ was calculated. Fig. 7.21 displays a theoretical calculation of bandwidths

$\Delta\lambda_{\text{multi,sat}}$, $\Delta\lambda_{\text{multi,one}}$, and $\Delta\lambda_{\text{multi,n-d}}$ using Eq. (5.19), Eq. (5.20), and Eq. (5.17),

$$\Delta\lambda_{\text{multi,sat}} \approx \left[\frac{\delta\lambda_{\text{stat}}}{R_{\text{sat}}|\text{TDD}_{\text{cav}}|f_{\text{cav}}}\left|\ln\left(\frac{f_0+\Delta f/2}{f_0-\Delta f/2}\right)\right|\right]^{1/2}, \tag{7.9}$$

$$\Delta\lambda_{\text{multi,one}} \approx \left[\frac{\delta\lambda_{\text{stat}}}{|\text{TDD}_{\text{cav}}|f_{\text{cav}}}\left|\ln\left(\frac{f_0+\Delta f/2}{f_0-\Delta f/2}\right)\right|\right]^{1/2}, \tag{7.10}$$

$$\Delta\lambda_{\text{multi,n-d}} = \frac{1}{|\text{TDD}_{\text{cav}}|(f_0+\Delta f/2)}, \tag{7.11}$$

respectively, as a function of Δf, with specific values of $\Delta\lambda_{\text{multi,sat}} \doteq 23\,\text{nm}$, $\Delta\lambda_{\text{multi,one}} \doteq 55\,\text{nm}$, and $\Delta\lambda_{\text{multi,n-d}} \doteq 30\,\text{nm}$ at $\Delta f = 740\,\text{MHz}$. For a moment, let us suppose that the the single-harmonic DTML was employed with a shortest cavity length of 1.542 m reported [18]. In this case, substituting $f_{\text{s}} = 0.944\,\text{MHz}$, $\delta\lambda_{\text{stat}} = 0.11\,\text{nm}$, and $R_{\text{sat}} \doteq 5.7$ in Eq. (4.17) and Eq. (4.19),

$$\Delta\lambda_{\text{single,sat}} \approx \frac{\delta\lambda_{\text{stat}} f_{\text{cav}}}{R_{\text{sat}} f_{\text{s}}}, \quad \Delta\lambda_{\text{single,one}} \approx \frac{\delta\lambda_{\text{stat}} f_{\text{cav}}}{f_{\text{s}}}, \tag{7.12}$$

limited bandwidths of $\Delta\lambda_{\text{single,sat}} \doteq 3\,\text{nm}$ (compare with $\Delta\lambda_{\text{multi,sat}} \doteq 23\,\text{nm}$) and $\Delta\lambda_{\text{single,one}} \doteq 15\,\text{nm}$ (compare with $\Delta\lambda_{\text{multi,one}} \doteq 55\,\text{nm}$) would be possible only.

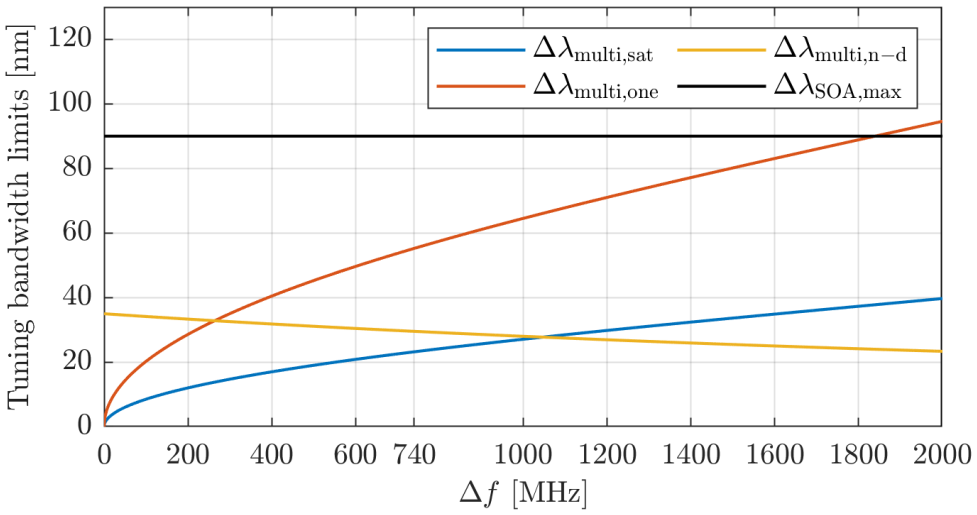

Figure 7.21: Theoretical calculation of the tuning bandwidth limits $\Delta\lambda_{\text{multi,sat}}$, $\Delta\lambda_{\text{multi,one}}$, and $\Delta\lambda_{\text{multi,n-d}}$ using Eq. (7.9), Eq. (7.10), and Eq. (7.11), respectively, as a function of Δf.

Fig. 7.22 shows peak-hold spectra of the laser under various detuning frequencies δf_s (without the BOA). The measured tuning bandwidths $|\Delta\lambda_\mathrm{multi}|$ of the spectra in Fig. 7.23 increases linearly with $|\delta f_\mathrm{s}|$, exhibiting a measured tuning sensitivity of $S'_\mathrm{multi} \doteq 27.5\,\mathrm{nm/kHz}$, in good agreement with the prediction given by Eq. (5.14),

$$\Delta\lambda_\mathrm{multi} = -\frac{\delta f_\mathrm{s}}{\mathrm{TDD}_\mathrm{cav} f_\mathrm{cav}^2} \ln\left(\frac{f_0 + \Delta f/2}{f_0 - \Delta f/2}\right) = S'_\mathrm{multi}\delta f_\mathrm{s}. \tag{7.13}$$

Two types of drift were observed in the spectra in Fig. 7.22 during extended measurements. The first was a drift in the central wavelength λ_0, caused by a gradual shift in the central modulation frequency f_0. Since the system uses a VCO with a high tuning sensitivity η_VCO, even small shifts in the DC voltage V_DC in Eq. (7.7) can lead to noticeable shift in the modulation frequency over time. To compensate for the drift in the central wavelength automatically, a feedback control scheme similar to that described in [19] could be implemented in future multi-harmonic DTML systems. The second type of drift originates from a shift in the bias point of the intensity modulator [20], which affects modulation depth and symmetry. This drift can be suppressed by employing an automatic bias control circuit. Both types of drift were observed to occur on a time scale of half an hour to units of hours. While no significant polarisation state drift was observed at least over several weeks of operation, dependence of the central wavelength and spectral modulation in the lasing spectra was observed by manually changing the polarisation state in the cavity using the PC in Fig. 7.18. This dependence could be eliminated by assembling an all polarisation-maintaining (PM) architecture including a PM-based cFBG, while preserving the theoretical framework of multi-harmonic operation developed in Chap. 5.

To evaluate coherence properties of the swept source, a mirror M was used as a sample in the setup depicted in Fig. 7.19. The interference signal resulting from interference using at the reference arm displacement $z = 0.25\,\mathrm{mm}$ is shown in Fig. 7.24 over one period T_s. This demonstrates that the multi-harmonic DTML-SS provides a continuous and monotonic wavelength tuning, despite involving many tuning bands in Fig. 5.6. The interference signal also exhibits a chirp requiring signal post-processing. To account for

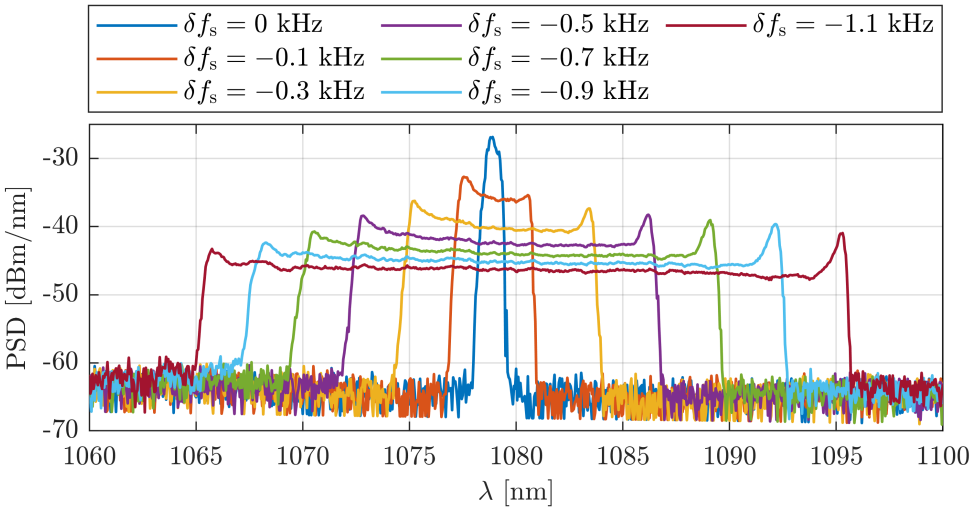

Figure 7.22: Peak-hold optical spectra for various δf_s in Eq. (7.13). The measured tuning bandwidths as a function of δf_s are plotted in Fig. 7.23.

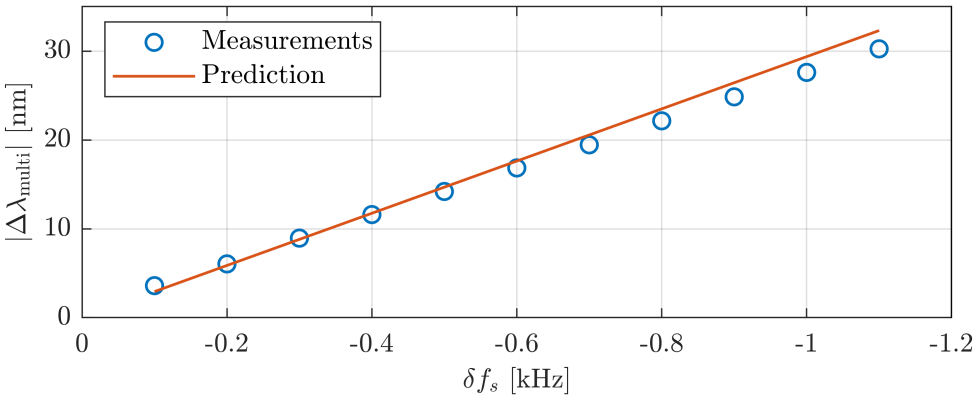

Figure 7.23: Measured tuning bandwidths $|\Delta\lambda_{\text{multi}}|$ of the spectra in Fig. 7.22 and the theoretical prediction according to Eq. (5.14) as a function of δf_s.

the chirp and produce A-scans, the method of Complex Leader-Follower interferometry (CLF) [10, 16, 17] is employed. Three sensitivity roll-off measurements for three different tuning bandwidths $|\Delta\lambda_{\text{multi}}|$ as a function of z are displayed in Fig. 7.25. The measured DTML-SS output powers without the BOA, P_{out}, output powers after the BOA, P_{BOA}, and 50% sensitivity drop imaging depths, $\Delta z_{6\text{dB}}$, are listed in Tab. 7.3. In agreement with estimated $\Delta\lambda_{\text{multi,sat}} \doteq 23\,\text{nm}$, the powers and coherence properties for $|\Delta\lambda_{\text{multi}}| \doteq 9\,\text{nm}$ and 19 nm are comparable with the stationary regime $|\Delta\lambda_{\text{multi}}| \doteq 0\,\text{nm}$. For $|\Delta\lambda_{\text{multi}}| \doteq 30\,\text{nm}$, however, a more significant reduction in coherence is observed. For this tuning bandwidth, a sensitivity between 85-90 dB and an axial resolution of 22 µm were measured, which is in close agreement with the theoretical prediction $\approx 0.6\lambda^2/\Delta\lambda \doteq 23\,\mu\text{m}$ for a top-hat optical spectral shape (see Eq. (2.7)).

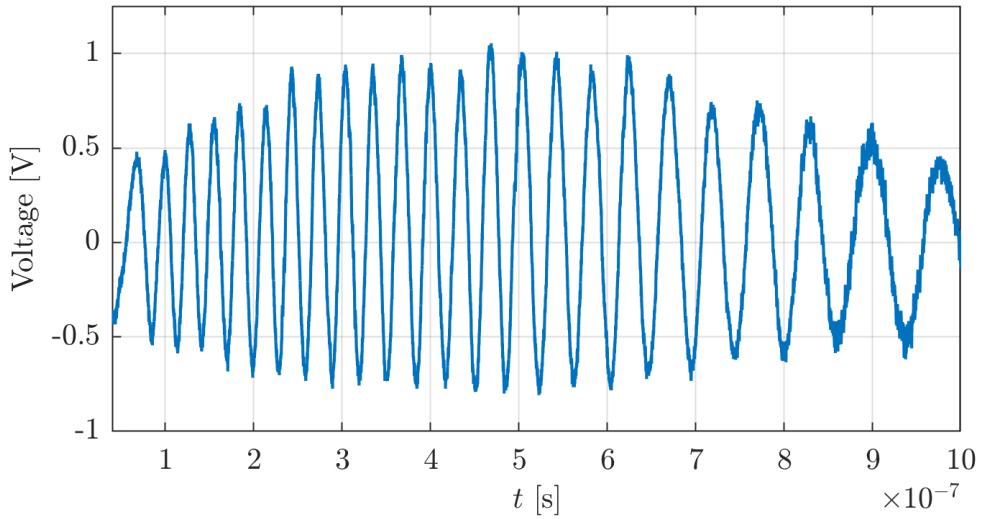

Figure 7.24: Photodetected signal showing the interference signal for a mirror M used as the sample in Fig. 7.19 at the reference arm displacement $z = 0.25\,\text{mm}$, obtained with a tuning bandwidth of $|\Delta\lambda_{\text{multi}}| \doteq 30\,\text{nm}$.

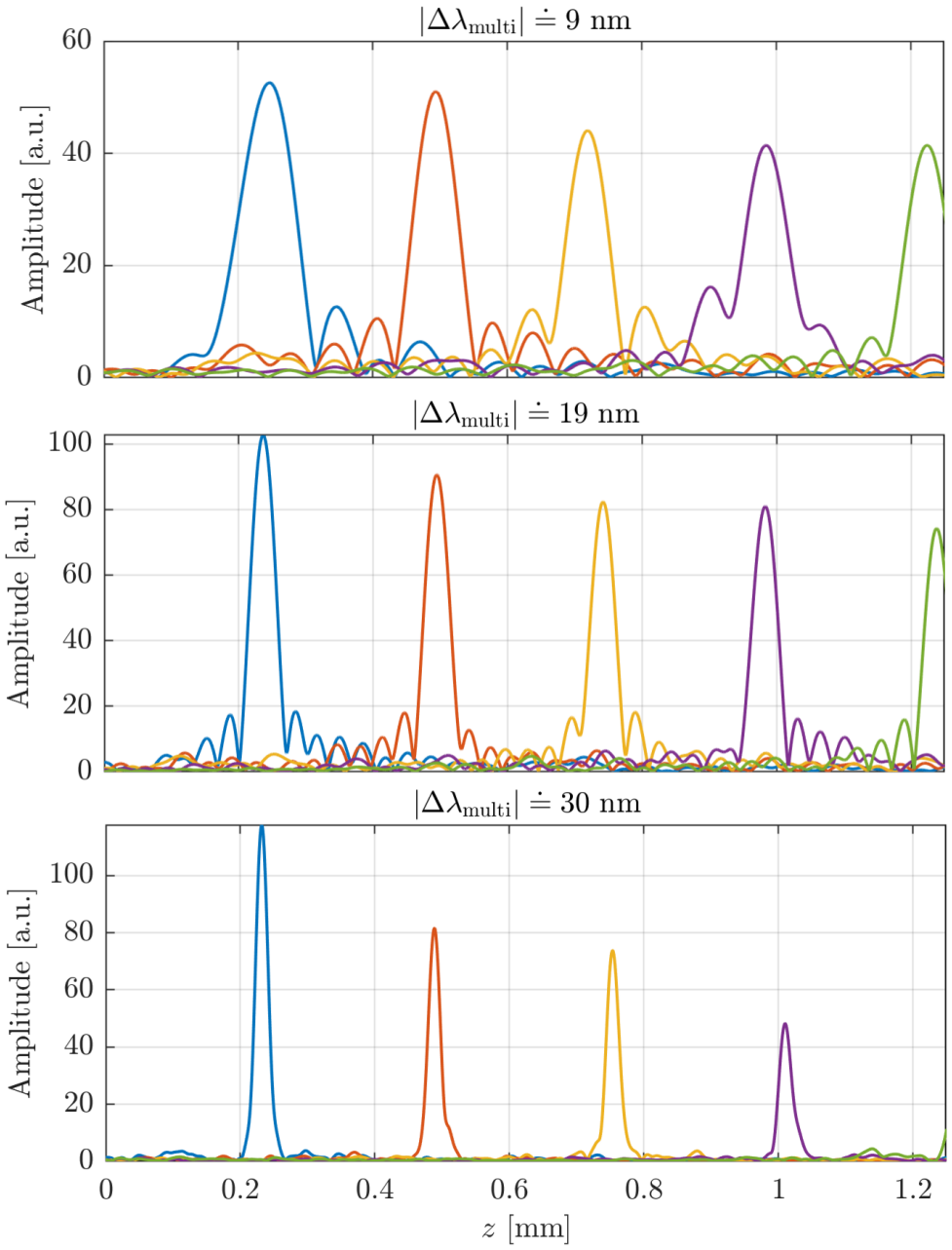

Figure 7.25: Point spread functions roll-off measurements for three different tuning bandwidths $|\Delta\lambda_{\text{multi}}|$.

Using the setup in Fig. 7.19, with the swept source adjusted to a tuning bandwidth of 30 nm, B-scan OCT images of sweat ducts in a finger and the retina of a volunteer were captured in Fig. 7.26. The images were taken with an average tissue surface incident power of 0.78 mW, below the American National Standards Institute (ANSI) limit of 1.925 mW at 1 m [18].

Table 7.3: Measured output powers P_{out} and P_{BOA} and 50% sensitivity drop imaging depths Δz_{6dB} for three different tuning bandwidths $|\Delta\lambda_{\text{multi}}|$. The imaging depth for $|\Delta\lambda_{\text{multi}}| = 0\,\text{nm}$ was estimated using the single sided imaging depth expression $\Delta z_{\text{6dB}} \approx 0.22\lambda^2/\delta\lambda_{\text{stat}}$ (see Eq. (2.13)).

$\lvert\Delta\lambda_{\text{multi}}\rvert$ [nm]	P_{out} [mW]	P_{BOA} [mW]	Δz_{6dB} [mm]
0	1.1	5.7	2.3
9	1.1	5.5	2
19	1	4.9	1.8
30	0.8	4.3	0.9

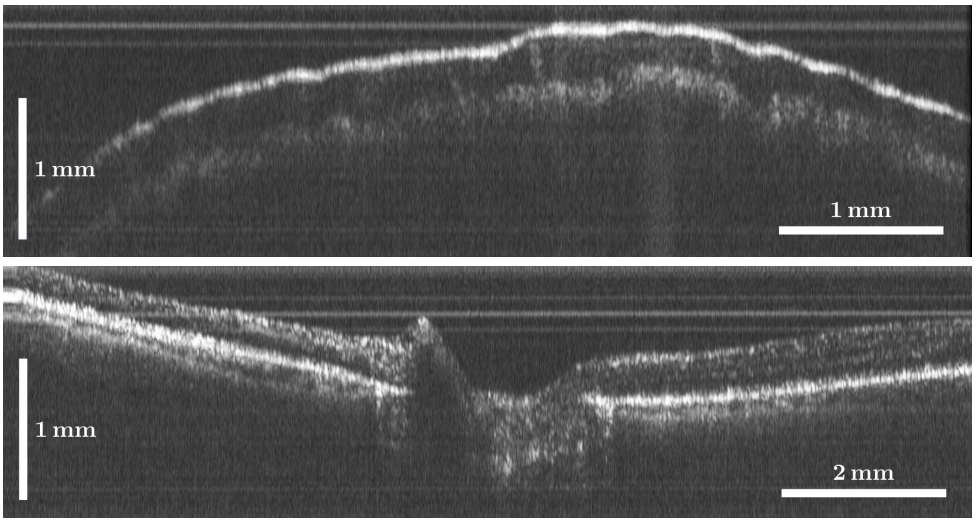

Figure 7.26: B-scans captured with the setup in Fig. 7.19. **Top:** A finger tip. **Bottom:** Retina.

7.4.3 Conclusion

The first multi-harmonic DTML swept source at 1 µm for OCT is demonstrated, exhibiting tuning over 30 nm bandwidth at nearly 1 MHz sweep rate. A 1 mm imaging depth is achieved and a sensitivity of up to 90 dB is measured at a small z value. The first OCT images of a finger tip and the retina are captured employing a multi-harmonic DTML-SS. The apparent course for future research is to achieve wider tuning bandwidths while preserving the coherence properties of the laser. To this end, the following optimisation steps are proposed to improve the multi-harmonic DTML performance:

- Applying narrower modulation windows below 50 ps to achieve stronger ASE suppression, potentially improving the signal-to-noise ratio and coherence performance of the laser, as demonstrated in Subsec. 6.4.2.
- Employing a wider electrical bandwidth VCO or a scheme of grouping several VCOs, which could enlarge both $\Delta\lambda_{\text{multi,sat}}$ and $\Delta\lambda_{\text{multi,one}}$ (see Fig. 7.21).
- Tolerating the dual-wavelength operation by employing CLF with stored channelled spectra, thereby removing the non-dual wavelength tuning bandwidth limit $\Delta\lambda_{\text{multi,n-d}}$ as given by Eq. (7.11).
- Assembling an all polarisation-maintaining (PM) architecture by identifying a manufacturer of PM-based cFBGs, which would eliminate the dependence of the central wavelength and the spectral modulation on the polarisation state inside the cavity.
- Splicing fibre components together to reduce losses inside the cavity and lower R_{sat} as given by Eq. (7.8), and thereby extending $\Delta\lambda_{\text{multi,sat}}$ in accordance with Eq. (7.9).

The multi-harmonic DTML laser emerges as a promising fully akinetic, simple in design, low cost solution for megahertz SS-OCT applications.

Bibliography

[1] R. Riha and A. Podoleanu, "An approximative fiber laser cavity dispersion assessment technique using mode-locked wavelength tuning," in *Optical Coherence Tomography and Coherence Domain Optical Methods in Biomedicine XXVII*. Optica, 2022, p. 512.

[2] R. Riha, A. M. Jimenez, G. Venugopal, M. Klufts, R. Huber, and A. Podoleanu, "Dispersion-tuned mode-locked laser for swept source OCT at 850 nm using a cFBG and the pulse modulation technique," *IEEE Photonics Journal*, vol. 16, no. 4, pp. 1–5, 2024.

[3] R. Riha, A. Bradu, and A. Podoleanu, "Dual resonance akinetic dispersive cavity swept source at 900 kHz using a cFBG and an intensity modulator," *Opt. Lett.*, vol. 47, no. 16, pp. 4032–4035, 8 2022.

[4] R. Riha, A. M. Jimenez, and A. Podoleanu, "Comprehensive theoretical model for multi-harmonic dispersion-tuned mode-locking (DTML) for use in swept-source OCT," *Opt. Express*, vol. 33, no. 19, pp. 40 969–40 996, Sep 2025.

[5] B.-K. Kim, J. C. Lee, Y. M. Jhon, M. W. Kim, S.-K. Kim, S. S. Choi, and M. S. Oh, "Characteristics of the intracavity dispersion in an erbium-doped fiber laser," *Optics Letters*, vol. 24, no. 6, pp. 391–393, 1999.

[6] Corning Incorporated. (2025) SMF-28e+® optical fiber — single-mode fiber. [Online]. Available: https://www.corning.com/optical-communications/worldwide/en/home/products/fiber/optical-fiber-products/smf-28e-.html

[7] VFibre. (2025) VFibre official website. [Online]. Available: http://www.vfibre.com/

[8] O/E Land Inc. (2025) O/e land inc. official website. [Online]. Available: https://www.o-eland.com/

[9] H. Nagai and S. Yamashita, "Coherence improvement in dispersion-tuned swept laser by pulse modulation," *Electronics Letters*, vol. 50, pp. 1729–1731, 2014.

[10] A. Bradu, S. Rivet, and A. Podoleanu, "Master/slave interferometry – ideal tool for coherence revival swept source optical coherence tomography," *Biomed. Opt. Express*, vol. 7, no. 7, pp. 2453–2468, 7 2016.

[11] S. Yamashita, N. Yuichi, K. Ryosei, and K. Osamu, "Wide and fast wavelength-swept fiber laser based on dispersion tuning for dynamic sensing," *Journal of Sensors*, vol. 2009, pp. 1–12, 01 2009.

[12] M. F. Shirazi, P. Kim, M. Jeon, and J. Kim, "Full-field optical coherence tomography using galvo filter-based wavelength swept laser," *Sensors*, vol. 16, no. 11, pp. 1–9, 2016.

[13] G.-H. Han, S.-W. Cho, N. S. Park, and C.-S. Kim, "Electro-optic swept source based on AOTF for wavenumber-linear interferometric sensing and imaging," *Fibers*, vol. 4, no. 2, pp. 1–8, 2016.

[14] R. F. Stancu and A. G. Podoleanu, "Dual-mode-locking mechanism for an akinetic dispersive ring cavity swept source," *Opt. Lett.*, vol. 40, no. 7, pp. 1322–1325, 4 2015.

[15] F. Toadere, R. F. Stancu, W. Poon, D. Schultz, and A. G. Podoleanu, "1 MHz akinetic dispersive ring cavity swept source at 850 nm," *IEEE Photonics Technology Letters*, vol. 29, no. 11, pp. 933–936, 2017.

[16] S. Rivet, M. Maria, A. Bradu, T. Feuchter, L. Leick, and A. Podoleanu, "Complex master slave interferometry," *Opt. Express*, vol. 24, no. 3, pp. 2885–2904, 2 2016.

[17] A. G. Podoleanu and A. Bradu, "Master–slave interferometry for parallel spectral domain interferometry sensing and versatile 3D optical coherence tomography," *Opt. Express*, vol. 21, no. 16, pp. 19 324–19 338, 2013.

[18] H. D. Lee, G. H. Kim, J. G. Shin, B. Lee, C.-S. Kim, and T. J. Eom, "Akinetic swept-source optical coherence tomography based on a pulse-modulated active mode locking fiber laser for human retinal imaging," *Sci Rep*, vol. 8, p. 17660, 2018.

[19] H. D. Lee, M. Y. Jeong, C.-S. Kim, J. G. Shin, B. H. Lee, and T. J. Eom, "Linearly wavenumber-swept active mode locking short-cavity fiber laser for in-vivo oct imaging," *IEEE Journal of Selected Topics in Quantum Electronics*, vol. 20, no. 5, pp. 433–440, 2014.

[20] J. P. Salvestrini, L. Guilbert, M. Fontana, M. Abarkan, and S. Gille, "Analysis and control of the dc drift in linbo3based mach–zehnder modulators," *Journal of Lightwave Technology*, vol. 29, no. 10, pp. 1522–1534, 2011.

Chapter 8

Conclusion

Over the years, several types of swept sources for use in SS-OCT have been reported, ranging from mechanical-based configurations, such are grating-based, MEMS-VCSELs, or FDML, to exploiting akinetic principles, such are acousto-optics, all-seminconductor designs, time-stretching, or SPML (see Chap. 3). The first tunable laser exploiting a fibre cavity with large dispersion was reported already in 1998, and a rapidly swept source using DTML was demonstrated for the first time in 2006. This thesis focused on description of underlying physical principles of DTML swept lasers and reviewed the historical development of this type of laser. It presented a rigorous theoretical model for a novel multi-harmonic DTML regime and reviewed trends in mathematical modelling of DTML lasers. Finally, several DTML swept sources architectures were designed and experimentally evaluated.

Starting with a brief description of the dispersion properties of fibre laser cavities, Chap. 4 explained the principle of tuning of standard single-harmonic DTML lasers and rigorously derived the expression for the tuning bandwidth of this type of laser. It was shown that the emission wavelength as a function of the modulation frequency forms tuning bands, each band corresponding to a harmonic order of mode-locking. The chapter then adopted a spectral filtering approach, introducing the saturation and one round trip operations and showing trade-offs between the achievable tuning bandwidth and coherence performance. In the last part of the chapter, the historical development of DTML swept lasers was reviewed, categorising the lasers chronologically into three generations. The

1st generation lasers consisted of long cavities with fibre-based dispersion, limiting the achievable sweep rates to a few kHz. The second generation introduced cFBGs as the dispersive element, reducing the cavity length, enabling anomalous dispersion across all wavelengths, and increasing sweep rates up to tens or hundreds of kHz. The 3rd generation designs replaced direct modulation of the gain medium with a fast external intensity modulator, enhancing the stability and coherence of mode-locking. The chapter concludes by identifying key parameters for optimising DTML performance, including short cavity lengths, anomalous dispersion, and narrow modulation windows.

Chap. 5 comprehensively described the advance from the single-harmonic to multi-harmonic DTML regime. To this goal, the many sweep cycles mathematical framework was developed, simplifying the description of the relationship between the spectral content of the modulation signal and the optical spectrum of the laser. Two key conditions for the multi-harmonic regime were identified: (i), the sweep rate must be close to the fundamental frequency of the cavity, and (ii), the modulation frequency range must be broad enough to span multiple tuning bands (i.e., harmonic orders). Within the many sweep cycles framework, it was shown that if the sweep rate exactly matches the fundamental frequency of a specific wavelength, a single, stationary emission at this wavelength is observed. In contrast, detuning the sweep rate from this fundamental frequency results in wavelength tuning, with a bandwidth proportional to the detuning. This linear dependency was also rigorously derived. Adopting the spectral filtering approach, the chapter also derived the saturation and one round trip operation bandwidth limits, revealing trade-offs between the tuning bandwidth and coherence performance in the multi-harmonic DTML regime. In the last part, the chapter compared multi-harmonic DTML to both single-harmonic DTML and the well established FDML technique. A key similarity with FDML is that, since the sweep rate is close to the fundamental frequency of the cavity in both cases, the whole wavelength bandwidth is stored inside the cavity at any time, unlike in the single-harmonic DTML, where only a small portion of the bandwidth is stored. Some advantages, such as a low complexity and much lower cost, and limitations, such as a limited photon number of round trips, of the multi-harmonic DTML over FDML were identified.

Chap. 6 reviewed trends in mathematical modelling of DTML lasers, extended with original contributions. The chapter began with a traditional average model based on the generalised nonlinear Schrödinger equation to describe cavity dynamics, while also highlighting its limitations for accurately modelling DTML lasers. A more accurate discrete approach to modelling lasers was then presented, in which an individual transfer function for each element appearing in a DTML cavity was derived, detailing also its effects on pulse propagation. These elements include loss, dispersion, fibre delay, SOA amplification, amplitude modulation, and a newly added phase noise term, representing a key extension to accurately simulate realistic DTML lasers. Utilising this discrete framework, a representative DTML cavity was modelled to examine two key performance parameters: the amount of cavity dispersion and the modulation window width. In agreement with prior modelling studies, it was confirmed that anomalous dispersions produce narrower linewidths than normal dispersions, due to the interplay between dispersion and nonlinear effects in the cavity. In the investigation of the modulation window width effect, it was observed that the lasing reaches its stabilised state after fewer number of round trips for narrower windows. Finally, for the first time, it was numerically demonstrated that narrower windows moderate the linewidth broadening in realistic DTML cavities with presence of phase noise, a result consistent with the experimental observations reported in the previous DTML studies. These findings assist in design and optimisation of DTML swept sources.

In the last experimentally focused Chap. 7, an approximative cavity dispersion assessment method was proposed and three DTML swept sources architectures were presented and experimentally evaluated. Sec. 7.1 provides a simple yet effective method for an approximative cavity dispersion assessment in a DTML laser cavity without the need for additional components required for DTML itself. The method exploits the linear dependence between the shift in the emission wavelength and change in the modulation frequency derived in Chap. 2. The method was validated using spools of a SMF-28e fibre, yielding results consistent with values found in the literature. After the validation, cavity dispersions were evaluated for two different cFBGs with unknown dispersions inserted in a DTML cavity. This approximative method was then used for dispersion assessment in

the DTML lasers presented throughout Chap. 7.

In Sec. 7.2, a (single-harmonic) DTML swept source operating at 850 nm was demonstrated, combining a cFBG and pulse modulation technique. This implementation was enabled by recent advances in high-speed modulator technology and the availability of cFBGs at this wavelength. Unlike previous DTML designs at 850 nm, which relied on direct SOA modulation or long dispersive fibre, the presented laser achieved improved coherence and higher sweep rates. The source demonstrated stable tuning over a 35 nm bandwidth at 10 kHz, with an imaging depth of approximately 1 mm, well suited for integration into FFSS-OCT systems, offering a compact, high-speed alternative to current commercial sources limited to 2 kHz sweep rates.

Sec. 7.3 presented a high speed akinetic swept source operating at 1550 nm using the multi-harmonic DTML regime, achieving a sweep rate of approximately 900 kHz. The design employed a high-speed external intensity modulator in combination with a cFBG, enabling MHz range operation with improved coherence and enhanced stability compared to previous multi-harmonic DTML implementations that relied solely on an SOA direct modulation and long fibre as the dispersive element. This design achieved a tuning bandwidth of 25 nm with an imaging depth exceeding 1 mm. The observed coherence degradation at larger tuning bandwidths experimentally confirms the trade-off between bandwidth and coherence predicted in Chap. 5.

Chap. 7 finished with Sec. 7.4, presenting a 1 MHz multi-harmonic DTML swept source operating at 1 µm. This swept source represents the culmination of the knowledge and optimisation practises accumulated over the years of research on the multi-harmonic DTML regime. Notably, it very accurately experimentally validated the tuning bandwidth predictions and bandwidth limits theoretically derived in Chap. 5. Owing to its coherence and high signal-to-noise performance of the source, the first OCT images of a finger tip and the retina were captured using a multi-harmonic DTML swept source. The section concluded with optimisation steps to improve the multi-harmonic DTML operation, which are here repeated for their key importance in the future research of this novel sweeping regime:

- Applying narrower modulation windows to achieve stronger ASE suppression, po-

tentially improving the signal-to-noise ratio and coherence performance of the laser, as demonstrated in Subsec. 6.4.2.

- Employing a wider electrical bandwidth VCO or a scheme of grouping several VCOs, which could enlarge both $\Delta\lambda_{\text{multi,sat}}$ and $\Delta\lambda_{\text{multi,one}}$ (see Fig. 7.21).

- Tolerating the dual-wavelength operation by employing CLF with stored channelled spectra, thereby removing the non-dual wavelength tuning bandwidth limit $\Delta\lambda_{\text{multi,n-d}}$ as given by Eq. (5.17).

- Assembling an all polarisation maintaining (PM) architecture by identifying a manufacturer of PM-based cFBGs, which would eliminate the dependence of the central wavelength and the spectral modulation on the polarisation state inside the cavity.

- Splicing fibre components together to reduce losses inside the cavity and lower R_{sat} as given by Eq. (4.16), and thereby extending $\Delta\lambda_{\text{multi,sat}}$ in accordance with Eq. (5.19).

Because for its key ability of mode-locking at different harmonic orders simultaneously by using a single modulation element, another possible future direction of research for the multi-harmonic DTML beyond swept source OCT is the feasibility and potential application as a source of electro-optic combs [1, 2].

Due to its distinctive ability to support simultaneous mode-locking at multiple harmonic orders using a single modulation element, multi-harmonic DTML offers potential for applications beyond swept-source OCT. One particularly promising direction is its possible use as a source of electro-optic frequency combs [1, 2]. In this context, the multi-harmonic operation could enable generation of combs with adjustable comb number, potentially extending the capabilities of existing electro-optic comb architectures. However, further research is required to assess the feasibility, spectral purity and long-term stability of such sources.

While DTML lasers do not achieve the imaging depths of FDML lasers or the tens of megahertz sweep rates obtainable with time-stretching and SPML lasers, they offer compelling advantages in terms of design simplicity, ease of operation, and a high stability considering their relatively low cost. Without any modifications to a standard DTML

cavity, a generalised multi-harmonic megahertz DTML regime was discovered and its principle of tuning and trade-offs between the tuning bandwidth and coherence performance have been rigorously described in this work. Given these findings, the multi-harmonic DTML laser is now a promising fully akinetic, simple in design, low cost solution for megahertz SS-OCT applications.

Bibliography

[1] A. Parriaux, K. Hammani, and G. Millot, "Electro-optic frequency combs," *Adv. Opt. Photon.*, vol. 12, no. 1, pp. 223–287, Mar 2020.

[2] I. Coddington, N. Newbury, and W. Swann, "Dual-comb spectroscopy," *Optica*, vol. 3, no. 4, pp. 414–426, Apr 2016.

Appendix A

Peer-reviewed articles published during the doctoral course

Peer-reviewed articles

[1] R. Riha, A. Bradu, and A. Podoleanu, "Dual resonance akinetic dispersive cavity swept source at 900 kHz using a cFBG and an intensity modulator," *Opt. Lett.*, vol. 47, no. 16, pp. 4032–4035, 8 2022.

[2] R. Riha, A. M. Jimenez, G. Venugopal, M. Klufts, R. Huber, and A. Podoleanu, "Dispersion-tuned mode-locked laser for swept source OCT at 850 nm using a cFBG and the pulse modulation technique," *IEEE Photonics Journal*, vol. 16, no. 4, pp. 1–5, 2024.

[3] A. M. Jimenez, R. Cernat, A. Bradu, R. Riha, E. A. P. Grijalva, B. O. Meyer, T. Ansbaek, K. Yvind, and A. Podoleanu, "Downconversion master slave OCT with a bidirectional sweeping laser," *Journal of Biophotonics*, 2024.

[4] R. Riha, A. M. Jimenez, and A. Podoleanu, "Comprehensive theoretical model for multi-harmonic dispersion-tuned mode-locking (DTML) or use in swept-source OCT," *Opt. Express*, vol. 33, no. 19, pp. 40 969–40 996, Sep 2025.

Peer-reviewed conference proceedings

[1] R. Riha and A. Podoleanu, "An approximative fiber laser cavity dispersion assessment technique using mode-locked wavelength tuning," in *Optical Coherence Tomography and Coherence Domain Optical Methods in Biomedicine XXVII*. Optica, 2022, p. 512.

[2] R. Riha, A. Bradu, and A. G. Podoleanu, "A dual resonance sweeping regime in dispersion tuned akinetic swept source at 1550 nm," in *Optical Coherence Tomography and Coherence Domain Optical Methods in Biomedicine XXVII*, vol. 12367. SPIE, 2023, p. 1236708.

[3] R. Riha and A. Podoleanu, "A fully akinetic FDML-like swept source for SS-OCT," in *Optical Coherence Imaging Techniques and Imaging in Scattering Media V*, vol. 12632. SPIE, 2023, p. 126320D.

Appendix B

Mathematical modelling code in MATLAB

```
%loss transfer function (Eq. (6.11) and Eq. (6.12))
function A_out = loss(A_in, l)
%l: linear insertion loss
%l =  1 - R_cFBG for a cFBG with a reflectivy R_cFBG
A_out = sqrt(1 - l) * A_in;
end
```

```
%dispersion transfer function  (Eq. (6.15))
function A_out = dispersion(A_in, T, GDD)
%T: time grid
%GDD: group delay dispersion
n = length(T);
d_T = T(2)-T(1);
tau = n*d_T;
Omega = 2*pi*(-1/(2*d_T) : 1/(tau) : 1/(2*d_T)-1/(tau)); %
   frequency grid
A_out = ifftshift(ifft(fftshift(exp(1i*(Omega).^2*GDD/2).*
   fftshift(fft(fftshift(A_in))))));
```

```
end
```

```
%fibre delay transfer function  (Eq. (6.17))
function A_out = fibre(A_in, T, L_f, GVD_f , rho_f , gamma_f)
%T: time grid
%L_f: fibre length
%GVD_f: fibre group velocity dispersion
%rho_f: fibre attenuation
%gamma_f: fibre nonlinear coefficient
n = length(T);
d_T = T(2)-T(1);
tau = n*d_T;
A_in_max = max(abs(A_in));
Omega = 2*pi*(-1/(2*d_T):1/(tau):1/(2*d_T)-1/(tau)); %
   frequency grid
phi_lin = Omega.^2*GVD_f*L_f/2; %linear phase delay
phi_nl = gamma_f*(1 - exp(-rho_f*L_f/2))/rho_f*abs(A_in).^2;
   %nonlinear phase delay
A_out = exp(-rho_f*L_f/2).*ifftshift(ifft(ifftshift(exp(1i*
   phi_lin).*fftshift(fft(fftshift(A_in.*exp(1i*phi_nl)))))))
   ;
end
```

```
%SOA transfer function (Eq. (6.21) and Eq. (6.22))
function A_out = soa(A_in, T, g_small, E_sat, alpha, tau_c);
%T: time grid
%g_small: small signal gain
%E_sat: saturation energy
%alpha: linewidth enhancement factor
%tau_c: carrier lifetime (= effective gain recovery time in
   the simulations)
```

```
g_small_log = log(small_gain); %logarithmic small gain
I_in = abs(A_in).^2/E_sat; %normalised intensity
g = zeros(1, length(T)); %gain
d_T = T(2) - T(1);
T_shift = T - T(1);
%Runge Kutta method for g
f = @(T_shift, g, I_in) (g_small_log - g)/tau_c - I_in(floor(
   T_shift/d_T) + 1)(exp(g) - 1);
for i = 1 : length(T_shift) - 1
k_1 = d_T*f(T_shift(i), g(i), I_in);
k_2 = d_T*f(T_shift(i) + d_T/2 , g(i) + k_1/2, I_in);
k_3 = d_T*f(T_shift(i) + d_T/2, g(i) + k_2/2, I_in);
k_4 = d_T*f(T_shift(i) + d_T, g(i) + k_3, I_in);
g(i + 1) = g(i) + (1/6)*(k_1 + 2*k_2 + 2*k_3 + k_4);
end
A_out = A_in.*exp(g/2).*exp(-1i*g*alpha/2);
end
```

```
%modulation transfer function (Eq. (6.26))
function A_out = modulation(A_in, T, tau_m);
%T: time grid
%tau_m: modulation window width
A_out = exp(-2*log(2)/(tau_m)^2*T.^2).*A_in;
end
```

```
%phase noise transfer function (Eq. (6.29))
function A_out = phase_noise(A_in, sigma_noise);
%sigma_noise: phase noise variance
phi_noise = randn([1, length(A_in)])*sigma_noise;
A_out = exp(1i * phi_noise).*A_in;
end
```

```
%round trip transfer function example (Eq. (6.30))
%N: number of round trips
for i = 1 : N
A = loss(A, l_CIRC);
A = dispersion(A, T, GDD_cFBG);
A = loss(A, l_cFBG);
A = loss(A, l_CIRC);
A = modulation(A, T, tau_m);
A = loss(A, l_IM);
A = soa(A, T, g_small, E_sat, alpha, tau_c);
A = phase_noise(A, sigma_noise);
end
```